



HAL
open science

3D Anderson transition of ultracold atoms in disordered potentials: observation of the mobility edge

Yukun Guo

► **To cite this version:**

Yukun Guo. 3D Anderson transition of ultracold atoms in disordered potentials: observation of the mobility edge. Optics [physics.optics]. Université Paris-Saclay, 2023. English. NNT : 2023UP-ASP032 . tel-04059506

HAL Id: tel-04059506

<https://pastel.hal.science/tel-04059506>

Submitted on 5 Apr 2023

HAL is a multi-disciplinary open access archive for the deposit and dissemination of scientific research documents, whether they are published or not. The documents may come from teaching and research institutions in France or abroad, or from public or private research centers.

L'archive ouverte pluridisciplinaire **HAL**, est destinée au dépôt et à la diffusion de documents scientifiques de niveau recherche, publiés ou non, émanant des établissements d'enseignement et de recherche français ou étrangers, des laboratoires publics ou privés.

3D Anderson transition of ultracold
atoms in disordered potentials :
observation of the mobility edge
*Transition d'Anderson 3D d'atomes ultra-froids dans des
potentiels désordonnés : observation du seuil de mobilité*

Thèse de doctorat de l'université Paris-Saclay

École doctorale n° 572, Ondes et Matière (EDOM)
Spécialité de doctorat : Physique
Graduate School : Physique

Thèse préparée dans Université Paris-Saclay, Institut d'Optique Graduate
School, CNRS, Laboratoire Charles Fabry, 91127, Palaiseau, France, sous la
direction de Vincent JOSSE, Maître de conférence

Thèse soutenue à Paris-Saclay, le 14 mars 2023, par

Yukun GUO

Composition du jury

Daniel Comparat
Directeur de recherche, Université Paris-Saclay
Jérôme Beugnon
Maître de conférence, Université Sorbonne
Patrizia Vignolo
Professeur, Institut de Physique de Nice
Juliette Billy
Maître de conférence, Université Toulouse III

Président
Rapporteur & Examineur
Rapporteuse & Examinatrice
Examinatrice

Acknowledgements

As I prepare to leave the lab where I have spent the last three years, I reflect on the privilege it has been to grow with this beautiful and complex experiment. There have been moments of great excitement as we achieved our goals, and moments of frustration and discouragement as we faced technical issues one after another. Through these experiences, I have learned to stop complaining and maintain my motivation, and as I gained experience in the lab, I also learned to effectively tackle these difficulties. Through this process, I have become more at peace with myself and more patient and realized that beautiful experimental results do not come from luck on a particular day, but are the result of constant effort, the accumulation of knowledge and experience, and the ability to explore and experiment. As a slow learner, three years may not seem like a long time, but I am grateful for the encouraging results we have achieved at the end of my thesis journey.

I am incredibly grateful to my supervisor, Vincent, for his guidance and support throughout my thesis. He is a highly skilled and talented physicist. He has a clear understanding of huge stories of physics behind our experiments and all the technical issues we were facing. He can memorize all the details of the experiments even in 2008, 15 years ago. Despite his busy schedule of teaching and administration, he always made time to discuss with us. His insight was invaluable in helping me navigate the research process. He is extremely dedicated to the pursuit of accurate and reliable results, and I learned a great deal from his rigorous approach to data analysis and interpretation. Beyond his expertise in physics, Vincent is also a compassionate and considerate supervisor. He made himself available to me, even during the difficult times of the lockdown. He took the time to check in on me and offer words of encouragement when I was feeling demotivated. He was always warm and approachable, and his team-oriented leadership style created a comfortable, relaxing and inclusive environment for everyone in the lab. I am truly grateful for the guidance and support he provided, not only in terms of my research, but also in becoming a better scientist and a more thoughtful team leader.

I am deeply grateful to Alain, who brought me to our group in the summer of 2019 through a mail sent to Munich. He was my professor in the first year of my master's program, where I began my journey in the field of quantum optics. Despite his fame and his age of 75, he is still incredibly passionate about the experiments. He is constantly present at the group seminars and pays close attention to every detail presented. He also frequently organizes

group meetings for our experiment and we discuss together our problems, progress and ideas. I remember when we were preparing for the paper [1], he derived all the equations himself. He is an incredibly dedicated physicist, and when we pointed out any inconsistencies in our data, he would question us until he was fully satisfied with the explanation. He also provided invaluable support and encouragement during my time in the lab, particularly when I was feeling demotivated. He is always enthusiastic about our progress and provided immense support, of course including the funding from the Simon Foundation, which made my thesis work possible. I am particularly grateful for the opportunity to have worked with him, a Nobel laureate, for more than three years. This is an experience that not every PhD student is fortunate enough to have. I am incredibly grateful for this opportunity.

I am also deeply grateful to my colleagues. Baptiste, the last PhD student in our group, made significant contributions to our work and without his work, we would not have achieved the encouraging results we have today. Xudong, the other PhD student. It is a great pleasure to work with. He is always clear in his mind about what we are doing and what is happening, and he is someone that we can fully trust. Niranjan, our post-doc, who joined us last year, brought a wealth of experience and was instrumental in helping us with technical problems. I would also like to thank Azer and Vasiliki for their help in understanding the experiment and teaching me the necessary skills when I first joined the lab. Adrien, who was the Post-Doc before I joined the lab. With Baptiste, they spent a long time to repair the experiment. I am also incredibly grateful to Romaric, Félix, and Gaétan for their invaluable support in providing wavemeters, mirrors, lenses, and other essential experimental materials. It was a great pleasure to work with Quentin, Alfred, and Victor, who were my classmates during my M2 program and it was amazing to reconnect with them in the same group. I am also grateful to all the other PhD students, post-docs, permanent members of the group for their friendliness and for creating a comfortable atmosphere in the group. Each and every one of them has played an essential role in my journey and I am deeply grateful for all of their support, guidance, and camaraderie. They have been a constant source of inspiration and motivation throughout my thesis. Furthermore, I would like to acknowledge the help and support of the technical staff in the lab, Jean-rené, Marc, and Gwenaél, they have always been willing to assist me with any technical issues I encountered and their expertise has been invaluable to the research of my thesis.

Lastly, I would like to extend my deepest gratitude to my family for their unwavering

support throughout my studies and my time in Europe. They have been a constant source of financial and emotional support, and I am grateful for the daily calls and conversations where I could share my progress, joys, and struggles with them. They have always been there to listen and offer their support. I am also deeply grateful to my friends who have accompanied me throughout my thesis journey. They have been an important source of support, laughter, and companionship during this challenging but rewarding experience.

Résumé en français

La localisation d'Anderson est un phénomène qui se produit dans les systèmes désordonnés, où la fonction d'onde d'une particule quantique (ou d'ondes cohérentes) se localise dans une petite région de l'espace au lieu de s'étendre. La localisation d'Anderson est due à l'interférence d'ondes multi-diffusées causée par le désordre dans le système, ce qui peut conduire à la suppression du transport. L'étude de la localisation d'Anderson a une longue histoire, qui remonte aux travaux pionniers de Philip Anderson en 1958 [2], lorsqu'il a prédit que les états électroniques d'un solide désordonné pouvaient être localisés. Depuis lors, la localisation d'Anderson a été observée dans divers systèmes, y compris les systèmes électroniques [3, 4, 5, 6], photonique [7, 8, 9, 10, 11, 12], et acoustique [13, 14, 15, 16, 17] au cours des 50 dernières années. En plus de ces plateformes, l'atome ultrafroid devient un excellent candidat pour étudier les phénomènes non triviaux liés à la localisation d'Anderson depuis que le premier condensat de Bose-Einstein a été réalisé [18, 19]. L'atome ultrafroid est très utile pour simuler la physique de la matière condensée [20, 21]. Le condensat de Bose-Einstein est une bonne source d'onde de matière cohérente, et la longueur d'onde de Broglie λ_{dB} des atomes peut être contrôlée de nm à μm . Nous pouvons établir le système d'une dimension à trois dimensions. Il est pratique de générer un potentiel conservateur pour les atomes par un potentiel dipolaire optique avec des lasers, et il est facile de contrôler les paramètres du potentiel, par exemple, la nature (attractive ou répulsive), la fréquence du piège, la profondeur du piège, et même la forme, etc. L'interaction peut être réglée par la résonance de Feshbach pour les interactions répulsives et attractives [22]. Il existe de nombreuses méthodes d'observation, par exemple l'imagerie directe in situ [23, 24], le temps de vol pour observer la distribution de la quantité de mouvement [25, 26, 27], la spectroscopie pour mesurer l'énergie, etc. Et les images sont directement l'imagerie d'absorption ou de fluorescence des atomes capturée dans une caméra CCD. Tous ces avantages : paramètres contrôlables, potentiel facile à utiliser, interaction accordable et observation directe, font des atomes ultrafroids un excellent candidat pour

simuler et étudier expérimentalement la localisation d'Anderson.

Voici les grandes lignes de ce manuscrit :

Chapitre 2 : Ce chapitre donne un aperçu du contexte physique de la localisation d'Anderson et de la transition d'Anderson en trois dimensions (3D). Il commence par une brève introduction à la théorie de la localisation d'Anderson, en mettant particulièrement l'accent sur la transition d'Anderson en 3D. Cela permet de comprendre les concepts de base et les motivations de l'étude de la transition d'Anderson en 3D. La seconde moitié du chapitre passe en revue les efforts expérimentaux antérieurs visant à mesurer le seuil de mobilité de la transition d'Anderson en 3D, en soulignant leurs réalisations et leurs limites. Le chapitre aborde également les principaux défis et goulets d'étranglement dans la mesure directe du seuil de mobilité au cours des 10 dernières années et la façon dont le protocole expérimental de spectroscopie proposé dans notre expérience relève ces défis et cherche à mesurer le seuil de mobilité.

Chapitre 3 : Ce chapitre présente une vue d'ensemble du dispositif expérimental et du protocole utilisés dans la recherche. La première section présente brièvement les propriétés des condensats de Bose-Einstein, jetant les bases du travail expérimental à venir. Le reste du chapitre se penche sur les détails du cycle expérimental, en fournissant une description détaillée des étapes expérimentales utilisées pour créer un condensat de Bose-Einstein et l'observer. Le chapitre couvre les techniques et les méthodes utilisées dans l'expérience, les procédures et l'équipement utilisé.

Chapitre 4 : Ce chapitre porte sur le speckle optique utilisé dans l'expérience. Le chapitre commence par examiner les propriétés statistiques du diffuseur utilisé pour générer le speckle, ce qui permet de bien comprendre les propriétés et les caractéristiques du diffuseur. Nous examinons ensuite les propriétés du champ de speckle, y compris la distribution de l'intensité et sa corrélation spatiale, ce qui permet de comprendre en détail le speckle laser. En outre, le chapitre comprend une description de la mise en œuvre expérimentale du potentiel de speckle, couvrant l'appareil et les méthodes utilisés pour créer un désordre dans les atomes.

Chapitre 5 : Ce chapitre porte sur le transfert de radiofréquences (rf) dans le désordre dépendant de l'état. Il explique le raisonnement qui sous-tend le choix des niveaux atomiques utilisés pour le transfert de rf. Il donne un aperçu du dispositif expérimental utilisé pour générer le désordre état-dépendant proche de la résonance utilisé dans des recherches antérieures en 2018. Le chapitre présente les résultats des mesures de la fonction spectrale publiés en 2018 [28]. En outre, il discute de la limitation principale de cette configuration de speckle monochromatique, qui empêche les mesures du seuil de mobilité dans cette plate-forme.

Chapitre 6 : Ce chapitre présente le schéma de speckle bichromatique, qui utilise deux lasers pour générer un désordre état-dépendant [1] afin de résoudre le problème de la durée de vie dans le désordre état-dépendant proche de la résonance en 2018. Ce chapitre démontre que cette approche améliore de manière significative la durée de vie des atomes en surmontant la limitation clé de la configuration de speckle monochromatique. Il présente une vue d'ensemble de la mise en œuvre expérimentale utilisée pour vérifier la dépendance d'état du potentiel de speckle et reproduire le transfert rf effectué en 2018. Il fournit également des résultats expérimentaux montrant l'amélioration de la durée de vie des atomes dans le désordre.

Chapitre 7 : S'appuyant sur les résultats du chapitre 6, ce chapitre présente la méthode utilisée pour mesurer le seuil de mobilité à l'aide d'un potentiel de speckle bichromatique dépendant de l'état. Il fournit des résultats expérimentaux détaillés et des preuves de la transition d'Anderson en 3D. Le chapitre démontre que l'estimation du seuil de mobilité basée sur la mesure est en excellent accord avec les prédictions numériques, ce qui a été l'objectif principal de notre équipe pendant un temps considérable. Cependant, il aborde également les problèmes techniques actuels et offre des perspectives d'amélioration. Les chapitres 6 et 7 mettent en lumière les principales réalisations expérimentales de ma recherche doctorale, menée en collaboration avec mes collègues.

Contents

Acknowledgements	i
Résumé en français	iv
1 Introduction	1
1.1 Outline	3
2 Anderson localization with ultracold atoms	7
2.1 Microscopic view for the transport in disordered media	7
2.1.0.1 Random walk in disordered media	8
2.1.0.2 Interference and weak localization	11
2.1.0.3 Anderson localization	13
2.1.0.4 Scaling theory for Anderson transition	15
2.2 Ultra cold atoms: a good platform to study Anderson localization	18
2.3 3D Anderson localization and the Anderson transition	19
2.3.1 Experiment of Urbana-Champaign	20
2.3.2 Experiment of Palaiseau	22
2.3.3 Experiment in Florence	24
2.4 Synthesis	26
3 Preparation of Bose-Einstein condensate	30
3.1 Bose-Einstein Condensate	30
3.1.0.1 Statistics for Bose-Einstein condensate	30
3.1.0.2 Gross-Pitaevskii equation for Bose-Einstein condensate	32
3.1.0.3 Thomas-Fermi regime	33
3.2 Properties of ^{87}Rb	35
3.3 Description of experimental cycle	36
3.4 Transverse molasses and Zeeman slowing	38
3.5 Magneto-optical trap	41
3.6 Magnetic trap	42
3.7 RF-evaporation	45
3.8 Loading the atoms in an optical tweezer and transport to the second chamber	46
3.9 Optical evaporation	48
3.10 Cool the atoms even more by adiabatic cooling	51

3.11	Magnetic levitation	51
3.12	Imaging system	55
	3.12.0.1 Absorption imaging	55
	3.12.0.2 Fluorescence imaging	57
4	Optical speckle	59
4.1	The property of diffuser	59
4.2	The distribution of light intensity	62
4.3	Spatially statistical properties of intensity	64
	4.3.0.1 Spatial correlation of the intensity	66
4.4	Experimental implementation	67
5	Transfer scheme in a monochromatic state-dependent disorder	70
5.1	The two-level system composed of $ 1\rangle$ and $ 2\rangle$	72
	5.1.1 Choose the state $ 2\rangle$ and magic point B_0^* of magnetic field.	72
	5.1.2 Two-photon transition	74
5.2	The state-dependent disorder	77
5.3	Spectral function and the transfer in the disorder	79
	5.3.1 Spectral function	79
	5.3.2 Connect the spectral function with the transfer rate of atoms	81
5.4	Experimental measurement of the spectral function with near-resonant speckle	82
5.5	To explore the Anderson transition in this platform?	84
6	Bichromatic state-dependent disordered potential	86
6.1	Bichromatic speckle scheme	87
6.2	Fundamental potential decoherence in state $ 1\rangle$	89
	6.2.0.1 Calculate the normalized bichromatic correlation function	91
	6.2.0.2 The decoherence effect in practice	91
6.3	Reduction of the photon-scattering rate for the disorder-sensitive state	94
6.4	Experimental realization	96
	6.4.1 Experimental set-up	97
	6.4.2 Probing the insensitivity of state $ 1\rangle$ to disorder using a quench	99
	6.4.3 Check the rf-transfer with bichromatic speckle	101
	6.4.4 Improve the lifetime of state $ 2\rangle$	103
7	Measurement of the mobility edge	104
7.1	Scaling law of the mobility edge versus amplitude of disorder	104
	7.1.1 Correlation energy	105
	7.1.2 Universality of the disorder	106
7.2	Experimental procedure	109
7.3	First experimental results and the analysis	112
	7.3.1 The first results for $V_R/h = 416\text{Hz}$	112
	7.3.2 First signature of the mobility edge	113
	7.3.3 Analysis of the central density	116
	7.3.4 Temporal dynamics	118

7.4	Future improvements	119
7.4.1	Improve the lifetime of disordered states	120
7.4.2	Horizontal trap due to magnetic levitation	121
7.4.2.1	Open the trap by increasing the bias field	121
7.4.2.2	Optical anti-trap	122
7.5	Conclusion	124
8	Conclusion and perspectives	126
8.1	Study near the critical regime	127
8.1.1	Critical exponent	127
8.1.2	Multi-fractality near the critical regime	128
8.2	Investigate various configurations of speckle	129
A	Optical evaporation	131
B	Calculation of the normalized bichromatic correlation function	136
B.1	Bichromatic correlation function of the diffuser	136
B.2	Correlation function of the amplitude	137
B.3	3D monochromatic correlation close to the Fourier plane	139
B.4	Bichromatic correlation function of the speckle	140
C	Green function	142
	Bibliography	144

Chapter 1

Introduction

Anderson localization is a phenomenon that occurs in disordered systems, where the wave function of a quantum particle (or coherent waves) becomes localized in a small region of space rather than spreading out. Anderson localization is due to the interference of multiply scattered waves caused by the disorder in the system, which can lead to the suppression of transport. The study of Anderson localization has a long history, dating back to the pioneering work of Philip Anderson in 1958 [2], when he predicted that the electronic states in a disordered solid could be localized. Since then, Anderson localization has been observed in a variety of systems, including electronic[3, 4, 5, 6], photonic[7, 8, 9, 10, 11, 12], and acoustic[13, 14, 15, 16, 17] systems in the past 50 years. In addition to these platforms, the ultracold atom becomes an excellent candidate to investigate the non-trivial phenomena related to Anderson localization[29], since the first Bose-Einstein condensate was realized [18, 19]. Ultracold atom is very useful for simulating condensed matter physics [20, 21]. Bose-Einstein condensate is a good source of the coherent matter wave, and the de Broglie wavelength λ_{dB} of atoms can be controlled from nm to μm . We can establish the system from one-dimensional to three-dimensional. It is convenient to generate a conservative potential for atoms through optical dipole potential with lasers[30], and it is easy to control the parameters of the potential, for example, the nature (attractive or repulsive), the trap frequency, the trap depth, and even the shape, etc. The interaction can be tuned by Feshbach resonance for both repulsive and attractive interactions [22]. There are many ways of observation, for example, direct in-situ imaging[23, 24], time of flight for observing the momentum distribution[25, 26, 27], spectroscopy for measuring the energy, etc. And the images are directly the absorption or fluorescence imaging of atoms captured in a CCD camera. All these advantages: controllable parameters, easy-to-operate potential,

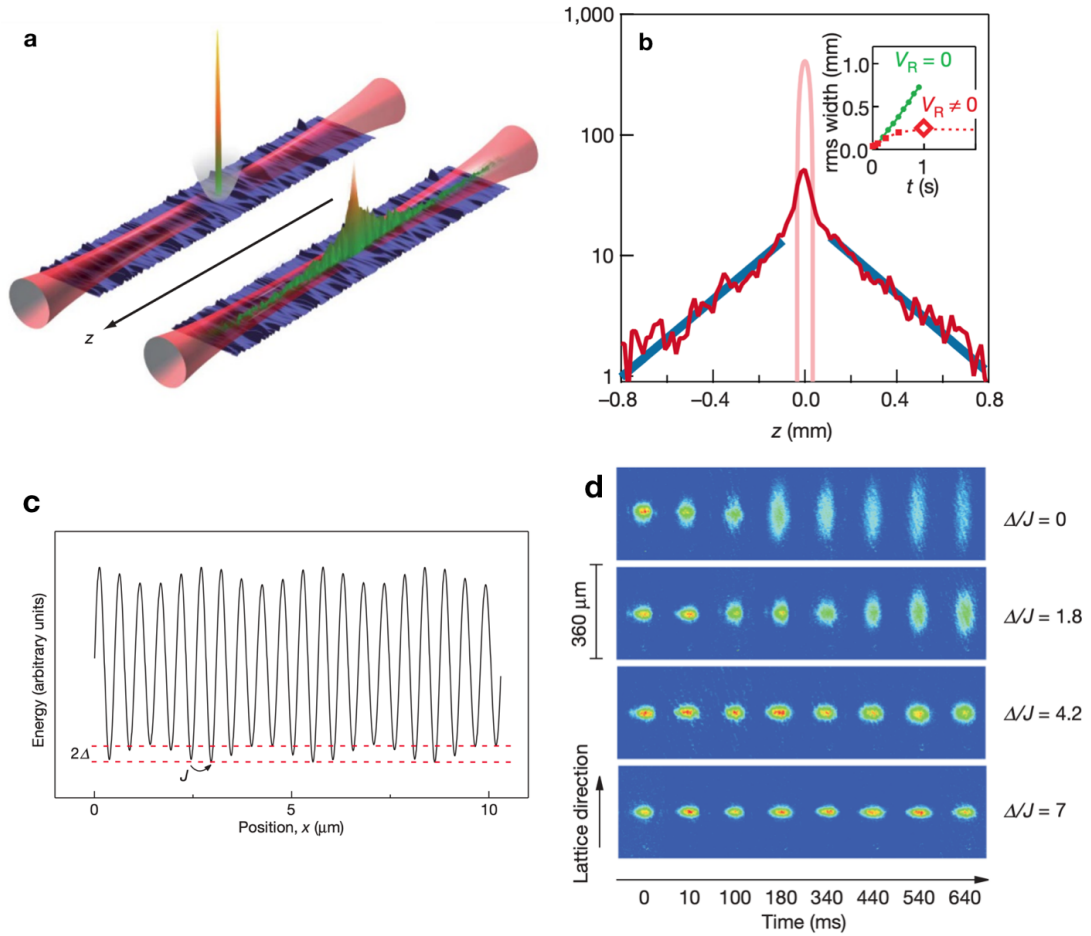


FIGURE 1.1: **The observation of Anderson localization in 1d with ultracold atoms.** **a.** In the experiment of Palaiseau, the disordered potential is generated by laser speckle. **b.** The experimental results of Palaiseau: density profile of the localized BEC after expansion of one second. In the inset, the r.m.s. (root mean square) width of the profile versus time shows that the expansion of atoms reaches a stationary regime after 0.5 s. **c.** In the experiment of Florence, the disordered potential is a quasi-periodic potential combining two lattices of incommensurate frequencies, known as Aubry-André model. J is the tunneling, and Δ represents the strength of disorder. **d.** The evolution of BEC at different strengths of disorder. Figures a and b are from [31], c and d are from [32].

tunable interaction, and direct observation, help the ultracold atoms to become an excellent candidate for simulating and studying Anderson localization experimentally.

The first direct observation of Anderson localization in 1d with ultracold atoms was realized in 2008, in Palaiseau by our team [31] using speckle and in Florence [32] using Aubry-André model, as shown in figures 1.1. These two experiments marked the beginning of the study of Anderson localization with ultracold atoms. Later, people tried to observe

the 3d Anderson localization and attempted to estimate the mobility edge of the Anderson transition with ultracold atoms [33, 34, 35]. But these previous experiments share a common difficulty of loading the atoms in the disorder with a narrow energy distribution. Because of this problem, their estimates of the mobility edge are all based on measuring the localized fraction, which means, not direct measurement. And with the broad energy distribution, one cannot study the critical regime of the Anderson transition. Observing the Anderson transition and measuring the mobility edge remains a very challenging task because of some bottlenecks, which have prevented the direct and precise measurement of the mobility edge for the past decade.

In order to carry out more direct measurements of mobility edge, and to open the possibility of studying the critical regime, our team proposed a spectroscopy scheme: loading the atoms in the disorder with a narrow energy distribution by an rf-transfer in a state-dependent disorder, then observing the transport property of the transferred atoms in the disorder. Our team realized rf-transfer of the atoms in state-dependent disorder by measuring the spectral function in 2018 [28] and demonstrated the energy-resolved loading of atoms in the disorder. But to observe the transport property, it was not enough because the set-up for the state-dependent disorder in 2018 was generated by near-resonant speckle laser, with which the atoms experience strong photon scattering in the disorder, thus destroying the motional wavefunction coherence easily. So the key problem is the photon scattering lifetime of atoms in the disorder is too short compared to the low dynamics of the wavefunction in the disorder.

In this thesis, we will see how we improve the scattering lifetime of the atoms in disorder by two orders of magnitude from using a bichromatic speckle disorder [1]. Then we use this set-up to study the the 3D Anderson transition and measure the mobility edge.

1.1 Outline

We list the outline of this manuscript:

Chapter 2: This chapter provides an overview of the physical background of Anderson localization and the Anderson transition in three dimensions (3D). It begins by giving a

brief introduction to the theory of Anderson localization, with a specific focus on the Anderson transition in 3D. This serves as a foundation for understanding the basic concepts and motivations for studying Anderson localization in 3D. The second half of the chapter reviews previous experimental efforts to measure the mobility edge of the 3D Anderson transition, highlighting their achievements and limitations. The chapter also discusses the main challenges and bottlenecks in directly measuring the mobility edge in the last 10 years and how the proposed experimental protocol of spectroscopy in our experiment addresses these challenges and aims to measure the mobility edge.

Chapter 3: This chapter presents an overview of the experimental setup and protocol used in the research. The first section briefly introduces the properties of Bose-Einstein condensates, laying the foundation for the experimental work to follow. The remainder of the chapter delves into the specifics of the experimental cycle, providing a detailed description of the experimental steps used to create a Bose-Einstein condensate and observe it. The chapter covers the techniques and methods used in the experiment, the procedures, and the equipment used.

Chapter 4: This chapter focuses on the optical speckle used in the experiment. The chapter begins by discussing the statistical properties of the diffuser used to generate the speckle pattern, providing a comprehensive understanding of the diffuser's properties and characteristics. We then examine the properties of the speckle field, including the intensity distribution and its spatial correlation, providing a detailed understanding of the laser speckle. Additionally, the chapter includes a description of the experimental implementation of the speckle potential, covering the apparatus and methods used to create disorder in the atoms.

Chapter 5: This chapter focuses on radio-frequency (rf) transfer in state-dependent disorder. It explains the reasoning behind the choice of atomic levels used for the rf-transfer. It provides an overview of the experimental setup used to generate the near-resonant state-dependent disorder used in previous research in 2018. The chapter presents the results of the measurements of the spectral function as published in 2018 [28]. Additionally, it discusses the key limitation of this monochromatic speckle configuration, which prevents measurements of the mobility edge in this platform.

Chapter 6: This chapter presents the bichromatic speckle scheme, which utilizes two lasers to generate state-dependent disorder[1] to address the problem of the lifetime in the near-resonant state-dependent disorder. The chapter demonstrates that this approach significantly improves the lifetime of atoms by overcoming the key limitation of the monochromatic speckle configuration. It presents an overview of the experimental implementation used to verify the state-dependence of the speckle potential and reproduce the rf-transfer done in 2018. It also provides experimental results showing the improvement in the lifetime of atoms in disorder.

Chapter 7: Building on the results of Chapter 6, this chapter presents the method used for measuring the mobility edge using a bichromatic state-dependent speckle potential. It provides detailed experimental results and presents evidence for the 3D Anderson transition. The chapter demonstrates that the estimation of the mobility edge based on the measurement is in excellent agreement with numerical predictions, which has been the main objective of our team for a considerable time. However, it also discusses the current technical issues and provides perspectives for improvements. Chapters 6 and 7 highlight the main experimental accomplishments of my PhD research, conducted in collaboration with my colleagues.

Résumé en français

Chapter 2

Anderson localization with ultracold atoms

In this chapter, we will delve into the topic of Anderson localization with ultracold atoms. We start by introducing how interference influences the diffusion of particles in disordered media, which will serve as an introduction to the concept of Anderson localization. We will then discuss the crucial role that the dimension of the system plays in Anderson localization and the resulting phase transition in three dimensional system, known as the 3d Anderson transition. In a three-dimensional system, the wave functions of the system fall into two distinct phases: localized and diffusive phases. After introducing the theory of Anderson localization and the Anderson transition, we will review some important experimental works that have been conducted to investigate Anderson localization and particularly 3d Anderson transition using the platform of ultracold atoms in speckle potentials [31, 32, 33, 34, 35, 28]. Finally, we will discuss the current challenges and limitations in experimentally studying the Anderson transition in the last decade[36].

2.1 Microscopic view for the transport in disordered media

We can start with an easy model, a random walk in 1D, to help us understand the diffusion process. Consider a random walk of a particle in a 1D regular lattice. For each step i , the particle can move to its left (moving by $-a$) or right (moving by a) neighbouring sites. We note the displacement of the particle for each step is $\delta\mathbf{x}_i$, so we have $\delta\mathbf{x}_i = \{a, -a\}$. Assuming the diffusion of the particle is *isotropic*, where the probability of going left and

right are equal: $P(\delta\mathbf{x}_i = -a) = P(\delta\mathbf{x}_i = a) = 1/2$. For each step, we can easily obtain the average displacement and its variance:

$$\begin{cases} \langle \delta\mathbf{x}_i \rangle = 0 \\ \langle \delta\mathbf{x}_i^2 \rangle = a^2. \end{cases} \quad (2.1)$$

After N steps, the position $\mathbf{x}(N)$ of the particle is just the sum of the displacement of all the N steps:

$$\mathbf{x}(N) = \sum_{i=1}^N \delta\mathbf{x}_i. \quad (2.2)$$

Each step $\delta\mathbf{x}_i$ is assumed to be independent, so $\{\delta\mathbf{x}_i\}$ is an ensemble of independent random variables. According to the *central limit theorem*, the position $\mathbf{x}(N)$ after N steps, which is the sum of these independent random variables $\delta\mathbf{x}_i$, tends to a Gaussian distribution [37]. We can calculate the average position and its variance after N steps:

$$\begin{cases} \langle \mathbf{x}(N) \rangle = N \langle \delta\mathbf{x}_i \rangle = 0 \\ \langle \mathbf{x}^2(N) \rangle = N \langle \delta\mathbf{x}_i^2 \rangle = N a^2. \end{cases} \quad (2.3)$$

Define the time for one step as τ , thus the time for N steps is $t = N\tau$. So the r.m.s. (root mean square) of the position $\sqrt{\langle \mathbf{x}^2(t) \rangle}$ is proportional to the square root of time: $\sqrt{\langle \mathbf{x}^2 \rangle} = a\sqrt{t/\tau}$. Figure 2.1 is an example of the simulation of a random walk in a 1D regular lattice.

2.1.0.1 Random walk in disordered media

Having the idea of a random walk in a 1D lattice, now we can generalize to a random walk in a disordered media in 2D. As shown in figure 2.2 a, we define mean free path l_s , which is the average distance that the particle experiences between two collisions. Suppose the collision is elastic, so the speed v of the particle is conserved before and after the collision. Every time the particle collides with the scatterer, its trajectory turns by a diffusing angle θ . After N collisions, the particle may turn back and completely lose its initial propagating direction, as shown in figure 2.2 a. We define the average length of this trajectory as the mean transport path l^* [38], and we can calculate it:

$$l^* = l_s + l_s \langle \cos\theta_{12} \rangle + l_s \langle \cos\theta_{12} \cos\theta_{23} \rangle + l_s \langle \cos\theta_{12} \cos\theta_{23} \cos\theta_{34} \rangle + \dots \quad (2.4)$$

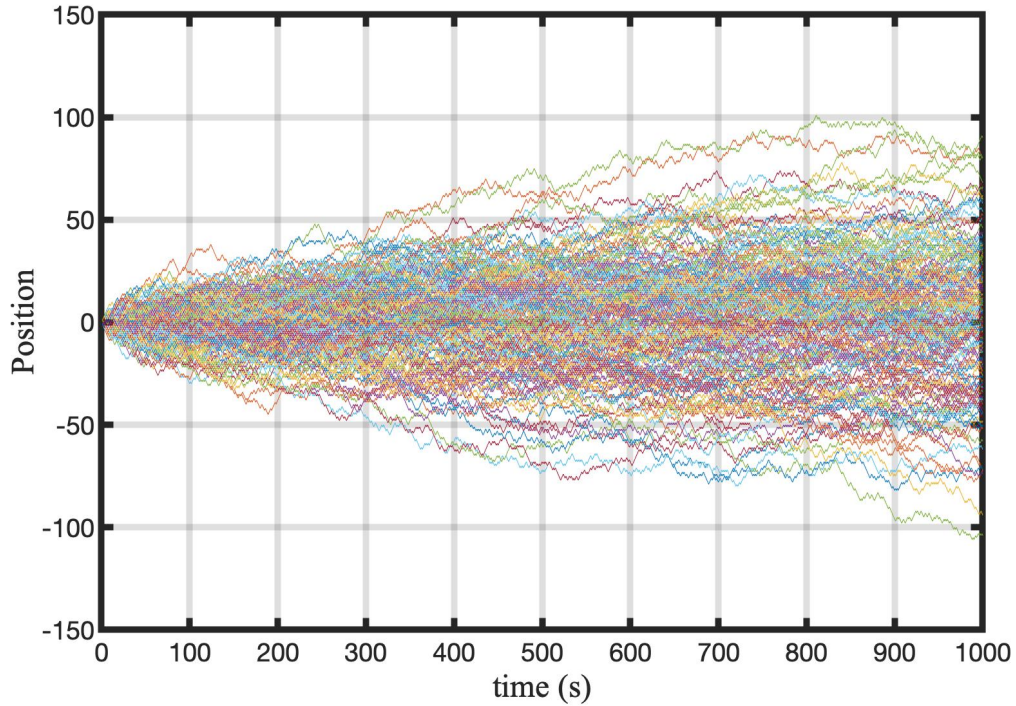


FIGURE 2.1: **Numerical computed 1D random walk.** The horizontal axis is time, one second for each step. The vertical axis is the position \mathbf{x} of the particle in the 1D line. There are 200 realizations and 1000 steps for each one.

The angles $\{\theta_{ii+1}\}$ are supposed to be statistically identical and independent, so we have:

$$\langle \cos\theta_{ii+1}\cos\theta_{i+1i+2} \rangle = \langle \cos\theta_{ii+1} \rangle \langle \cos\theta_{i+1i+2} \rangle = \langle \cos\theta \rangle^2. \quad (2.5)$$

Then the mean transport path l^* is just:

$$l^* = l_s \sum_{i=0}^{N \rightarrow +\infty} \langle \cos\theta \rangle^i = \frac{l_s}{1 - \langle \cos\theta \rangle} \quad (2.6)$$

It deserves to highlight the situation of $l^* = l_s$, meaning that the transport length is equal to the mean free path in this system. From the expression of l^* in equation 2.6, $l^* = l_s$ corresponds to $\langle \cos\theta \rangle = 0$, meaning that the diffusing angle θ is **uniformly** distributed in the interval $[0, 2\pi]$. This is called *isotropic* diffusion.

Consider an isotropic diffusion. The displacement of the particle in one step i is $\delta\mathbf{x}_i$. We can show that the probability $P(\mathbf{x})$ of the particle propagating freely in a distance $|\mathbf{x}|$

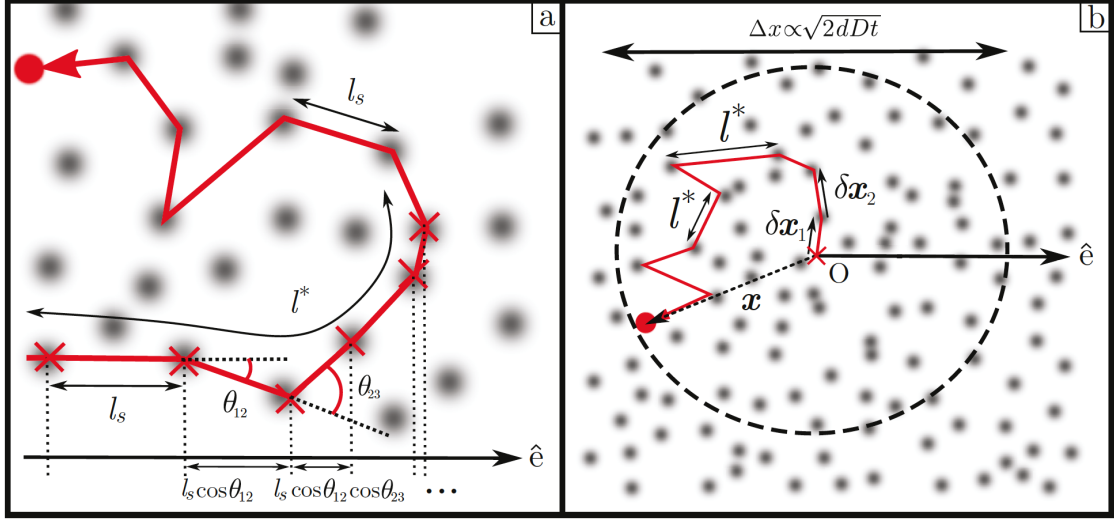


FIGURE 2.2: **Representation of random walk in disordered media.** **a**, Mean free path l_s is the average distance between two collisions. Transport length l^* is the average distance after which the particle loses its initial direction of movement. **b**, In isotropic diffusion, the random walk in disordered media is described by $\{\delta \mathbf{x}_i\}$.

before being scattered by the disorder is :

$$P(\mathbf{x}) = \frac{1}{l^*} \exp\left(-\frac{|\mathbf{x}|}{l^*}\right), \quad (2.7)$$

where l^* is the mean transport path.

Then we can obtain the average displacement for one step and its variance:

$$\begin{cases} \langle \delta \mathbf{x}_i \rangle = 0 \\ \langle \delta \mathbf{x}_i^2 \rangle = 2l^{*2}. \end{cases} \quad (2.8)$$

Since diffusion is isotropic, so each step is independent of others. Using the same argument as before, the sum of N independent steps tends to a Gaussian distribution, therefore, the average position and its variance can be calculated as:

$$\begin{cases} \langle \mathbf{x} \rangle = N \langle \delta \mathbf{x}_i \rangle = 0 \\ \langle \mathbf{x}^2 \rangle = N \langle \delta \mathbf{x}_i^2 \rangle = 2Nl^{*2}. \end{cases} \quad (2.9)$$

We remark that similar as the situation of random walk in 1D lattice, we have $\sqrt{\langle \mathbf{x}^2 \rangle} \propto \sqrt{t}$. Now we define **the diffusion constant \mathbf{D}** by $\langle \mathbf{x}^2 \rangle = 2dDt$. We introduce τ^* , the mean transport time, defined by $\tau^* = l^*/v$, where v is the average speed of the particle. So this mean transport time can be interpreted as an average time between two isotropic collisions. For N collisions, the time is $t = N\tau^*$. Then the diffusion constant \mathbf{D} can be written as:

$$D = \frac{vl^*}{d}. \quad (2.10)$$

We see that the more disordered the media is, the smaller the mean transport length l^* would be, so the diffusion constant \mathbf{D} is small in strongly disordered media. d is the dimension of the system (in our example here, $d=2$).

2.1.0.2 Interference and weak localization

So far, the diffusion we have described is for classical particles or incoherent propagation of classical waves. Now we consider the situation of a coherent propagation for **quantum particle**, which has a finite de Broglie wavelength $\lambda_{dB} = 2\pi/k$. So now we need to take into account the interference of different paths experienced by the quantum particle when propagating in the disordered media, and the interference will modify the dynamics of diffusion that we have described in the previous section. Consider the probability $P(\mathbf{x}, \mathbf{x}')$ for a quantum particle leaving from position \mathbf{x} to position \mathbf{x}' in the disordered media. As illustrated in figure 2.3 a, there are an infinite number of paths from position \mathbf{x} to position \mathbf{x}' . Each path (j) corresponds to an amplitude $A_j = |A_j|e^{i\phi_j}$, where ϕ_j is the phase accumulated for the quantum particle experiencing the path (j). The probability for path (j) is the square of the norm of the amplitude, $P_j = |A_j|^2$. Thus by summing over all the paths, we can get the total probability $P(\mathbf{x}, \mathbf{x}')$ for a quantum particle in disordered media leaving from position \mathbf{x} to position \mathbf{x}' :

$$\begin{aligned} P(\mathbf{x}, \mathbf{x}') &= \left| \sum_j A_j \right|^2 = \left| \sum_j |A_j| e^{i\phi_j} \right|^2 \\ &= \sum_{m,j} |A_m| |A_j| e^{i(\phi_j - \phi_m)} \\ &= \sum_j |A_j|^2 + \sum_{j \neq m} |A_j| |A_m| e^{i(\phi_j - \phi_m)}. \end{aligned} \quad (2.11)$$

The first term is very classical and trivial, just the independent sum of the probability of all the paths. The second term describes the interference between path (j) and path (m). Consider that the phase ϕ for one path is uniformly distributed over $[0, 2\pi]$, and the paths are independent of each other, so the phase difference between (j) and (m) $\phi_j - \phi_m$ is also uniformly distributed over $[0, 2\pi]$. As the result, in the average of realizations of disorder, we have $\overline{e^{i(\phi_j - \phi_m)}} = 0$, thus the probability $P(\mathbf{x}, \mathbf{x}')$ for a quantum particle going from \mathbf{x} to \mathbf{x}' is:

$$P(\mathbf{x}, \mathbf{x}') = \sum_j |A_j|^2. \quad (2.12)$$

Nevertheless, things are different if we consider $\mathbf{x} = \mathbf{x}'$. We want to know the probability of a quantum particle turning back to its original point $P(\mathbf{x}, \mathbf{x})$. As illustrated in 2.3 b, consider path (1), which is a loop, meaning the particle turns back to its original point. There exists path 2, which is the same path as path (1) but circulates in the opposite direction. In this case, $|A_1| = |A_2|$ and $\phi_1 = \phi_2$. There are an infinite number of such loops for the particle turning back to its origin, such as path (3), and for each loop, there always exists its time reversal symmetrical path so that the pair of the time reversal symmetrical loops always have the same amplitude and accumulate the same phase. Each loop interferes with its time reversal symmetrical path constructively. As the result, the second term in equation 2.11 for the probability $P(\mathbf{x}, \mathbf{x})$ is not zero in average anymore :

$$\begin{aligned} P(\mathbf{x}, \mathbf{x}) &= \sum_j |A_j|^2 + \sum_{j \neq m} |A_j| |A_m| e^{i(\phi_j - \phi_m)} \\ &= 2 \sum_j |A_j|^2. \end{aligned} \quad (2.13)$$

Compared with $P(\mathbf{x}, \mathbf{x}')$ where $\mathbf{x} \neq \mathbf{x}'$, the probability of turning back to origin $P(\mathbf{x}, \mathbf{x})$ is coherently enhanced. So we can conclude when propagating in disordered media from position \mathbf{x} to \mathbf{x}' , the probability of paths with loops, as illustrated in figure 2.3 c, are coherently enhanced. Finally, the mechanism of enhanced return to the origins makes the diffusion of a particle with a finite wavelength λ_{dB} less efficient than the diffusion of a classical particle or incoherent propagation of classical waves in the disordered media. This is the mechanism for *weak localization*. Particularly, the weak localization effect introduces a correction for the diffusion constant D:

$$D = D_0 - \delta D, \quad (2.14)$$

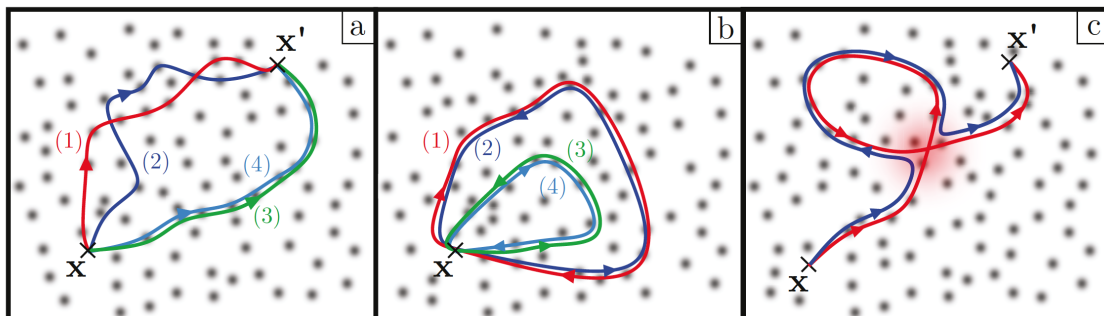


FIGURE 2.3: **Coherently enhanced 'loops' and weak localization.** **a**, The propagation amplitude between x and x' is determined by the interference between pairs of paths. The interference between paths (1) and (2) does not participate in the transport on average over the realizations of disorder. Paths (3) and (4) participate in the first term of 2.11. **b**, The pairs (1,2) and (3,4) are time-reversal symmetrical paths of each other. Their constructive interference doubles the probability of return to the origin 2.13. **c**, Formation of a quantum crossover backscattering loop during propagation from x to x' , a mechanism responsible for the correction of weak localization 2.15.

where D_0 is the diffusion constant for the classical particle that we have introduced in the previous section, see equation 2.10, and δD is the correction due to the weak localization. The correction of the weak localization actually depends on many microscopic details of the system, particularly on the dimension d and the size L of the system. We can show that [38]:

$$\delta D/D_0 = \begin{cases} \mathcal{O}(L/t^*) & \text{in 1D,} \\ \mathcal{O}\left(\frac{1}{kt^*} \ln \frac{L}{l^*}\right) & \text{in 2D,} \\ \mathcal{O}\left(\frac{1}{(kt^*)^2}\right) & \text{in 3D.} \end{cases} \quad (2.15)$$

This strong dependence of transport properties on the system's dimension is critical, and we will discuss it in the following.

2.1.0.3 Anderson localization

The correction of weak localization in equation 2.15 reveals a remarkable phenomenon: the correction δD can be equal to the classical diffusion constant D_0 under some certain conditions, and thus the total diffusion constant D drops to zero, then the diffusion of the quantum particle in disordered media is completely suppressed. The complete suppression of the diffusion is called *Anderson localization*. In the regime of Anderson localization, the wave function is localized around the original point, and the profile of the wave function

tends to exponential decay in space [39]:

$$|\psi(\mathbf{x})|^2 \propto e^{-x/L_{\text{loc}}}, \quad (2.16)$$

L_{loc} being a typical length of the profile of localized wave function, called *localization length*.

The equations 2.15 tells us that the correction of diffusion δD depends on the dimension of the system, so now we discuss how diffusion is affected by dimensions.

For $d=1$, according to equations 2.15: $\delta D/D_0 = \mathcal{O}(L/l^*)$. So we have $\delta D \sim D_0$ as long as $L \sim l^*$. The localization length appears $L_{\text{loc}} \sim l^*$, meaning that under a distance L_{loc} , the diffusion constant drops to zero (we can show that $L_{\text{loc}} = 2l^*$ [39]). The localization in 1d is very efficient so we can observe Anderson localization even in a very weak disorder in 1d [31, 32].

For $d=2$, according to equations 2.15: $\delta D/D_0 = \frac{1}{kl^*} \ln(L/l^*)$. To suppress the diffusion: $\delta D(L_{\text{loc}}) \sim D_0$, we have the localization length $L_{\text{loc}} \sim l^* \exp(kl^*)$. We can remark that for the weak disorder ($kl^* \gg 1$), the localization length L_{loc} can be much longer than l^* , even longer than the system size. The localization is much less efficient in 2d and therefore to observe localization in 2d, generally, we need strong disorder [40]. It is very hard to observe Anderson localization in a weak disorder in 2d.

In this manuscript, the situation that interests us most is $d=3$, according to the equations 2.15: $\delta D/D_0 = \mathcal{O}\left(\frac{1}{(kl^*)^2}\right)$. We see that the correction of diffusion depends on kl^* , which represents the *strength* of the disorder. In a strong disorder where $kl^* < 1$, we have $\delta D \sim D$, the diffusion is suppressed and the localization can happen. In a weak disorder where $kl^* \gg 1$, we have $\delta D_0 \ll 1$, the correction of diffusion is too weak to suppress the diffusion so there is no localization in the weak disorder. It is therefore expected that there is a phase transition in 3d, between the two regimes: localization phase and diffusive phase, separated by the criterion: $kl^* \sim 1$. This is called **Ioffe – Regal criterion** [41]. In the next section, we will study this phase transition (Anderson transition) from the point of view of scaling theory.

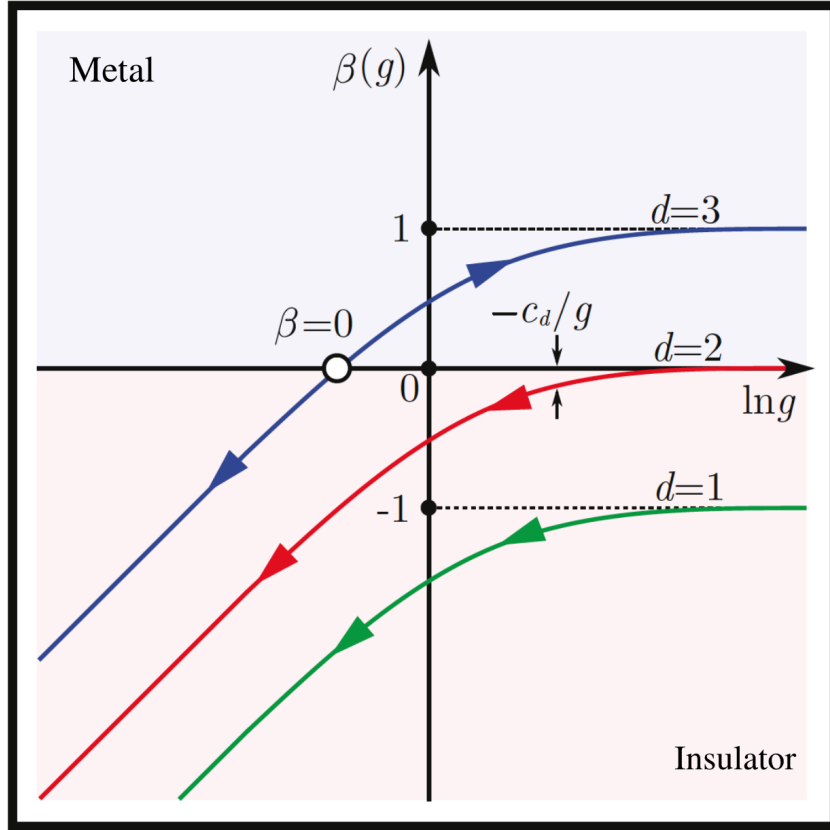


FIGURE 2.4: **Scaling function β of the conductance g .** In the limit of $g \gg 1$, the conductance recovers Ohm's law, $\beta \sim d - 2$. The sign of β determines the system to be metal or insulator. For $d \leq 2$, β is always negative, in the limit of infinite size, $\beta \sim -L/L_{\text{loc}}$, the system is localized (insulator). For $d = 3$, there is a critical value $\ln g_c$ for which the scaling function β changes the sign, which is the mark of a phase transition

2.1.0.4 Scaling theory for Anderson transition

The scaling theory can provide a more general and formal approach to studying how the localization properties depend on the dimension of the system.

We define a dimensionless conductance g [42]:

$$g(L) = \frac{G(L)}{e^2/2\hbar}, \quad (2.17)$$

where $G = 1/R$ is the classical conductance of the system, L is the size of the system.

According to Thouless [42],

$$g \sim \begin{cases} L^{d-2} & g \gg 1 \\ e^{-L/L_{\text{loc}}} & g \ll 1 \end{cases} \quad (2.18)$$

The regime where $g \gg 1$ refers to the classical diffusion where the correction of localization is negligible, and the results recover the Ohm's law.

We define the **scaling function** β [43]:

$$\beta(g) = \frac{dg/g(L)}{dL/L} = \frac{d \ln g}{d \ln L}. \quad (2.19)$$

The sign of the scaling function β can define the system to be metal or insulator. For $\beta < 0$, the diffusion of the particles in the system is slowed down when propagating through the disordered media until g becomes small enough to stop the diffusion. Therefore the system is **insulator** (localized) when $\beta < 0$. On the contrary, for $\beta > 0$, the diffusion accelerates when propagating through the disordered media, and therefore, the system is **metal** (diffusive).

In Abrahams et al. [43], the authors present the plot of $\beta(g)$ versus $\ln g$ for $d=1$, $d=2$ and $d=3$, as illustrated in figure 2.4. According to the asymptotic expressions of conductance g in equations 2.18, the asymptotic curves for β can be expressed as:

$$\beta(g) \sim \begin{cases} d-2 & g \gg 1 \\ -L/L_{\text{loc}} & g \ll 1 \end{cases} \quad (2.20)$$

We can remark that for $d=1$ and $d=2$, β is always negative. Therefore, when the wave (or quantum particle) propagates through the media, it tends toward the left part of the curves in figure 2.4, where $\beta \sim -L/L_{\text{loc}}$. The system is localized (insulator) for $d=1$ and $d=2$. Actually, $d=2$ is more sensitive than $d=1$. In the regime of weak disorder where $g \gg 1$, even though the scaling function $\beta(g)$ is still negative, it can be very close to zero. In this case, if the time-reversal symmetry is broken by some perturbation, e.g. spin-orbit coupling or magnetic impurities[44], or when a time dependent potential is applied to the system (e.g., using high frequency rf fields)[45, 46], the weak localization loops can be suppressed, and the scaling function $\beta(g)$ can fluctuate to positive values and thus these

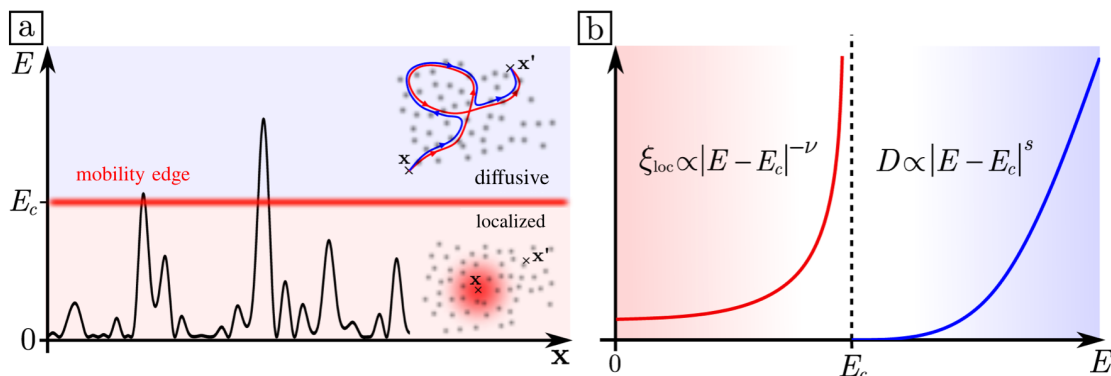


FIGURE 2.5: **Anderson transition in terms of energy.** **a**, The mobility edge E_c is the critical energy separating the localized states from the diffusive states. **b**, Approaching the mobility edge E_c , the localized states have a localization length that diverges with the exponent ν , and the diffusive states have a diffusion constant that scales with the exponent s .

perturbation can induce a phase transition in 2d .

3. In $d = 3$, some states have $\beta > 0$, thus they are metallic states, while other states have $\beta < 0$ and they are insulating states. So a well-defined **phase transition** exists in $d=3$. The critical point corresponds to $\beta(g_c) = 0$.

We can also look at the phase transition in the picture of energy. As shown in figure 2.5 a, in the spectrum for a three-dimensional disordered system, E_c is the critical energy (mobility edge) of the phase transition. The eigenstates with energies above E_c are diffusive, and those lower than E_c are localized states. In Abrahams et al. [43], the authors predict that near the critical regime, as shown in figure 2.5 b, the diffusion constant D and localization length ε_{loc} follow scaling laws with energy:

$$\begin{aligned} \varepsilon_{\text{loc}} &\propto |E - E_c|^{-\nu} \\ D &\propto |E - E_c|^s. \end{aligned} \tag{2.21}$$

where ν and s are called critical exponents. Although the scaling theory predicts the existence of the phase transition from a general picture, it cannot predict the exact value for the critical exponents. There is no exact theory that can describe well the critical regime of the Anderson transition. Some numerical work [47, 48] predicted that the critical exponents $s = \nu = 1.58$. Measuring the critical exponent is very difficult in experiments. So far, there is only experimental validation in the system of periodically driven quantum

kicked rotors, exhibiting an analog of localization in momentum space[49]. By modulating the amplitude of the kick quasi-periodically in an appropriate way[50], it is possible to observe a dynamical localization transition which is believed to be in the same universality class as the Anderson transition. But the direct experimental measurement in real space is challenging and remains an open question.

2.2 Ultra cold atoms: a good platform to study Anderson localization

After the publication of the paper of P.W.Anderson [2] in 1958, observations of Anderson localization and investigation towards the Anderson transition were first performed in electronic systems in the experiments in the domain of condensed matter physics [3, 4, 5, 6]. Although there are many beautiful results in the experiment using electrons, there are always some difficulties that are not easy to bypass. It is hard to eliminate the Coulomb interaction of the electrons, which can induce dephasing to the wavefunction. And it is not easy to control the disorder due to the phonon modes of the lattice.

Experiments with classical waves have also been a candidate for studying Anderson localization since the 90s, with light [7, 8, 9, 10, 11], microwaves[12, 51, 52] and acoustic wave[13, 14, 15, 17, 16]. Compared with electronic systems, interaction is naturally absent in these systems. Nevertheless, it has been shown recently that the vectorial nature of the light can kill the Anderson localization in 3d [53].

Among these experimental platforms, ultracold atom becomes an excellent candidate to explore Anderson localization. The first direct observation of Anderson localization with ultracold atoms was realized at Institut d'Optique in Palaiseau [31] and at LENS in Florence [32] in 2008 in one-dimensional systems. These two experiments use different techniques to generate the disorder. In Palaiseau, they use laser speckle while in Florence they use a bichromatic lattice to play the role as the disordered potential. A few years later, the experimental observations of 3D Anderson localization were realized in 2011 in Urbana-Champaign[35], in 2012 at Institut d'Optique in Palaiseau [33], and at LENS in Florence in 2015 [34]. For 2D Anderson localization, as we have explained above in section 2.1.0.3, the localization length L_{loc} can be extremely large ($> 100\mu\text{m}$) in the regime of

weak disorder, so it is very hard to observe Anderson localization in weak disorder. To my knowledge, in 2d, with ultracold atoms, there has only been the experimental observation of Anderson localization in the regime of strong disorder [40]. There are some important experimental studies in 2d in the regime of weak localization, e.g., coherent backscattering[54] and the role of time-reversal symmetry in weak localization[55]. In this section, we will focus on the developments of the experimental investigation in Anderson localization in 3d with ultracold atoms. We will review the three experimental works in 3d mentioned above, and discuss their achievements and limitations. At the end of the section, we will discuss the bottlenecks of the study for the Anderson transition, and we will briefly explain how we overcome these bottlenecks to go further toward the mobility edge of the Anderson transition with our state-of-the-art platform.

There is another platform to study Anderson localization with cold atoms, called *dynamical localization*, using quantum kicked rotor. A quantum kicked rotor is realized by placing cold atoms in a pulsed standing wave. Each pulse gives a kick to the atoms. In momentum space, the atom experiences a random walk, and the momentum distribution diffuses, as shown in figure 2.6. If the pulse is periodically driven, one observes the suppression of the diffusion in momentum space. It is shown that there is a complete analogy between Anderson localization (in real space) and dynamical localization (in momentum space) [56]. It was experimentally observed with cold atoms in 90s[50, 57, 58].

In the platform of quantum kicked rotor, it is easy to extend from 1d to 3d by performing a *quasi-periodic* driven. In the team in Lille, with the quantum kicked rotor, they observed the Anderson transition and measured the critical exponent. They get $\nu = 1.4 \pm 0.3$. This is so far the only experimental measurement of the critical exponents of the Anderson transition that is compatible with numerical calculations [59, 60].

2.3 3D Anderson localization and the Anderson transition

So far, three experiments of Anderson localization in 3d have been performed with ultracold atoms, using laser speckle[61] to generate disordered potential [33, 34, 35]. These three experiments have tried to demonstrate the existence of the phase transition and measure the mobility edge E_c separating the diffusive and localized states, as illustrated

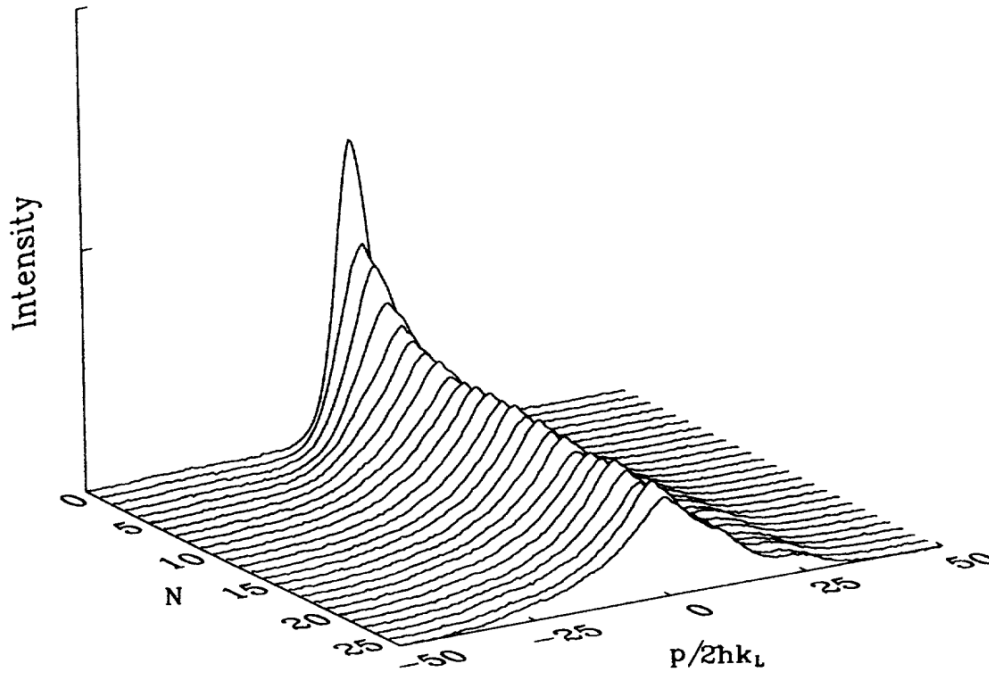


FIGURE 2.6: **The time evolution of the momentum distribution.** The atoms are subjected to periodic kicks, and that induces a random walk in the momentum space. After a certain number of kicks, the momentum distribution is frozen and has an exponential profile. The figure is from [58].

in fig 2.5 a. In this section, we will present the three experiments' main results and show the advantages and drawbacks of each. At the end of the section, after reviewing these important experimental investigations, we will discuss the bottleneck limiting us to going toward the critical regime and measure the mobility edge E_c .

2.3.1 Experiment of Urbana-Champaign

The experiment at the University of Illinois Urbana Champaign in 2011 [35] was performed with ultracold ^{40}K in speckle potential. The authors' analysis is based on observing a double structure of the atomic density profile for expansion time $t \geq 20\text{ms}$. The profile of the final atomic density is interpreted as the coexistence of localized and diffusive states, as shown in figure 2.7. Defining the localized fraction $f_{\text{loc}} = N_{\text{loc}}/(N_{\text{loc}} + N_{\text{diff}})$, it is possible to estimate the mobility edge E_c by noting that only energy atoms lower than E_c remain localized:

$$f_{\text{loc}} = \int_{-\infty}^{E_c} dE \mathcal{D}_E(E), \quad (2.22)$$

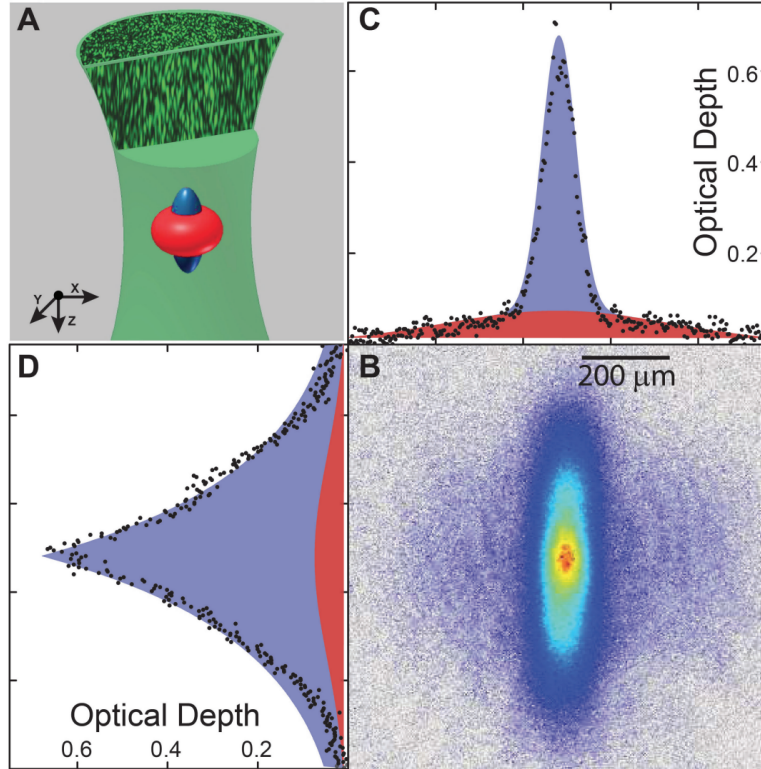


FIGURE 2.7: The experimental observation of Anderson localization in 3d in Urbana Champaign.

where $\mathcal{D}_E(E)$ is the energy distribution of atoms in the disorder.

We see that to determine E_c , it is required to know the energy distribution of atoms $\mathcal{D}_E(E)$. The energy distribution of atoms $\mathcal{D}_E(E)$ can be expressed as:

$$\mathcal{D}_E(E) = \int \frac{d^d \mathbf{k}}{(2\pi)^d} A(\mathbf{k}, E) \mathcal{D}_{\mathbf{k}}(\mathbf{k}), \quad (2.23)$$

where $A(\mathbf{k}, E)$ is the spectral function, corresponding to the probability of a particle with momentum \mathbf{k} and energy E . In the presence of the disordered potential, the spectral function is far different from that of free particles. But the authors hypothesize that their slow introduction of the disordered potential does not modify the spectral function so that it remains the same as for free particles:

$$A(\mathbf{k}, E) = \delta \left(E - \frac{\hbar^2 \mathbf{k}^2}{2m} \right). \quad (2.24)$$

Some criticisms have been made regarding the interpretation of their experimental data

[36, 62]. Notably, this hypothesis for the spectral function is too much naive, and it makes them use a completely incorrect energy distribution of atoms $\mathcal{D}_E(E)$ to estimate the mobility edge E_c . Actually, since 2018, in our experiment, the team has investigated a lot in spectral function. The numerical prediction and experimental results show that the spectral functions are deeply modified from that of free particles [28], especially for the strong disorder. We will see what the spectral functions look like in chapter 5. Another important imperfection is their expansion time, only 20ms, which is too short to measure the slow dynamics of the diffusive states. Close to the critical regime, the order of magnitude for the diffusion constant $D \sim 250\mu\text{m}^2/s$. The distance for the diffusion after a time t is $l \sim \sqrt{2dDt}$, where $d = 3$ (dimension = 3). So we can estimate that for 20ms, the diffusion distance is only a few μm , making the difference between localized and diffusive states not evident. We thus conclude that some severe imperfections impair these results.

2.3.2 Experiment of Palaiseau

The second experiment to realize Anderson localization in $d=3$ was performed in Palaiseau in 2012 [33]. The experiment measured the temporal evolution of the expansion of a Bose-Einstein condensate of ^{87}Rb in a speckle potential. In this experiment, the disorder is composed of two crossed speckle laser fields[61, 63] to make the 3D disorder more isotropic. The wave packet of Bose-Einstein condensate is prepared with a narrow energy distribution in the absence of disorder. The BEC is diluted before illuminating the disordered potential to lower the interaction energy. Hence, as a result, the energy distribution is very narrow, and the atomic sample can be considered to be a plane wave with $|\mathbf{k} = 0\rangle$. Then the disorder is applied abruptly, and the atoms are left to expand in the disorder for as long as 6 s. Magnetic levitation can hold the atoms against gravity, which is necessary for the extremely long expansion time. Since the disorder is applied abruptly (within $100\mu\text{s}$), the energy distribution of the atoms in the presence of the disorder is very broad, extending on both sides of the mobility edge, resulting in a localized fraction and a diffusive fraction existing together. The temporal evolution of the atomic density is:

$$n(\mathbf{x}, t) = f_{\text{loc}}n_i(\mathbf{x}) + n_D(\mathbf{x}, t), \quad (2.25)$$

where n_i being the initial atomic density and n_D being the atomic density for the diffusive atoms.

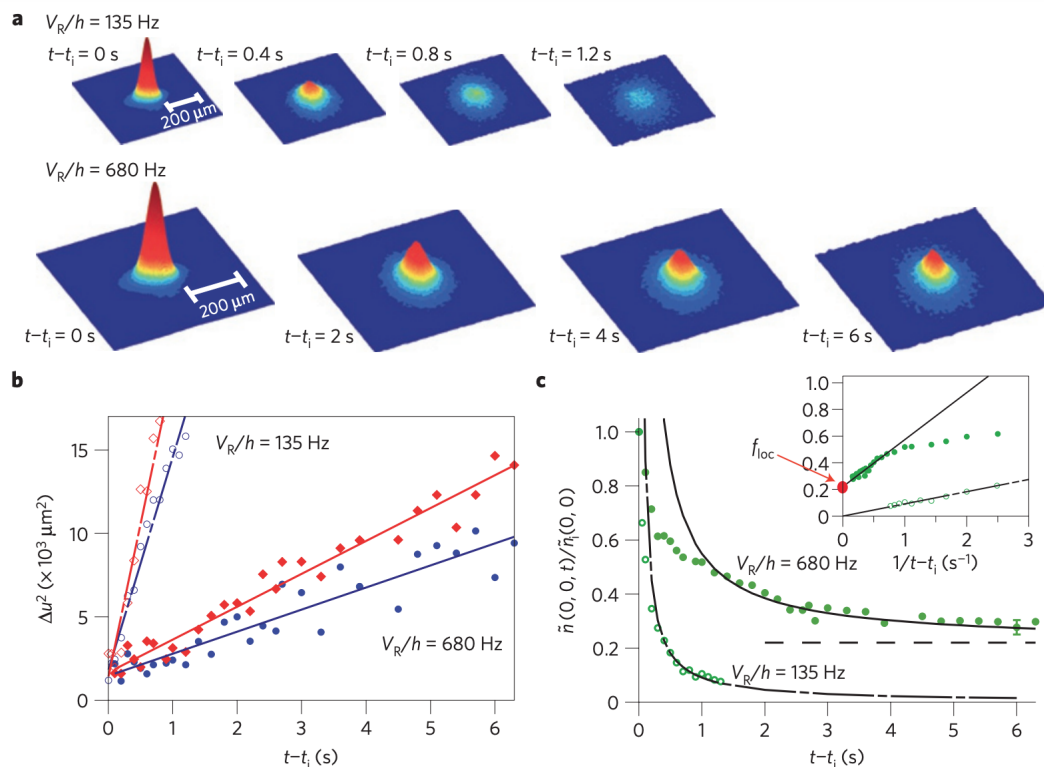


FIGURE 2.8: **Measure E_c in the experiment of Palaiseau.** **a**, The expansion of atoms for 6s with weak ($V_R/h = 135\text{Hz}$) and strong ($V_R/h = 680\text{Hz}$) disorder. **b**, Time evolution of the mean squared widths along y (blue circles) and z (red diamonds) of the column density profiles, and their fits by straight lines, yielding the diffusion coefficients along y and z . **c**, Time evolution of the central density of atoms (green circles).

The localized fraction is estimated from the evolution of the central atomic density, fitted by an asymptotic function $f_{\text{loc}} + A/t$ in the long time limit, as shown in figure 2.8 c. Knowing the localized fraction, to estimate the mobility edge, it is still required to know the energy distribution of atoms due to the relation:

$$f_{\text{loc}} = \int_{-\infty}^{E_c} dE \mathcal{D}_E(E). \quad (2.26)$$

Since the atomic sample can be considered to be a plane wave with $|\mathbf{k} = 0\rangle$, the relevant energy distribution of atoms is for $|\mathbf{k} = 0\rangle$:

$$\mathcal{D}_E(E) = A(\mathbf{k} = 0, E). \quad (2.27)$$

In this situation, one needs to know the spectral function of the atoms at null momentum. In this work [33], the authors calculate $A(\mathbf{k} = 0, E)$ numerically, and then using

the knowledge of spectral function, they estimate the mobility edge E_c from the measured localized fraction using equation 2.26.

Compared with the experiment in Urbana-Champaign [35], in this work, the 6s' expansion time is long enough, and the numerically calculated spectral function is more reasonable than the naive hypothesis in [35]. But the observation is very indirect because the spectral function is numerically calculated but not directly measured. And the estimation of the mobility edge relies on the measurement of the localized fraction due to the broad energy distribution of atoms in the disorder.

2.3.3 Experiment in Florence

The third experiment for Anderson localization in $d = 3$ and measuring the mobility edge for Anderson transition with ultracold atoms was realized in 2015 in Florence [34]. This experiment shares some similarities with the previous two, e.g., they also use crossed optical speckles as disordered potential and estimate the mobility edge by counting the localized fraction. But they have a narrower energy distribution of atoms in disorder, and more importantly, they demonstrate a new method of spectroscopy to study the mobility edge.

In this experiment, they use ultracold ^{39}K , whose interaction can be conveniently adjusted by Feshbach resonances. Their measurement procedure is shown in figure 2.9. After the preparation of BEC, they ramp down the trap and interaction while illuminating the disorder in a quasi-adiabatic way. At the end of the ramp, the energy distribution of atoms in the disorder is narrow. This quasi-adiabatic loading of disorder allows loading the majority of atoms into the low energy states, as illustrated in figure 2.9 a.I.

Once loading the atoms into the disorder with a certain energy distribution $\mathcal{D}_E(E)$, as in the previous experiments, it is required to know the energy distribution to determine the mobility edge. In this experiment, they measure the momentum distribution of atoms $\mathcal{D}_{\mathbf{k}}(\mathbf{k})$ directly. According to the equation 2.23, to determine the energy distribution $\mathcal{D}_E(E)$ one needs to know the spectral function $A(\mathbf{k}, E)$. In this experiment, the authors numerically calculate the spectral function $A(\mathbf{k}, E)$, as illustrated in figure 2.9 b.

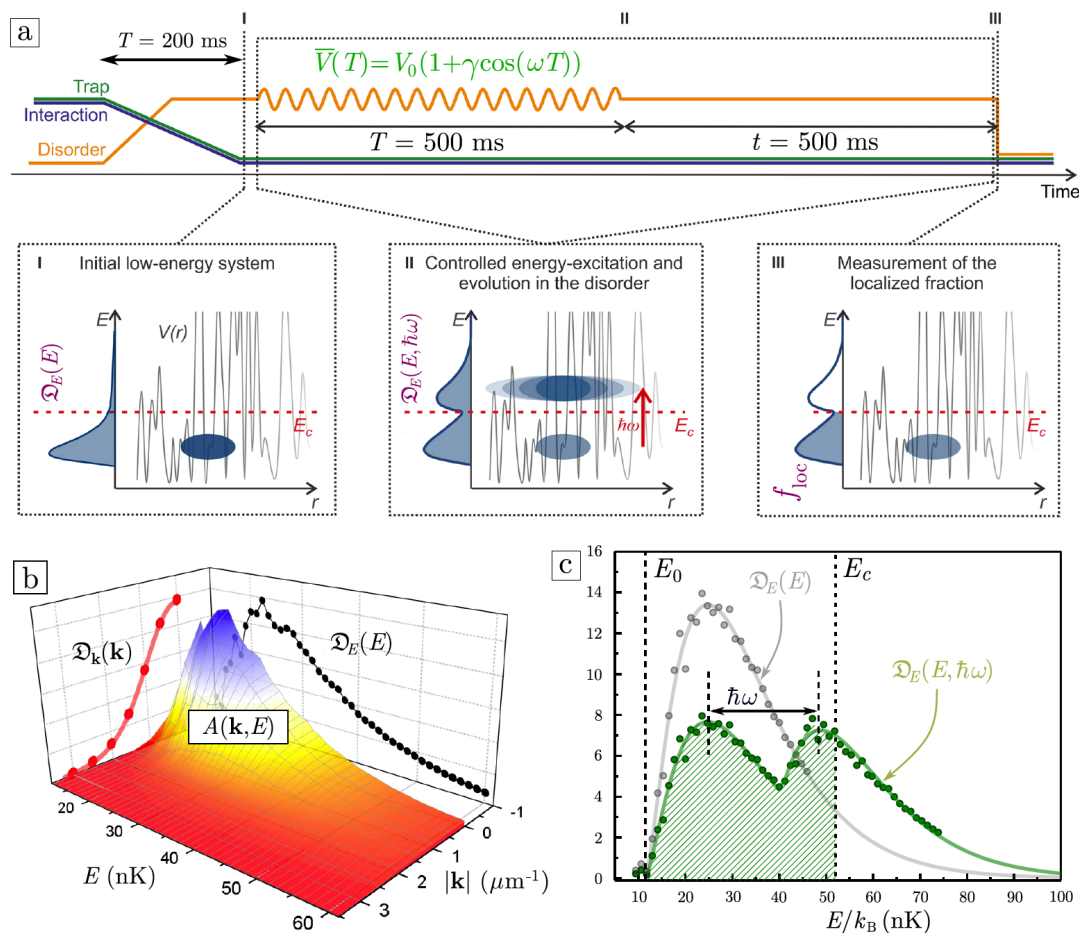


FIGURE 2.9: **Experiment in Florence.** **a**, The experiment sequence. **b**, The reconstruction from the measured momentum distribution of atoms $\mathcal{D}_{\mathbf{k}}(\mathbf{k})$ to the energy distribution of atoms $\mathcal{D}_E(E)$ via the spectral function $A(\mathbf{k}, E)$. **c**, The initial energy distribution of atoms $\mathcal{D}_E(E)$ (gray curve) and the energy distribution of atoms $\mathcal{D}_E(E, \hbar\omega)$ after the modulation by $\hbar\omega$ (green curve).

The second step is modulating the disordered potential periodically with frequency $\omega/2\pi$, in a duration $T = 500$ ms to excite the atoms by an energy $\hbar\omega$, as shown in figure 2.9 a. After the excitation, the energy distribution of atoms in disorder is modified from the initial energy distribution, and the new energy distribution $\mathcal{D}_E(E, \hbar\omega)$ is:

$$\mathcal{D}_E(E, \hbar\omega) = (1 - \alpha)\mathcal{D}_E(E) + \alpha\mathcal{D}_E(E - \hbar\omega), \quad (2.28)$$

where α being the fraction of atoms excited by an energy $\hbar\omega$, $\mathcal{D}_E(E - \hbar\omega)$ being the corresponding shifted energy distribution for the excited atoms. The illustration of the distribution of energy after excitation $\mathcal{D}_E(E, \hbar\omega)$ is shown in figure 2.9 a.II.

The excitation of $\hbar\omega$ can transfer some atoms from the initial low energy states to the energies above the mobility edge E_c to be diffusive states, as shown in figure 2.10 a. Therefore the third step is to leave disorder at fixed value for another 0.5s, allowing the atoms transferred to diffusive states to expand enough to be effectively invisible to the imaging system. The transfer to diffusive states is hence detected as atom losses.

Figure 2.10 a shows an example of the variation of the final atom number N as a function of the transferred energy $\hbar\omega$. To determine E_c , they fit these data with $f_{\text{loc}} = \int_{-\infty}^{E_c} dE D_{\text{E}}(E, \hbar\omega)$ where the mobility edge E_c is the only free parameter. Then they repeat the measurements for different amplitudes of disorder, and at the end, they get the mobility edge for different amplitudes of disorder, as shown in figure 2.10 b.

This experiment proposed a new method of studying Anderson's transition by selecting the energy of atoms in the disorder with resolved energy. However, the disorder needed to reach localization is strong so they still end up with a broad energy distribution in the disorder. Because of the low energy resolution, their measurement of the mobility edge is still by counting the localized fraction. And as the authors remark in their paper [34], in this experiment, the expansion time is 500ms, not long enough to distinguish all the diffusive states. Similar to the experiment in Palaiseau, their estimation of the mobility edge relies on numerically calculated spectral functions. So although this experiment is more direct than the previous ones, it is still an indirect measurement.

2.4 Synthesis

The three experiments introduced above aimed to measure the mobility edge of the Anderson transition in 3D. Pasek et al. [36] calculated the mobility edge E_c numerically for different amplitudes of disorder V_R . They demonstrated that the relation between the mobility edge and the amplitude of disorder follows a universal scaling law: $E_c/V_R = \mathcal{F}(V_R/E_\sigma)$, where V_R is the amplitude of the disorder, and E_σ is a constant known as the "correlation energy" (this correlation energy E_σ will be discussed in section 7.1.1). They compared the experimental results in the three experiments with the numerical calculations of the mobility edge, as shown in figure 2.11.

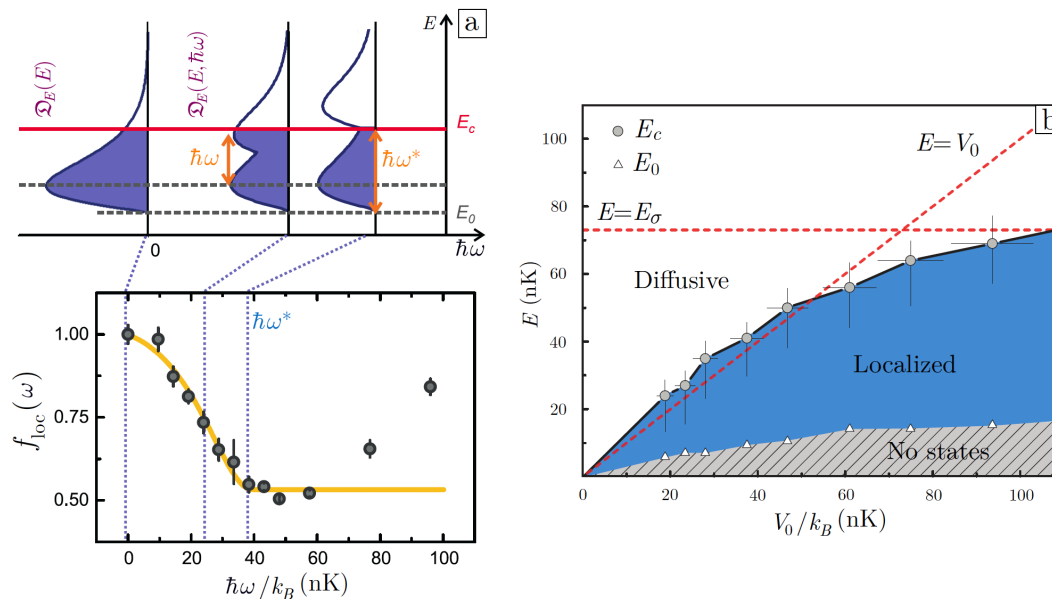


FIGURE 2.10: **Determination of E_c in Florence.** **a.** A fraction of the atoms get transferred by energy $\hbar\omega$, due to the modulation of the potential of frequency $\omega/2\pi$. After the modulation, the atoms are distributed with a new energy distribution. Some of the atoms can be transferred to diffusive states (with energy above mobility edge E_c). The figure of f_{loc} shows the fraction of atom number remaining after the expansion of 0.5s in the disorder. We see a saturation of the localized fraction f_{loc} at transfer energy $\hbar\omega^*$, meaning that it transfers maximum atom number to diffusive states, corresponding to $\hbar\omega^* = E_c - E_0$. **b.** Measuring mobility edge for different amplitudes of disorder.

As shown in figure 2.11, there is a significant discrepancy by orders of magnitude between the mobility edge measured by the team in Urbana Champaign (green dots) and the numerical curve. As previously discussed, their hypothesis for the spectral function is too simplistic and the duration of the expansion of atoms in disorder is only 20ms, which is too short to observe the difference between the localized and diffusive states. These imperfections can explain the strong overestimation of the mobility edge. The experimental results in Palaiseau (red curve) have a fair agreement with the numerical work of Pasek et al. [36]. Nevertheless, the numerically calculated spectral function still makes the measurement of the mobility edge indirect. In Florence, they used a spectroscopic method, and their experimental results present a qualitative agreement with the numerical curve. However, their results may overestimate the mobility edge due to the short expansion time of 500ms.

In all of these experiments, the mobility edge is estimated by measuring the localized fraction f_{loc} , which is not direct measurement. That is due to the coexistence of localized and diffusive phases caused by the broad energy distribution of atoms in the disorder.

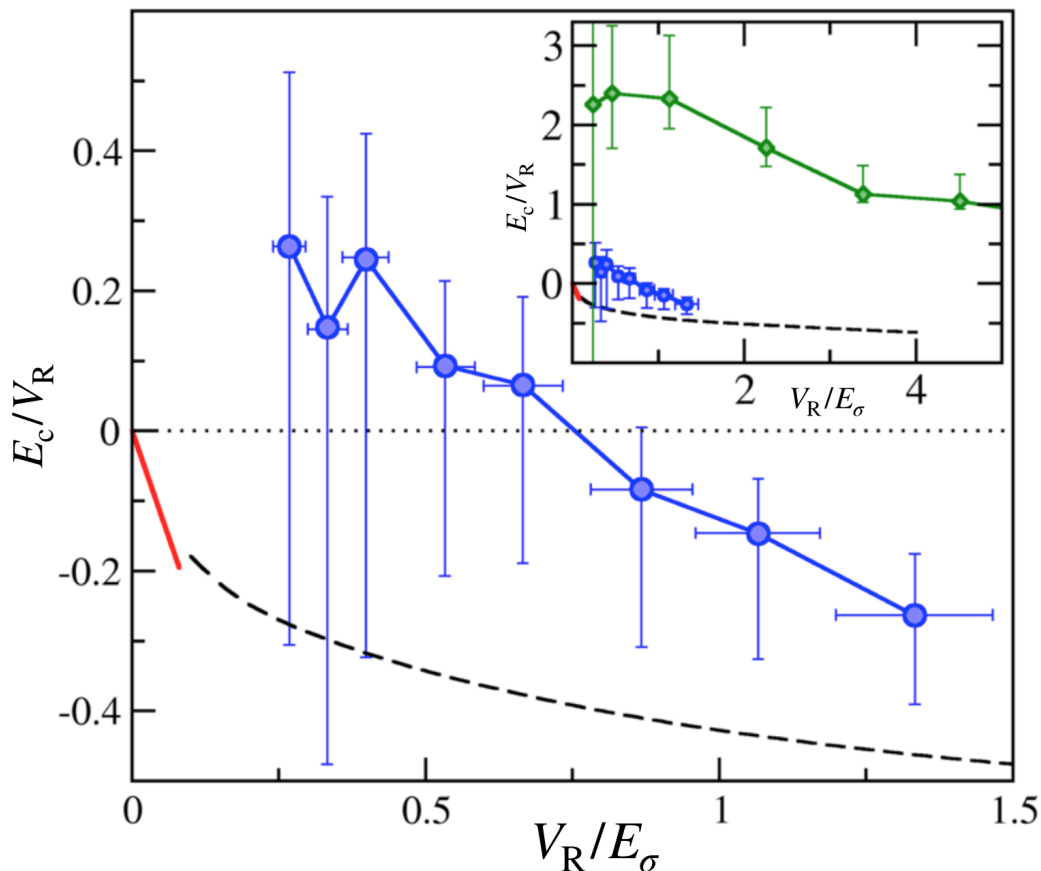


FIGURE 2.11: **Comparison between numerical simulations and experimental results for the mobility edge.** E_σ is correlation energy. The horizontal axis is the rescaled amplitude of disorder. The vertical axis is the rescaled mobility edge. The black dashed curve is the numerical simulations by Pasek et al. [36]. The red line is the experimental results of Palaiseau [33]. The blue dots are the experimental results of Florence [34]. The green dots are the experiment results of Urbana-Champaign [35].

To perform a more direct measurement of the mobility edge, it is crucial to narrow the energy distribution of atoms in the disorder. Additionally, to determine the energy distribution of atoms $\mathcal{D}_E(E)$, knowledge of the spectral function $A(\mathbf{k}, E)$ is necessary, which is calculated in these three experiments instead of being directly measured. Therefore, these experiments are not direct measurements of mobility edge, and to study the critical regime, new experimental approaches that allow for high resolution of energy distribution and the selection of energy of atoms in disordered potential are needed.

Our team proposes a high-resolution spectroscopy method for studying the Anderson localization transition. The method is illustrated in figure 2.12. We first prepare atoms in an initial state $|i\rangle$ with a well-defined energy E_i , free of disorder. Then, we use radio-frequency (rf) transfer to load some atoms into a final state $|f\rangle$ within the disordered

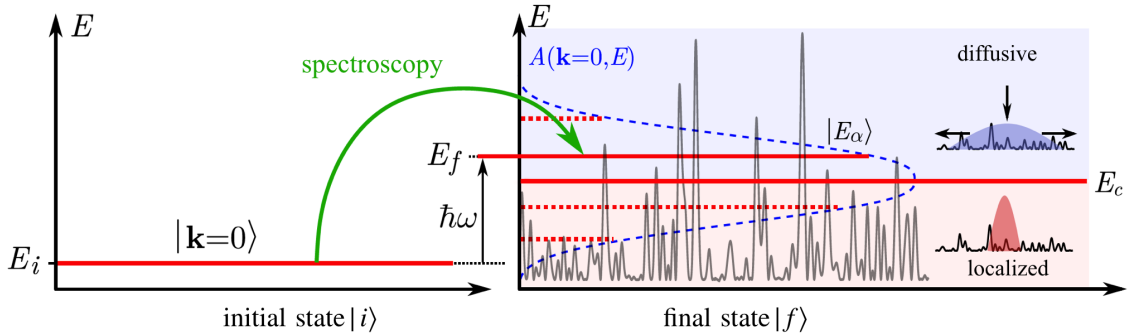


FIGURE 2.12: **The scheme of our spectroscopy method.** The atoms are prepared in an initial state $|i\rangle$, with energy E_i , with momentum $|\mathbf{k} = \mathbf{0}\rangle$. The rf with energy $\hbar\omega$ transfers some atoms to a state $|f\rangle$, with energy E_α .

potential with high energy resolution. This ensures that the atoms in the disorder have a much narrower energy distribution than in previous experiments, making it possible to distinguish between purely localized and diffusive states a priori. By expanding the atoms for sufficient duration in the disordered potential with a fixed amplitude, we can directly probe the transport properties of the state $|E_\alpha\rangle$ and identify it as diffusive or localized. By controlling the rf frequency, which corresponds to the transfer energy $\hbar\omega$, we can select the desired energy to load. By scanning across the spectrum of the disorder, we can then locate the mobility edge. Additionally, this method enables us to measure the spectral function $A(\mathbf{k} = 0, E)$ directly, rather than calculating it numerically. This can be used to calibrate the amplitude of disorder V_R , which is necessary for determining the mobility edge (as we will see in Chapter 5). This approach may also open up opportunities for studying the critical regime in the near future.

Chapter 3

Preparation of Bose-Einstein condensate

In the previous chapter, we have introduced the physical background of Anderson localization briefly and we have especially reviewed the important experimental investigation using ultracold atoms. In this chapter, firstly, we recall the main properties of Bose-Einstein condensate. Secondly, we introduce our experimental cycle.

3.1 Bose-Einstein Condensate

A Bose-Einstein condensate is a state of matter when an ensemble of bosons is cooled to ultra-low temperature, that a macroscopic fraction of bosons occupies the lowest state. To describe a Bose-Einstein condensate, we need to first know its statistics.

3.1.0.1 Statistics for Bose-Einstein condensate

Bosons and fermions follow different quantum statistics. Fermions follow Fermi-Dirac distribution, while bosons follow Bose-Einstein distribution. The average population $N_{\mathbf{n}}$ of bosonic particles occupying the energy level $E_{\mathbf{n}}$ is:

$$N_{\mathbf{n}} = \frac{g_{\mathbf{n}}}{e^{(E_{\mathbf{n}} - \mu)/k_{\text{B}}T} - 1}, \quad (3.1)$$

where $g_{\mathbf{n}}$ is the degeneracy in the energy level $E_{\mathbf{n}}$, and μ is the chemical potential. The chemical potential can take the values from $-\infty$ to the energy of the ground state $E_{\mathbf{0}}$. For the chemical potential higher than the energy of ground state $\mu > E_{\mathbf{0}}$, the population of the atoms on the ground state becomes negative, so there is no physical meaning.

Consider the particle number in all the excited states:

$$N_e = \sum_{\mathbf{n} \neq \mathbf{0}} N_{\mathbf{n}} = \sum_{\mathbf{n} \neq \mathbf{0}} \frac{g_{\mathbf{n}}}{e^{(E_{\mathbf{n}} - \mu)/k_{\text{B}}T} - 1}. \quad (3.2)$$

in the situation $\mu < E_{\mathbf{0}}$, there exists an upper limit N_e^{max} for the number of particles that can occupy all the excited states:

$$N_e \leq N_e^{\text{max}} = \sum_{\mathbf{n} \neq \mathbf{0}} \frac{g_{\mathbf{n}}}{e^{(E_{\mathbf{n}} - E_{\mathbf{0}})/k_{\text{B}}T} - 1}. \quad (3.3)$$

We can see that the upper limit for the number of particles that can occupy the excited states, N_e^{max} , becomes less when the temperature T is lower. When the temperature T is low enough so that $N_e^{\text{max}} < N$, thus all the excited states are saturated, then the atoms have to occupy the ground state $E_{\mathbf{0}}$. When $\mu \rightarrow E_{\mathbf{0}}$, the number of particle that can occupy the ground state $N_{\mathbf{0}} = \frac{g_{\mathbf{0}}}{e^{(E_{\mathbf{0}} - \mu)/k_{\text{B}}T} - 1}$ can tend to $+\infty$. Thus a macroscopic number of particles gather on the ground state to form a macroscopic wavefunction. That is how Bose-Einstein condensate forms.

Consider a perfect gas in a trap to have a clearer image of the transition to Bose-Einstein condensate. We can define the average de Broglie wavelength of the particles λ_{dB} , which depends on the temperature of the gas:

$$\lambda_{\text{dB}} = \sqrt{\frac{2\pi\hbar^2}{mk_{\text{B}}T}}. \quad (3.4)$$

As shown in figure 3.1, when the temperature of the gas is high, the average wavelength of particle λ_{dB} is small compared to $\langle r \rangle$, the average distance between the particles in the trap. But when the temperature becomes lower, λ_{dB} increases. Until the temperature reaches a critical value T_c , where $\lambda_{\text{dB}} \simeq \langle r \rangle$, the wavefunction of individual particles overlaps with others. A portion of the particles condensate into the ground state, and the phase transition occurs at temperature T_c . In a 3-d harmonic trap, this condition for the

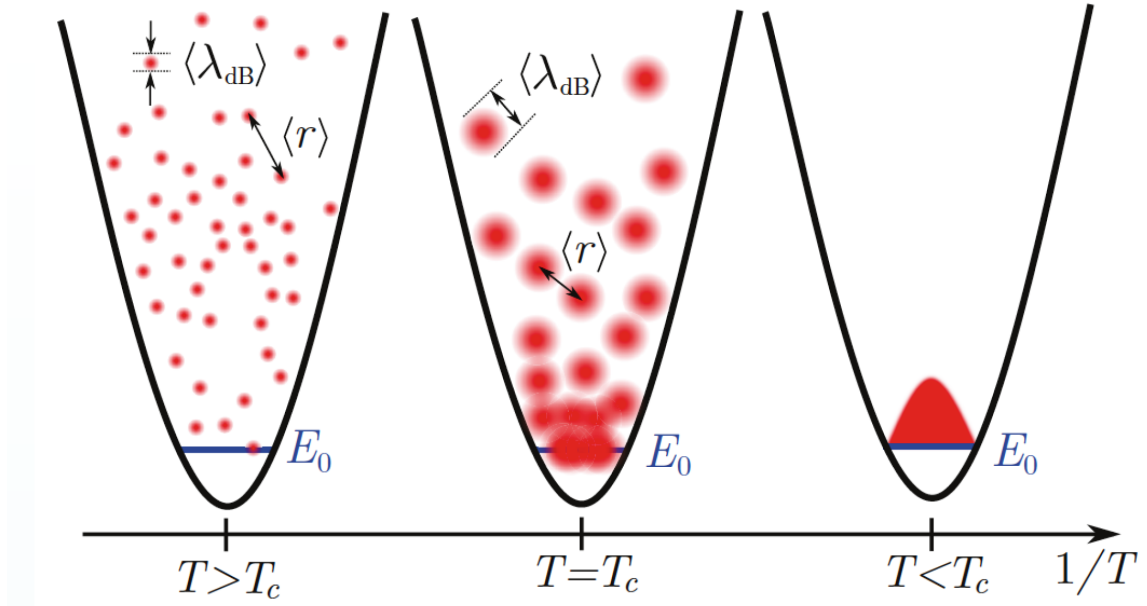


FIGURE 3.1: **Phase transition to BEC.** When temperature T is lower than the critical temperature T_c , $\langle \lambda_{dB} \rangle$ is comparable to with $\langle r \rangle$, so it becomes impossible to distinguish different particles in real space, and the particles gather to the fundamental state E_0 .

phase transition to condensate can be written as:

$$n\lambda_{dB}^3 \geq 1, \quad (3.5)$$

$n\lambda_{dB}^3$ is called *phase – space density*. When the gas becomes colder and colder, phase-space density becomes larger, and the wavefunction of particles becomes more degenerate. In the end, a macroscopic number of particles condensate on the ground state, that is a Bose-Einstein condensate.

3.1.0.2 Gross-Pitaevskii equation for Bose-Einstein condensate

The last part explains how an ideal Bose gas in a 3-d harmonic trap *without interaction* transitions to Bose-Einstein condensate. But in reality, as shown in figure 3.1, below the critical temperature T_c , the particles accumulate heavily on the ground state in the trap, and that will result in a drastic increase of the particle density so that we cannot ignore the interaction between the particles anymore. If the gas is dilute enough, the interaction between the particles can be treated as collisions at low energy, which is an s-wave collision. In this regime, the interaction between particles is considered contact interaction and can be described as $U(\mathbf{x}_1 - \mathbf{x}_2) = g\delta(\mathbf{x}_1 - \mathbf{x}_2)$ [64]. The coefficient g characterizes the strength

of the contact interaction, and $g = \frac{4\pi\hbar^2}{m}a_s$ [65], with a_s the scattering length for the s-wave collision between the particles. Even though the particle density of Bose-Einstein condensate n is high, in the order of 10^{19} to 10^{21}m^{-3} , the scattering length is generally small, so that $na_s^3 \ll 1$. So in the general case, the scattering length is much smaller than the average distance between the particles in BEC, satisfying the dilute condition. For example, for the BEC of ^{87}Rb , the scattering length is about $5 \times 10^{-9}\text{m}$, $na_s^3 \sim 10^{-4}$ to 10^{-6} , much smaller than one.

In the regime of dilute bosonic gas, using mean field approximation, one can describe the gas by a *nonlinear Schrödinger equation*, the famous Gross-Pitaevskii equation [66, 67]:

$$\left[-\frac{\hbar^2}{2m}\Delta + V(\mathbf{x}) + g|\phi_0(\mathbf{x})|^2 \right] \phi_0(\mathbf{x}) = \mu\phi_0(\mathbf{x}), \quad (3.6)$$

where $\phi_0(\mathbf{x})$ is the macroscopic wave function for the Bose-Einstein condensate and μ is the chemical potential. The particle density is $n(\mathbf{x}) = |\phi_0(\mathbf{x})|^2$. The nonlinear term $g|\phi_0(\mathbf{x})|^2$ is from the mean-field approximation for interaction. For an individual particle, its interaction with other particles can be treated approximately as a pseudo-potential applied to this particle. So the mean-field approximation helps to simplify a many-body problem to a one-body nonlinear Schrödinger equation.

3.1.0.3 Thomas-Fermi regime

Consider a Bose-Einstein condensate in a harmonic trap [65]. In Gross-Pitaevskii equation 3.6, the term of external potential $V(x)$ is the potential of harmonic trap, $V(x) = \frac{1}{2}m\omega^2x^2$ (consider an isotropic trap, $\omega_x = \omega_y = \omega_z = \omega$). The size of the condensate is about ζ , so the potential energy given by the harmonic trap per particle $E_p/N_0 \sim \frac{1}{2}m\omega\zeta^2$, and the kinetic energy per particle $E_k/N_0 \sim \hbar^2/2m\zeta^2$. The interaction energy per particle for one particle $E_{int}/N_0 = gn$.

Now compare the three terms of energy: kinetic energy, potential energy and interaction energy. When kinetic energy is equal to potential energy, $E_k = E_p$:

$$\frac{1}{2}m\omega\zeta_h^2 = \hbar^2/2m\zeta_h^2 \quad \text{that is} \quad \zeta_h = \sqrt{\frac{\hbar}{m\omega}}. \quad (3.7)$$

In reality, e.g., for Bose-Einstein condensate of ^{87}Rb , ζ_h is in the order of μm . This length means that when the condensate size is much larger than this length ζ_h , the kinetic energy is much smaller than the trapping potential. Generally, the typical size of a Bose-Einstein condensate ζ is tens of μm . So the potential energy is higher than kinetic energy by at least two orders of magnitude, $\mathbf{E}_p \gg \mathbf{E}_k$.

Then we compare the kinetic energy with interaction energy:

$$\frac{E_{int}}{E_k} \sim \frac{gn}{1/\zeta^2} \sim N_0 \frac{a}{\zeta}. \quad (3.8)$$

For ^{87}Rb , a is about 5 nm, as mentioned above ζ is tens of μm , $N_0 \sim 10^5$, so in this regime, the interaction energy is much higher than the kinetic energy, $\mathbf{E}_{int} \gg \mathbf{E}_k$.

According to the analysis above, the kinetic energy can be neglected compared to interaction and trapping potential energy. This approximation is called *Thomas – Fermi approximation*, and the Gross-Pitaevskii equation 3.6 is simplified to:

$$[V(\mathbf{x}) + g|\phi_0|^2] \phi_0(\mathbf{x}) = \mu\phi_0(\mathbf{x}). \quad (3.9)$$

By solving this equation, we can get the local density of the condensate:

$$n(\mathbf{x}) = \begin{cases} (\mu - V(\mathbf{x}))/g & \text{when } \mu > V(\mathbf{x}) \\ 0 & \text{otherwise} \end{cases} \quad (3.10)$$

So in a harmonic trap of frequency ω , the density distribution of the condensate is a parabola of radius $R_{\text{TF},i} = \sqrt{\frac{2\mu}{m\omega_i}}$ as shown in figure 3.2 a. One can consider the sum of the trapping potential $V(\mathbf{x})$ and the interaction pseudo-potential $gn(\mathbf{x})$ as an **effective energy** applied to each individual particle: $V_{\text{eff}}(\mathbf{x}) = V(\mathbf{x}) + gn(\mathbf{x})$. Thus, according to the density distribution 3.10, the effective potential $V_{\text{eff}}(\mathbf{x})$ is:

$$V_{\text{eff}}(\mathbf{x}) = \begin{cases} \mu & \text{when } \mu > V(\mathbf{x}) \\ V(\mathbf{x}) & \text{otherwise} \end{cases} \quad (3.11)$$

The shape of the effective potential $V_{\text{eff}}(\mathbf{x})$ is shown in figure 3.2(b). The energy of the condensate is constant, and its value is just the chemical potential μ . The chemical potential of the condensate characterizes an energy scale above which the condensate would

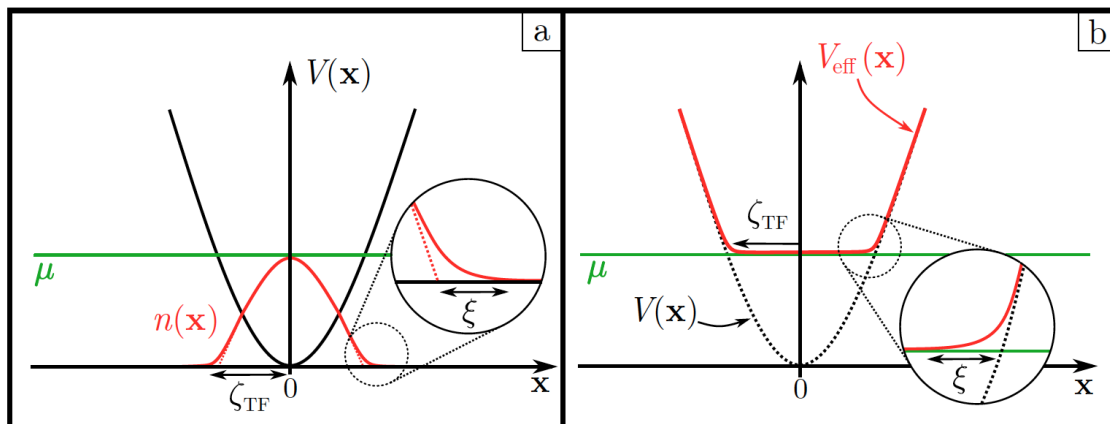


FIGURE 3.2: **a**: **Density distribution in Thomas – Fermi regime.** The density distribution is a parabola, given by the form of the trapping potential. At the edge of the trap, the density is too low to satisfy the Thomas-Fermi approximation. Healing length ξ describes the region where the Thomas-Fermi approximation fails. **b**: **The effective potential felt by each individual particle.** $V_{\text{eff}} = V(\mathbf{x}) + gn(\mathbf{x})$. In the center of the trap, the external potential $V(\mathbf{x})$ is screened by the mean-field interaction $gn(\mathbf{x})$.

be excited, and this idea is very important for the test of our bichromatic speckle set-up (in chapter 6). The chemical potential can be calculated as follows [64]:

$$\mu = \frac{1}{2} (15aN_0\hbar^2\bar{\omega}^3)^{2/5} m^{1/5}, \quad (3.12)$$

where a is scattering length, N_0 is the central density of condensate, $\bar{\omega} = (\omega_x\omega_y\omega_z)^{1/3}$ is the geometric average trap frequency of the harmonic trap.

3.2 Properties of ^{87}Rb

We use ^{87}Rb atoms in our experiment. As an alkali element with an atomic number of 37, ^{87}Rb is a bosonic isotope, and its relevant physical properties are listed in Table 3.2 [68]. ^{87}Rb has two main groups of transition lines: the D1 and D2 lines, as shown in Figure 3.3.

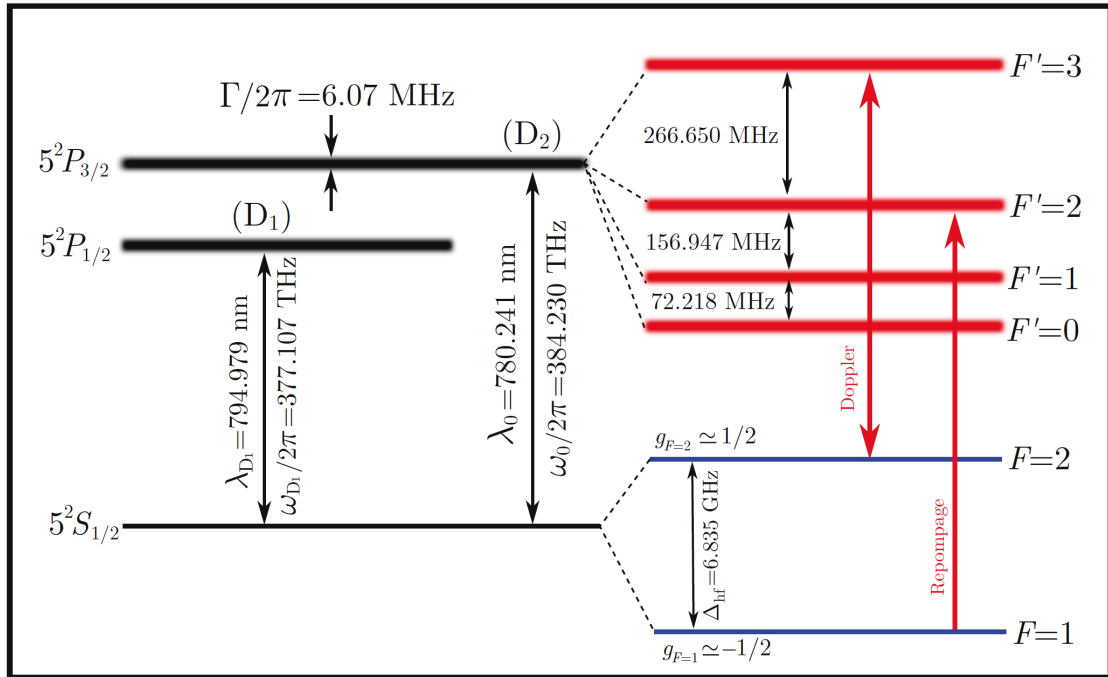
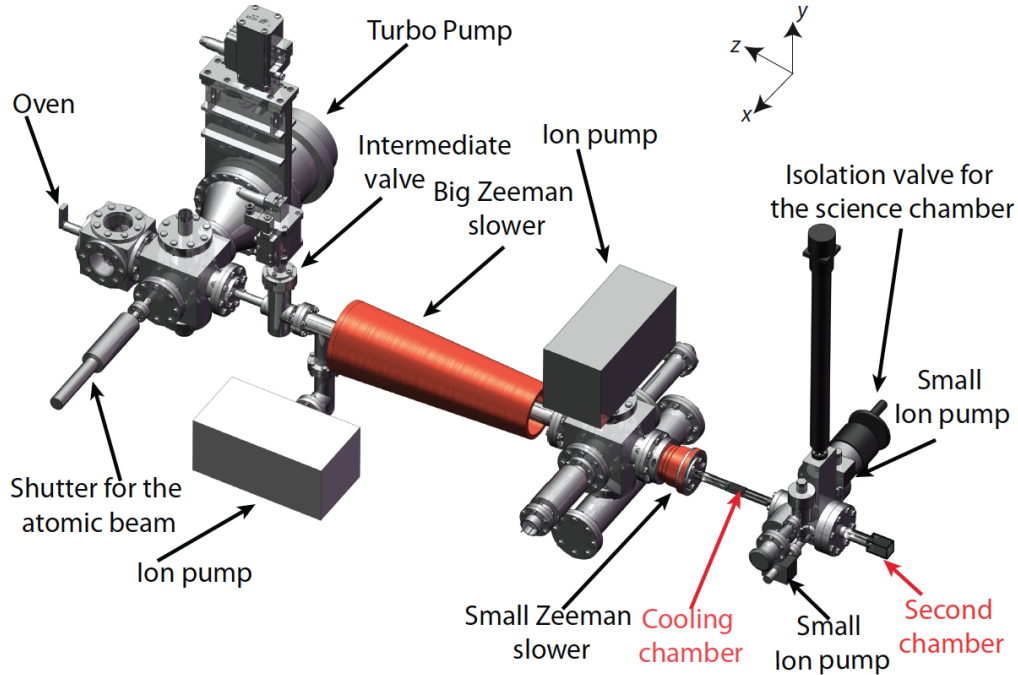
Quantity	Symbol	Value
Mass	m	1.44×10^{-25} kg
Frequency of D ₂ transition	ω_0	$2 \pi \times 384.230$ THz
Wavelength of D ₂ transition (vacuum)	λ_0	780.241nm
Wavelength of D ₂ transition (air)	λ_0^{air}	780.033nm
Linewidth of D ₂ transition	Γ	$2 \pi \times 6.07$ MHz
Hyperfine splitting frequency	Δ_{hf}	6.834682611 GHz
Recoil velocity	v_r	0.59 cm.s ⁻¹
Intensity of saturation	I_{sat}	1.66mW.cm ⁻²

The D2 line refers to the transitions between the $5^2S_{1/2}$ and $5^2P_{3/2}$ energy levels, with wavelength of $\lambda_0 \simeq 780\text{nm}$. The D2 line provides convenient channels for atom-laser interaction for the lasers that are commonly available in the industry. Due to hyperfine structure, the $5^2P_{3/2}$ energy level splits into four energy levels: $|F' = 0\rangle$, $|F' = 1\rangle$, $|F' = 2\rangle$, $|F' = 3\rangle$. The $5^2S_{1/2}$ energy level also splits into two energy levels: $|F = 1\rangle$ and $|F = 2\rangle$, which are differentiated by the hyperfine energy gap of $\Delta_{\text{hf}} \approx 6.83\text{GHz}$. In most ultra-cold atom experiments with ^{87}Rb , the cooling channel is the transition $|F = 2\rangle \rightarrow |F' = 3\rangle$. This transition can be used for techniques such as Doppler cooling, Zeeman slowing, MOT, and imaging.

However, $|F = 2\rangle \rightarrow |F' = 3\rangle$ is not a closed transition. According to the selection rules, atoms in the $|F = 2\rangle$ state can not only transition to the $|F' = 3\rangle$ state, but can also transition to the $|F' = 2\rangle$ or $|F' = 1\rangle$ states, and subsequently decay back to the $|F = 1\rangle$ state. These atoms in the $|F = 1\rangle$ state cannot be excited to the $|F' = 3\rangle$ state, which means that they escape from the cooling cycle of $|F = 2\rangle \rightarrow |F' = 3\rangle$. To address this, we need to repump these escaping atoms back into the cooling cycle by using the transition $|F = 1\rangle \rightarrow |F' = 2\rangle$.

3.3 Description of experimental cycle

The global view of our experiment is described in figure 3.4. The experiment cycle can be divided into two parts, the operations in the *cooling chamber* and the *second chamber*.

FIGURE 3.3: Hyperfine structure of D_2 line of ^{87}Rb FIGURE 3.4: **Global view of the experimental apparatus.** The axis x, y, z are set in the way shown in the figure and this standard of the axis will be used in this manuscript and in our experiment.

First, we heat rubidium metal in an oven set to 120°C to vaporize the rubidium gas and introduce it into the vacuum chamber. After a series of cooling processes, such as transverse molasses and Zeeman slowing, we are able to capture more than 10^9 atoms in a magneto-optical trap within a glass cell, referred to as the *cooling chamber*. Then, we load about 1×10^9 atoms into a magnetic trap and cool them further by RF evaporation to reach temperatures of around $5\mu\text{K}$. Following RF evaporation, we use an optical tweezer to capture more than 1×10^7 atoms from the magnetic trap and move them into the *second chamber*. Here, we load the atoms into a quasi-isotropic 3D optical dipole trap and cool them further by optical evaporation until we reach a Bose-Einstein condensate. Finally, we manipulate the BEC in a disordered potential and conduct measurements.

The vacuum pressure is maintained at a level of 10^{-9} mbar in the region where transverse molasses and Zeeman slowing are performed, and 10^{-11} mbar in the cooling chamber and the second chamber. This minimizes collisions between the atoms and residual air molecules, thus reducing heating and loss of cooled atoms.

The laser system used in the experiment is illustrated in figure 3.5. This system generates the beams needed for all cooling, pumping, and imaging of atoms. L1 is locked to ^{87}Rb using saturated absorption spectroscopy. The locked L1 serves as the reference frequency for L2 and L3. L2 is the repumping laser, and L3 is the cooling laser. The laser source for L1 is an assembly of an external cavity diode laser developed in Observatoire de Paris (SYRTE). The external cavity can reduce the linewidth of the laser $< 1\text{MHz}$ [69]. The laser can provide a power of 20 mW. At the beginning of my PhD, we used to use the same laser for L2 and L3. But they have been used for many years and the power was decreasing gradually, so we replaced L2 and L3 with new lasers called *Cheetah* from *Sacher – Lasertechnik*. This *Cheetah* laser can provide power up to about 120 mW at 780 nm. The linewidth is about 5 MHz. The tuning range is within 20 GHz so that it can work both for cooling (L3) and repumping (L2).

3.4 Transverse molasses and Zeeman slowing

First, the atomic jet from the oven is collimated by two pairs of counter-propagating laser beams, performing transverse Doppler cooling on the atomic jet. The cooling laser

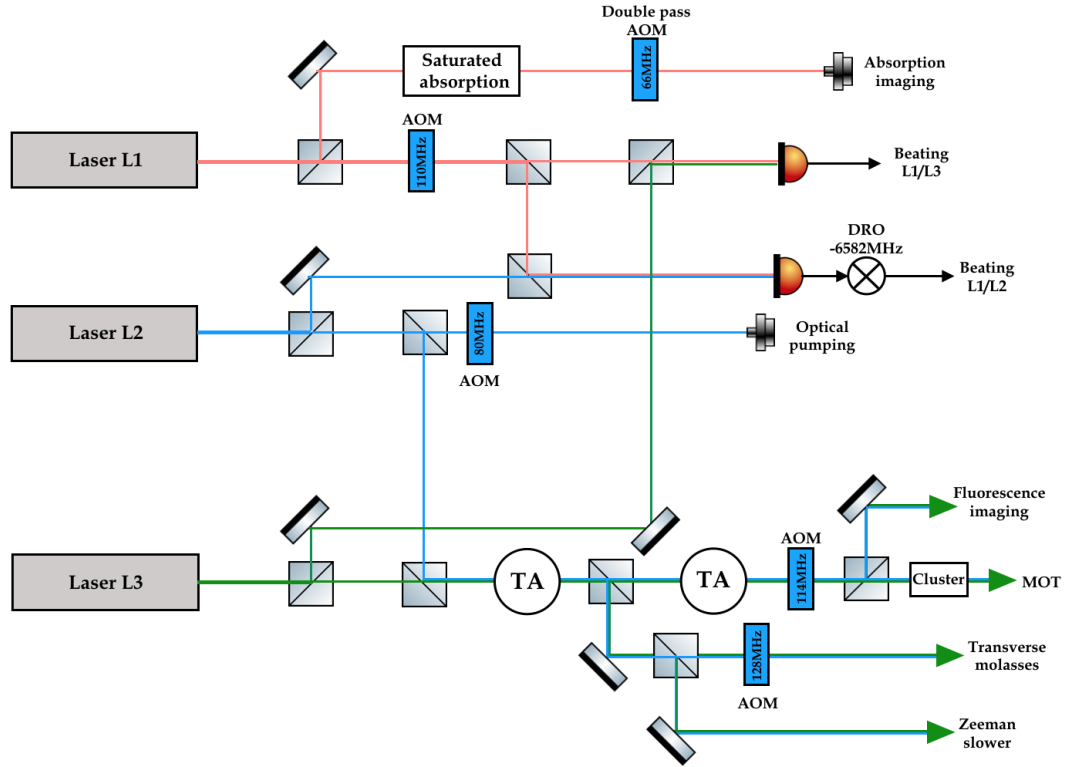


FIGURE 3.5: Laser systems of L1, L2 and L3. AOM is acousto-optical modulator. TA is tapered amplifier for lasers.

is red-detuned from the transition $|F = 2\rangle \rightarrow |F' = 3\rangle$ to slow down the atoms in the transverse direction along \mathbf{x} and \mathbf{y} , a process known as transverse molasses. With the aid of transverse molasses cooling, the atomic beam is collimated along the \mathbf{z} direction. The atomic beam is then filtered spatially by a metal plate pierced by a diaphragm and in contact with a 'cold finger' at -30°C . The atoms that do not pass through the tube connecting the chamber of transverse molasses and the Zeeman slower are adsorbed on the surface of the cold finger, so that these atoms do not increase the pressure inside the chamber and do not attach to the surface of the glass, which would affect the transverse cooling.

The collimated atomic beam is then exposed to a counter-propagating laser beam moving in the $-\mathbf{z}$ direction. This laser beam is red-detuned with respect to the transition $|F = 2\rangle \rightarrow |F' = 3\rangle$, with a frequency of ω . This laser beam applies Doppler cooling on the longitudinal velocity of atoms along \mathbf{z} direction, reducing the longitudinal velocity of the atoms, a process known as Zeeman slowing.

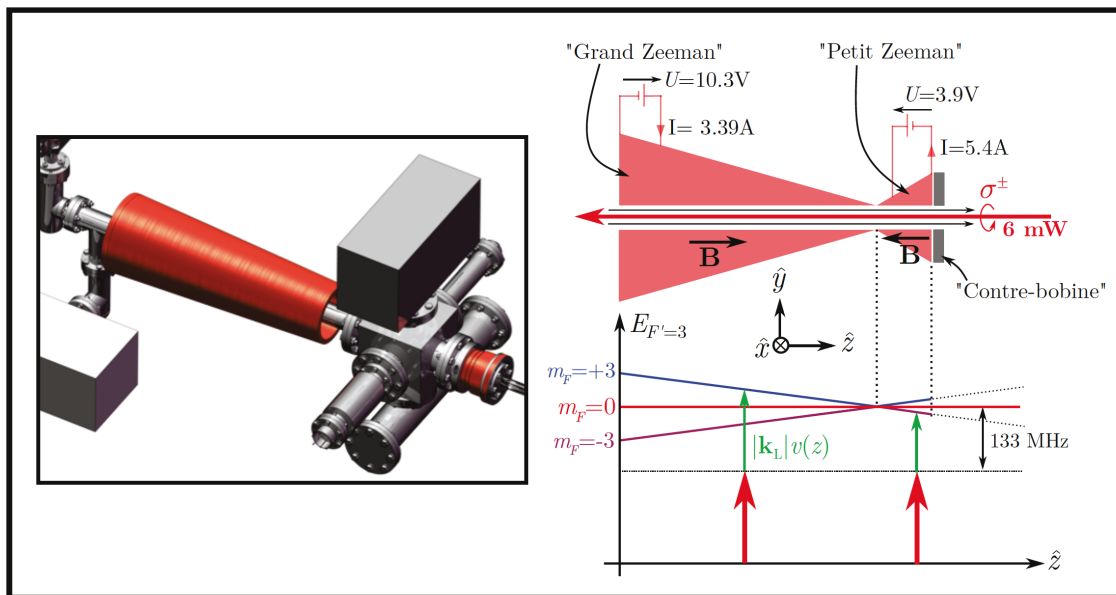


FIGURE 3.6: **Principal of Zeeman slower.** The atoms are kept resonant for the laser cooling along \mathbf{z} by the magnetic field $B(z)$. The laser is red-detuned from the transition $|F = 2\rangle \rightarrow |F' = 3\rangle$ by 133MHz so that the Zeeman laser is not resonant with the atoms in the MOT, which can induce loss of atoms. The magnetic field defines the magnetic polarization of atoms along \mathbf{z} . The circular polarization of the laser is adjusted for the cooling transition $|F = 2, m_F = \pm 2\rangle \rightarrow |F' = 3, m_F = \pm 3\rangle$ according to the direction of the magnetic field.

However, after several cooling cycles along \mathbf{z} , the velocity of the atoms $v(z)$ becomes increasingly smaller, making it difficult to maintain the resonance condition for Doppler cooling. To address this issue, we adjust the energy gap of the transition $|F = 2\rangle \rightarrow |F' = 3\rangle$ along \mathbf{z} to ensure that the resonance condition is always met during the Zeeman cooling process.

In order to adjust the energy gap between $|F = 2\rangle$ and $|F' = 3\rangle$, we apply a magnetic field ramping along \mathbf{z} , $B(z)$ as shown in figure 3.6. The magnetic field induces an energy shift due to the Zeeman effect, proportional to $\mu_B B$ [70], as shown in figure 3.6. By well selecting the polarization of the cooling laser, we select the transition $|F = 2\rangle \rightarrow |F' = 3, m_F = \pm 3\rangle$. So for the relevant transition that we select, the condition of resonance can be satisfied along \mathbf{z} :

$$\omega_0 = \omega + |\mathbf{k}|v(z) - \frac{\mu_B B(z)}{\hbar}, \quad (3.13)$$

where $v(z)$ is the velocity of atoms along \mathbf{z} direction. This Zeeman slowing is highly efficient that the velocity of the atomic beam can be slowed from a typical velocity of about

100 m.s⁻¹, to about 20 m.s⁻¹ after the Zeeman slower of about one meter.

3.5 Magneto-optical trap

With velocity 20 m.s⁻¹, the atoms are slow enough to be captured by the magneto-optical trap (MOT) in the cooling chamber, as shown in figure 3.8. We briefly introduce the basic principle of MOT.

The basic principle of MOT [71, 72] is illustrated in figure 3.7. To simplify the explanation, a 1D version is considered, but it can be easily extended to 3D. A magneto-optical trap consists of pairs of counter-propagating laser beams and a magnetic field gradient. In the example shown in figure 3.7, the transition $J = 0 \rightarrow J = 1$ forms the cooling cycle of the MOT. The two laser beams in each direction have opposite circular polarizations. The σ_+ beam generates the cycle $|J = 0\rangle \rightarrow |J = 1, m_J = +1\rangle$, while the σ_- beam generates the cycle $|J = 0\rangle \rightarrow |J = 1, m_J = -1\rangle$. Both lasers are red-detuned from the relevant transitions. If an atom is located at $x > 0$, it experiences two forces: one from the σ_+ beam pushing it towards the right, and one from the σ_- beam pushing it towards the center. Since the detuning of the σ_- beam is smaller than the detuning of σ_+ , the total force experienced by the atom is towards the center. Since the force applied to the atom is the radiation pressure from the laser, the atom also experiences Doppler cooling in the MOT. This allows the magneto-optical trap to cool and trap the atoms around the center of the magnetic field gradient.

In our experiment of ⁸⁷Rb, we have a 3D MOT. The cooling cycle is the transition $|F = 2\rangle \rightarrow |F' = 3\rangle$. As shown in figure 3.8, for 3D MOT, we have three pairs of counter-propagating laser beams, σ_+ and σ_- for each pair. The gradient of the magnetic field is generated by a pair of anti-Helmholtz coils (the current circulating in opposite directions). The coils produce a spherically symmetric quadrupole magnetic field to assure the presence of a gradient of the magnetic field along each pair of counter-propagating laser beams.

In our experiment, the loading time for the MOT is 3.5 seconds to saturate the MOT. Then once the loading of MOT is finished, the mechanical shutter is closed, and the atomic beam from the oven is blocked. The temperature of the MOT is estimated to be about

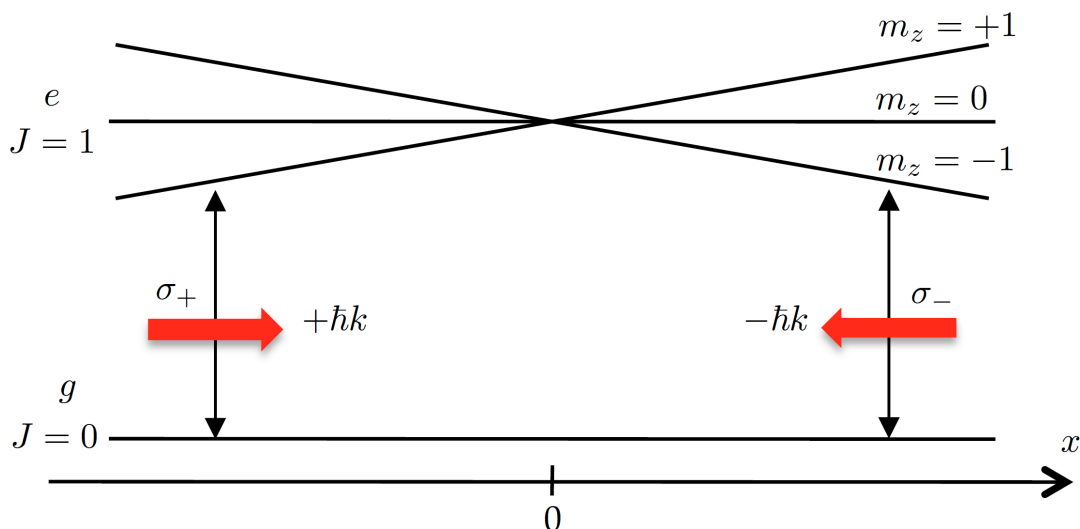


FIGURE 3.7: **Basic principle of the magneto-optical trap (one-dimensional version).** The radiation pressure force created by each light wave depends on the position due to the presence of a magnetic field gradient. The resultant of the two radiation pressure forces is a restoring force towards the origin. The figure is from [71].

$500\mu\text{K}$. Then the magnetic field of MOT is switched OFF, and we apply another 3D optical molasses of the atoms, by the cycle $|F = 2\rangle \rightarrow |F' = 3\rangle$ and that permits us to lower the temperature of the atoms to $50\mu\text{K}$ before loading the atoms into a magnetic trap.

3.6 Magnetic trap

To understand how atoms can be trapped by a magnetic potential, we briefly introduce the magnetic potential principle. The magnetic potential arises from the interaction between the magnetic dipole of an atom and a magnetic field. The total angular internal momentum of the atom $\mathbf{F} = \mathbf{I} + \mathbf{L} + \mathbf{S}$, where \mathbf{I} is nuclear spin, \mathbf{L} is orbital angular momentum, and \mathbf{S} is electronic spin. The interaction between the magnetic momentum of the atom and the magnetic field induces an energy shift $U_{\text{mag}} = -\vec{\mu}_F \cdot \mathbf{B}$ for the atomic level $|F\rangle$, where $\vec{\mu}_F = -\mu_B g_F \mathbf{F}$, and μ_B is Bohr magneton, g_F is Landé-g factor. In the regime of the weak magnetic field, the energy shift is approximately linear to the magnetic field, and the energy shift induced by the magnetic field can be described by linear Zeeman shift:

$$U_{\text{mag}}(\mathbf{x}) = m_F g_F \mu_B B(\mathbf{x}), \quad (3.14)$$

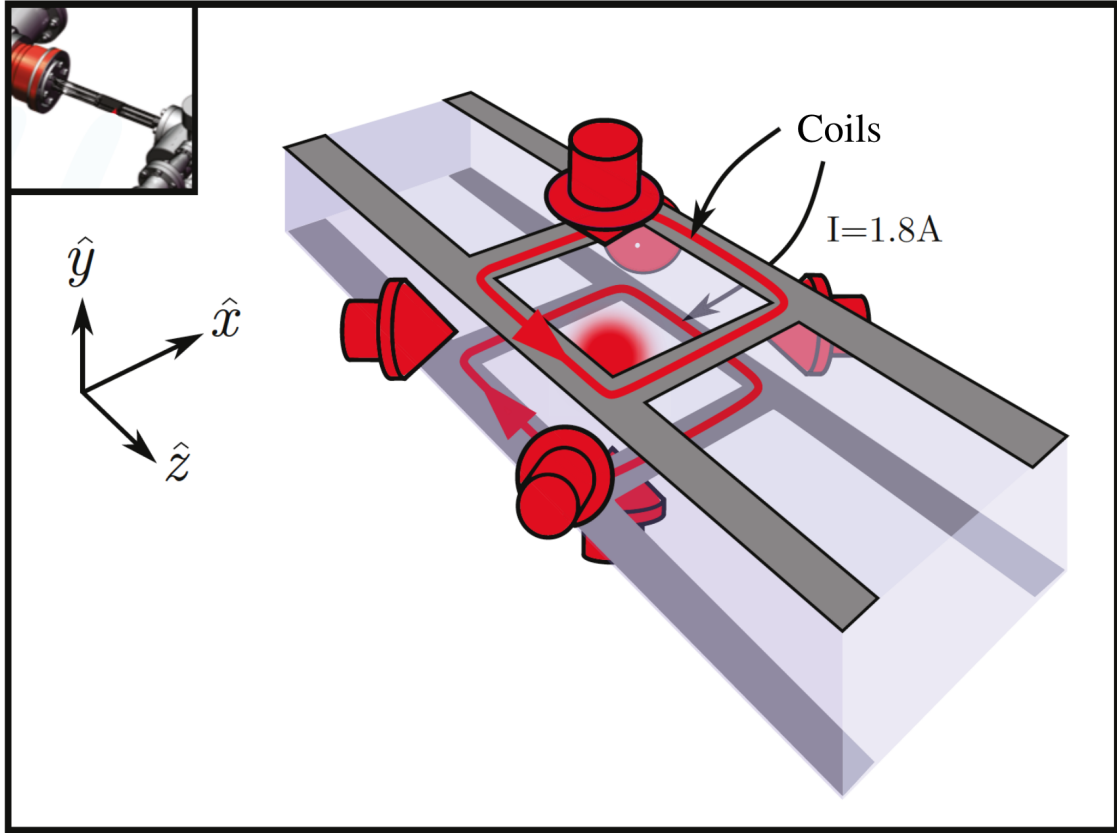


FIGURE 3.8: **Magneto-optical trap in our experiment.** Three pairs of counter-propagating lasers and a magnetic gradient can cool and trap the atoms (magneto-optical trap). The three pairs of lasers come from the *cluster*, and each laser is about 15mW.

where $B = |\mathbf{B}|$, $g_{F=2} = 1/2$ for $|F = 2\rangle$, $g_{F=1} = -1/2$ for $|F = 1\rangle$. Therefore a magnetic field $B = B(\mathbf{x})$ variant in space $\{\mathbf{x}\}$ can produce a conservative magnetic potential $U_{\text{mag}}(\mathbf{x})$.

In our experiment, the ^{87}Rb atoms are trapped in the minimum of the magnetic potential, so we need $g_F m_F > 0$. Since $g_{F=1} = -1/2$ and $g_{F=2} = 1/2$, the states that can be trapped by the minimum of the magnetic field are $|F = 1, m_F = -1\rangle$, $|F = 2, m_F = 1\rangle$, and $|F = 2, m_F = 2\rangle$. We choose $|F = 1, m_F = -1\rangle$ to be the state trapped in our magnetic trap.

The realization of our magnetic trap is shown in figure 3.9 [73]. It is an *Ioffe–Pritchard* trap [74], composed of a quadrupole field and a dipole field. The quadrupole field is generated by a pair of coils in an anti-Helmholtz configuration (the current circulating in

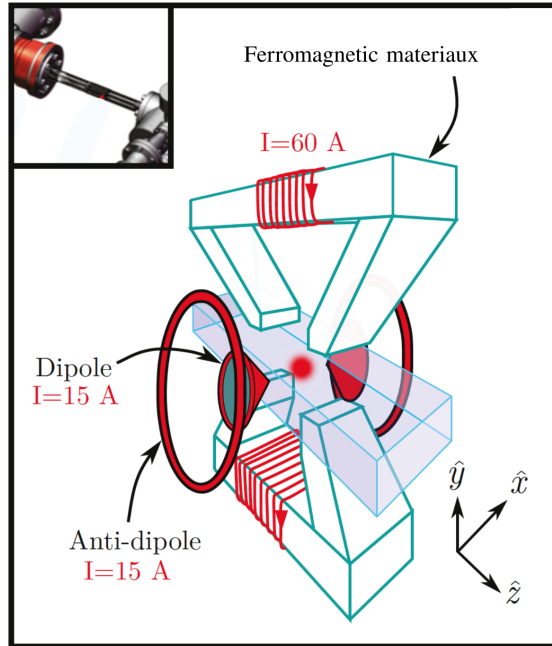


FIGURE 3.9: **Realization of our magnetic trap.** The magnetic trap is formed by combining a quadrupole field generated by an electromagnet of 60 A, and a dipolar field created by a pair of coils of 15 A.

opposite directions in the two coils), twining around a piece of ferromagnetic material, forming an electromagnet. Using the ferromagnetic material can help to induce a relatively large gradient with a smaller current. Here we can generate a gradient of $830\text{G}\cdot\text{cm}^{-1}$ with a current of 60A. If we use only a pair of coils, that will cost 100A to generate the same level of the gradient. The dipole field is produced by a pair of coils in Helmholtz configuration.

In our experiment, after loading the MOT with atoms in state $|F = 2\rangle$, we apply a pulse called *optical pumping* to transfer the atoms from $|F = 2\rangle$ to $|F = 1\rangle$ for the magnetic trap. Finally we have about 1×10^9 atoms trapped in the state $|F = 1, m_F = -1\rangle$ in the magnetic trap, about $300\ \mu\text{K}$. The density of atoms is in the order of $10^{15}\ \text{m}^{-3}$. Then we compress the magnetic trap to increase the density in order to make sure that the collision between the atoms in the trap is efficient enough to perform the RF-evaporation.

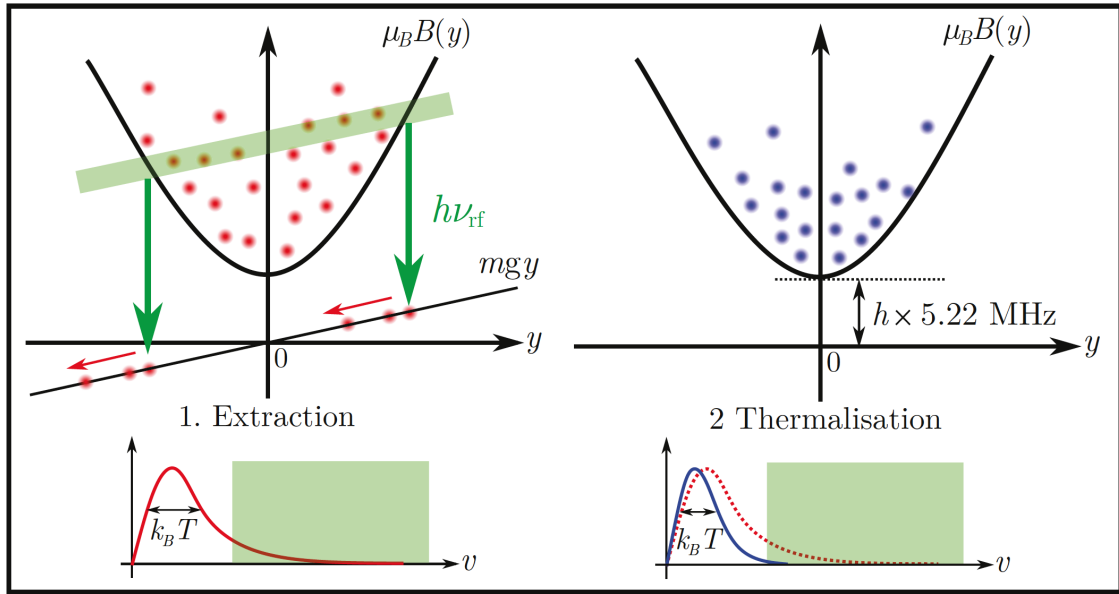


FIGURE 3.10: **Principal of RF-evaporation.** The atoms in high energy levels (relatively hot atoms) in the trap are excited by an rf field with energy $h\nu_{\text{rf}}$. These atoms are excited from $|F = 1, m_F = -1\rangle$ to state $|F = 1, m_F = 0\rangle$. The atoms excited to state $|F = 1, m_F = 0\rangle$ are no longer trapped by the magnetic potential and they leave the trap by gravity. Then the rest of the atoms thermalize by collision to a lower temperature.

3.7 RF-evaporation

Evaporative cooling is a widely used for cooling atoms to a Bose-Einstein condensate state. Two main methods for implementing evaporative cooling are RF-evaporation and optical evaporation. The basic principle behind both techniques is the same: by selectively extracting the relatively hot atoms from the ensemble, the remaining atoms thermalize to a lower temperature. In optical evaporation, this is achieved by gradually lowering the trap depth, allowing the hot atoms to escape, while in RF-evaporation, a radio-frequency 'knife' is used to remove the hot atoms. In our experimental cycle, we use RF-evaporation to cool the atoms in the magnetic trap in the cooling chamber. We do optical evaporation in the second chamber (see section 3.9) to create Bose-Einstein condensate.

For the RF-evaporation in the magnetic trap, we use a radio-frequency '*knife*' to excite the hot atoms from the **trapped** state $|F = 1, m_F = -1\rangle$ to **untrapped** state $|F = 1, m_F = 0\rangle$. The atoms excited to the state $|F = 1, m_F = 0\rangle$ are no longer trapped in the magnetic field, and they will leave the magnetic trap by gravity. Then the rest of the atoms get thermalization to a lower temperature. Then we scan the RF frequency to continuously extract the relatively hot atoms when they are getting thermalized. Scanning

the RF-knife can be equivalently seen as diminishing the trap depth of the magnetic trap.

In our experiment, the process of the RF-evaporation is about 10s. During this process, we scan the frequency of RF-knife from 90MHz to 6MHz to continuously evaporate the hot atoms. Finally we get an ensemble of about 6×10^7 atoms in state $|F = 1, m_F = -1\rangle$, with density of 10^{17}m^{-3} and temperature about $5 \mu\text{K}$. In our experiment, we do not get BEC with this step of RF-evaporation. After RF-evaporation, the de Broglie wavelength of the atoms is about 100nm, and the phase density $n\lambda_{\text{dB}}^3$ can reach about 10^{-4} . This step helps to cool the atoms cold enough for efficient loading in an optical tweezer.

3.8 Loading the atoms in an optical tweezer and transport to the second chamber

The optical tweezer is a dipole trap produced by a far-detuned and highly focused Gaussian beam. The beam can induce an optical dipole potential variant in real space. If the beam is red-detuned from the resonance of atom, the minimum of the potential is at the focal point of the beam. So the potential induced by the Gaussian beam forms a trap, and the atoms can be captured in the minimum, which is the focal point of the beam. That is the so-called **optical tweezer**.

The general expression for optical dipole trap is [30]:

$$U_{\text{dip}} = \frac{3\pi c^2 \Gamma}{2\omega_0^3 \Delta} I(\mathbf{r}) \quad \text{with} \quad \frac{1}{\Delta} = \left(\frac{1}{\omega - \omega_0} - \frac{1}{\omega + \omega_0} \right), \quad (3.15)$$

where Γ is the spontaneous decay rate of the excited level (6.6MHz for D2 line of ^{87}Rb), ω_0 is the frequency of the relevant resonance of the atom (780nm for D2 line of ^{87}Rb), ω is the frequency of the trapping laser and $I(\mathbf{r})$ is the intensity of the trapping laser. The intensity of the laser $I(\mathbf{r})$ at point $\mathbf{r} = \{x, y, z\}$ can be converted into the power of laser:

$$I(\mathbf{r}) = \frac{2P}{\pi w^2(z)} e^{-2x^2/w^2(z)} \quad \text{with} \quad w(z) = w_0 \sqrt{1 + \frac{z^2}{z_R^2}}, \quad (3.16)$$

where P is the power of trapping laser, $w(z)$ is the beam diameter at position z , w_0 is the beam waist, z_R is Rayleigh length of the laser, $z_R = \pi w_0^2/\lambda$. Since the atoms are

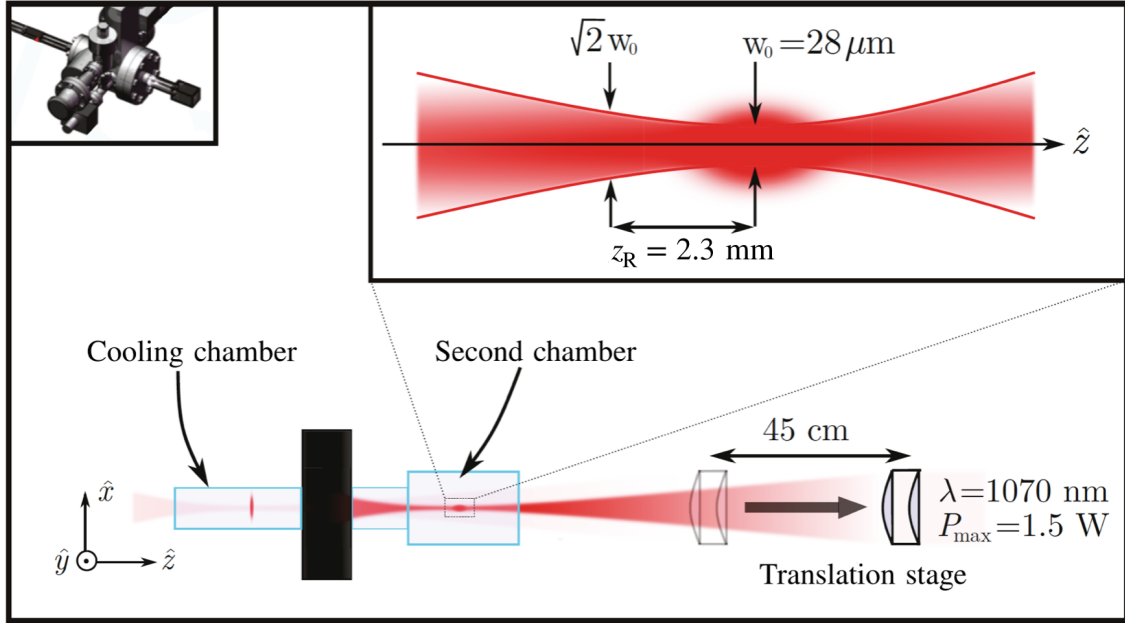


FIGURE 3.11: **Optical tweezer and translation of the atoms.** The laser beam is focused to the atoms by a lens to have a waist of $28 \mu\text{m}$. The lens is mounted on a translation stage. The atoms trapped by the focal point of the laser are translated by 45 cm from the cooling chamber to the second chamber.

trapped in the focal point of the beam, we can develop the trapping potential at the focal point $x = y = z = 0$ to the first order, and in this regime, the potential can be seen as a harmonic trap:

$$U(\mathbf{r}) = \frac{3\pi c^2 \Gamma}{2\omega_0^3 \Delta} \times \frac{2P}{\pi w_0^2} \left(1 - \frac{2x^2}{w_0^2} - \frac{z^2}{z_R^2} \right). \quad (3.17)$$

From the equation 3.17, the trap depth of the optical potential is:

$$U_0 = \frac{3c^2 \Gamma P}{\omega_0^3 w_0^2 \Delta}, \quad (3.18)$$

and the radial trapping frequency $\omega_{x=y}$ and longitudinal trapping frequency ω_z are:

$$\omega_{x=y} = \sqrt{\frac{4U_0}{mw_0^2}} \quad \text{and} \quad \omega_z = \sqrt{\frac{2U_0}{mz_R^2}}. \quad (3.19)$$

In our experiment, the laser we use for the optical tweezer is a laser *Keopsis* of $\lambda = 1070 \text{ nm}$. Therefore the trapping is far red-detuned from the D_2 transition of ^{87}Rb . The power of the laser we use to produce the optical tweezer is about 1.5W. As shown in figure 3.11, we focus the laser through a lens mounted on a translation stage into the atoms in the cooling chamber, the waist of the laser $w_0 = 28 \mu\text{m}$, and Rayleigh length $z_R = 2.3 \text{ mm}$. According

to the equations 3.18 and 3.19, the transverse trapping frequency $\omega_{x=y} \simeq 2\pi \times 1.03\text{kHz}$ and the longitudinal trapping frequency $\omega_z = 2\pi \times 89\text{Hz}$.

More than 1×10^7 atoms can be captured in the optical tweezer after the RF evaporation. The large detuning guarantees the absence of the photon scattering of the atoms by the trapping laser. The lifetime of the atoms trapped in the tweezer is measured to be about 25 seconds, and the loss is mainly due to the collision of the atoms with the residual background gas in the vacuum.

After loading the atoms into the tweezer, we transport the atoms from the cooling chamber into the second chamber. As shown in figure 3.11, with the help of the translation stage, we move the lens by 45 cm in 2 seconds. The translation stage is supported by compressed air. The transport will inevitably slightly heat the atoms, from 5 μK to about 10 μK , and about 6×10^6 atoms are lost during the transport. Finally, about 4×10^6 atoms are transported into the second chamber by the optical tweezer.

3.9 Optical evaporation

Once the atoms are transported into the second chamber, another laser beam propagating along \mathbf{y} , vertical direction, is focused on the atoms to form a 3D quasi-isotropic trap as shown in figure 3.13 a, a crossed optical dipole trap. In our experiment, this vertical laser beam is called the **dimple** beam. The focal point of the tweezer and dimple beams are superimposed, and the atoms are trapped in the crossed focal point of the two beams. The dimple beam comes from the same *Keopsis* laser, $\lambda = 1070\text{ nm}$, and the power of the dimple beam is about 7 W to form the crossed optical dipole trap. To make the crossed optical dipole trap isotropic along \mathbf{x} , \mathbf{y} and \mathbf{z} , the dimple beam is reshaped to be elliptical by a cylindrical telescope, and at the focal point, the waist of the dimple beam is $w_z = 91\ \mu\text{m}$ and $w_x = 203\ \mu\text{m}$. Thus we have a cloud of more than 2×10^6 atoms in crossed optical dipole trap, the temperature of the cloud $\sim 10\ \mu\text{K}$ and the phase space density $n\lambda_{\text{dB}}^3$ at this step is in the order of 10^{-2} .

Now in the optical trap, we can conveniently perform the optical evaporation by diminishing the trap depth. As mentioned in the last section, the basic idea of optical evaporation

is to extract the hot atoms in the optical trap by simply lowering the trap depth, and the rest of the atoms thermalizes to a lower temperature.

In the first year of my PhD, with my colleagues, I spent quite some time optimizing the optical evaporation. Because of the lock-down of Covid-19, I spent two months in my home mainly on studying the theories of evaporation, and at the end, we optimized the ramp of our optical evaporation from five separate ramps to a single ramp following a power law as:

$$P(t) = \frac{P_0}{(1 + t/\tau)^\beta}, \quad (3.20)$$

the parameters of the ramp τ and β decide the efficiency of the optical evaporation. In appendix A we explain in detail why we ramp the laser power as this power law from a general picture of thermodynamics .

The efficiency of optical evaporation can be defined as $\gamma = \frac{dD}{D} = -\frac{dN}{N}$, where D is the phase-space density (This definition of efficiency is explained in the appendix A). The efficiency γ represents the ratio of atoms lost to the increase in phase-space density. In our experiment, the efficiency of the optical evaporation is very high, with γ reaching about 4, as shown in figure 3.12.

The process of optical evaporation in our experiment lasts for 2 seconds. During this time, the power of the tweezer beam is reduced from around 500mW to 10mW and the power of the dimple beam is reduced from around 7W to 218mW. At the end of the evaporation, the trap frequencies are $\omega_x \simeq 2\pi \times 30\text{Hz}$, $\omega_y \simeq 2\pi \times 40\text{Hz}$, $\omega_z \simeq 2\pi \times 25\text{Hz}$. We achieve a Bose-Einstein condensate of 2×10^5 atoms at around 60 nK.

There are some conveniences for optical evaporation. The optical trap does not interact with the magnetic spin states of atoms, so a priori, it can trap the atoms with any magnetic spin without specific selection. It is beneficial for the experiment studying many-body physics with Feshbach resonances because it is much easier to play with Feshbach resonances in an optical trap.

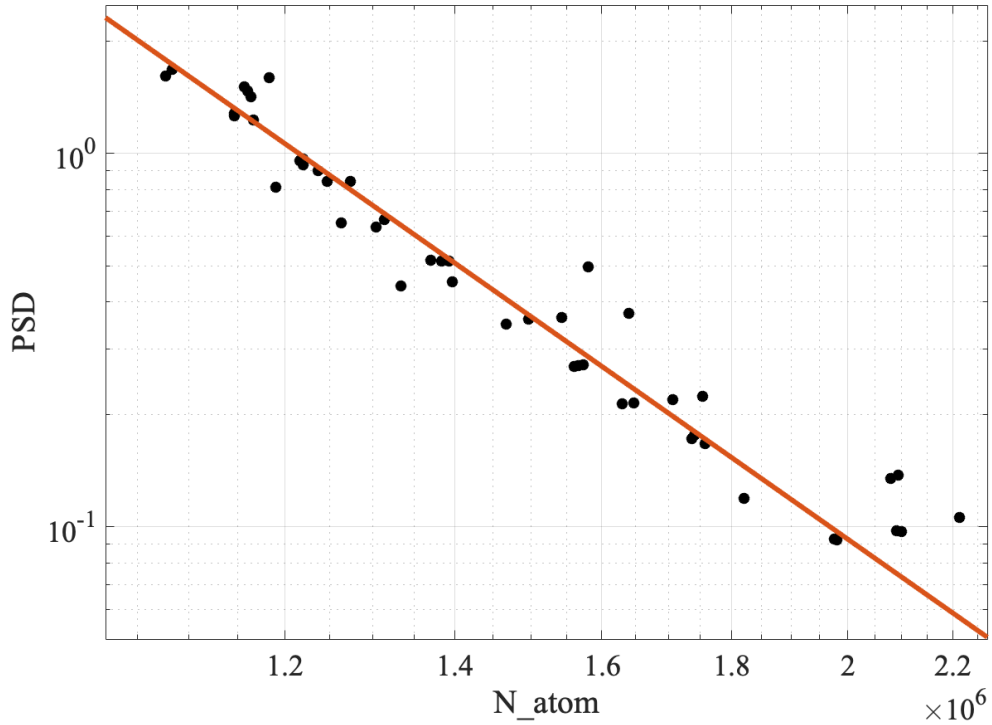


FIGURE 3.12: **Efficiency of optical evaporation in our experiment.** The efficiency γ means how much we gain in phase-space density(PSD) by losing how many atoms. In our experiment, the efficiency of optical evaporation γ is measure to be about 4.

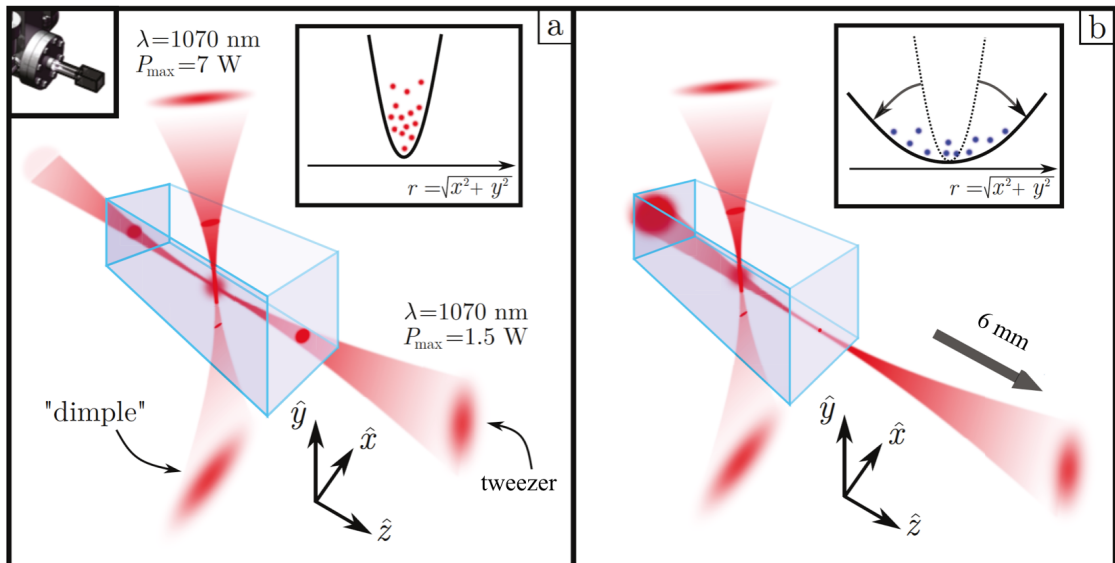


FIGURE 3.13: **Crossed optical dipole trap and adiabatic opening.** **a**, the configuration of the crossed optical dipole trap. **b**, the adiabatic cooling through moving the focus of the tweezer beam by 6 mm along z direction.

3.10 Cool the atoms even more by adiabatic cooling

Adiabatic cooling is a technique that allows us to achieve even lower temperatures after optical evaporation. The process involves moving the focal point of the optical tweezer beam, which results in an increase in the waist of the tweezer and a decrease in the trap frequency. This is because in thermodynamic equilibrium, the temperature of the atomic gas T is directly proportional to the trap frequency f . By decreasing the trap frequency, we are able to lower the temperature of the gas. To avoid confusion, we use the symbol f instead of the usual symbol ω for the trap frequency, as it is visibly distinguishable from the beam waist w .

As illustrated in figure 3.13b, the focal point of the tweezer beam is moved by 6mm in 1 second with the help of the translation stage. At the crossing point with the dimple beam, the waist of the tweezer beam w is enlarged from $28\mu\text{m}$ to $78\mu\text{m}$. Since the trap frequency is inversely proportional to the square of the beam waist, $f \propto 1/w^2$, the trap frequency f' after the decompression is:

$$f' = \frac{w^2}{w'^2} f \simeq 0.13 f. \quad (3.21)$$

Thus, by adiabatic cooling, the temperature of the gas is lowered from T to T' :

$$T' = \left(\frac{f'}{f}\right) T \simeq 0.13 T. \quad (3.22)$$

Finally, by a TOF measurement, the temperature of the gas is measured to be about 7.5nK. So the adiabatic cooling helps to cool the gas from $\sim 60\text{nK}$ to $\sim 7.5\text{nK}$, without increasing the phase-space density. At this temperature, the BEC is in a good condition of being a plane wave with $|\mathbf{k} = 0\rangle$. The profile of our Bose-Einstein condensate after the adiabatic cooling is shown in figure 3.14.

3.11 Magnetic levitation

As previously discussed in section 2.4, the dynamics of Anderson localization involve the long-time evolution of the atoms in a disordered potential. In order to observe these dynamics in experiments, it is necessary to compensate for the effects of gravity on the atoms. This can be achieved by applying a force in the opposite direction of gravity, such

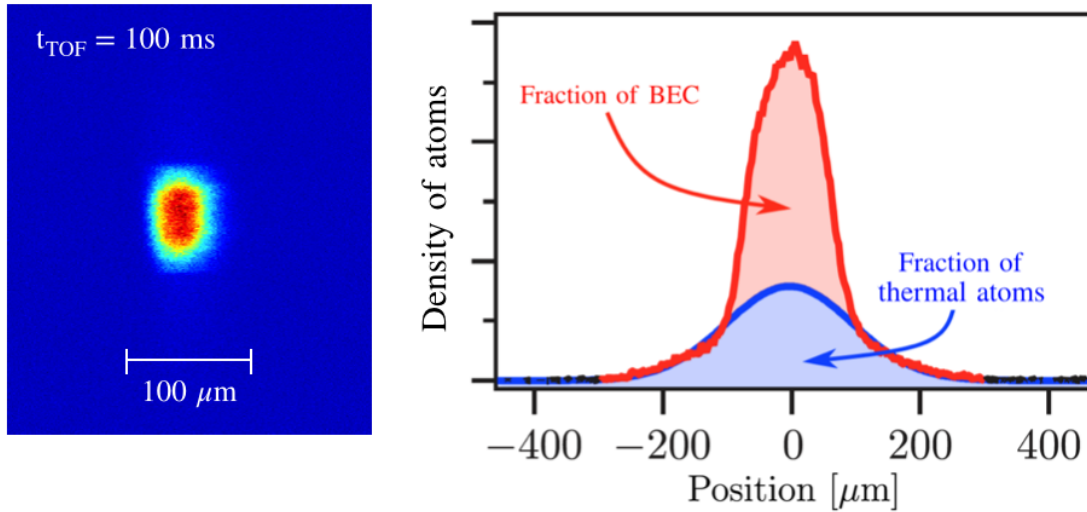


FIGURE 3.14: **Experimental image of BEC.** The picture of BEC is taken after a time of light (TOF) = 150ms. In the gas, we have both condensed atoms and thermal atoms. The profile of BEC is a parabola and the profile of thermal atoms is Gaussian.

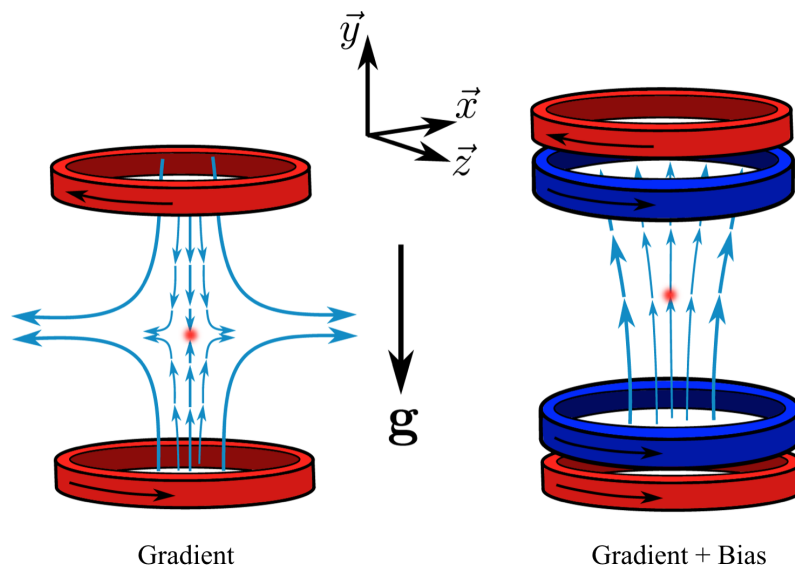


FIGURE 3.15: **The coils for the magnetic levitation.** The coils in the anti-Helmholtz configuration generate the magnetic gradient field (red coils). The coils in the Helmholtz configuration generate the magnetic bias field (blue coils). On the right, the magnetic field is the situation for a strong bias field.

as through levitation techniques.

To compensate for the effects of gravity on the atoms in a disordered potential, a magnetic force can be applied. This can be achieved by using a magnetic potential with a gradient of mgy in the opposite direction of gravity (along the y -axis). This gradient is typically generated using a pair of coils in an anti-Helmholtz configuration, where the current flows in opposite directions in the two coils. However, due to the nature of the magnetic field, where $\nabla \cdot \mathbf{B} = 0$, the presence of a gradient along one direction (such as the y -axis) also implies the presence of gradients along other directions (such as the x - and z -axes). Thus, a single pair of coils in an anti-Helmholtz configuration cannot produce a completely homogeneous field. To address this inhomogeneity, another pair of coils can be added in a Helmholtz configuration, where the current flows in the same direction in the two coils. This pair of coils generates a bias field B_0 and curvature b'' , which can be used to smooth out the inhomogeneities in the magnetic field.

The total norm of the magnetic field produced by these two pairs of coils is:

$$B(\mathbf{x}) \sim B_0 + b'y + \frac{1}{2}b''y^2 + \left(\frac{b'^2}{8B_0} - \frac{b''}{2} \right) \rho^2, \quad (3.23)$$

where B_0 is the bias, b' is the linear gradient, b'' is the curvature, and $\mathbf{x} = \{y, \rho\}$, $\rho = \sqrt{x^2 + y^2}$.

In our experiment, the linear gradient b' is approximately 3.04G/mm and the curvature b'' is approximately 10^{-5} G/mm² (more details about measuring the configurations of the magnetic field can be found in the master thesis of Vasiliki Angelopoulou). We work in a low bias regime, with $B_0 \simeq 3.23$ G, and we will explain the reason for this in section 5.1.1. Given the small value of b'' , the curvature can be considered negligible in our experiment. So we have:

$$B(\mathbf{x}) \sim B_0 + b'y + \frac{b'^2}{8B_0} \rho^2. \quad (3.24)$$

The magnetic potential is $U_{\text{mag}}(\mathbf{x}) = g_F m_F \mu_B B(\mathbf{x})$. Therefore, in order to compensate for gravity and levitate the atoms in place, the magnetic potential $U_{\text{mag}}(\mathbf{x}) = g_F m_F \mu_B B(\mathbf{x})$ must be adjusted such that its gradient along the y -axis is equal to the force of gravity:

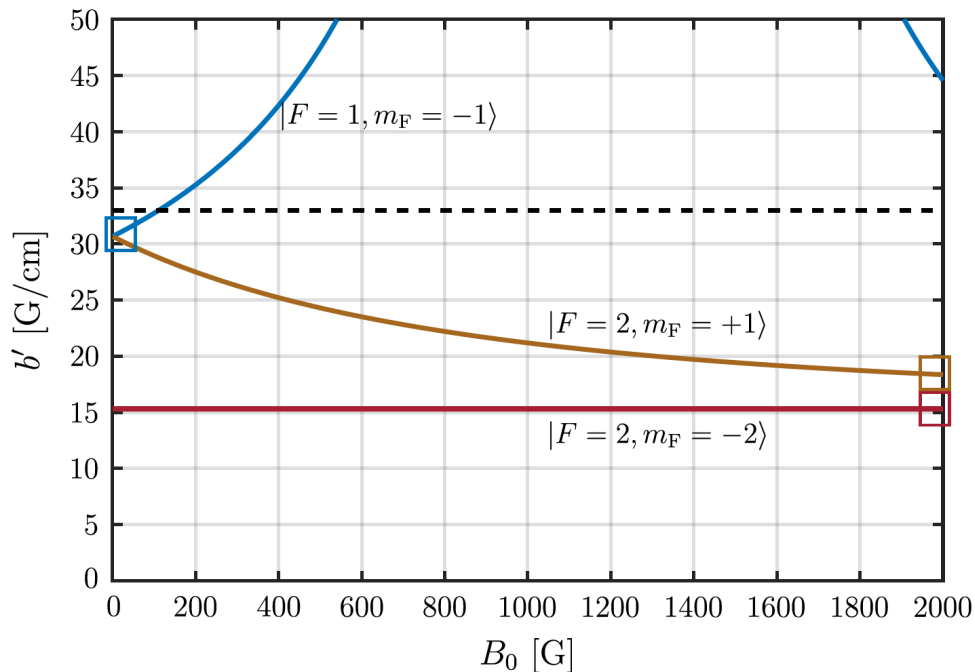


FIGURE 3.16: **The dependence of gradient b' on the bias field B_0 for different atomic levels.** The blue curve is for $|F = 1, m_F = -1\rangle$, the yellow curve is for $|F = 2, m_F = +1\rangle$, and the red curve is for $|F = 2, m_F = -2\rangle$ (this state was used in the experiment of 3d Anderson localization in 2012 [33]).

$\nabla_y U_{\text{mag}}(\mathbf{x}) = mg$. This is achieved by controlling the current flowing through the gradient coils:

$$b' = \frac{mg}{m_F g_{F, m_F} \mu_B}. \quad (3.25)$$

where m is the mass of one atom, g_{F, m_F} is the Landé factor.

To determine the value of the gradient b' needed to compensate for gravity, it is necessary to know the Landé factor g_{F, m_F} in equation 3.25. The Landé factor can be written as [70]:

$$g_{F, m_F}(B_0) = \frac{1}{m_F \mu_B} \frac{dE}{dB}(B_0). \quad (3.26)$$

In the regime of a weak field, where the energy shift caused by the bias field can be seen as linear, the Landé factor can be considered approximately constant. However, in the regime of a strong field, where the linearity is no longer valid, the dependence on the magnetic bias field B_0 of the Landé factor cannot be neglected anymore. Therefore, according to equation 3.25, the value of the gradient b' required to compensate for gravity also depends

on the bias B_0 .

The Landé factor, which is related to the atomic spin, varies for different atomic levels. Figure 3.16 shows the relation between the gradient b' required to compensate for gravity and the bias field B_0 for three atomic levels: $|F = 1, m_F = -1\rangle$, $|F = 2, m_F = +1\rangle$, and $|F = 2, m_F = -2\rangle$ on the bias field B_0 . These levels are chosen because 1) our BEC is produced in state $|F = 1, m_F = -1\rangle$, 2) state $|F = 2, m_F = +1\rangle$ is used to perform rf-spectroscopy as will be discussed in chapter 5, and 3) state $|F = 2, m_F = -2\rangle$ was used in a study in 2012 to investigate 3D Anderson localization and the mobility edge [33].

In equation 3.24, the quadratic term $\frac{b'^2}{8B_0}(x^2 + z^2)$ means that the magnetic field for levitation applies a horizontal harmonic trap on the atoms along x- and z-axis, with a trap frequency $\omega_{\perp} \propto 1/\sqrt{B_0}$, so this horizontal trap frequency depends on the bias field. In figure 3.17, we measure the horizontal trap frequency ω_{\perp} in function of the bias field B_0 . We use a fitting curve $\omega_{\perp} \propto 1/\sqrt{B_0}$ to fit the measured the trap frequencies. Here we use the very simple model by supposing the curvature $b'' = 0$, as introduced in section 3.11, but in reality, for strong current, the curvature b'' cannot be neglected (more details of our magnetic levitation can be found in the master thesis of Vasiliki Angelopoulou).

As mentioned above, in our experiment, we work with a low bias field $B_0 \simeq 3.23\text{G}$ (that is the magic point for our rf-transfer, see section 5.1.1). Under this condition, the horizontal trap frequency $\omega_{\perp} = \omega_{x,z}$ of the magnetic field is measured to be: $\omega_{\perp} \simeq 2\pi \times 7$ Hz. In section 7.4.2, we will discuss this horizontal magnetic trap ω_{\perp} .

3.12 Imaging system

In our experiment, to image the atoms, we use two methods of imaging, absorption imaging and fluorescence imaging.

3.12.0.1 Absorption imaging

Absorption imaging is a technique that can be used to image the atoms. A laser beam is shined through the atoms, and the resulting absorption of the light by the atoms is

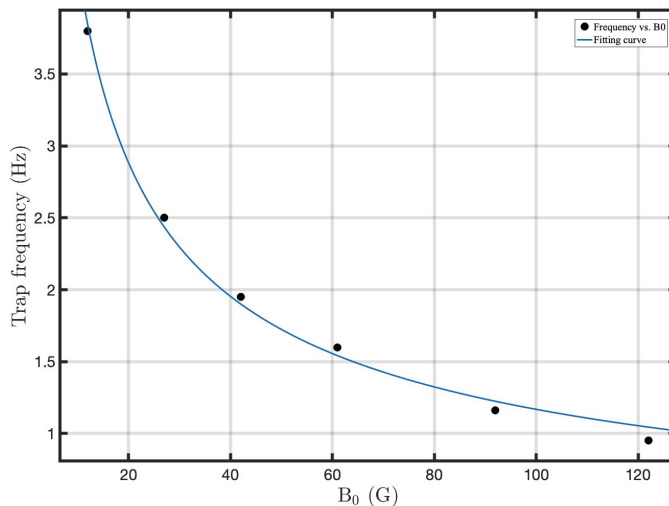


FIGURE 3.17: **The horizontal trap frequency ω_{\perp} in function of bias field B_0 .** The black dots are the data of the trap frequency ω_{\perp} measured at various bias field B_0 .

detected to create an image of the distribution of atoms, as shown figure 3.18.

We perform absorption imaging for the atoms in the cooling chamber in our experiment. The probe laser is resonant with the transition $|F = 2\rangle \rightarrow |F' = 3\rangle$ of the atoms. This laser beam is directed along the \mathbf{x} axis, towards the camera put next to the cooling chamber, and illuminates the atoms for a short period of time, typically around $50\mu\text{s}$. As the light passes through the atoms, in low-saturation regime where the light is very weak, $I_0 \ll I_{\text{sat}}$, a portion of it is absorbed according to the Beer-Lambert law:

$$I(y, z) = I_0(y, z)\exp(-\sigma n_{2D}(y, z)) \quad \text{with} \quad n_{2D}(y, z) = \int dx n(x, y, z), \quad (3.27)$$

where I is the intensity of the light after passing through the atoms, $I_0(y, z)$ is the intensity of the incident laser, σ is the cross section of absorption of the atoms:

$$\sigma = \mathcal{C} \frac{3\lambda^2}{2\pi} \frac{1}{1 + \left(\frac{2\delta}{\Gamma}\right)^2 + \frac{I}{I_{\text{sat}}}} \quad (3.28)$$

where δ is the detuning of the probe laser with respect to the atomic resonance, Γ is the linewidth of the atomic transition and $I_{\text{sat}} \simeq 1.67\text{mW/cm}^2$. \mathcal{C} takes into account the multi-level structure of the atom and depends on the polarization. $\mathcal{C} \simeq 7/15$ if we suppose there is no preferred polarisation. In the regime of low saturation ($I_0 \ll I_{\text{sat}}$), σ can be

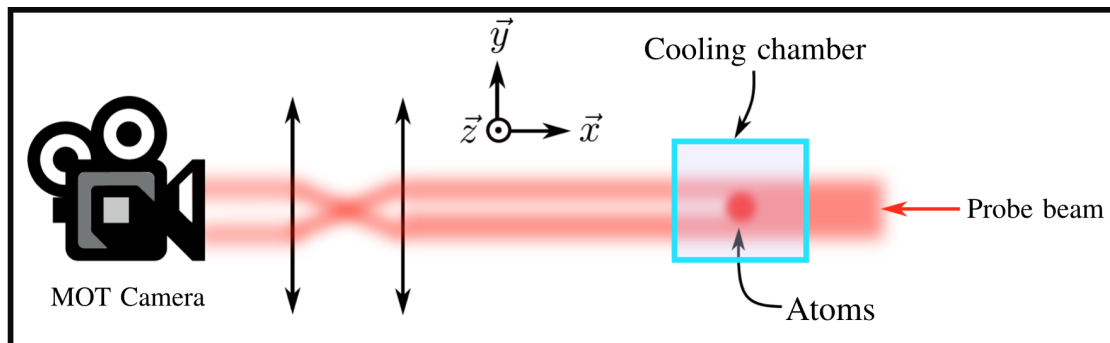


FIGURE 3.18: **Absorption imaging.** A collimated beam is sent to the atoms, which can absorb a part of the photons. So the camera takes an image of the laser with a part of photons absorbed by the atoms and another image of the laser without atoms. By comparing the two images, we can determine the atomic density integrated along the longitudinal direction of the beam. The camera for imaging in the cooling chamber is called 'MOT camera'.

seen as a constant independent of the light intensity, and n_{2D} is the density of atoms integrated along \mathbf{x} direction. To satisfy the low saturation condition, the power of the probe laser is generally about $70\mu\text{W}$ in our experiment.

By measuring the intensity of the light before and after it passes through the atoms, we can deduce the density of atoms along \mathbf{y} and \mathbf{z} :

$$n_{2D}(y, z) = \frac{1}{\sigma} \ln \left(\frac{I(y, z)}{I_0(y, z)} \right). \quad (3.29)$$

3.12.0.2 Fluorescence imaging

We use fluorescence imaging to image the atoms in the second chamber. Compared with absorption imaging, fluorescence imaging has a better sensitivity. It is particularly useful for detecting the atoms after a long-time expansion in the disordered potential, generally, only a few thousand atoms surviving.

To perform the fluorescence imaging, we use a laser beam resonant with the transition $|F = 2\rangle \rightarrow |F = 3\rangle$ to illuminate the atoms for $50 \mu\text{s}$ off the camera axis. The atoms then emit the light by fluorescence to all the directions. A part of the light emitted is collected by an objective lens with a high numerical aperture, $\text{NA} \sim 0.4$, then the image

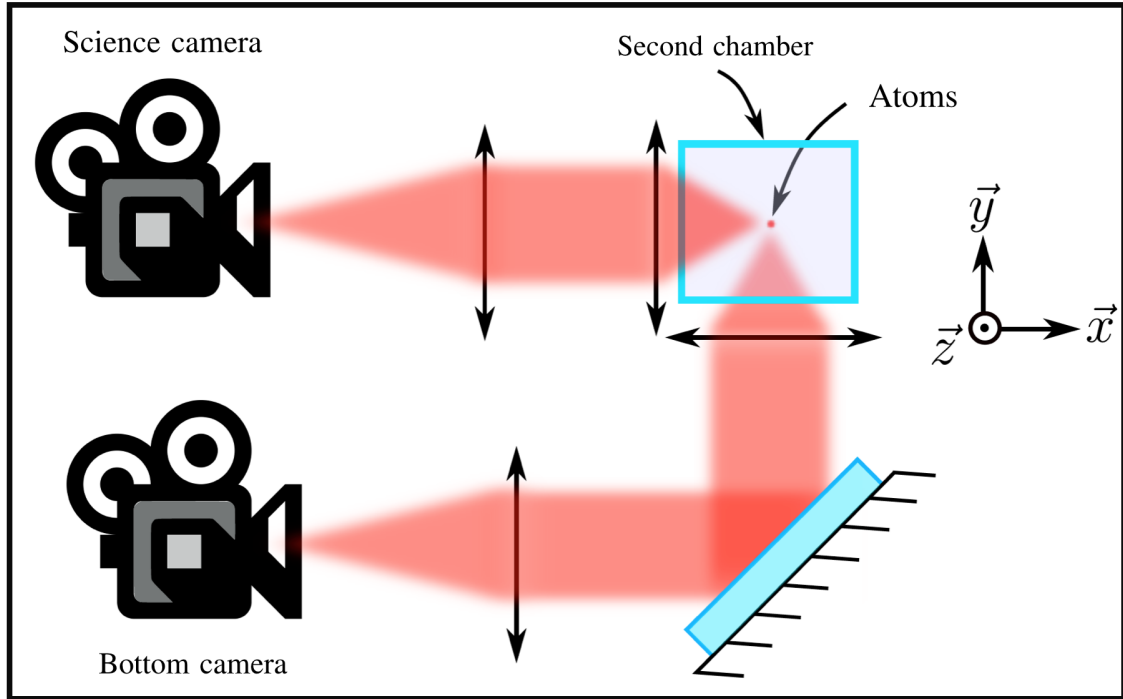


FIGURE 3.19: **Fluorescence imaging.** The beam for fluorescence imaging is about 10 mW. We have two cameras to perform a 3D imaging.

of the atoms is focused on the sensor of our CCD camera by another lens. The intensity detected by the camera is:

$$I_{\text{flu}}(y, z) \simeq \frac{\Omega}{4\pi} \Gamma_{\text{sp}} \hbar \omega_0 n_{2D}(y, z), \quad (3.30)$$

where $\Omega \simeq \pi \text{NA}^2$ is the solid angle where the photons are captured by the imaging system.

To perform the absorption and fluorescence imaging, we setup three cameras *EMCCD C9102* from *Hamamatsu*. One camera is set next to the cooling chamber, imaging along x direction. For the second chamber, one camera is put along x direction and the other one is put under the chamber, along y direction to perform a 3D imaging together, as illustrated in figure 3.19. Each camera has 1000×1000 pixels of size $8\mu\text{m} \times 8\mu\text{m}$. In the second chamber, the telescope for the imaging system has an enlargement of a factor = 3 for the atoms, so the resolved pixel is $2.7\mu\text{m} \times 2.7\mu\text{m}$.

Chapter 4

Optical speckle

In the previous chapter, we presented the characteristics of Bose-Einstein condensates and explained how we cooled and manipulated ^{87}Rb atoms to achieve a Bose-Einstein condensate in our experiment. Bose-Einstein condensates are an excellent source of matter waves, and to study Anderson localization, we also require another crucial component: disorder. An optical speckle pattern is an ideal candidate to simulate disorder[61, 63].

An optical speckle is a random pattern of light intensity created when a laser beam is shown through a glass with a rough surface (diffuser), as shown in figure 4.1 a. The fluctuation of light intensity gives a distribution of bright and dark grains of light. When the laser passes through the diffuser, each point of the speckle pattern receives many wavelets issued from different points of the diffuser. The wavelets' interference gives rise to the speckle pattern. In this chapter, we will describe the statistical properties of the diffuser, then the statistical properties of the speckle field, and of the intensity. We will then show how we implement such an optical speckle and introduce the important parameters of the speckle in our experiment.

4.1 The property of diffuser

The first element to introduce for the speckle field is the diffuser. The roughness of the diffuser is characterized by its thickness $l(\mathbf{x}_0)$ distributing randomly on the surface. In the following, we suppose the thickness $l(\mathbf{x}_0)$ is distributed as a Gaussian distribution $p(l)$,

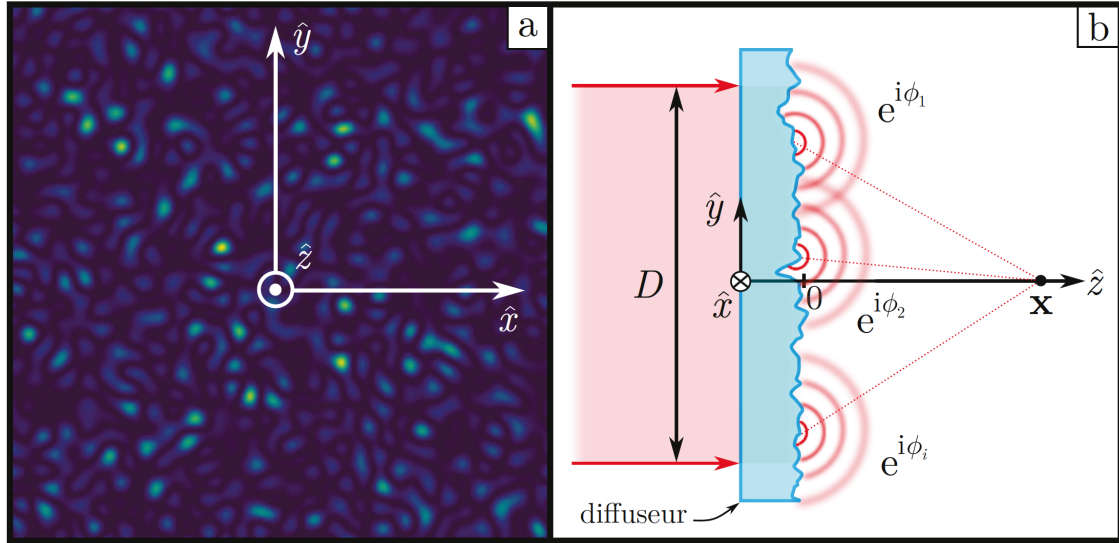


FIGURE 4.1: **Speckle field and its generation.** **a**, The speckle field consists of a random distribution of light intensity. **b**, The diffuser prints a random phase to the wavefront.

with an average \bar{l} and a width σ_l , where $\bar{\cdot}$ describes the average for different realizations of random thickness. We suppose that this diffuser has been homogeneously etched so that the statistics of the thickness does not depend on the position on the surface of the diffuser. The distribution of the thickness is therefore considered to be stationary.

In the limit of thin diffuser, an incident wave with amplitude $E_{\text{inc}}(\mathbf{x})$ passing through the diffuser acquires a phase shift $\phi(\mathbf{x}_0)$:

$$\phi(\mathbf{x}_0) = \frac{2\pi}{\lambda}(n-1)l(\mathbf{x}_0), \quad (4.1)$$

where λ is the wavelength of the incident light, and n is the refractive index of the diffuser. $\{\mathbf{x}_0\}$ is the position on the surface of the diffuser. The phase shift created through the diffuser is added to the amplitude of the field via a transmission factor $t_{\text{diff}}(\mathbf{x}_0)$:

$$t_{\text{diff}}(\mathbf{x}_0) = e^{i\phi(\mathbf{x}_0)}. \quad (4.2)$$

The diffusing power is characterized by the average of the transmission factor $\overline{t_{\text{diff}}}$ and can be calculated as:

$$\overline{t_{\text{diff}}} = \overline{e^{i\phi}} = \int d\phi e^{i\phi} p(\phi) \quad (4.3)$$

where $p(\phi)$ is the probability distribution of the phase shift.

As mentioned above, we suppose the distribution of thickness follows a Gaussian with width σ_l , and according to equation 4.1, the phase shift is proportional to the thickness, so the distribution of the phase shift is also a Gaussian with width $\sigma_\phi = \frac{2\pi}{\lambda}(n-1)\sigma_l$:

$$p(\phi) = \frac{1}{\sigma_\phi \sqrt{2\pi}} e^{-(\phi - \bar{\phi})^2 / 2\sigma_\phi^2} \quad (4.4)$$

So we have:

$$\overline{t_{\text{diff}}} = e^{-\bar{\phi}^2 / 2} = e^{-\sigma_\phi^2 / 2} \quad (4.5)$$

To understand the physical meaning of $\overline{t_{\text{diff}}}$, we can think of an extreme rough glass, where $\sigma_l \gg 1$ (equivalently $\sigma_\phi \gg 2\pi$). The diffusing power $\overline{t_{\text{diff}}}$ tends to zero. On the contrary, for a diffuser whose surface is very little rough, $\sigma_\phi \sim 0$, the diffusing power $\overline{t_{\text{diff}}}$ tends to one. In the limit of an extremely rough diffuser, we have $\sigma_\phi \gg 2\pi$, meaning the width of the distribution of the dephase ϕ is much larger than 2π , so we can consider $p(\phi)$ as a uniform distribution in the interval $[0, 2\pi]$

Beyond the average transmission, it is important to estimate the spatial correlation of the transmission, C_{diff} , which describes the correlation of field on the surface of the diffuser:

$$C_{\text{diff}}(\mathbf{x}_0, \mathbf{x}'_0) = \overline{t_{\text{diff}}(\mathbf{x}_0) t_{\text{diff}}^*(\mathbf{x}'_0)} = \overline{e^{i(\phi(\mathbf{x}_0) - \phi(\mathbf{x}'_0))}}. \quad (4.6)$$

We suppose that $(\phi(\mathbf{x}_0) - \phi(\mathbf{x}'_0))$ to be also a Gaussian variable, then with the diffusing power calculated in equation 4.5, we have (more details of the calculation can be found in thesis of Vincent Denechaud[75]):

$$C_{\text{diff}}(\mathbf{x}_0, \mathbf{x}'_0) \simeq \exp\left(-\frac{|\mathbf{x}_0 - \mathbf{x}'_0|^2}{2r_{\text{diff}}^2}\right), \quad \text{with } r_{\text{diff}} = r_l / \sigma_\phi, \quad (4.7)$$

where r_l corresponds to the typical size of the grains of the surface of the diffuser, which is the correlation length of the fluctuation of the thickness of the diffuser. The correlation length r_{diff} of the transmission factor also depends on the variance of the phase shift σ_ϕ , and it describes an effective size of the independent emitters on the surface of the diffuser. In the situation of an extremely rough surface where $\sigma_\phi \gg 2\pi$, the typical size of an emitter is much smaller than the size of a grain on the surface of the diffuser: $r_{\text{diff}} \ll r_l$, as

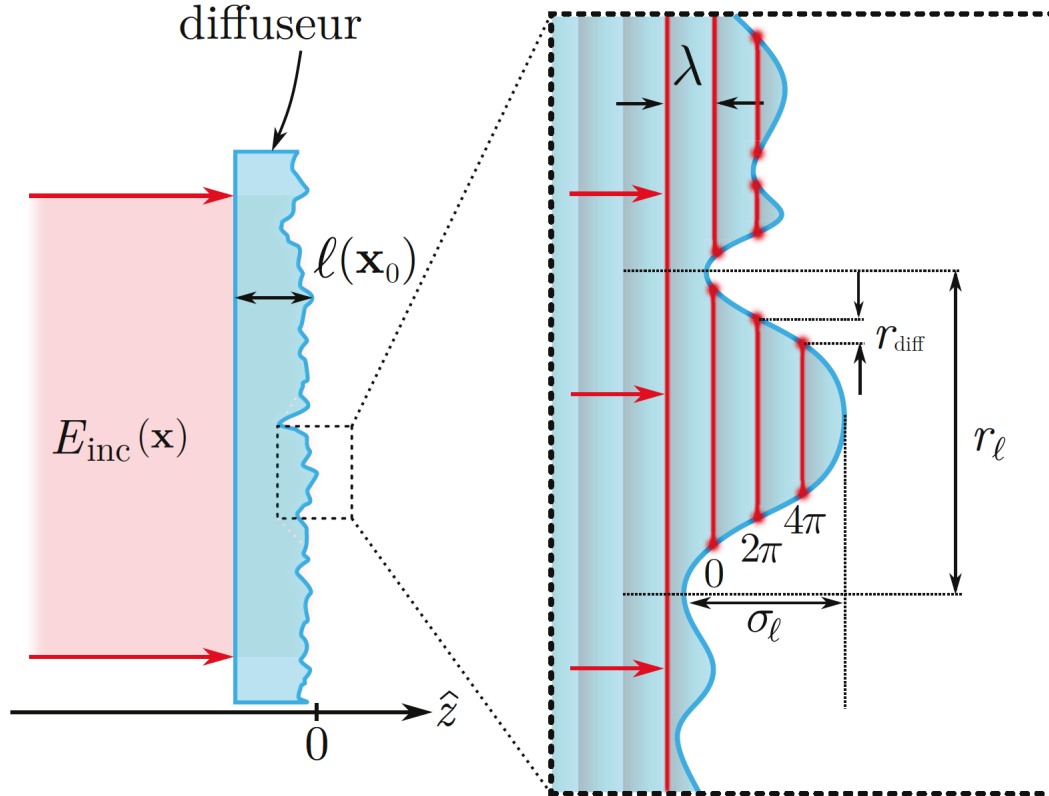


FIGURE 4.2: **The correlation of the transmission of the diffuser.** The thickness of the diffuser at position \mathbf{x}_0 is $l(\mathbf{x}_0)$. r_l is the typical size of the fluctuation of the roughness. σ_l is the variance of the distribution of the thickness. The limit $\sigma_\phi \gg 2\pi$ can be equivalently written as $\sigma_l \gg \lambda$. That means the phase of the transmitted field on the surface of the diffuser varies many times beyond 2π in a single grain of roughness.

shown in figure 4.2

4.2 The distribution of light intensity

In the previous section, we described the field on the surface of the diffuser. In the following, we will describe the propagation of such a field beyond the surface of the diffuser according to the diffraction and interference to study the statistical properties of light intensity after the propagation.

As shown in figure 4.1 b, the field at point \mathbf{x} is created from the interference of wavelets diffracted from the different emitters of the diffuser, characterized by r_{diff} . So the field

$E(\mathbf{x})$ at point \mathbf{x} is the sum of the fields of all the wavelets :

$$E(\mathbf{x}) = \sum_{i=1}^N E_0 e^{i\phi_i(\mathbf{x})}. \quad (4.8)$$

Each emitter can be seen as independent with a typical size r_{diff} . Therefore the statistical properties of ϕ_i do not depend on the emitter i . So $\{\phi(\mathbf{x})\}_i$ is an ensemble of independent random variables. The complex field issued from each emitter can be written into real and imaginary parts, $E_0 e^{i\phi_i} = E_{\mathcal{R},i} + iE_{\mathcal{I},i}$. Since the phase of the field is an ensemble of independent random variables, hence, $\{E_{\mathcal{R},i}\}_i$ and $\{E_{\mathcal{I},i}\}_i$ are also independent random variables. According to the central limit theorem, the sum of the independent random variables tends towards a Gaussian distribution. So the real and imaginary part of the total field $E_{\mathcal{R}} = \sum_i E_{\mathcal{R},i}$ and $E_{\mathcal{I}} = \sum_i E_{\mathcal{I},i}$ are Gaussian distributed:

$$p(E_{\mathcal{R},\mathcal{I}}) = \frac{1}{\sqrt{2\pi}\sigma_E^2} \exp\left(-\frac{E_{\mathcal{R},\mathcal{I}}^2}{2\sigma_E^2}\right). \quad (4.9)$$

The light intensity I of the field, $I = |E|^2 = E_{\mathcal{R}}^2 + E_{\mathcal{I}}^2$, so a pair of $\{E_{\mathcal{R}}, E_{\mathcal{I}}\}$ correspond to a unique pair of $\{\sqrt{I} \cos \phi, \sqrt{I} \sin \phi\}$. Hence, the probability distribution of light intensity with a phase ϕ is:

$$p(I, \phi) = \frac{1}{4\pi\sigma_E^2} \exp\left(-\frac{I}{2\sigma_E^2}\right). \quad (4.10)$$

We suppose that ϕ is uniformly distributed over $[0, 2\pi]$ with $p(\phi) = 1/2\pi$. Then by integrating ϕ over $[0, 2\pi]$, we can get the distribution of light intensity $p(I)$:

$$p(I) = \int_0^{2\pi} d\phi p(I, \phi) = \frac{1}{2\sigma_E^2} \exp\left(-\frac{I}{2\sigma_E^2}\right). \quad (4.11)$$

We see that the distribution of light intensity of the speckle is exponential. The average intensity \bar{I} is:

$$\bar{I} = \int_0^{+\infty} dI I p(I) = 2\sigma_E^2. \quad (4.12)$$

We can calculate \bar{I}^2 :

$$\bar{I}^2 = \int_0^{+\infty} dI I^2 p(I) = 8\sigma_E^4 = 2\bar{I}^2, \quad (4.13)$$

thus the standard variation σ_I of the distribution of light intensity is:

$$\sigma_I = \sqrt{\bar{I}^2 - \bar{I}^2} = \sqrt{2\bar{I}^2 - \bar{I}^2} = \bar{I}. \quad (4.14)$$

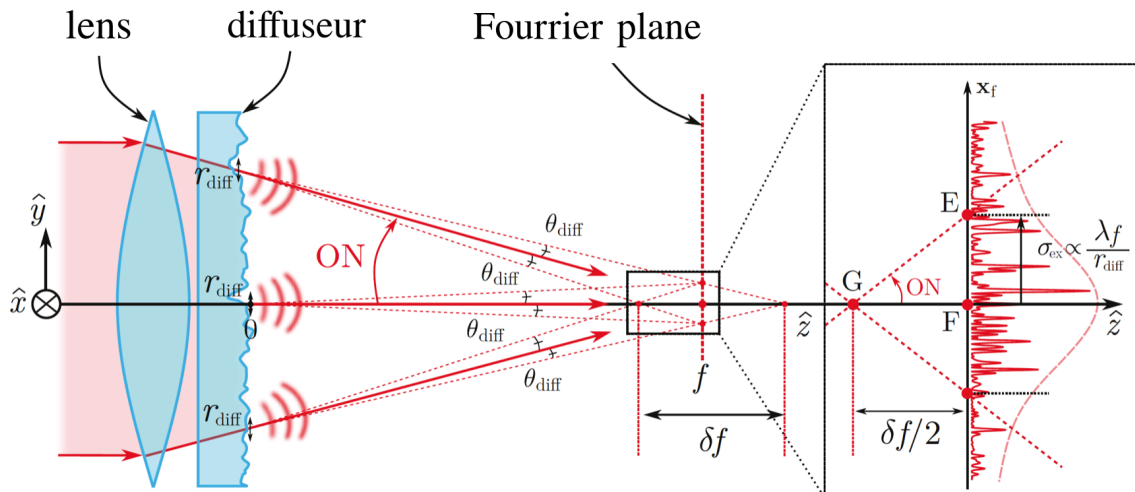


FIGURE 4.3: **Intensity and Rayleigh length of speckle.** The emitters on the diffuser can be characterized by a size r_{diff} , so the diffraction in the focal plane induces the pattern with a width $\sigma_{\text{ex}} \propto \lambda f / \pi r_{\text{diff}}$. The Rayleigh length δf of the speckle pattern describes the regions where all the beams diffracted from the emitters participate.

So the distribution of light intensity can be rewritten in a simple form:

$$p(I) = \frac{1}{I} \exp\left(-\frac{I}{\bar{I}}\right) \quad (4.15)$$

We can remark that the distribution of light intensity is exponential, and its standard variation σ_I is equal to the average intensity. We will use this property when we study the correlation of bichromatic speckles in chapter 6.

4.3 Spatially statistical properties of intensity

Consider an incident plane wave $E_{\text{inc}}(\mathbf{x})$ illuminating a convergent thin lens of focal length f attached with the diffuser, as shown in figure 4.3. In the following, we note $\{\mathbf{x}_0\} = \{x, y, z = 0\}$ to be the coordinates of the points in the plane of the diffuser, and note $\{\mathbf{x}_f\} = \{x, y, z = f\}$ to be the coordinates of the points of in the focal plane of the lens. In the regime of Fraunhofer diffraction, we show that in the focal plane, the field $E(\mathbf{x}_f)$ is:

$$E(\mathbf{x}_f) \propto \text{TF}[E_{\text{inc}}(\mathbf{x}_0)t(\mathbf{x}_0)]\left(\frac{\mathbf{x}_f}{\lambda f}\right) = \int d\mathbf{x}_0 E_{\text{inc}}(\mathbf{x}_0)t(\mathbf{x}_0)e^{-i\frac{2\pi}{\lambda f}\mathbf{x}_f \cdot \mathbf{x}_0}, \quad (4.16)$$

where $t(\mathbf{x}_0)$ describes the combined transmission of the lens and the diffuser:

$$t(\mathbf{x}_0) = m(\mathbf{x}_0)t_{\text{diff}}(\mathbf{x}_0). \quad (4.17)$$

$m(\mathbf{x}_0)$ is the aperture, and we suppose it to be a circle of diameter D , so $m(\mathbf{x}_0) = \Theta(\mathbf{x}_0 - D/2)$, $\Theta(x)$ is Heaviside function.

Knowing the field $E(\mathbf{x})$ in the focal plane, we can calculate the intensity $I(\mathbf{x}) = E(\mathbf{x})E^*(\mathbf{x})$. In the focal plane, we can demonstrate that the average intensity is (more details of calculation can be found in [75]):

$$\bar{I}(\mathbf{x}_f) = \overline{E(\mathbf{x}_f)E^*(\mathbf{x}_f)} \propto \text{TF}[C_{\text{diff}}](\mathbf{x}_f/\lambda f) \propto \exp\left(-\frac{2|\mathbf{x}_f|^2}{\sigma_{\text{ex}}^2}\right) \quad \text{with } \sigma_{\text{ex}} = \frac{\lambda f}{\pi r_{\text{diff}}}. \quad (4.18)$$

where C_{diff} is the correlation of the field on the surface of the diffuser, introduced in equation 4.7, and σ_{ex} is the typical width of the spatial extension of average intensity $\bar{I}(\mathbf{x}_f)$ in the focal plane.

The average intensity $\bar{I}(\mathbf{x}_f)$ in the focal plane is issued from the Fourier transform of the correlation C_{diff} function of transmission factor t_{diff} in the diffuser, so that can explain why the typical width σ_{ex} of the average intensity in the focal plane is inversely proportional to the correlation length r_{diff} of the transmission factor: $\sigma_{\text{ex}} = \frac{\lambda f}{\pi r_{\text{diff}}}$. As shown in figure 4.3, we can define the diffusing angle $\theta_{\text{diff}} = \sigma_{\text{ex}}/f$. In our experiment, for the diffuser that we use, the diffusing angle $\theta_{\text{diff}} \simeq 5^\circ$ and $f = 16.4\text{mm}$ (the assembly will be introduced in the following) so we can calculate $\sigma_{\text{ex}} = \theta_{\text{diff}}f \simeq 1.43\text{mm}$. In the thesis of J.Richard [76], there is the explanation of how to measure σ_{ex} . The value of σ_{ex} is measured to be $1.47 \pm 0.01\text{mm}$.

As shown in figure 4.3, by analogy with a Gaussian beam, we can define a *Rayleigh length* of the speckle δf . The Rayleigh length δf describes the region where all the beams diffracted from all the emitters in the diffuser participate. The inset of the figure 4.3 shows that $\delta f/2 \simeq \sigma_{\text{ex}}/\text{NA}$. NA is numerical aperture and in our experiment, $\text{ON} \simeq 0.5$, so $\delta f \sim 5.88\text{mm}$. In the experiment, this δf gives an upper limit of the uncertainty for the position of the atoms.

In our experiment, the spatial extension σ_{ex} of the average intensity is much larger than the size of the speckle grain. We will see in the following that the typical size σ_{\perp} of

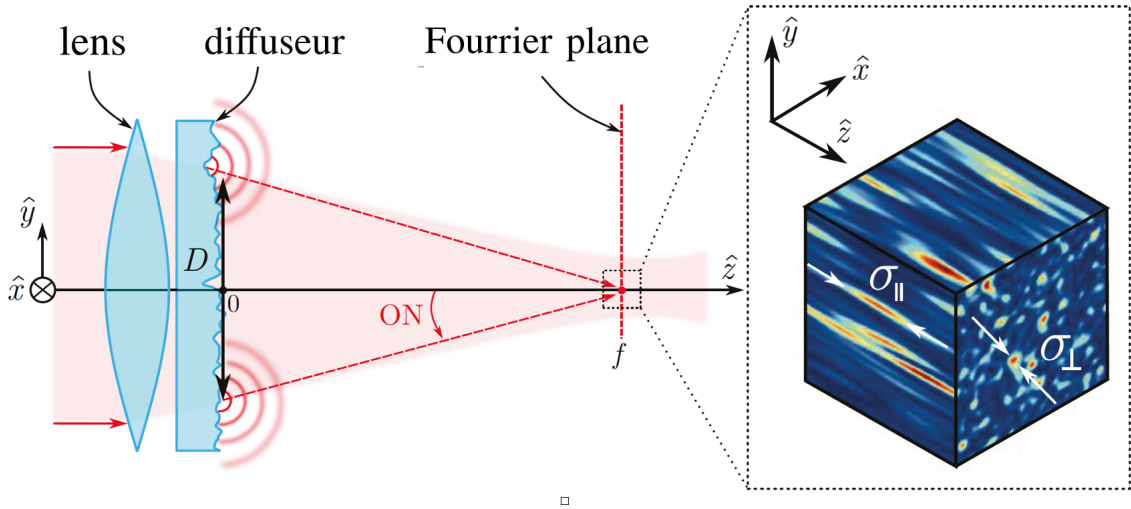


FIGURE 4.4: **Correlation of the speckle field.** The size of the grains of light in focal plane is limited by the diffraction. The transverse size of grain $\sigma_{\perp} \sim \lambda/2\text{NA}$ is limited by the numerical aperture of the diffuser. The longitudinal size of grain is limited by the Rayleigh length: $\sigma_{\parallel} \sim \lambda/\text{NA}^2$.

the speckle grain is about $0.42\mu\text{m}$, and $\sigma_{\text{ex}} \simeq 1.4\text{mm}$, so we have $\sigma_{\text{ex}} \gg \sigma_{\perp}$. And when we measure the expansion of our BEC in the speckle potential, the size of BEC after a long expansion (~ 3 seconds) is generally less than $100\mu\text{m}$. Therefore, in practice, we can consider the average intensity $\overline{I(\mathbf{x}_f)}$ to be constant in the region of interest near the focal point in the Fourier plane.

4.3.0.1 Spatial correlation of the intensity

The grain size is characterized by the correlation of the intensity in Fourier plane, as shown in figure 4.4:

$$\begin{aligned}
 \overline{I(\mathbf{x})I(\mathbf{x} + \delta\mathbf{x})} &= \overline{E(\mathbf{x})E^*(\mathbf{x})E(\mathbf{x} + \delta\mathbf{x})E^*(\mathbf{x} + \delta\mathbf{x})} \\
 &= \overline{E(\mathbf{x})E^*(\mathbf{x})E(\mathbf{x} + \delta\mathbf{x})E^*(\mathbf{x} + \delta\mathbf{x})} + \overline{E(\mathbf{x})E^*(\mathbf{x} + \delta\mathbf{x})E^*(\mathbf{x})E(\mathbf{x} + \delta\mathbf{x})} \\
 &= \overline{I(\mathbf{x})I(\mathbf{x} + \delta\mathbf{x})} + \left| \overline{E(\mathbf{x})E^*(\mathbf{x} + \delta\mathbf{x})} \right|^2.
 \end{aligned}
 \tag{4.19}$$

We can show that in the Fourier plane the second term in the equation 4.19, the correlation of the field is [75]:

$$\overline{E(\mathbf{x}_f)E^*(\mathbf{x}_f + \delta\mathbf{x}_f)} \propto \text{TF}[I_0](\delta\mathbf{x}_f/\lambda f) \cdot \text{TF}[C_{\text{diff}}](\mathbf{x}_f - \delta\mathbf{x}_f/2)/\lambda f.
 \tag{4.20}$$

The transverse grain size is characterized by the transverse correlation of the intensity in Fourier plane perpendicular to the optical axis (direction z). As we mentioned above, we can consider the average intensity $\overline{I(\mathbf{x}_f)}$ to be constant, therefore, in the equation 4.19, the first term can be treated a constant \overline{I}^2 . The grain size is then given by the correlation of the fluctuation of intensity $\delta I(\mathbf{x}_f) = I(\mathbf{x}_f) - \overline{I}$:

$$\overline{\delta I(\mathbf{x}_f)\delta I(\mathbf{x}_f + \delta\mathbf{x}_f)} = \left| \overline{E(\mathbf{x}_f)E^*(\mathbf{x}_f + \delta\mathbf{x}_f)} \right|^2. \quad (4.21)$$

Since we consider the average intensity to be constant in the region of interest, the second factor in the expression of the correlation of field 4.20 can be seen as a constant. Then we can simplify the correlation of the intensity as:

$$\overline{\delta I(\mathbf{x}_f)\delta I(\mathbf{x}_f + \delta\mathbf{x}_f)} \propto |\text{TF}[I_0](\delta\mathbf{x}_f/\lambda f)|^2. \quad (4.22)$$

We see that the correlation of the intensity in the Fourier plane is completely determined by the intensity of the incident light in the diffuser plane via the Fourier transform. We consider the incident light as a homogeneous plane wave, where I_0 is constant, and the aperture is a circle of diameter D . In this case, by Fourier transform, the correlation of the intensity in Fourier plane $\overline{\delta I(\mathbf{x}_f)\delta I(\mathbf{x}_f + \delta\mathbf{x}_f)}$ is an Airy function with width $\sigma_\perp \sim \lambda/2NA$, where NA is the numerical aperture of the optical system formed by the lens and aperture. So the transverse grain size is the transverse correlation length σ_\perp .

4.4 Experimental implementation

We have seen that the transverse grain size $\sigma_\perp \sim \lambda/2NA$, so in order to realize a speckle field with small grains, we need to have an incident beam with large beam size. Figure 4.5 shows how we shape the speckle beam. The beam is enlarged by a telescope composed of -75mm and $+200\text{mm}$ lenses. With this telescope, the beam waist is increased from 5.6mm to 14.6mm .

Now let us look at near the vacuum chamber and how the diffuser is assembled. As illustrated in figure 4.6, the diffuser and the lens are mounted in a tube of diameter 1" (inner diameter of 22.9mm), which is placed extremely close to the glass vacuum chamber, by only 0.5mm , in order to have a large NA. The lens is aspherical *Thorlabs ACL2520 - B*, with a focal length of 16mm , and the distance between the plane face of the lens and the focal

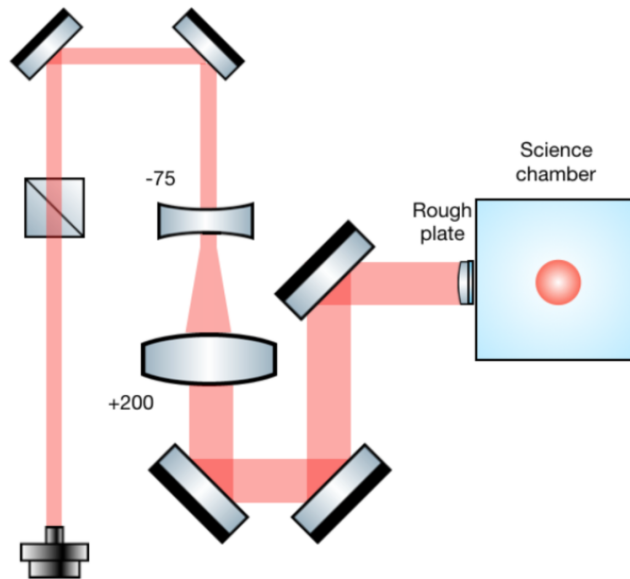


FIGURE 4.5: **Experimental realization of speckle beam.** At the output the fiber, the waist of the beam is 5.6 mm. The beam waist is then broadened to 14.6 mm by a telescope before going to the science chamber.

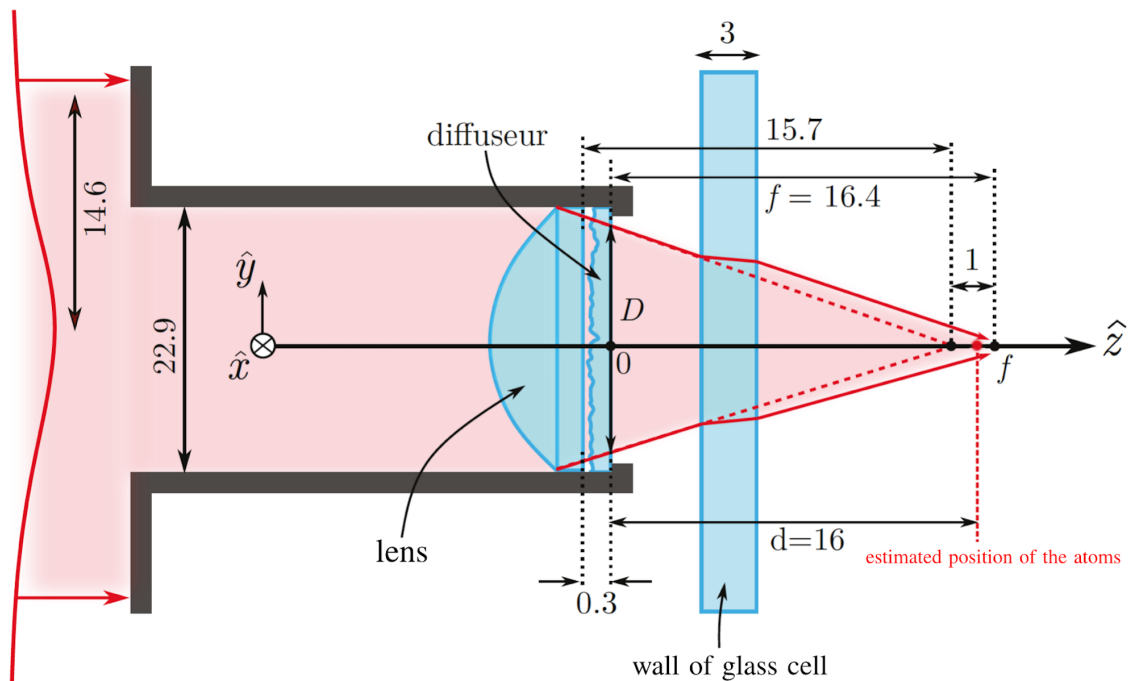


FIGURE 4.6: **Assembly of the diffuser near the glass cell.** All the lengths in this figure are in millimetres.

point is 15.7mm. The diffuser is from *Newport FSD10-3*, with a diffusing angle $\theta_{\text{diff}} \simeq 5^\circ$ and thickness of 0.3mm. It is attached to the plane surface of the lens. The wall of the glass vacuum chamber has a thickness of 3mm. So we need to estimate the displacement of the focal plane by 1mm caused by the finite thickness of the glass chamber. The position of the focal point with respect to the surface of the diffuser is estimated to be $f = 16.4\text{mm}$.

Now we can characterize the transverse σ_{\perp} and longitudinal size σ_{\parallel} (correlation length) of grain in the speckle pattern that we generate onto the atoms. The correlation length is defined as the *HWHM* (Half Width of Half Maximum) of the correlation function. The transverse grain size σ_{\perp} is determined by the diffraction limit $= \lambda/2\text{NA}$. In our experiment, the numerical aperture NA is 0.5. But since here the NA is huge, and that is beyond the regime of paraxial approximation, so in order to calculate the correlation length, M.Pasek and D.Delande proposed a numerical calculation based on the principle of Huygens-Fresnel. Here in this manuscript, we give the result directly (the procedure of how to measure the correlation lengths and the details of the numerical calculation can be found in thesis of J.Richard [76]) :

$$\sigma_{\perp} = 0.42 \pm 0.01 \mu\text{m} \text{ and } \sigma_{\parallel} = 2.02 \pm 0.03 \mu\text{m}. \quad (4.23)$$

In this chapter, we first describe the spatially statistical properties of the diffuser and introduce r_{diff} , which defines the typical size of the independent emitters on the diffuser. Next, we derive the distribution of intensity. Then we study the spatially statistical properties of intensity near the Fourier plane: the average intensity $\bar{I}(\mathbf{x}_f)$ and the correlation of the intensity which defines the grain size of the speckle. At the end of the chapter, we show the assembly of the speckle in our experiment. In the next chapter, we will see how we perform the energy-resolved transfer in the speckle potential.

Chapter 5

Transfer scheme in a monochromatic state-dependent disorder

In section 2.4, we review the three experiments that have tried to measure the mobility edge of the Anderson transition with ultracold atoms in speckle disorder[33, 34, 35], but precise quantitative measurements are still lacking[36]. In experiments performed so far, the atoms loaded in the disorder have a large energy dispersion so evaluating the mobility edge demands a deconvolution leading to large uncertainties.

In section 2.4, we introduce that our team has proposed a method of spectroscopy to load the atoms in the disorder with a narrow energy distribution. Scanning the energy around the mobility edge would allow us to determine precisely the mobility edge. One might even evaluate critical exponents for further investigation with this platform.

This chapter is to explain our method of spectroscopy. Our strategy for loading atoms with a precisely defined energy, as described in figure 5.1, consists in performing an rf transition from the state insensitive to disorder (in this manuscript and in our experiment, this disorder-insensitive state is called state $|1\rangle$) to the state sensitive to disorder (called state $|2\rangle$). The energy of the populated eigenstates in the disorder can be adjusted by controlling the frequency of the rf.

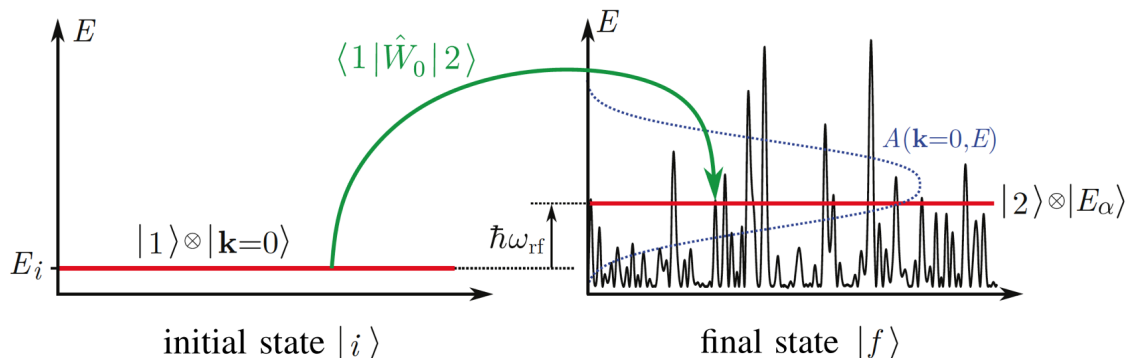


FIGURE 5.1: **Rf transfer scheme with a state-dependent disorder.** The state $|1\rangle$ is insensitive to the disorder and we prepare the BEC $|\mathbf{k}=\mathbf{0}\rangle$ in this state. The state $|2\rangle$ is sensitive to the disorder. By a radio-frequency ω_{rf} , we transfer the atoms from the state $|1\rangle$ to state $|2\rangle$ in the disorder. By controlling ω_{rf} , we can scan the spectral function $A(\mathbf{k}=\mathbf{0}, E)$ of the disorder.

The first implementation of that scheme was demonstrated in the work of Volchkov et al. [28] in our team. They performed an rf transfer between the atomic hyperfine states with different sensitivities to a monochromatic laser speckle disorder. These different sensitivities stemmed from the very different detunings of the laser for the initial state $|1\rangle$ and the final state $|2\rangle$, used to produce the state-dependent disordered potential. The narrow Fourier-limited energy distribution they obtained—two orders of magnitude lower than in previous experiments [28, 36]—allowed us to make a quantitative study of the spectral function of the atoms in that disorder, and to explore different regimes of quantum transport from the low disorder regime (quantum regime) to the strong disorder regime (classical regime) [77, 78, 79].

In this chapter, we will first introduce the transition $|1\rangle \rightarrow |2\rangle$ that we choose to use. Next, we will explain how to generate a state-dependent disordered potential with our monochromatic speckle configuration. Then we will describe the rf transfer of $|1\rangle \rightarrow |2\rangle$ in the state-dependent disorder and show the experimental results of Volchkov et al. [28].

At the end of the chapter, we will see the method is, however, strongly limited by a serious problem, that prevents us from measuring the mobility edge. It relies on a laser tuned between the two resonances associated with the two atomic hyperfine states, and the detuning for the upper state $|2\rangle$ cannot be large enough to avoid the resonant scattering of photons in that state. This entails a rapid destruction of the coherence of the spatial

wave function describing the atomic motion and thus of Anderson localization. During my thesis, we have overcome this bottleneck, and that is the content for the next chapter.

5.1 The two-level system composed of $|1\rangle$ and $|2\rangle$

In this section, we will first explain why we choose to use another hyperfine state $|F = 2, m_F = +1\rangle$ to be the state $|2\rangle$ in our rf transfer scheme and how we suppress the fluctuation of the resonance between $|1\rangle$ and $|2\rangle$ due to the fluctuation of magnetic fields. Then we will show the Rabi oscillation between the two states. The narrow Rabi spectrum shows the ability of energy-resolved transfer.

5.1.1 Choose the state $|2\rangle$ and magic point B_0^* of magnetic field.

As introduced in the section 3.11, the Bose-Einstein condensate is prepared in state $|1\rangle = |F = 1, m_F = -1\rangle$. We design the magnetic field to levitate the atoms in this state to compensate the gravity. We use this state $|F = 1, m_F = -1\rangle$ as state $|1\rangle$ for the RF-transfer. In our experiment, we choose $|F = 2, m_F = +1\rangle$ to be state $|2\rangle$ to realize the rf-transfer. There are two reasons why we choose this state. First, this state $|2\rangle = |F = 2, m_F = +1\rangle$ experiences the same magnetic potential as $|1\rangle = |F = 1, m_F = -1\rangle$ so that it is also levitated by the same gradient of magnetic fields. This is crucial for observing the long-time expansion of the atoms in the disorder.

The second and the more important reason is to minimize the fluctuation of the position of the resonance due to the fluctuation of magnetic fields. The energy separation Δ_{hf} between the two magnetic hyperfine states $|1\rangle$ and $|2\rangle$ fluctuates if the magnetic field fluctuates. Figure 5.2 a shows the dependence of the energy of the hyperfine states with magnetic fields. This fluctuation of the resonance Δ_{hf} limits the precision of our rf-spectroscopy. To minimize this fluctuation, we impose a bias field at the so-called magic point $B_0^* \simeq 3.23$ G. At this bias field B_0^* , the magnetic susceptibilities χ_B of state $|1\rangle$ and $|2\rangle$ are identical, as shown in figure 5.2 b. That means at B_0^* , the variation of the energy with the magnetic bias field is the same for the two states, leading that the energy separation Δ_{hf} between these two states is insensitive with the magnetic fluctuation.

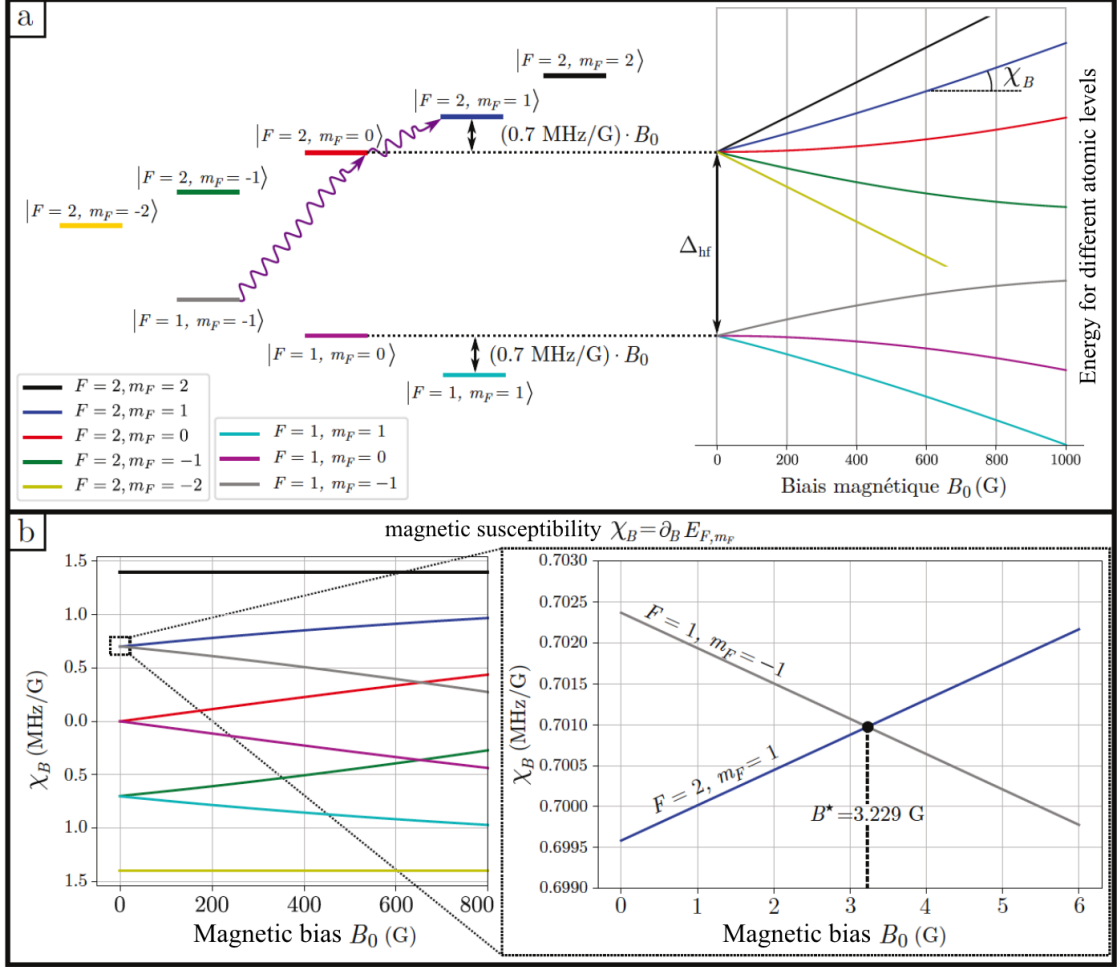


FIGURE 5.2: **The dependence of the hyperfine sub-levels to magnetic field.** a. The dependence of the energy shift on the magnetic bias B_0 for different atomic sublevels in $|F=1\rangle$ and $|F=2\rangle$. b. The magnetic susceptibility of each state. We find that the two states $|F=1, m_F=-1\rangle$ and $|F=2, m_F=+1\rangle$ have the magnetic susceptibility at bias $B_0 = 3.23 \text{ G}$.

We can calculate the magic point B_0^* of the magnetic field. According to the Breit-Rabi formula[70], we can write the energy shift of the two states in the regime of weak magnetic field up to the second order:

$$\begin{aligned}
 E_{F=2, m_F=+1} &\sim \frac{h\Delta_{\text{hf}}}{2} + g_{F=2}\mu_B B + \frac{3(g_J - g_I)^2 \mu_B^2}{16h\Delta_{\text{hf}}} B^2 \\
 E_{F=1, m_F=-1} &\sim - \left(\frac{h\Delta_{\text{hf}}}{2} + g_{F=1}\mu_B B + \frac{3(g_J - g_I)^2 \mu_B^2}{16h\Delta_{\text{hf}}} B^2 \right),
 \end{aligned} \tag{5.1}$$

the Landé factors for the two states are $g_{F=2} = (g_J + 3g_I)/4$ and $g_{F=1} = (-g_J + 5g_I)/4$.

The energy separation $\Delta E_{1,2} = E_{F=2, m_F=+1} - E_{F=1, m_F=-1}$ between $|1\rangle$ and $|2\rangle$ depending on the magnetic field B can be written as:

$$\begin{aligned}\Delta E_{1,2} &= h\Delta_{\text{hf}} + 2g_I\mu_B B + \frac{3(g_J - g_I)^2\mu_B^2}{8h\Delta_{\text{hf}}} B^2 \\ &= a \left(B + \frac{b}{2a} \right)^2 - \frac{b^2}{4a} + h\Delta_{\text{hf}},\end{aligned}\tag{5.2}$$

where we set $a = 3(g_J - g_I)^2\mu_B^2/8h\Delta_{\text{hf}}$ and $b = 2g_I\mu_B$.

Equation 5.2 indicates that there exists a magnetic field B_0^* so that close to this magnetic bias, the energy separation $\Delta E_{1,2}$ between $|1\rangle$ and $|2\rangle$ does not change with the fluctuation of magnetic field:

$$B_0^* = -\frac{b}{2a} \simeq 3.228917\text{G} \quad \text{for} \quad \partial_B \Delta E_{1,2}(B = B_0^*) = 0.\tag{5.3}$$

In the experiment, we calibrate the magic point B_0^* by measuring how the energy separation of $|1\rangle$ and $|2\rangle$ shifts depending on the bias field B_0 and then fit it with equation 5.2 to find the magic point B_0^* , as shown in figure 5.3.

5.1.2 Two-photon transition

Once we select $|F = 2, m_F = 1\rangle$ to be $|2\rangle$, now we have the two-level system. The next step is to perform the transition between $|F = 1, m_F = -1\rangle$ (state $|1\rangle$) and $|F = 2, m_F = 1\rangle$ (state $|2\rangle$). However, we cannot realize the transition $|F = 1, m_F = -1\rangle \rightarrow |F = 2, m_F = 1\rangle$ directly by a single photon excitation because for this transition, $|\Delta m_F| = 2$, which is forbidden by selection rules (spin of a single photon is 1). Therefore to realize the transition $|F = 1, m_F = -1\rangle \rightarrow |F = 2, m_F = 1\rangle$, we need to use a 2-photon excitation, intermediated by state $|F = 2, m_F = 2\rangle$, as illustrated in figure 5.4.

The energy separation between $|F = 1, m_F = -1\rangle$ and $|F = 2, m_F = 1\rangle$ is about 6.834678GHz. In our experiment, we use a microwave at about 6.89GHz (ω_{mw}) to be the first photon and a radio-frequency at about 2.75MHz (ω_{rf}) to be the second photon. We keep a detuning $\delta_{mw} \simeq 500\text{kHz}$ between the frequency of microwave and the transition frequency of $|F = 1, m_F = -1\rangle \rightarrow |F = 2, m_F = 0\rangle$, to avoid atoms populating into the intermediate state which can induce strong decoherence for the 2-photon transition. Note

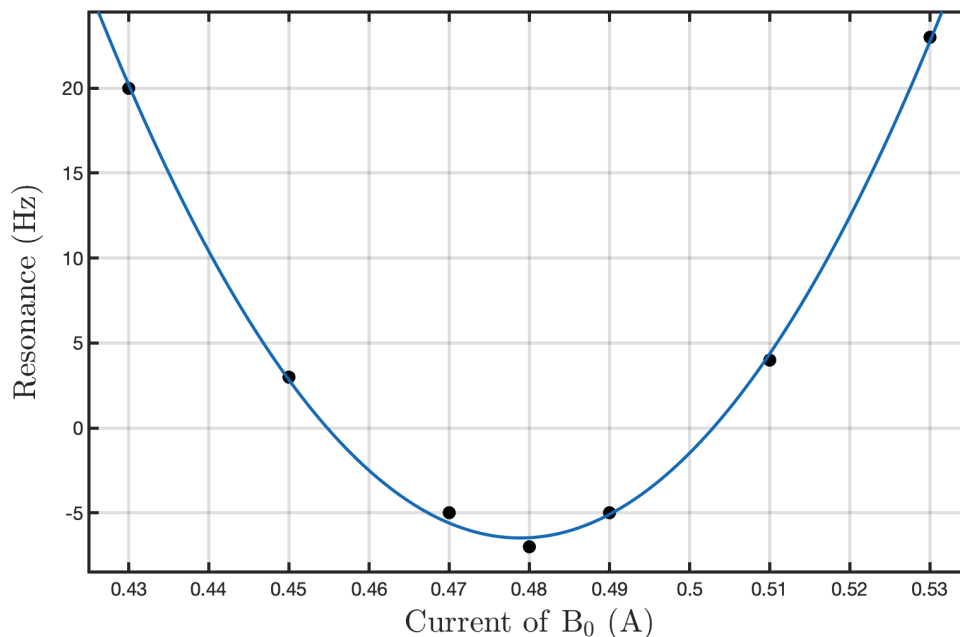


FIGURE 5.3: **The dependence of the energy separation $\Delta E_{1,2}$ on the magnetic bias field B_0 .** The vertical axis 'Resonance' is just the energy separation $\Delta E_{1,2}$ by an offset set in our program of parameters. The horizontal axis is the current of Bias A, which is linear to B_0 . We adjust the bias field B_0 by simply tuning the current of Bias A. The black dots are the energy separation measured by Rabi spectrum, the blue curve is the fitting function in the form of equation 5.2.

Ω_{mw} to be the Rabi frequency of $|F = 1, m_F = -1\rangle \rightarrow |F = 2, m_F = 0\rangle$, and Ω_{rf} to be the Rabi frequency of $|F = 2, m_F = 0\rangle \rightarrow |F = 2, m_F = 1\rangle$, in the regime of:

$$|\delta_{\text{mw}}| \gg \Omega_{\text{mw}}, \Omega_{\text{rf}}, \quad (5.4)$$

we can neglect the richness of the three-level transition and consider it to be an effective two-level system composed of $|F = 1, m_F = -1\rangle$ and $|F = 2, m_F = 1\rangle$. The effective Rabi frequency of the 2-photon transition $|F = 1, m_F = -1\rangle \rightarrow |F = 2, m_F = 1\rangle$ is [80]:

$$\Omega_{\text{eff}} = \frac{\Omega_{\text{mw}}\Omega_{\text{rf}}}{2\delta_{\text{mw}}}. \quad (5.5)$$

In the experiment, by measuring the population in state $|2\rangle = |F = 2, m_F = 1\rangle$, we know how many atoms transferred from $|1\rangle$ to state $|2\rangle$ during a duration $= t_p$ with a Rabi frequency $= \Omega_{\text{eff}}$. The fraction of the atoms in state $|2\rangle$ is [80]:

$$|\langle 2|\psi(t_p)\rangle|^2 = \frac{\Omega_{\text{eff}}^2}{\Omega_{\text{eff}}^2 + \delta^2} \sin^2 \left(\pi \sqrt{\Omega_{\text{eff}}^2 + \delta^2} t_p \right) = \pi^2 \Omega_{\text{eff}}^2 t_p^2 \text{sinc}^2 \left(\pi \sqrt{\Omega_{\text{eff}}^2 + \delta^2} t_p \right). \quad (5.6)$$

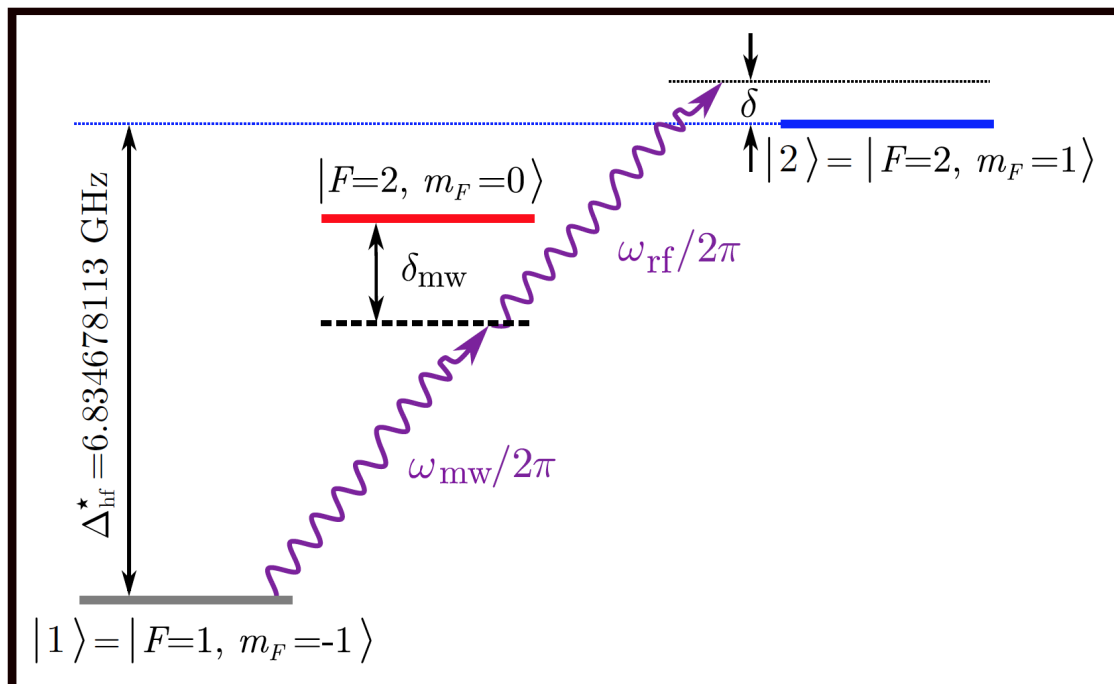


FIGURE 5.4: The principle of two-photon transition $|F=1, m_F=-1\rangle \rightarrow |F=2, m_F=1\rangle$, using $|F=2, m_F=0\rangle$ as an intermediate state.

In the picture of spectroscopy, we can fix the duration of transfer t_p and scan the rf-frequency to observe the number of atoms transferred to $|2\rangle$, and that is Rabi spectrum. The energy resolution δE of the rf-transfer can be characterized by the width of the Rabi spectrum (FWHM). Figure 5.5 shows two examples of Rabi spectrum. We fix the duration of transfer $t_p = 30$ ms in figure 5.5 a, $t_p = 40$ ms in figure 5.5 b, and scan the rf-frequency to observe the atom number in state $|2\rangle$. We fit the experimental data with the equation 5.6. According to the figures, we see that for the duration of transfer $t_p = 30$ ms, the energy resolution of the Rabi spectrum $\delta E/h \simeq 30$ Hz. For $t_p = 40$ ms, the energy resolution $\delta E/h \simeq 23$ Hz. So we verify that the energy resolution δE corresponds well to the Fourier limit of the transfer: $\delta E/h \sim 1/t_p$. By adjusting the duration of the transfer from 8 ms to 100 ms, the energy resolution can vary from ~ 10 Hz to ~ 125 Hz in our experiment.

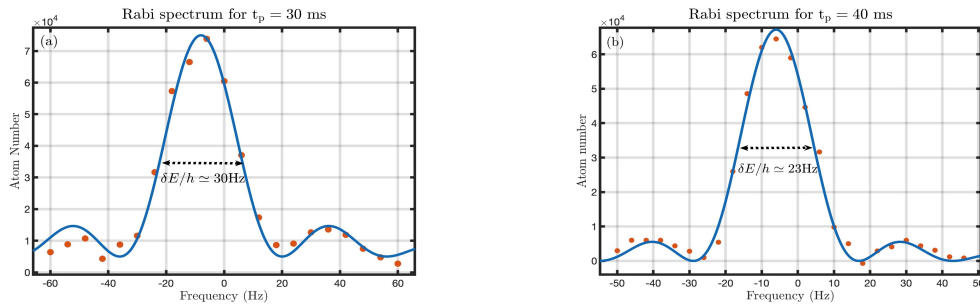


FIGURE 5.5: **Rabi sepctrum.** The orange dots are the experimentally measured atom number in state $|2\rangle$ and the blue curve is the fitting curve in equation 5.6. a. Rabi spectrum for the duration of transfer $t_p = 30$ ms. The width of the spectrum (FWHM) is about 30 Hz. b. Rabi spectrum for the duration of transfer $t_p = 40$ ms. The width of the spectrum is about 23 Hz.

5.2 The state-dependent disorder

In the last section, we introduced the first element for the rf-transfer scheme: the choice of the state $|2\rangle = |F = 2, m_F = +1\rangle$. And we also explained how we minimize the fluctuation of the energy separation Δ_{hf} due to the magnetic field fluctuation. In this section, we introduce the other element for the rf-transfer: the state-dependent disordered potential.

The creation of state-dependent potential for alkali atoms has been widely investigated in the context of optical lattices using circularly polarized light tuned between the D1 and D2 lines [81, 82, 83]. However, such scheme is efficient only if the two states have different magnetic susceptibilities [30]. But in our experiment, both of the two states are required to be levitated against gravity by the magnetic levitation during their expansion in the disorder [33, 34, 35], and to minimize the effect of magnetic fluctuation, the two states must have similar magnetic susceptibility. So in our experiment, we use an alternative method to generate the state-dependent potential by a near-resonant laser.

In section 3.8, we introduced the principle of the optical dipole potential. The speckle beam can generate such an optical potential applying on the atoms. As shown by equation 3.15, the potential depends on the light intensity $I(\mathbf{x})$ and the detuning of the laser with respect to the atomic resonance Δ :

$$V(\mathbf{x}) \propto \frac{I(\mathbf{x})}{\Delta}. \quad (5.7)$$

We introduced in chapter 4 how to generate a speckle configuration, and we showed the spatial statistical properties of the light intensity of the speckle field. Since the potential

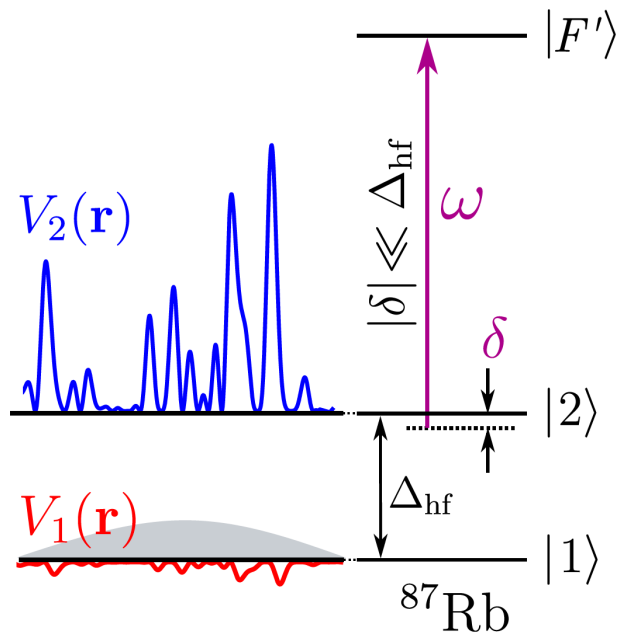


FIGURE 5.6: **State-dependent disorder generated by a single laser.** The speckle laser is near the resonance of state $|2\rangle$, so that the detuning is much smaller than the energy gap Δ_{hf} between $|1\rangle$ and $|2\rangle$: $|\delta| \ll \Delta_{\text{hf}}$.

is proportional to the light intensity, the disordered potential shares the same spatial statistical properties as the light intensity of the speckle field. As shown in figure 5.6, δ is the detuning of the speckle laser with respect to the resonance of state $|2\rangle$. Since the natural linewidth of the transitions $|1\rangle \rightarrow |F'\rangle$ and $|2\rangle \rightarrow |F'\rangle$ ($\Gamma_{\text{Rb}}/2\pi \simeq 6.07\text{MHz}$) is small compared to the energy separation Δ_{hf} between $|1\rangle$ and $|2\rangle$ ($\Delta_{\text{hf}}/2\pi \simeq 6.8\text{GHz}$), it is possible to operate in the regime of $\Gamma_{\text{Rb}} \ll \delta \ll \Delta_{\text{hf}}$. Thus, the detuning from resonance for state $|1\rangle$ is almost equal to Δ_{hf} . The ratio between the average potentials for $|1\rangle$ and $|2\rangle$ is:

$$\frac{V_1}{V_2} \sim \frac{\delta}{\Delta_{\text{hf}}} \ll 1. \quad (5.8)$$

In Volchkov et al.[28], the detuning $\delta/2\pi \simeq \pm 80\text{MHz}$, and that can lead to the ratio between the disordered potentials $|V_2/V_1| \sim 100$, the disorder in state $|1\rangle$ being much smaller than the disorder in state $|2\rangle$ by two orders of magnitude.

So we see that in this configuration, we are unable to completely eliminate the potential in state $|1\rangle$, resulting in a residual disorder $V_1(\mathbf{x})$ potential in state $|1\rangle$. Therefore, we need to analyze the disorder-insensitivity of state $|1\rangle$. To do this, we compare V_1 with the chemical potential μ of the BEC. According to Volchkov et al. [28], the chemical potential

of the BEC is approximately $\mu/h \simeq 50$ Hz. In the regime of the disordered potential they work with in [28], the range is $V_2/h \in [\sim 60\text{Hz}, \sim 4\text{kHz}]$. Since $|V_2/V_1| \sim 100$, the corresponding residual potential in state $|1\rangle$ $V_1/h \in [\sim 0.6\text{Hz}, 40\text{Hz}]$. This ensures that the residual potential in state $|1\rangle$ is smaller than the chemical potential of the BEC, $V_1 \leq \mu$, making state $|1\rangle$ insensitive to the residual disorder.

This simple generation of a state-dependent disordered potential allows one to determine the spectral functions of ultracold atoms in a speckle potential at various amplitudes. In the following, we will discuss the spectral function and show the experimental results of the measurement of spectral functions in Volchkov. et al. [28].

5.3 Spectral function and the transfer in the disorder

We highlight that the objective of the rf-spectroscopy protocol is to prove that we can load the atoms into a highly-resolved energy state in the disordered potential. As we discussed in section 2.4 the limit of the previous experiments for the Anderson transition, our rf-spectroscopy protocol is an important step towards launching a direct measurement of mobility edge, that will allow one to characterize directly the localized and diffusive phases by selecting the energy state in disorder.

In this section, we first introduce rapidly the definition of the spectral function and we will connect the spectral function with the transfer rate of atoms by Fermi-Golden rule (more details of spectral function is found in the thesis of V.Denechaud [75]). Then we will point out that for my work in PhD, to measure the mobility edge E_c at a given disorder with amplitude V_R , spectral function is the excellent tool to calibrate V_R .

5.3.1 Spectral function

We define the spectral function $A(\mathbf{k}, E)$ for the quantum system with Green function $\mathcal{G}(\mathbf{k}, E)$:

$$A(\mathbf{k}, E) = -\frac{1}{\pi} \text{Im} \mathcal{G}(\mathbf{k}, E). \quad (5.9)$$

The spectral function $A(\mathbf{k}, E)$ can be seen as the overlap $|\langle E|\mathbf{k}\rangle|^2$ between the momentum $|\mathbf{k}\rangle$ and energy $|E\rangle$ under the Hamiltonian $\hat{\mathcal{H}}$, so the spectral function can be written as:

$$A(\mathbf{k}, E) = -\frac{1}{\pi} \langle \mathbf{k} | \text{Im} \hat{\mathcal{G}}(E) | \mathbf{k} \rangle = \langle \mathbf{k} | \delta(E - \hat{H}) | \mathbf{k} \rangle. \quad (5.10)$$

By inserting the basis of eigenstates $\{|E_\alpha\rangle\}_\alpha$ of Hamiltonian $\hat{\mathcal{H}}$, the spectral function can be further expressed as:

$$A(\mathbf{k}, E) = \sum_{\alpha} \langle \mathbf{k} | \delta(E - \hat{\mathcal{H}}) | E_\alpha \rangle \langle E_\alpha | \mathbf{k} \rangle = \sum_{\alpha} \delta(E - E_\alpha) |\langle E_\alpha | \mathbf{k} \rangle|^2. \quad (5.11)$$

We use the example of the free particle in absence of potential \hat{V} . Its Green function is $\mathcal{G}_0(\mathbf{k}, E) = \frac{1}{E - \varepsilon_{\mathbf{k}} + i0^+}$. According to the equation 5.11, the spectral function for free particle is:

$$A_0(\mathbf{k}, E) = -\frac{1}{\pi} \text{Im} \mathcal{G}_0(\mathbf{k}, E) = \delta(\varepsilon_{\mathbf{k}}). \quad (5.12)$$

Therefore we see that for free particle, the spectral function is a Dirac function. That means given a momentum $|\mathbf{k}\rangle$, there is no dispersion of energy, the only possible energy that momentum $|\mathbf{k}\rangle$ can overlap with is $\varepsilon_{\mathbf{k}} = \frac{\hbar^2 \mathbf{k}^2}{2m}$.

Now we consider the situation in presence of the potential, introducing a self-energy Σ to the system. We separate the real and imaginary part of the self-energy: $\Sigma = \Sigma' + i\Sigma''$, and according to the equation C.9, the spectral function can be expressed as with self-energy [84]:

$$A(\mathbf{k}, E) = \frac{1}{\pi} \frac{\Sigma''(\mathbf{k}, E)}{(E - \mathcal{E}_{\mathbf{k}} - \Sigma'(\mathbf{k}, E))^2 + \Sigma''^2(\mathbf{k}, E)} \quad (5.13)$$

Figure 5.7 can help to understand how the self-energy $\Sigma(\mathbf{k}, E)$ plays an effect to the spectral function $A(\mathbf{k}, E)$. The real part of the self-energy In figure 5.7 a, the real part of the self-energy shift the maximum of the spectrum and the imaginary part induces a broadening of the spectrum. We can take an example of a harmonic oscillator with frequency ω_0 , corresponding to the energy $\varepsilon_{\mathbf{k}}$, embedded in a viscous fluid that gives a damping term, can be considered as a "quasi-harmonic oscillator" with a new frequency ω_r and a finite lifetime τ . The interaction of the harmonic oscillator with the viscous fluid is coded in self-energy Σ . The energy of this "quasi-harmonic oscillator" is $\varepsilon_{\mathbf{k}} + \Sigma'$, shifted by Σ' compared to the free harmonic oscillator. The finite lifetime $\tau = \hbar/\Sigma''$, given by the imaginary part of the self-energy Σ , and in the domain of energy, the finite lifetime causes

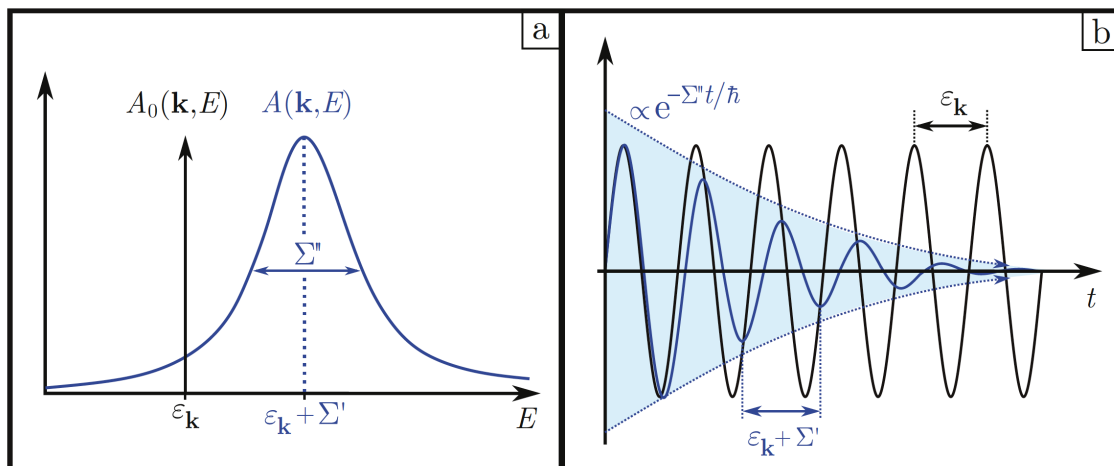


FIGURE 5.7: **Example of self-energy for harmonic oscillator.** **a.** Without the viscous fluid, the self-energy Σ is zero, and the spectral function of the 'free' harmonic oscillator is $A_0(\mathbf{k}, E) \sim \delta(E - \epsilon_{\mathbf{k}})$. In the presence of the viscous fluid, the maximum of the spectral function is shifted by Σ' (real part of the self-energy Σ) and the width is broadened by Σ'' (imaginary part of the self-energy Σ). **b.** In the picture of time domain, in the presence of viscous fluid, the frequency of oscillation is shifted by Σ' , and the lifetime of the oscillator is \hbar/Σ'' which corresponds to the broadening of the spectrum.

the broadening of the spectrum.

5.3.2 Connect the spectral function with the transfer rate of atoms

In our two-level systems in the state-dependent disorder, we prepare a Bose-Einstein condensate in disorder-insensitive state $|1\rangle$, then by rf-transfer, we load the atoms into the disorder-sensitive state $|2\rangle$, as shown in figure 5.1. The rf coupling for the transition from state $|1\rangle$ to $|2\rangle$ can be written as $\hat{W}(t) = \hat{W}_0 \cos(w_{\text{rf}}t)$. The Bose-Einstein condensate can be seen as a plane wave with null momentum $|\mathbf{k} = \mathbf{0}\rangle$. Then the coupling is actually from an initial state $|i\rangle = |1\rangle \otimes |\mathbf{k} = \mathbf{0}\rangle$ to a continuum of final states $\{|f\rangle\}_f = \{|2\rangle \otimes |E_\alpha\rangle\}_\alpha$, where $\{|E_\alpha\rangle\}_\alpha$ is the ensemble of the eigenenergies for the atoms in the disordered potential.

In this context, the transition from a discrete state $|i\rangle$ to a continuum of states $|f\rangle_f$ can be described by the well-known Fermi golden rule, in the limit of first-order perturbation of the Hamiltonian by a disordered potential. The transfer rate Γ is given by [80]:

$$\begin{aligned}
\Gamma &= \frac{2\pi}{\hbar} \overline{\sum_f |\langle f | \hat{W}_0 | i \rangle|^2 \delta(E_f - E_i - \hbar\omega)} \\
&= \frac{2\pi}{\hbar} |\langle 2 | \hat{W}_0 | 1 \rangle|^2 \overline{\sum_\alpha |\langle E_\alpha | \mathbf{k} = 0 \rangle|^2 \delta(E_\alpha - E_i - \hbar\omega_{\text{rf}})}
\end{aligned} \tag{5.14}$$

We set the initial energy E_i of the condensate as the origin of energy: $E_i = 0$, and recall the expression of the spectral function in equation 5.11, we get the connection between the transfer rate and the spectral function:

$$\Gamma(\omega_{\text{rf}}) \propto A(\mathbf{k} = 0, E = \hbar\omega_{\text{rf}}) \tag{5.15}$$

So we conclude that measuring the spectral function $A(\mathbf{k} = 0, E)$ is just need to measure the transfer rate of the transition from the BEC $|i\rangle = |1\rangle \otimes |\mathbf{k} = \mathbf{0}\rangle$ to the disorder-sensitive states $\{|f\rangle\}_f = \{|2\rangle \otimes |E_\alpha\rangle\}_\alpha$. In the next section, we will show the experimental results of measurement of spectral function in 2018 with the quasi-resonant speckle [28].

5.4 Experimental measurement of the spectral function with near-resonant speckle

The experiment starts with the realization of a ^{87}Rb BEC of about $N_1 = 2 \times 10^5$ atoms in the state $|1\rangle$. Then the disordered potential for state $|2\rangle$ is turned on with a given amplitude V_R , at the same time, the microwave and rf fields is applied to transfer the atoms in the $|1\rangle$ to $|2\rangle$, for a time duration t . The rf coupling is weak enough such that the transfer rate Γ can be calculated via the Fermi golden rule[80, 85, 86, 87]. The duration t is chosen to be short, i.e. $\Gamma t \ll 1$, so that only small fraction of atoms are transferred to state $|2\rangle$ (only a few percent). In this regime, the population N_2 in state $|2\rangle$ grows linearly in time: $N_2(t) = N_2(0) \Gamma t$. So measuring the transfer rate Γ is directly measuring the atom number transferred to state $|2\rangle$. Then by repeating the measurement with different rf-detuning δ , we can obtain the transfer rate $\Gamma(\delta)$, thus measuring the spectral function $A(\mathbf{k} = 0, E = \hbar\delta)$ in the disorder with amplitude V_R .

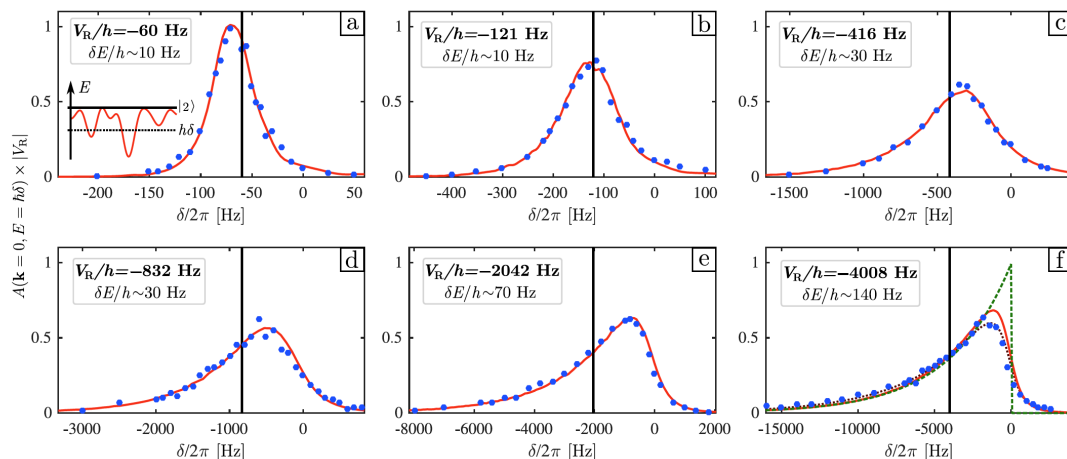


FIGURE 5.8: **The measurement of spectral functions $A(\mathbf{k} = 0, E)$ in attractive disorders.** From **a** to **f**, the amplitude of disorder V_R/h is -60 Hz, -121 Hz, -416 Hz, -832 Hz, -2042 Hz, -4008 Hz. The blue dots are the measured data. The red curves are the numerical simulations from D.Delande for the corresponding disordered potential. The black vertical line in each figure marks the amplitude of the disorder V_R/h . The duration of transfer t_p is adjusted for various V_R so that the energy resolution δE is much smaller than the width of the spectral function. Figure **f** is in the regime of strong disorder, $V_R/h = -4008$ Hz. The green dashed curve is the distribution of potential $p(V)$ as introduced in equation 4.15. The marron dotted line is the numerical simulation considering the residual disorder in state $|1\rangle$.

Change the amplitude of disorder potential V_R and do the same measurement as described above, we can obtain the spectral function $A(\mathbf{k} = 0, E = \hbar\delta)$ with various V_R . In [28], they measured from low amplitude to strong amplitude of disorder [77, 78, 79], for both repulsive and attractive disorder. The experimental results are shown in figures 5.8 for attractive disorder and in figures 5.9 for repulsive disorder, with V ranging from 60 Hz to 4 kHz.

In the figures, the experimental results are compared with the numerical simulation realized by M. Pasek and D. Delande [28]. We see that the agreement between the experimental results and the numerical curves is remarkable. The experimental data overlap excellently with the numerical simulations given by M. Pasek and D. Delande without any fitted parameters.

This work has demonstrated a method to probe the spectral functions with state-dependent disorder. That proves that we can load the atoms in the disorder with selected energy $E_f = E_i + \hbar\delta$, and with a high energy resolution which is only Fourier-limited: $\delta \sim h/t$. It also proves that spectral function is an excellent tool to calibrate the amplitude of disorder

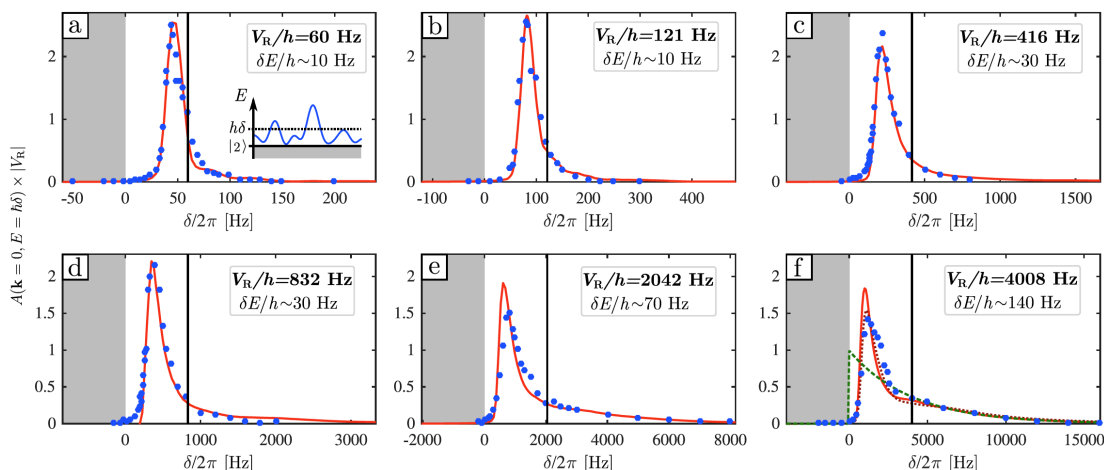


FIGURE 5.9: **The measurement of spectral functions $A(\mathbf{k} = 0, E)$ in repulsive disorders.** From **a** to **f**, the amplitude of disorder V_R/h is 60 Hz, 121 Hz, 416 Hz, 832 Hz, 2042 Hz, 4008 Hz. The blue dots are the measured data. The red curves are the numerical simulations from D.Delande for the corresponding disordered potential. The black vertical line in each figure marks the amplitude of the disorder V_R/h . The duration of transfer t_p is adjusted for various V_R so that the energy resolution δE is much smaller than the width of the spectral function. Figure **f** is in the regime of strong disorder, $V_R/h = -4008$ Hz. The green dashed curve is the distribution of potential $p(V)$ as introduced in equation 4.15. The marron dotted line is the numerical simulation considering the residual disorder in state $|1\rangle$.

V_R . The precision of calibration is within 5%. It is very important if we want to trust the measurement of the mobility edge in a given amplitude of disorder V_R .

5.5 To explore the Anderson transition in this platform?

To measure the mobility edge E_c , the strategy can be divided into two steps: 1. The first step is to load the atoms into a disordered state at energy $E_f = E_i + \hbar\delta$ by an rf field with frequency δ . 2. The second step is to expand the atoms in the disorder. We need to characterize its transport properties of the energy state E_f from the long time evolution of the atomic profile.

In this chapter, we show that the first step has been realized [28]. Can we go further towards the second step, measure the mobility edge by the expansion of atoms? Unfortunately, the answer is no, because in state $|2\rangle$, the atom experience a strong spontaneous scattering, which can destroy the motional wave function coherence. In our protocol of

state-dependent disorder, illustrated in figure 5.6, the speckle laser is close to the resonances of state $|2\rangle$, detuned by $\sim 80\text{MHz}$. Thus during the expansion in state $|2\rangle$ embedded in the disorder, the atoms experience a strong photon scattering. The photon scattering rate in state $|2\rangle$, Γ_2 can be calculated as:

$$\Gamma_2 \simeq \frac{1}{\hbar} |\bar{V}| \frac{\Gamma}{\delta}, \quad (5.16)$$

where \bar{V} is the average amplitude of disordered potential, $\Gamma = 2\pi \times 6.07\text{MHz}$, the linewidth of the D_2 transition of ^{87}Rb , and δ is the detuning.

For a disorder with amplitude $|V_2|/h = 416\text{Hz}$, according to the equation 5.16 above, the photon scattering lifetime of the state $|2\rangle$ in disorder, $\tau_2 \simeq 1/\Gamma_2$ is about 5.3ms. Compared with the required lifetime in the order of seconds, 5ms is far from being enough. So the strong photon scattering of the atom in state $|2\rangle$ is the main limitation of this near-resonant speckle protocol.

In summary, using the protocol outlined in Figure 5.6, we are able to generate a state-dependent disordered potential and measure the spectral function at different levels of disorder. However, the near-resonant speckle laser used in this process causes intense atom loss due to photon scattering, and destroys the coherence of the atomic wavefunction. The corresponding photon scattering lifetime is only a few milliseconds for atoms in state $|2\rangle$ (with a disorder of $V_R/h = 416\text{Hz}$). To measure the mobility edge, we need to improve the photon scattering lifetime by two orders of magnitude. In the following chapter, we will introduce a new set-up called *bichromatic speckle* that overcomes this limitation of the *monochromatic speckle* (near-resonant speckle potential) and allows for long-lasting energy-resolved quantum transport experiments.

Chapter 6

Bichromatic state-dependent disordered potential

In the previous chapter, we have presented how to generate the state-dependent disordered potential with a laser speckle. At the end of the chapter, we have shown the limitations of this scheme: the strong photon scattering of the atoms in the disorder prevents us from measuring the mobility edge.

To overcome this problem, the basic idea is to tune the frequency of speckle laser far from the atomic resonances of state $|2\rangle$. Nevertheless, by doing so, in state $|1\rangle$, the laser produces a disordered potential comparable with the potential in state $|2\rangle$. Thus we lose the state-dependence of the disorder. But if we use two lasers to generate the disorder, as illustrated in figure 6.1, whose frequencies and power are adjusted so that their potentials cancel each other in state $|1\rangle$ ($|1\rangle$ is insensitive to the disordered potentials in other words) and add-up in state $|2\rangle$ while keeping their frequency far away from the resonance of state $|2\rangle$, we can produce a state-dependent disorder (we call it bichromatic speckle in the following). With this bichromatic speckle, the photon scattering rate in state $|2\rangle$ is reduced by orders of magnitude to allow for long observation of quantum transport. In this chapter, we will introduce our experimental investigation of this bichromatic speckle.

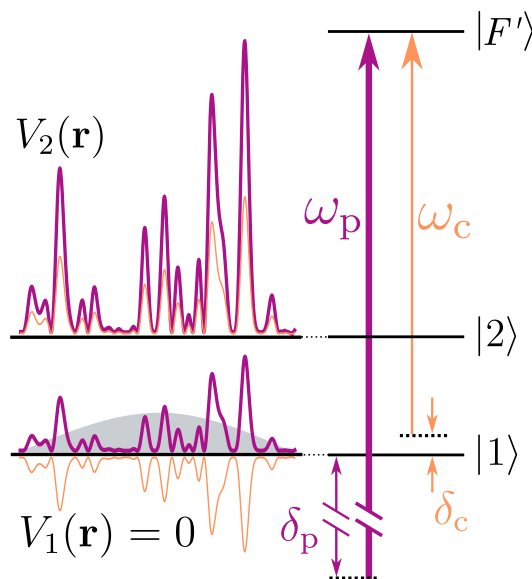


FIGURE 6.1: **State dependent disorder in a bichromatic speckle.** ω_p is the frequency of principal laser and ω_c is the frequency of compensating laser. The detunings of the two lasers with respect to the atomic resonance are δ_p and δ_c respectively. $V_1(\mathbf{r})$ and $V_2(\mathbf{r})$ are the total potentials created by the two lasers in state $|1\rangle$ and $|2\rangle$ respectively.

6.1 Bichromatic speckle scheme

In the scheme of bichromatic speckle, as shown in figure 6.1, the two lasers that we apply to generate the bichromatic speckle are called *principal laser* and *compensating laser* respectively. The detuning δ_p of the principal laser with respect to the transition $|1\rangle \rightarrow |F'\rangle$ is rather large, about 100GHz. It produces a repulsive potential $V_{p,1}(\mathbf{r})$ in state $|1\rangle$. The other laser is called compensating laser, as its name implies, we use it to compensate the potential produced by the principal laser $V_{p,1}(\mathbf{r})$ in state $|1\rangle$. It is less detuned, by about 1 to 2 GHz with respect to the transition $|1\rangle \rightarrow |F'\rangle$ in the red side. Thus the compensation laser produces an attractive potential $V_{c,1}(\mathbf{r})$ in state $|1\rangle$.

In our scheme of bichromatic speckle, in state $|1\rangle$, the potentials created by the principal laser and the compensating laser should cancel each other so that the total potential $V_1(\mathbf{r})$ in state $|1\rangle$ is zero, and in state $|2\rangle$ the total potential $V_2(\mathbf{r})$ is just the sum of the two potentials. We denote V_R as the average amplitude of the total potential in state $|2\rangle$. These two conditions are:

$$\begin{cases} V_1(\mathbf{r}) = V_{p,1}(\mathbf{r}) + V_{c,1}(\mathbf{r}) = 0 \\ V_2(\mathbf{r}) = V_{p,2}(\mathbf{r}) + V_{c,2}(\mathbf{r}) \quad \text{with} \quad \overline{V_2} = V_R \end{cases} \quad (6.1)$$

In this scheme, since the principal laser is detuned from the atomic resonances by about 100GHz, the photon scattering lifetime of state $|2\rangle$ is essentially limited by the compensating laser. Remember the photon scattering rate Γ_2 for state $|2\rangle$ is calculated as:

$$\Gamma_2 \simeq \frac{1}{\hbar} |\bar{V}| \frac{\Gamma}{\delta}, \quad (6.2)$$

where $|\bar{V}|$ is the average amplitude of the potential in state $|2\rangle$, δ is the detuning, and $\Gamma \simeq 2\pi \times 6.07\text{MHz}$ is the linewidth of the atomic resonance.

As we mentioned above, $\delta_p \simeq 100\text{GHz}$, $\delta_c \sim 1 - 2\text{GHz}$, here we do a very simple calculation to have some ideas on the order of magnitude, so we only consider the detuning of compensating laser δ_c and neglect the δ_p at the moment. For a disordered potential of $|\bar{V}|/h = 416\text{ Hz}$, we get that the lifetime of state $|2\rangle$ $\tau_2 \sim 1 - 2\text{ s}$. Remind that for the scheme of monochromatic speckle in the last chapter, for the same amplitude of disorder $|\bar{V}|/h = 416\text{ Hz}$, the photon scattering lifetime τ_2 is only 5ms. Therefore, in principle the bichromatic speckle can help to improve the lifetime by more than two orders of magnitude.

We have introduced the basic idea of the bichromatic speckle scheme and given a simple analysis of how this scheme can help to improve the photon scattering lifetime by two orders of magnitude. The analysis so far is oversimplified. In reality, the speckle pattern depends on the diffraction of the incident waves, thus, since the wavelengths of the two lasers are different by $\sim 100\text{GHz}$, the two speckle patterns cannot be strictly identical to cancel each other completely, as shown in figure 6.2 a. That means we cannot satisfy the condition $V_1(\mathbf{r}) = 0$ for all $\{\mathbf{r}\}$. So the different laser wavelengths lead to the decorrelation between the two speckle potentials and it prevents the complete canceling of the disordered potential in state $|1\rangle$. As the result, this decorrelation effect between the two speckle patterns induces a residual disorder in state $|1\rangle$.

To perform the energy-resolved transfer between $|1\rangle$ and $|2\rangle$, it is required that our speckle potential should be state-dependent, and $|1\rangle$ should be insensitive to the disorder. So we need to ask the question, does the residual disorder due to the decorrelation of the two lasers kill the insensitivity of state $|1\rangle$ to the disorder?

To answer this question, we need to calculate the variance σ_{V_1} of the residual disorder, and compare it with the chemical potential μ of our BEC in state $|1\rangle$. If $\sigma_{V_1} < \mu$, that means

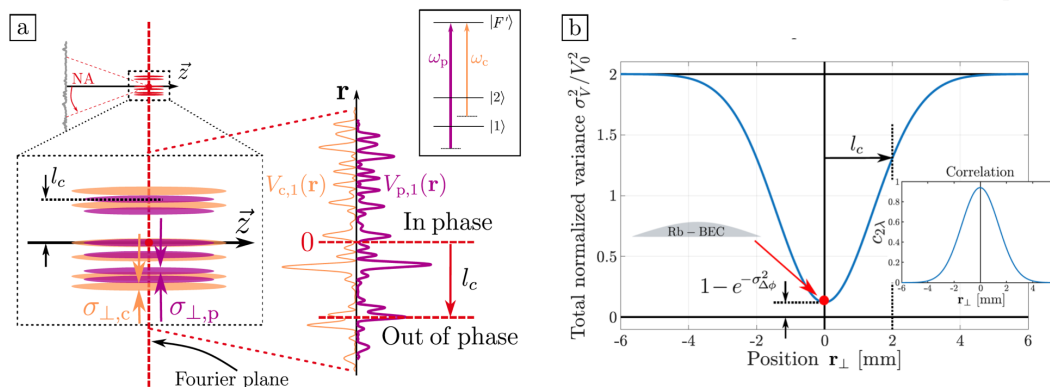


FIGURE 6.2: **Illustration of the correlation between two speckle potentials by the same diffuser.** **a.** Close to the Fourier plane, the two patterns are identical up to a spatial scaling factor, yielding an almost perfect overlap of the potential that decreases with the distance to the optical axis. The correlation length l_c describes the typical distance for which the speckle patterns become out of phase. **b.** Plot of the variance of the total potential as a function of the position in the Fourier plane. Close to the optical axis, the two speckle patterns are similar and the only decorrelation term arises from the phase difference due to the propagation through the diffuser. Far away from the optical axis, the two speckle patterns do not superimpose and the variance of the total potential is the sum of the two individual variances. In our experiment, the correlation length l_c is about 2 mm.

the fluctuation residual disordered potential can be screened by the chemical potential of the BEC thus the BEC in state $|1\rangle$ is not excited by the residual disorder. In the following, we will prove that in our experiment the residual disorder does not kill the insensitivity of the disordered in state $|1\rangle$. We will show our experimental realization of the bichromatic speckle scheme and the experimental check of the insensitivity of the disorder in state $|1\rangle$.

6.2 Fundamental potential deccorelation in state $|1\rangle$

Recalling equation 6.1, we need to first adjust the detunings and power of the two lasers to make the average potential in state $|1\rangle$ zero:

$$\overline{V}_1(\mathbf{r}) = \overline{V}_{p,1}(\mathbf{r}) + \overline{V}_{c,1}(\mathbf{r}) = 0. \quad (6.3)$$

Then we characterize the residual spatial fluctuation $\delta V_1(\mathbf{r}) = \delta V_{c,1}(\mathbf{r}) + \delta V_{p,1}(\mathbf{r})$ of the total potential in state $|1\rangle$. To characterize the spatial fluctuation of $V_1(\mathbf{r})$, we need to

calculate its variance $\sigma_{V_1}^2$:

$$\begin{aligned}
\sigma_{V_1}^2 &= \overline{\delta V_1^2} \\
&= \overline{(\delta V_{p,1} + \delta V_{c,1})^2} \\
&= \sigma_{V_{p,1}}^2 + \sigma_{V_{c,1}}^2 + 2\overline{\delta V_{p,1}(\mathbf{r})\delta V_{c,1}(\mathbf{r})} \\
&= \overline{V_{p,1}^2} + \overline{V_{c,1}^2} + 2\overline{\delta V_{p,1}(\mathbf{r})\delta V_{c,1}(\mathbf{r})} \\
&= 2|\overline{V_{p,1}}\overline{V_{c,1}}| \left(1 - \frac{\overline{\delta V_{p,1}(\mathbf{r})\delta V_{c,1}(\mathbf{r})}}{\overline{V_{p,1}}\overline{V_{c,1}}} \right).
\end{aligned} \tag{6.4}$$

In the derivation, we have used the property due to the exponential distribution of the intensity demonstrated in section 4.2: $\sigma_V = \overline{V}$ ($\sigma_I = \overline{I}$ in section 4.2). From equation 6.4, we define the normalized bichromatic correlation function $c_{2\lambda}$ as a function of the two lasers' wavelengths. $c_{2\lambda}$ quantifies the correlation of the two disordered potentials at position \mathbf{r} :

$$c_{2\lambda}(\mathbf{r}, \lambda_p, \lambda_c) = \frac{\overline{\delta V_{p,1}(\mathbf{r})\delta V_{c,1}(\mathbf{r})}}{\overline{V_{p,1}}\overline{V_{c,1}}} \tag{6.5}$$

The interpretation is rather direct: if the two potentials are completely decorrelated, then the correlation function $c_{2\lambda}(\mathbf{r}, \lambda_p, \lambda_c) = 0$. According to equation 6.4, the variance of the residual potential in state $|1\rangle$ is:

$$\begin{aligned}
\sigma_V^2 &= 2|\overline{V_{p,1}}\overline{V_{c,1}}| (1 - c_{2\lambda}(\mathbf{r}, \lambda_p, \lambda_c)) \\
&= 2|\overline{V_{p,1}}\overline{V_{c,1}}| \\
&= \overline{V_{p,1}^2} + \overline{V_{c,1}^2} \\
&= \sigma_{V_{p,1}}^2 + \sigma_{V_{c,1}}^2.
\end{aligned} \tag{6.6}$$

So in the situation where the two speckle potentials are completely decorrelated, the variance of the residual potential in state $|1\rangle$ is simply the sum of the variance of each potential: $\sigma_{V_1}^2 = \sigma_{V_{p,1}}^2 + \sigma_{V_{c,1}}^2$.

While in contrast, for exactly identical speckle patterns, their potential is perfectly correlated: $c_{2\lambda}(\mathbf{r}, \lambda_p, \lambda_c) = 1$. According to equation 6.4, the variance of the residual potential σ_{V_1} is zero, meaning that the two speckle potentials cancel each other completely.

Studying the amplitude of the residual potential then comes down to investigating the behavior of the normalized bichromatic correlation function $c_{2\lambda}(\mathbf{r}, \lambda_p, \lambda_c)$.

6.2.0.1 Calculate the normalized bichromatic correlation function

In order to facilitate the calculation of the normalized bichromatic correlation function $c_{2\lambda}(\mathbf{r}, \lambda_p, \lambda_c)$, we convert the expression of the correlation function $c_{2\lambda}(\mathbf{r}, \lambda_p, \lambda_c)$ in function of light intensity I instead of amplitude of potential:

$$\begin{aligned} c_{2\lambda}(\mathbf{r}, \lambda_p, \lambda_c) &= \frac{\overline{\delta V_{p,1}(\mathbf{r}) \delta V_{c,1}(\mathbf{r})}}{\overline{V_{p,1}} \overline{V_{c,1}}} \\ &= \frac{\overline{\delta I_p(\mathbf{r}) \delta I_c(\mathbf{r})}}{I_0^2(\mathbf{r})}. \end{aligned} \quad (6.7)$$

Therefore in order to calculate the correlation function $c_{2\lambda}(\mathbf{r}, \lambda_p, \lambda_c)$, we need to calculate the correlation between the intensity of the two lasers. The calculation is rather complicated, so to make it clear, we divide it into four steps: 1. the bichromatic correlation function of the diffuser, 2. the correlation function of the amplitude, 3. 3D monochromatic correlation close to the Fourier plane, and finally, we combine all these elements together to get the bichromatic correlation function of the speckle.

6.2.0.2 The decorrelation effect in practice

The calculation is in appendix B and in the thesis of Baptiste Lecoutre[88]. The bichromatic correlation function $c_{2\lambda}$ can be expressed as :

$$c_{2\lambda}(\mathbf{r}_\perp, z, \lambda_p, \lambda_c) = e^{-\sigma_{\Delta\phi}^2} c_{3D} \left(\mathbf{r}_\perp \frac{\delta\lambda}{\lambda}, z \frac{\delta\lambda}{\lambda} \right), \quad (6.8)$$

where \mathbf{r}_\perp is the transverse position in the Fourier plane, z is the longitudinal position near the Fourier plane, $\sigma_{\Delta\phi}^2$ is the variance of the local phase difference $\Delta\phi(\mathbf{r}_0)$ of the speckle fields on the surface of the diffuser: $\Delta\phi(\mathbf{r}_0) = \phi_p(\mathbf{r}_0) - \phi_c(\mathbf{r}_0)$, and c_{3D} is the monochromatic correlation function close to the Fourier plane and its expression can be found in appendix B.

We define *finess* \mathcal{F} , to characterize the frequency difference between the two lasers, and $\mathcal{F} = \lambda/\delta\lambda$. Then we can rewrite the bichromatic correlation function $c_{2\lambda}(\mathbf{r}_\perp, z, \lambda_p, \lambda_c)$ as:

$$c_{2\lambda}(\mathbf{r}_\perp, z, \lambda_p, \lambda_c) = e^{-\sigma_{\Delta\phi}^2} c_{3D}\left(\frac{\mathbf{r}_\perp}{\mathcal{F}}, \frac{z}{\mathcal{F}}\right). \quad (6.9)$$

The equation 6.9 is the major result of the calculation on the decorrelation effect of the two speckle potentials. Now we discuss the interpretation of the two terms of the bichromatic correlation function separately.

The first term $\exp(-\sigma_{\Delta\phi}^2)$ is associated with the fluctuations of the phase difference for the laser with two different wavelengths λ_p and λ_c , propagating inside the diffuser at the same point. To be more precise, at point \mathbf{r}_0 on the diffuser, the phase acquired by the principal laser is $\phi_p = 2\pi(n-1)\delta e(\mathbf{r}_0)/\lambda_p$ and the phase acquired by the compensating laser is $\phi_c = 2\pi(n-1)\delta e(\mathbf{r}_0)/\lambda_c$ where $\delta e(\mathbf{r}_0)$ is the thickness of the diffuser at point \mathbf{r}_0 . So the phase difference for the two lasers at point \mathbf{r}_0 is $\Delta\phi(\mathbf{r}_0) = \phi_p - \phi_c = 2\pi(n-1)(\lambda_p^{-1} - \lambda_c^{-1})\delta e(\mathbf{r}_0)$. Consider the Gaussian distribution for the phase ϕ_p and ϕ_c , their difference $\Delta\phi(\mathbf{r}_0)$ is also Gaussian distributed. When averaged over the diffuser, i.e. over \mathbf{r}_0 , we obtain that the average for the phase term $\overline{\exp(i\Delta\phi)} = \exp(-\sigma_{\Delta\phi}^2/2)$, with $\sigma_{\Delta\phi}^2$ the variance of $\Delta\phi$. This fluctuating phase difference term, therefore, results in a decorrelation factor in the speckle pattern. In the final analysis, the decorrelation factor is due to the roughness of the diffuser. It can be rewritten as $\exp(-\sigma_{\Delta\phi}^2) \simeq \exp(-4\pi^2(n-1)^2\sigma_e^2/\lambda_p^2\mathcal{F}^2)$. Here σ_e is the thickness fluctuation of the diffuser. So from the expression of $\exp(-\sigma_{\Delta\phi}^2/2)$, we know that the rougher the diffuser is and the bigger the frequency difference is, the less correlated the two speckle potentials will be.

In practice, the roughness of the diffuser σ_e is given by manufacturing. It is measured at the optical workshop of Institut d'Optique, using a profilometer. We get that the roughness of diffuser $\sigma_e = 1.3\mu m$. For $\mathcal{F} = \lambda/\delta\lambda \simeq 4000$, (this value 4000 corresponds to our bichromatic setup), the term $\exp(-\sigma_{\Delta\phi}^2)$ is $\sim 1 - 10^{-6}$, indicating almost perfect correlation between the two speckles on the surface of the diffuser, and thus the decorrelation produced when the two lasers transmitting through the diffuser can be negligible.

The second term in equation 6.9, $c_{3D}\left(\frac{\mathbf{r}_\perp}{\mathcal{F}}, \frac{z}{\mathcal{F}}\right)$, describes the loss of correlation between the two speckle potentials as shifted away from the optical axis, as shown in figure 6.2 b. It is due to the different geometrical scaling factors of the two speckle patterns, proportional

to the wavelengths. We find this term $c_{3D}(\frac{r_{\perp}}{\mathcal{F}}, \frac{z}{\mathcal{F}})$ is nothing but the correlation function of a monochromatic speckle in equation B.11 with a magnifying factor \mathcal{F} . As illustrated in figure 6.2 a, close to the center in the Fourier plane, the two potentials are identical up to a spatial scaling factor, yielding an almost perfect overlap of the potential, and the overlap decreases with the distance to the optical axis. So just as the monochromatic correlation function has a width of σ_{\perp} , the bichromatic correlation function then has a width $l_c = \mathcal{F}\sigma_{\perp}$, which defines its correlation length. As shown in figure 6.2 b, this correlation length l_c characterizes the distance from the center where the two speckle potentials are shifted by one speckle grain size, therefore losing the spatial overlap.

In the experiment, what does matter is the comparison of the bichromatic correlation length l_c with the size of the expansion of the atoms. Taking again $\mathcal{F} \simeq 4000$, the bichromatic correlation length is in the order of $l_2 \sim 2\text{mm}$. In our experiment, generally, after a long expansion (~ 3 seconds), even for a very diffusive state, the size L of the atoms is less than $100\mu\text{m}$. So the bichromatic correlation length l_2 is much larger than the size of the expansion of the atoms. Thus we can estimate the decorrelation factor to be at most $1 - c_{3D}(L/\mathcal{F}) \sim 10^{-4}$. Using equation 6.4, we estimate that the decorrelation effect between the two speckle potentials leads typically to a residual disordered potentials in state $|1\rangle$, with the variance in the order of:

$$\sigma_{V_1} \sim 0.02 \times V_R, \quad (6.10)$$

where V_R is the average amplitude of the disordered potential in state $|2\rangle$.

Equation 6.10 is the main result of this section. It shows that given amplitude of disorder V_R in state $|2\rangle$ what is the variance of the residual disorder in state $|1\rangle$. As mentioned above, to judge whether the state $|1\rangle$ is insensitive to the disorder, we need to compare the variance of the residual disorder σ_{V_1} with the chemical potential μ of our BEC. If $\sigma_{V_1} < \mu$, that means the residual disorder cannot excite the BEC and therefore state $|1\rangle$ is insensitive to the disorder. For instance, for $V_R/h = 416\text{Hz}$ in state $|2\rangle$, the variance of the residual disorder $\sigma_{V_1}/h \sim 11.4\text{Hz}$. The chemical potential μ of our BEC is about 250Hz , so according to equation 6.10, the BEC can sustain a residual disorder for $V_R/h \sim 10\text{kHz}$ in state $|2\rangle$. That is largely sufficient for our experiment because we are interested in the regime of $V_R/h \in [\sim 100\text{Hz}, \sim 1\text{kHz}]$ in state $|2\rangle$.

6.3 Reduction of the photon-scattering rate for the disorder-sensitive state

Recall that a strong reduction of the photon scattering rate in state $|2\rangle$ is the main goal of bichromatic speckle potential, as mentioned at the beginning of this chapter. To study Anderson localization, a lifetime of the atoms on the order of one second or more is essential[33, 34]. Note that the limitation of the lifetime for state $|1\rangle$ is much less stringent. The state $|1\rangle$ is only a source of atoms with well-defined energy for the rf-transfer. So the limitation is: $\Gamma_1^{-1} > t_{\text{rf}}$, the lifetime in state $|1\rangle$ needs to be longer than the duration of rf-transfer. In our experiment, t_{rf} depends on the amplitude of the disorder V_{R} . For a typical value of $V_{\text{R}}/h = 416\text{Hz}$, t_{rf} is generally less than 50ms. So Γ_1^{-1} must be longer than tens of milliseconds.

The photon scattering rate Γ_{sc} is the sum of the scattering rate from principal Γ_{p} and compensating disorder Γ_{c} . To calculate the scattering rate, we know that atomic polarizability α has real and imaginary parts. The real part introduces an energy shift, so we use this part to form the conservative trap, which is optical dipole trap. The imaginary part is the damping term, that limits the lifetime of the atoms. Therefore the scattering rate Γ_{sc} is proportional to the imaginary part of polarizability α [30]:

$$\Gamma_{\text{sc}}(\mathbf{r}) = \frac{1}{\hbar\epsilon_0 c} \text{Im}(\alpha) I(\mathbf{r}). \quad (6.11)$$

For a given hyperfine level state of atom $|F, m_F\rangle$, the total scattering rate is the sum of the effect from principal laser and compensating laser. For a given level:

$$\Gamma_{F, m_F} = \frac{1}{\hbar\epsilon_0 c} (\text{Im}[\alpha_{F, m_F}(\delta_{\text{p}}) I_{\text{p}} + \text{Im}[\alpha_{F, m_F}(\delta_{\text{c}}) I_{\text{c}}]). \quad (6.12)$$

In order to calculate it, the explicit expression for scattering rate for large detuning and negligible saturation (linear regime) is:

$$\Gamma_{\text{sc}}(\mathbf{r}) = \frac{3\pi c^2}{2\hbar\omega_0^3} \left(\frac{\omega}{\omega_0}\right)^3 \left(\frac{\Gamma}{\omega_0 - \omega} + \frac{\Gamma}{\omega_0 + \omega}\right)^2, \quad (6.13)$$

where ω is the frequency of laser, ω_0 is the relevant resonant frequency of atom, $\Gamma = \frac{\omega_0^3}{3\pi\epsilon_0\hbar c^3} |\langle e|\mu|g\rangle|^2$ is the dipole matrix element between ground and excited state of the relevant transition of atom.

With the explicit expression of scattering rate 6.13, we can numerically calculate the scattering rates Γ_1 and Γ_2 for state $|1\rangle$ and state $|2\rangle$ respectively.

Table 6.1 shows the result of the numerical calculation of the scattering rates, with the experimental parameters for a bichromatic speckle potential corresponding to $V_R/h = 416$ Hz in state $|2\rangle$. This value for the amplitude of disorder is typical in our experimental study of Anderson localization or the spectral functions [28] (see correlation energy in section chapter 7). Here, the detuning of the principal laser δ_p is chosen to be 95GHz. We choose $\delta_p/2\pi = 95$ GHz because we need the detuning to be large enough to reduce the photon scattering in state $|2\rangle$. At the same time, the difference between the frequencies of the two lasers cannot be too large so that the two speckle potentials can be *identical* enough to cancel each other well in state $|1\rangle$. So $\delta_p = 95$ GHz is a good compromise. The choice of δ_p is not that strict. We have tried some frequencies around 100 ± 10 GHz. In the experiment, we choose $\delta_p = 95$ GHz mainly because we can find a clean and stable mode of laser at this frequency. It can change if we find another better mode of laser.

The compensating laser limits both the lifetime of state $|1\rangle$ and $|2\rangle$. We choose its detuning δ_c to be large enough from $|2\rangle$ to have long time $\Gamma_2^{-1} \sim$ seconds, while at the same time, the lifetime in state $|1\rangle$ needs to be longer than the duration of rf-transfer ($\gamma_1^{-1} > t_{\text{rf}}$). For the measurement we do in this section, $t_{\text{rf}} = 40$ ms. For the reason of this compromise, we choose $\delta_c/2\pi = 1.4$ GHz and in state $|1\rangle$ the corresponding lifetime $\Gamma_1^{-1} = 73$ ms. So we have $\Gamma_1^{-1} > t_{\text{rf}}$.

With these parameters, $\delta_p/2\pi = 95$ GHz, $\delta_c/2\pi = 1.4$ GHz, and $V_R/h = 416$ Hz, we can deduce the amplitudes of the potential generated by each laser in $|1\rangle$ and $|2\rangle$: $V_{p,1}/h = -V_{c,1}/h = 366$ Hz, $V_{p,2}/h = 348$ Hz and $V_{c,2}/h = 68$ Hz ($V_R/h = V_{p,2}/h + V_{c,2}/h = 416$ Hz).

The most important result with these parameters of bichromatic speckle shown in table 6.1 is the improvement of the lifetime Γ_2^{-1} in state $|2\rangle$. According to the calculation, the lifetime Γ_2^{-1} can be improved from 5.3ms to 1.66s for $V_R/h = 416$ Hz, by two orders of magnitude compared with the monochromatic speckle [28]. Another additional point is that in our bichromatic speckle scheme, for $V_R/h = 416$ Hz, the variance of the residual disorder in state $|1\rangle$ is $\sigma_{V_1}/h \sim 11.4$ Hz, the same order as monochromatic speckle [28], $\sigma_{V_1}/h \sim 6.3$ Hz,

TABLE 6.1: Comparison of the state-dependent disordered potential parameters between the monochromatic configuration and the bichromatic one.

Quantity	Monochromatic	Bichromatic
$\delta/2\pi$	81MHz	-
$\delta_p/2\pi$	-	95GHz
$\delta_c/2\pi$	-	-1.4GHz
Γ_1^{-1}	26.6s	73ms
Γ_2^{-1}	5.3ms	1.66s
σ_{V_1}/h	6.3Hz	11.4Hz
P	0.49 μW	-
P_p	-	430 μW
P_c	-	4.6 μW

yielding the same state-selectivity as in [28].

The analysis in this section for $V_R/h = 416\text{Hz}$ can be easily generalized to a wide range of V_R by adjusting the parameters of the two lasers, from quantum regime to classical regime, both for repulsive ($V_R > 0$) and attractive ($V_R < 0$) potentials. We check that we can obtain similar improvements for the lifetime Γ_2^{-1} in state $|2\rangle$ for $V_R/h \in [\sim 40\text{Hz}, \sim 4\text{kHz}]$.

6.4 Experimental realization

In this section, we present how we realize the scheme of the bichromatic speckle in our experiment. There are two main objectives. Firstly, we need to check insensitivity to the disorder of state $|1\rangle$ experimentally, to prove that the variance of the residual potential in state $|1\rangle$ can be neglected in front of our Bose-Einstein condensate. This is done by studying the mechanical excitation of the BEC in state $|1\rangle$ by the residual disorder, following a quench of the disordered potential. We will explain how we measure the excitation of the disordered potential and how to characterize the cancellation of the two speckle potentials in state $|1\rangle$.

Secondly, with this new bichromatic speckle setup, we perform the rf-transfer protocol as what has been done with the monochromatic speckle in 2018 [28]. We check that with our bichromatic speckle setup, we are able to reproduce the spectral function measured in [28], and that proves that we can achieve the energy-resolved loading of atoms in the bichromatic disorder. Then we check the photon scattering lifetime of the disordered states

in the bichromatic speckle potential. As predicted, we find a large improvement by two orders of magnitude compared to the monochromatic speckle case, the photon scattering lifetime for the disordered states now being on the time scale of several seconds.

6.4.1 Experimental set-up

The laser source for the principal laser is *Toptica TA-Pro*, which can provide up to 1.5W of the beam at 780nm. The tuning range is more than 10nm. In the scheme of bichromatic speckle, we need this principal laser to be tuned away from the D2 line by 100GHz, so this laser can easily satisfy our demands. The typical linewidth of this laser is about 50kHz. If we compare the linewidth with the detuning of 100GHz, it can be negligible. It is hard to lock the frequency of this laser in our experiment due to the huge detuning of 100GHz. Since the linewidth is negligible compared with the detuning, we do not lock it in our experiment.

For the compensating laser, the laser source we use is *Cheetah* from *Sacher-Lasertechnik*. It is the same laser that we use for the repumper laser (L2) and the cooling laser (L3). This laser can provide power up to about 120mW, at 780nm. Here for generating the bichromatic speckle, generally, the power we use is about 30mW. The tuning range for the frequency is less than 20GHz, which explains why we use this laser to play the role of the compensating laser, which is generally tuned to be only 1-2GHz away from the transitions for $|F = 1\rangle$. The linewidth of this laser is about 5MHz. Since this laser works in a much smaller detuning $\sim 1 - 2$ GHz, we need to lock its frequency with a reference. We choose our repumper laser (L2) to be the reference of frequency. The passing band of the PID system is 10kHz. So finally the precision of the frequency of compensating laser is controlled within 10kHz.

The assembly allowing the shaping and stabilization of the beams for the generation of the bichromatic speckle is illustrated in figure 6.3. The optical schema in the left box shows the optics to combine the principal laser and the compensating laser together. The two lasers are combined by a beam splitter. Then a polarizer filters the two lasers to have the same polarisation before sending them into a monomode optical fiber. The spatial mode and the polarisation of the beam are filtered with the help of the monomode optical fiber

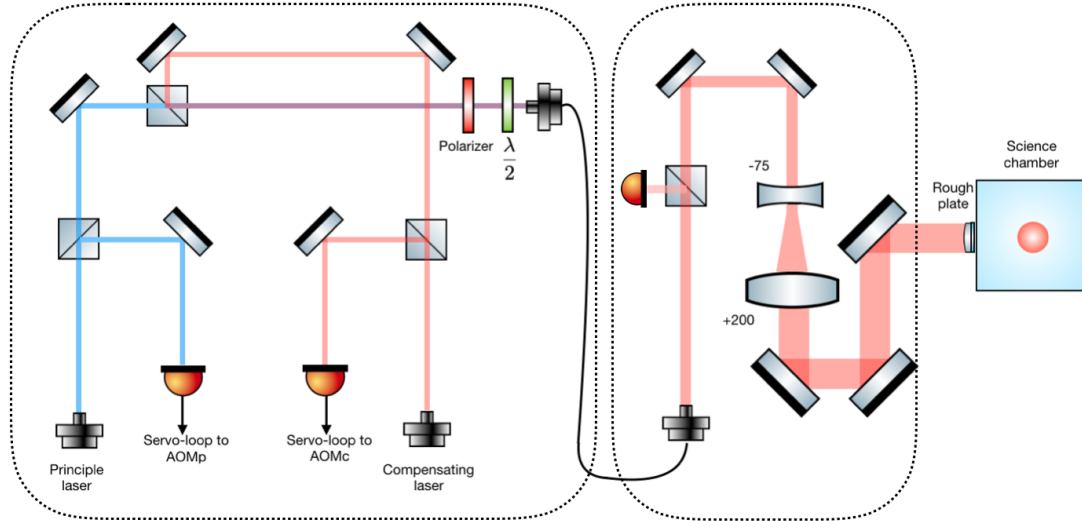


FIGURE 6.3: **Experimental set-up for bichromatic speckle.** The optics in the left and right parts represents the setup in two optical tables. The left part shows how we combine the principal laser and the compensating laser. For each of them, there is a servo-loop for controlling and stabilizing their power. The two lasers are combined by a beam splitter, and they are filtered to the same polarization by a polarizer before being injected into the fiber. The right part is the same as figure 4.5 to shape the beam to have a large waist of 14.6 mm. In this optical table, we put a PD before the beam going to the telescope to monitor the power fluctuation of the beam.

to maintain the polarisation of the beams.

The output of the fiber goes to another optical table (the right box in figure 6.3). The polarization of the beam is adjusted by a half-wave plate ($\lambda/2$) so that the beam can be transmitted through two PBS. These steps assures the linear polarisation of the beam is always well maintained. Then the next step is to reshape the beam to have a large waist, and the optics to do so are the same as what we have introduced in section 4.4. The beam is enlarged by a telescope composed of -75mm to +200mm lenses. With this telescope, the waist of the beam is increased from 5.6mm to 14.6mm.

To control the power of each laser individually, at the optical table in the left box in figure 6.3, we have servo-loop to AOM for each laser before combining them together with the beam splitter. The precision of the power control is better than 1 %. After the beams are combined together, we do not have power control of them anymore. Thus, if there is any fluctuation of power, there is no servo-loop to correct the fluctuation. The fluctuation of power can come from the fluctuation of polarization. If the polarization of the

beam is not well adjusted before going to the optical fiber, then at the output of the fiber, the polarization of the beam will fluctuate, then after the PBS, the fluctuation of the polarization causes the fluctuation of power. Therefore, we need to monitor the fluctuation of power after the PBS. As shown in figure 6.3, after the beam transmits through the PBS and before going to the telescope, by a beam splitter, we distribute 10% of the power to the telescope, and 90% of the power to a photo-diode which is used to monitor the fluctuation of power. This photo-diode is independent of the servo-loops of each beam.

In our experiment, the photo-diode shows that the fluctuation of the power is within 1%. That can induce a fluctuation of the amplitude of the disordered potential $\delta V_R \sim 1\%V_R$. The precision of the calibration for the amplitude of the disordered potential by spectral function is about 5%. Therefore, we can remark that the fluctuation of power does not introduce additional fluctuation to the disordered potential.

Generally, in our experiment, the power of the principal laser that we use is the range $[200\mu\text{W}, 2\text{mW}]$ and the compensating laser is the range of $[2\mu\text{W}, 20\mu\text{W}]$. With this range of power, we can generate the disordered potential with amplitude $V_R/h \in [100\text{Hz}, 1\text{kHz}]$ in state $|2\rangle$, and the corresponding fluctuation is in the range of $[1\text{Hz}, 10\text{Hz}]$.

6.4.2 Probing the insensitivity of state $|1\rangle$ to disorder using a quench

In our experiment, we have a BEC with around 2×10^5 atoms, in a very decompressed trap configuration: $\omega_y/2\pi \simeq 5\text{Hz}$, $\omega_z/2\pi \simeq 25\text{Hz}$, $\omega_x/2\pi \simeq 30\text{Hz}$. That corresponds to a chemical potential around $\mu/h \simeq 250\text{Hz}$ and a Thomas-Fermi radii around $R_{\text{TF}} \sim 45\mu\text{m}, 10\mu\text{m}, 8\mu\text{m}$ along each direction. In the experiment in order to quantify the effect of the residual disorder in state $|1\rangle$, we use a quench protocol. After we got the BEC, we switch abruptly on the disordered potential within $100 \mu\text{s}$, at the same time we switch off the optical trap for the BEC, and keep the disordered potential on for 4ms [89]. Then after the evolution of 4ms , we switch off the disorder and do a time of flight measurement with duration $t_{\text{ToF}} = 200\text{ms}$ to measure the momentum distribution of the atoms.

The measurement is shown in figure 6.4. In this figure, we fix the power and the frequency of the principal laser, thus keeping the amplitude of the disordered potential generated by principal laser $V_{p,1}$ unchanged. Here in our measurement shown in figure 6.4,

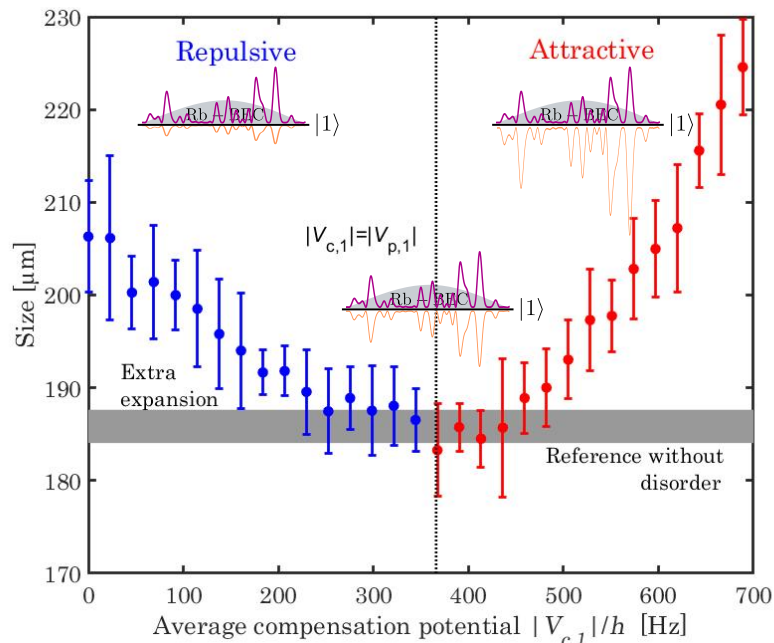


FIGURE 6.4: **Evolution of the momentum distribution of the atoms in state $|1\rangle$ following a quench of the bichromatic speckle potential.** The amplitude of the principal potential is fixed to $V_{p,1}/h = 366$ Hz, and we scan the amplitude of compensating potential $|V_{c,1}|/h$ from 0 to 700 Hz. The dots correspond to the size of the atomic cloud measured after a time of flight of 200 ms. The size is fitted by a Gaussian function. The error bars is estimated over five repeated measurements. The blue dots refer to the regime where $|V_{p,1}| > |V_{c,1}|$, thus the total potential V_1 being repulsive. The red dots refer to the regime of V_1 being attractive. The horizontal line corresponds to the reference where the same measurement is performed without disorder. The vertical dotted line corresponds to the theoretical prediction for an optimal cancellation of the total disorder in state $|1\rangle$.

$V_{p,1}/h = 366$ Hz. We scan the power of the compensating laser (fixing its frequency), thus scanning its amplitude of disordered potential. We scan the compensating potential $|V_{c,1}|/h$ from 0 to 700 Hz. The principal laser is blue-detuned, so $V_{p,1}$ is positive, while the compensating is red-detuned, therefore, $V_{c,1}$ is negative. Here to simplify, when we discuss the amplitude of disorder, we actually discuss its norm $|V|$.

The BEC is excited when the disorder is switched on abruptly, a part of the disordered potential energy being transferred to the kinetic energy. This excited kinetic energy results in an extra broadening of the momentum distribution of the atoms. After time of flight, the momentum distribution is converted into the size of the atoms. So this extra kinetic energy is reflected by an extra gain of the size of the atoms.

In the figure, we see that for a very low amplitude of compensating disorder, where

$|V_{c,1}| \ll V_{p,1}$, the total disordered potential $V_{p,1} + V_{c,1}$ is mainly from principal disorder, and the total disorder is repulsive (the blue color means the repulsive regime). Then as the amplitude of compensating disorder is increased, the total disordered potential $V_1 = V_{p,1} + V_{c,1}$ in state $|1\rangle$ decreases, and the excitation to the atoms becomes less strong accordingly. It is shown in the figure that the broadening of the momentum distribution becomes smaller. Then when $|V_{c,1}| > V_{p,1}$, the total disordered potential $V_1 = V_{p,1} + V_{c,1}$ in state $|1\rangle$ turns to negative, thus attractive potential (the red color means the attractive regime). Now when we increase $|V_{c,1}|$, the amplitude of V_1 increases again. Thus the excitation becomes stronger, and accordingly, the broadening of momentum distribution becomes stronger.

The minimum is reached as expected around $|V_{c,1}| = V_{p,1}$ ($V_{c,1} = -V_{p,1}$), which is the vertical thin dotted line in the figure. And what's more, we observe that the momentum spread is equal to the one in the absence of disorder within uncertainty $\sim 15\%$. So that means in this minimum, there is no excitation to the BEC. This observation is strong evidence of the efficient cancellation of the two disordered potentials, the residual potential yielding no observable excitation of the atomic cloud in state $|1\rangle$.

6.4.3 Check the rf-transfer with bichromatic speckle

In the previous section, we have shown the suppression of the disordered potential in state $|1\rangle$ being verified. Now we have a state-dependent potential, where state $|1\rangle$ is disorder-insensitive, and state $|2\rangle$ is disorder-sensitive. With the state-dependent disorder, we perform the rf-transfer, to transfer the atoms from state $|1\rangle$ to state $|2\rangle$, with the energy defined by $\delta_{\text{rf}} = \omega_{\text{rf}} - \Delta_{\text{hf}}$, the same method as introduced in section 5.1 (see the insert in figure 6.5 a). Here we take again the configuration in table 6.1: we set the bichromatic disorder parameters at the minimum point of figure 6.4, where $|V_{c,1}|/h = V_{p,1}/h = 366\text{Hz}$, so that the total potential in state $|1\rangle$ $\bar{V}_1/h = 0\text{Hz}$. In state $|2\rangle$, the total potential $\bar{V}_2/h = 416\text{Hz}$.

The rf power is chosen low enough to operate in the weak coupling regime where the transfer rate $\Gamma(\delta_{\text{rf}})$ is well predicted by the Fermi Golden rule. The rf field is applied in the regime of $\Gamma t_{\text{rf}} \ll 1$ (with the duration of transfer $t_{\text{rf}} = 40\text{ms}$) so that only a small fraction of the atoms are transferred to state $|2\rangle$ (no more than 15% at most). As discussed in section 6.3, note that the duration of the transfer is also chosen to be shorter than the

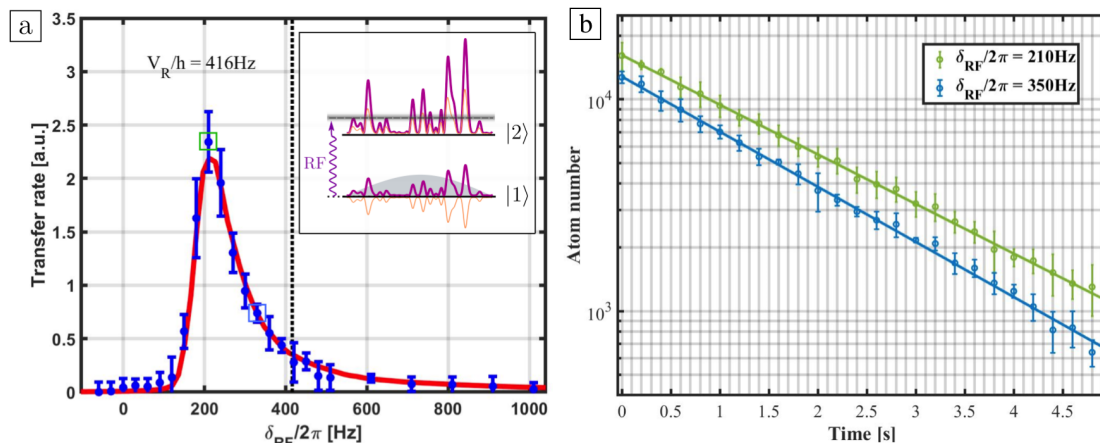


FIGURE 6.5: **Implementation of the rf transfer scheme and lifetime measurement for $V_R/h=416\text{Hz}$.** **a**, Normalized transfer rate $\Gamma(\delta_{\text{rf}})$ from disorder insensitive state $|1\rangle$ to the disorder sensitive state $|2\rangle$. The compensation and principal disorder amplitudes are set to $|V_{c,1}|/h = V_{p,1}/h = 366\text{Hz}$. That is the optimal cancellation condition for the disorder in state $|1\rangle$. The rf power is fixed during the scan of rf frequency. The rf pulse is applied for $t_{\text{rf}} = 20\text{ms}$ in order to avoid the photon scattering in state $|1\rangle$ during rf transfer. The blue dots are the measured points, and the red curve is the numerical calculation in [28] by M.Pasek and D.Delande, taking into account that the resolution of energy is 50Hz . The squared points are chosen to be used to measure the photon scattering lifetime. **b**, Atom number decay in the state $|2\rangle$ after the transfer in the disorder. The fits with exponential decays yield the lifetime of $1.85(5)\text{s}$ and $1.67(6)\text{s}$ respectively, in a good agreement with the predicted calculation in Table 6.1.

lifetime in state $|1\rangle$, to avoid the photon scattering during rf transfer. Remind in Table 6.1, in the configuration that we work in, the photon scattering lifetime in state $|1\rangle$ is about 73ms , so $t_{\text{rf}} = 40\text{ms}$ is in a safe regime. In these conditions, the energy resolution is time Fourier-limited to $\Delta E/h = 1/t_{\text{rf}} = 25\text{Hz}$.

In figure 6.5 a, we show our measurement for the transfer rate of atoms, versus the rf frequency. The experiment is the same as the rf spectroscopy for the monochromatic disorder. We prepare the BEC in an optical dipole trap, then switch on the bichromatic disorder and at the same time apply the rf field with a fixed amplitude. During the rf transfer, the optical dipole trap is kept on. Then after the transfer is finished, we switch off the optical dipole trap and the bichromatic disordered potential, doing a time of flight for 50ms , then image the atoms transferred to state $|2\rangle$. The curve in figure 6.5 a is the direct measurement of spectral function for $V_2/h = 416\text{Hz}$. As discussed in section 5.1, the excellent agreement is used to calibrate precisely the disorder amplitude in the experiments (with a 5% uncertainty). This measurement shows good evidence that with the new bichromatic speckle potential, we are able to load the atoms into the disordered

states with a narrow and controllable energy distribution ($\Delta E/h = 1/t_{\text{rf}}$). And by scanning δ_{rf} we can investigate all the states in the disorder. So we can do as good as for the monochromatic speckle potential in the work in 2018[28].

6.4.4 Improve the lifetime of state $|2\rangle$

After we can check the rf-transfer in the disordered potential, the next step is to study the photon scattering lifetime of the atoms in the disorder. In the experiment, we choose a certain rf detuning $\delta_{\text{rf}}/2\pi$, and once the rf transfer is done, we hold the atoms in the disorder to observe its decay in time.

We take again the same configuration corresponding to $\bar{V}_2/h = 416\text{Hz}$. We choose to study the lifetime of two states in the disorder. As shown in figure 6.5 a, the two squares are the two states that we choose, and the corresponding rf detuning for the two states are $\delta_{\text{rf}}/2\pi = 210\text{Hz}$, and 350Hz . We choose these two states because, first, they are close to the maximum transfer rate, so the atom number is good enough to have a good signal-to-noise ratio for studying the longtime decay, and second, according to numerical prediction in the work [36], the state $\delta_{\text{rf}}/2\pi = 210\text{Hz}$ is supposed to be a localized state, and $\delta_{\text{rf}}/2\pi = 350\text{Hz}$ is supposed to be a diffusive state.

As shown in figure 6.5 b, the fits by exponential curves yield very similar lifetime for the two states, $\tau_{210} = 1.85(5)\text{s}$ and $\tau_{350} = 1.67(6)\text{s}$ respectively. These values of photon scattering lifetime are in good agreement with the predicted value of 1.66s in table 6.1, thus validating our analysis. We prove that compared to the monochromatic speckle potential, we do improve the photon scattering lifetime for the disorder sensitive state by two orders of magnitude. We check this improvement of photons scattering lifetime for various amplitudes of disorder. The long photon scattering lifetime, larger than one second, is crucial for our investigation of the Anderson transition. We have checked the state-dependence of the disorder, the energy-resolved transfer, and the long lifetime in the bichromatic speckle. In the next chapter, we will introduce our experiment hint of the Anderson transition and we will show the mobility edge estimated from our experimental results.

Chapter 7

Measurement of the mobility edge

In the last chapter, we introduced our bichromatic speckle scheme. We demonstrated that with this platform, the transferred atoms can have a typical photon scattering lifetime on a time scale of seconds. We improved the lifetime of atoms by two orders of magnitude compared to the monochromatic speckle configuration [28], as shown in figure 6.5 and table 6.1. With this long lifetime of transferred atoms, our bichromatic speckle scheme opens the possibility for precise and direct measurements of the mobility edge of the Anderson transition. As discussed in section 2.4, the precise and direct measurement of the mobility edge remains an utmost experimental challenge [33, 34, 35].

In this chapter, we present our method for measuring the mobility edge using the bichromatic speckle potential and present our preliminary experimental results. We are in the process of understanding our observations and will provide an analysis in the following sections. At the end of the chapter, we will address some current technical problems and provide some perspectives for future improvements.

7.1 Scaling law of the mobility edge versus amplitude of disorder

Our aim is to measure the mobility edge E_c for various values of the disorder amplitude V_R and compare the results to the numerical curve obtained by Pasek et al.[36] in figure

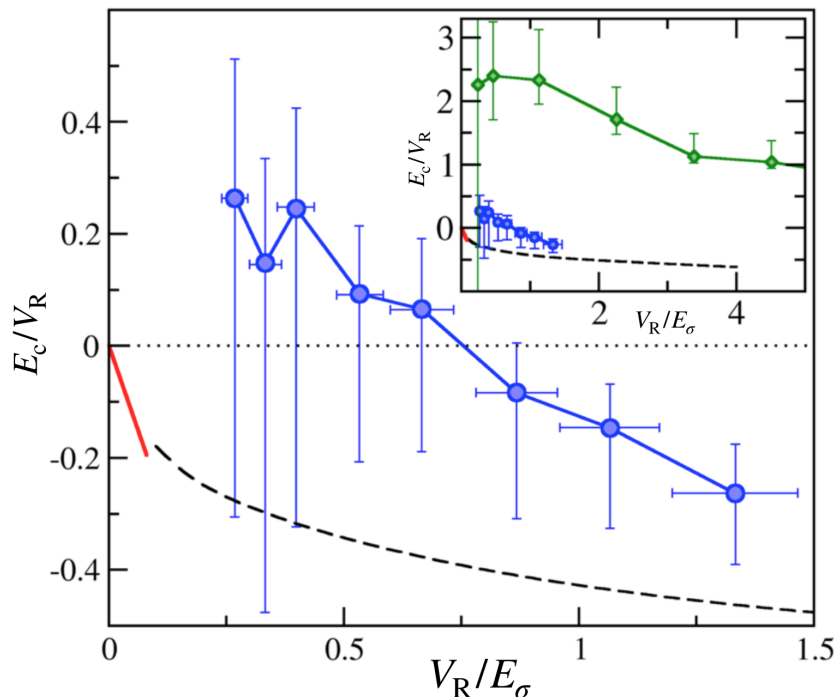


FIGURE 7.1: **The mobility edge E_C versus amplitude of disorder V_R .** The same figure as 2.11. To remind, the red curve is the experimental results of Palaiseau [33], the blue curve is the experimental results of Florence [34], the green curve is the results of Urbana-Champaign [35], and the black curve is the numerical prediction in [36].

7.1, which is a scaling law:

$$\frac{E_c}{V_0} = \mathcal{F}\left(\frac{V_0}{E_\sigma}\right). \quad (7.1)$$

It is important to note that the horizontal axis of the curve is expressed in terms of the correlation energy E_σ , which is a unit of measurement for the disorder amplitude. Therefore, in order to carry out a meaningful measurement of the mobility edge, it is necessary to first discuss the value of the correlation energy E_σ .

7.1.1 Correlation energy

In an isotropic disordered potential, the correlation energy is defined as:

$$E_\sigma = \frac{\hbar^2}{m\sigma^2}, \quad (7.2)$$

where σ is the correlation length of the disordered potential and describes the typical size of the grains of the disordered potential. To understand what correlation energy E_σ means,

we can consider in a relatively strong disordered potential as shown in figure 7.2, the two adjacent minima of the potential form a harmonic trap, so in this context, the localized states can be seen as the bound states trapped by in these minima. The correlation length σ is the typical size of the bound states trapped by the harmonic potential. Therefore, the correlation energy E_σ represents the typical energy of such harmonic oscillator. If the trap is deep to sustain many levels of bound states, then E_σ describes the energy gap between the levels.

For $E_\sigma \ll V_0$, that is the strong disorder regime. The energy gap between the levels is much smaller than the average energy of the potential, so many levels of bound states can be sustained by the potential. The atoms in these bound states are classically trapped in the local region. This classical trapping effect is the main mechanism for the localization in the regime of strong disorder so we call this regime 'classical regime'.

For $E_\sigma \gg V_0$, that is the weak disorder regime. The energy of the bound state is much higher than the average energy of the potential, so the atom can tunnel to the adjacent region, and thus the wavefunction extends over many speckle grains. There is no bound state that can be sustained by the potential. In this regime, the mechanism for localization is quantum interference. So we call this regime of low disorder 'quantum regime'.

We remark that the correlation energy E_σ is a unit of measurement for the disorder amplitude, and that explains why the correlation energy E_σ is so important when we talk about the amplitude of disorder.

7.1.2 Universality of the disorder

Different from the crossed speckle used in 2012 [33], we now use only single speckle in our experiment, resulting in a more anisotropic speckle pattern. So an important question is whether the scaling law of equation 7.1 in figure 7.1 is universal for different levels of anisotropy of the disorder.

In Pasek et al. [36], they performed quasi-exact numerical calculations for different speckle configuration to understand the effect of the anisotropy of disorder. Figures 7.3 show their

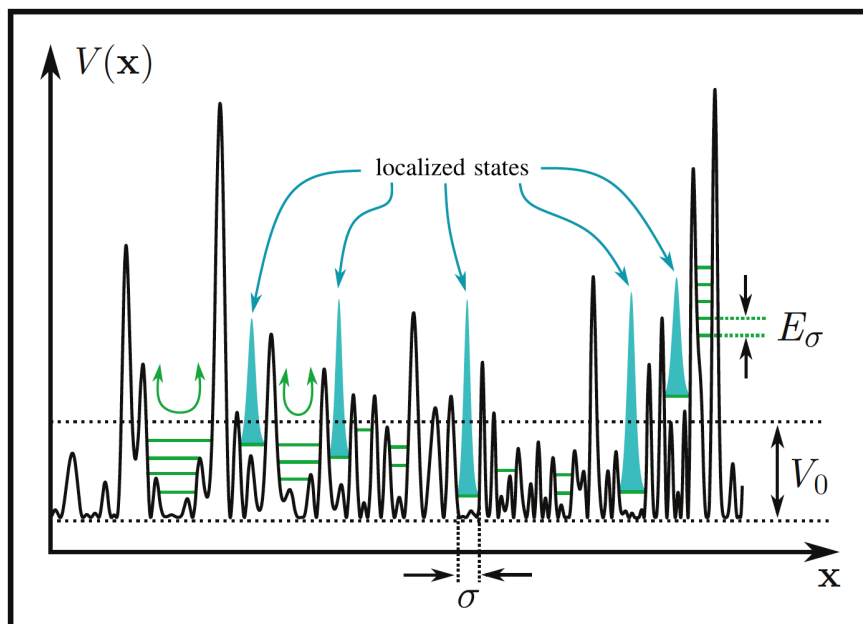


FIGURE 7.2: **Example of correlation energy.** V_0 is the average potential of the disorder. σ is the correlation length of the potential, corresponding to the typical size of the local minima. The correlation energy E_σ can be seen as the energy gap between adjacent levels in the trap formed by the local minima in the disorder.

results. In figures 7.3 a and b, they plot the normalized mobility edge E_c/V_0 for single speckle configuration as a function of the disorder amplitude V_0 , for five different anisotropy of disorder. In figure 7.3 c and d, they plot E_c/V_0 for two-crossed speckle configuration with different numerical aperture, corresponding to different correlation energy E_σ . In figures 7.3 a and c, the horizontal axis for amplitude of disorder are expressed in the unit of $E_L = \hbar^2 k_L^2/m$, while in b and d, the unit is the correlation energy E_σ .

We have given the definition of correlation energy for isotropic disorder: $E_\sigma = \hbar^2/m\sigma^2$. For anisotropy disorder, we can use the geometric average the correlation length to define the correlation energy E_σ [36]:

$$E_\sigma = \frac{\hbar^2}{m(\sigma_x\sigma_y\sigma_z)^{2/3}}, \quad (7.3)$$

where $\sigma_{x,y,z}$ are the correlation lengths of the disorder along \mathbf{x} , \mathbf{y} , \mathbf{z} directions respectively. In [36], they are defined as the HWHM of the central correlation peak divided by the numerical factor $\gamma \simeq 1.39156$ (such that $\sin \gamma/\gamma = 1/\sqrt{2}$).

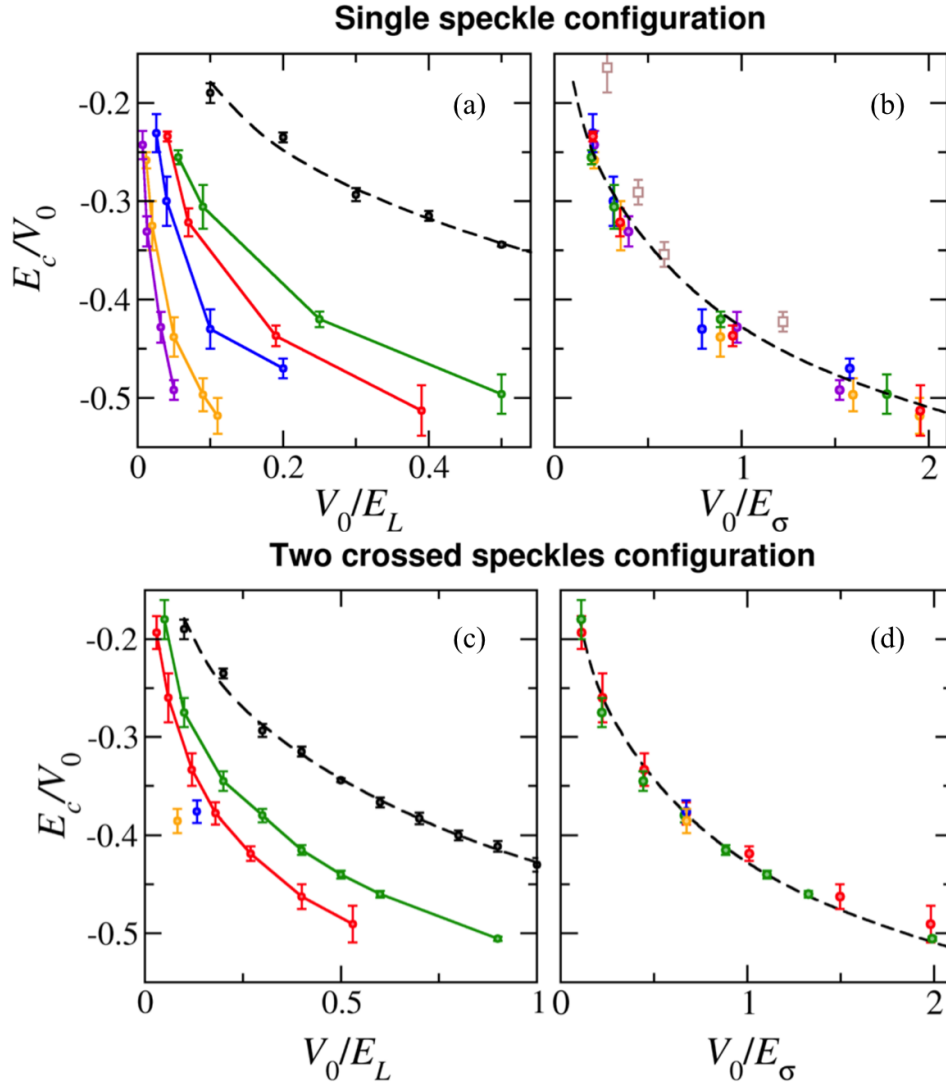


FIGURE 7.3: **Mobility edge for different speckle configuration.** The figures are from [36]. Figures (a) and (b) are for single speckles with different numerical apertures $\theta_0 = \{0.4, 0.5, 0.7, 0.85, 1.0\}$ (from lower to upper solid colored curves), corresponding to different anisotropy. (c) and (d) are for two-crossed speckle configurations with different numerical aperture $\theta_0 = \{0.5, 0.8\}$ (from lower to upper solid colored curves). (a) and (c) show the calculated values of the normalized mobility edge E_c/V_0 vs the disorder amplitude V_0 in the units of $E_L = \hbar^2 k_L^2/m$ (k_L is the wave vector of the laser beam and m is the atomic mass). (b) and (d) show the same data of E_c/V_0 vs the rescaled disorder strength V_0/E_σ . In (b), the correlation energy $E_\sigma = \hbar^2/m(\sigma_\perp^2\sigma_\parallel)$ where σ_\parallel and σ_\perp are the correlation lengths along and perpendicular to the laser beam respectively. The black dashed line is the same for single and two-crossed speckle.

The speckle geometries in figure 7.3 a are different (five curves with different anisotropy, thus different correlation energies) and the speckle geometries in figure 7.3 c are also different (two curves with different isotropic correlation length σ), resulting in different correlation energies E_σ for these different speckle geometries. When the mobility edge for these different speckle geometries are replotted together in function of the rescaled disorder strength V_0/E_σ in figures 7.3 b and d, we find that they collapse onto a **single universal curve** despite having different correlation energies! This demonstrates that the scaling law in 7.1 is independent of the speckle geometry no matter whether they are isotropic or anisotropic, created by single or two-crossed speckle and the scaling law is also independent of the correlation energy. The universality of the scaling law allows us to compare the experimental results from different experiments with different speckle geometries. So that explains why we can put the different results from the three groups [33, 35, 34] together and compare their results with a single universal numerical curve.

In our experiment, the transverse and longitudinal correlation lengths of our anisotropic speckle are noted as $\sigma_\perp = \sigma_{y,z}$ and $\sigma_\parallel = \sigma_x$, respectively, with $\sigma_\perp = 0.42 \pm 0.01\mu\text{m}$, and $\sigma_\parallel = 2.02 \pm 0.03\mu\text{m}$, as shown in section 4.4. Using the definition of correlation length from Pasek et al. [36], we divide our correlation length by γ , then according to equation 7.3, the correlation energy of our anisotropic disorder is $E_\sigma/h \simeq 441 \pm 18\text{Hz}$.

Our aim is to measure the mobility edge for various amplitudes of disorder and compare the data with the universal scaling curve from Pasek et al.[36]. In our experiment, the range of the amplitudes of disorder that is accessible for us is $V_R \in [\sim 100\text{Hz}, \sim 1\text{kHz}]$. Considering the correlation energy $E_\sigma/h \simeq 441\text{Hz}$ in our experiment, this range of amplitude of disorder covers from low disorder to strong disorder, spanning the quantum to classical regimes.

7.2 Experimental procedure

In this section we present a detailed experimental procedure for measuring the mobility edge for a fixed amplitude of disorder $V_R = 416\text{Hz}$, in order to compare our experimental measurements with the universal scaling curve, which takes into account our correlation energy $E_\sigma \simeq 441\text{Hz}$.

1. Parameters of bichromatic speckle. We fix the frequency of principal laser δ_p and compensating laser δ_c , as in table 6.1 (the detunings can change depending on the condition of the laser mode). Then we calculate the power of the two lasers P_p and P_c to satisfy the conditions for V_1 and V_2 :

$$\begin{cases} V_1(\mathbf{r}) = V_{p,1}(\mathbf{r}) + V_{c,1}(\mathbf{r}) & \text{with } \overline{V_1} = 0 \\ V_2(\mathbf{r}) = V_{p,2}(\mathbf{r}) + V_{c,2}(\mathbf{r}) & \text{with } \overline{V_2} = V_R \end{cases} \quad (7.4)$$

2. Check the disorder-insensitivity of $|1\rangle$. Then we do the quench measurement and follow the 'quench' procedure introduced in section 6.4.2: quench the disorder to measure the excitation of BEC by the residual disorder, and scan P_c while keeping δ_p , δ_c , P_p fixed to find the minimum excitation of BEC where the two speckles cancel each other in $|1\rangle$. The measurement checks that the parameters of the two lasers that we found in step 1 for $\overline{V_1} = 0$ satisfies the cancellation of the disorder in state $|1\rangle$, shown as figure 6.4. This step confirms the disorder-insensitivity of state $|1\rangle$.

3. Check the rf-transfer and lifetime in $|2\rangle$. Once we have found and verified the appropriate parameters for the bichromatic speckle potential, we use rf-transfer to measure the spectral function in this speckle configuration with an amplitude of disorder in state $|2\rangle$ given by V_R , as described in section 6.4.3. This step demonstrates our ability to load atoms in the disorder in an energy-resolved way. By comparing the measured spectral function with the numerical curve in [28], we can calibrate the amplitude of disorder V_R with an uncertainty of approximately 5%.

After performing the rf-transfer, we check the lifetime of the transferred atoms, as shown in figure 6.5, to ensure that we can make observations of expansion over a timescale of seconds.

These steps serve as preparation before measuring the mobility edge. We can then study the transport properties of the atoms.

4. Expansion at given energy in disorder. Given the disordered potential with the amplitude V_R , we perform the rf-transfer of the atoms with a certain rf-frequency δ_{rf} (duration of transfer t_{rf} is adjusted depending on V_R) to load the atoms at a given energy

$E_f = h\delta_{\text{rf}}$. Then we switch off the optical dipole trap and let the atoms expand in the disordered potential V_{R} for a duration t_{exp} . Afterwards, we image the atomic profile after a time-of-flight of $t_{\text{TOF}} = 1\text{ms}$ immediately following the expansion. By scanning the expansion time t_{exp} , we can observe the time-evolution of the atomic profile at this energy $E_f = h\delta_{\text{rf}}$.

In our experiment, we only measure the atomic profile along the y -axis (vertical axis). As explained in section 3.11, the magnetic field for the levitation induces a horizontal residual harmonic trap to the atoms along the x - and z -axis, with trap frequency $\omega_{\perp} \propto 1/\sqrt{B_0}$. In section 5.1.1, we have explained that to suppress the fluctuation of the magnetic field, we choose to work with a magic magnetic bias field $B_0^* \simeq 3.23\text{G}$. With this B_0^* , the horizontal trap frequency is measured to be: $\omega_{\perp} \simeq 2\pi \times 7\text{Hz}$. It is a very weak trap and the atoms can expand almost 'freely' in the disorder up to $\sim 20 \mu\text{m}$ along the x - and z - axis in this residual trap. Consider that the grain size of speckle along \mathbf{x} and \mathbf{z} (correlation lengths) $\sigma_x = 0.42 \mu\text{m}$ and $\sigma_z = 2.02 \mu\text{m}$, in presence of this residual trap, the expansion of the atoms in the disorder is locally 3D. If we want to have a completely 3D expansion, we need to eliminate the trapping effect along \mathbf{x} and \mathbf{z} induced by the magnetic levitation.

5. Expansion at different energies in disorder. We repeat step 4 and scan the rf-frequency δ_{rf} . Then we can obtain the time evolution of the atomic profile at different energies $E_f = h\delta_{\text{rf}}$ in the disorder.

In this disordered potential with amplitude V_{R} , we hope to observe a clear distinction between two regimes separated by critical energy $\simeq E_c$: 1) for all the energies E_f below E_c , we could expect that the expansion of cloud should be frozen because in our experiment the localization length (\sim a few μm) is small compared to the size of the atomic cloud ($\sim 45\mu\text{m}$). 2) for energies above E_c , the expansion of the cloud size is significantly stronger and the diffusion increases with energy E_f . The distinction between the different behavior of the transport of the atoms in the disorder may show the signature of the Anderson transition and we may probably estimate the mobility edge.

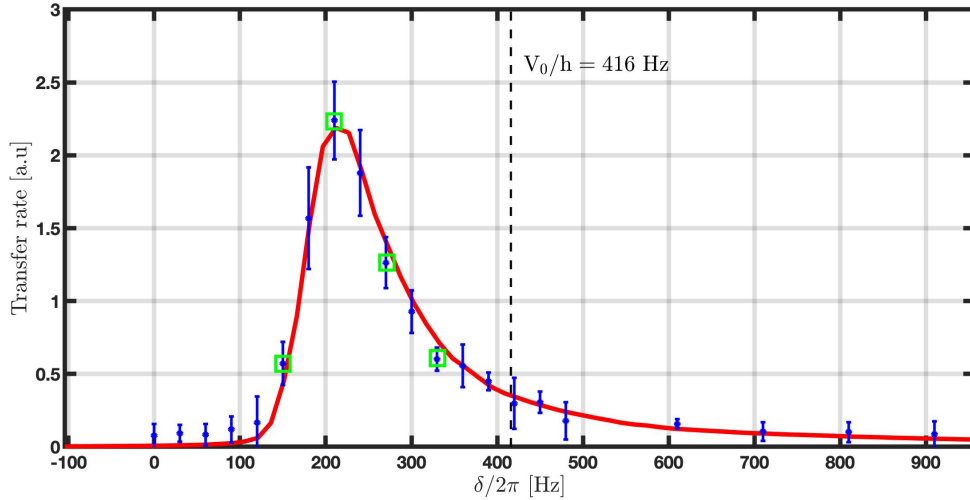


FIGURE 7.4: Spectral function for $V_R/h = 416$ Hz. The green dots mark the loading energies $\delta_{\text{rf}} = 156\text{Hz}$, $\delta_{\text{rf}} = 216\text{Hz}$, $\delta_{\text{rf}} = 276\text{Hz}$, and $\delta_{\text{rf}} = 336\text{Hz}$.

7.3 First experimental results and the analysis

Now we show some preliminary experimental results that have been observed recently from October to December 2022. We concentrate mainly on two amplitudes of disorder: $V_R/h = 416$ Hz ($V_R/E_\sigma \simeq 0.94$) and $V_R/h = 832$ Hz ($V_R/E_\sigma \simeq 1.89$). For these two specific amplitudes of disorder, we have the spectral function numerically calculated by D.Delande [28], so we can use them for calibration.

7.3.1 The first results for $V_R/h = 416\text{Hz}$

We scan the expansion time t_{exp} from 0.01s to 2.71s and observe the time evolution of the atomic profile at different energies $E_f = h\delta_{\text{rf}}$. Figure 7.5 shows our direct measurement of the atomic profile evolving at energies $\delta_{\text{rf}} = 156\text{Hz}$, $\delta_{\text{rf}} = 216\text{Hz}$, $\delta_{\text{rf}} = 276\text{Hz}$, and $\delta_{\text{rf}} = 336\text{Hz}$. These energies were chosen because they span a wide range of states in the spectral function for $V_R/h = 416\text{Hz}$, as shown in figure 7.4, from low to high energy, and we still have a sufficient number of atoms to achieve a good signal-to-noise ratio, particularly after a long expansion of about 3 seconds.

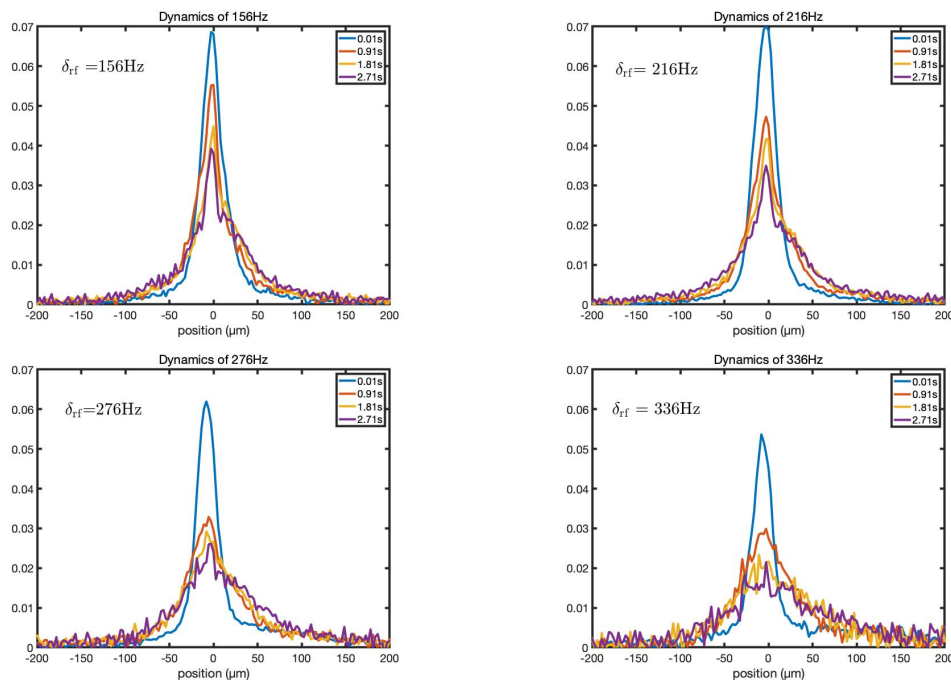


FIGURE 7.5: **Evolution of the atomic profile.** The atomic profiles show the expansion along y -axis. The image of the atoms is y - and z -axis, and the atomic profiles shown here is by integrating the atom number over z -axis. Considering the decay of atoms due to the photon scattering, for each picture, the atoms profile is normalized by the atom number so that we can compare the atomic profile for short- and long-time evolution at the same scale of figure.

7.3.2 First signature of the mobility edge

In the previous subsection, we presented our direct measurements of the atomic profile evolving at different energies. We observed that for relatively high energies, such as $\delta_{rf} = 276\text{Hz}$ and $\delta_{rf} = 336\text{Hz}$ in the disorder with amplitude $V_R/h = 416\text{Hz}$, the wavefunction can fully expand in 2.11 seconds, which is slightly longer than the corresponding photon scattering lifetime $\tau \simeq 1.66\text{ s}$, and the atom number decreases significantly for longer expansion times. Therefore, we fixed the expansion time at $t_{\text{mes}} = 2.11\text{ s}$ and compared the size of the expansion at different energies $E_f = h\delta_{rf}$.

In Figure 7.6 a, we show our experimental results for the size of expansion after 2.11 seconds at different energies δ_{rf} in the disorder with amplitude $V_R/h = 416\text{Hz}$. The size we show is the root mean square (r.m.s.) of the atomic profile as shown in the figures 7.5. We can see that there appear to be two regimes separated by a critical energy E_c : for all loading energies $E_f = h\delta_{rf} < E_c$, the size of the atomic cloud after 2.11 s of expansion is almost the same, consistent with the behavior of localized states. In contrast, for loading

energies $E_f = h\delta_{\text{rf}} > E_c$, the size of the atomic cloud increases with the energy of the atoms, and the expansion is much stronger at high energies in this regime compared to the regime where $E_f < E_c$.

Our results provide a hint of the Anderson transition apparently. According to our experimental data, for $V_{\text{R}}/h = 416\text{Hz}$, the critical energy is estimated to be: $E_c^{\text{mes}}/h \simeq 238\text{Hz}$. It's worth noting that the calculation of the r.m.s is not easy at all and the r.m.s. obtained depends strongly on noise and the region of interest chosen for calculation.

Next, we increase the disorder amplitude to $V_{\text{R}}/h = 832\text{Hz}$ and repeat the same experimental procedure for a 2s expansion. The results, shown in figure 7.6 b, also indicate the hint of the Anderson transition, with the estimated critical energy $E_c^{\text{mes}}/h \simeq 420\text{Hz}$.

In figure 7.6 c, we compare our estimates of the critical energies E_c from our measurement for $V_{\text{R}}/h = 416\text{Hz}$ and $V_{\text{R}}/h = 832\text{Hz}$ with the mobility edge numerically predicted by Pasek et al. [36]. We have estimated experimentally: $E_c^{\text{mes}} \simeq 238\text{Hz}$ for $V_{\text{R}}/h = 416\text{Hz}$ and $E_c^{\text{mes}} \simeq 420\text{Hz}$ for $V_{\text{R}}/h = 832\text{Hz}$, while the numerical prediction in [36] is: $E_c^{\text{num}} \simeq 240\text{Hz}$ for $V_{\text{R}}/h = 416\text{Hz}$ and $E_c^{\text{num}} \simeq 416\text{Hz}$ for $V_{\text{R}}/h = 832\text{Hz}$.

We mark the horizontal and vertical uncertainties for our data in the figure. The horizontal uncertainty takes into account the uncertainty of our calibration of V_{R} (about 5%) and the uncertainty of E_{σ} (about 4%), resulting in an overall uncertainty of about 6.4%. The vertical uncertainty is estimated roughly by considering that the uncertainty of our measurement of E_c is primarily due to the Fourier limited finite energy resolution of the rf-transfer: $\Delta E/h = 1/t_{\text{rf}}$. For $V_{\text{R}}/h = 416\text{Hz}$, the duration of the transfer t_{rf} is chosen to be 40 ms, resulting in an energy resolution of $\Delta E/h \simeq 25\text{ Hz}$, giving $\Delta E_c \simeq 10.4\%$, so by including the uncertainty of V_{R} , the overall vertical uncertainty is estimated to be about 11%. For $V_{\text{R}}/h = 832\text{Hz}$, the duration of the transfer t_{rf} is chosen to be 20 ms, resulting in an energy resolution of $\Delta E/h \simeq 50\text{ Hz}$, giving $\Delta E_c \simeq 12\%$, and thus the vertical uncertainty is estimated to be about 12.7%.

Our measurements of critical energies show excellent agreement with the numerically predicted mobility edge with a reasonable uncertainty, indicating that our measured critical energies apparently correspond to the mobility edge we are looking for. Compared to

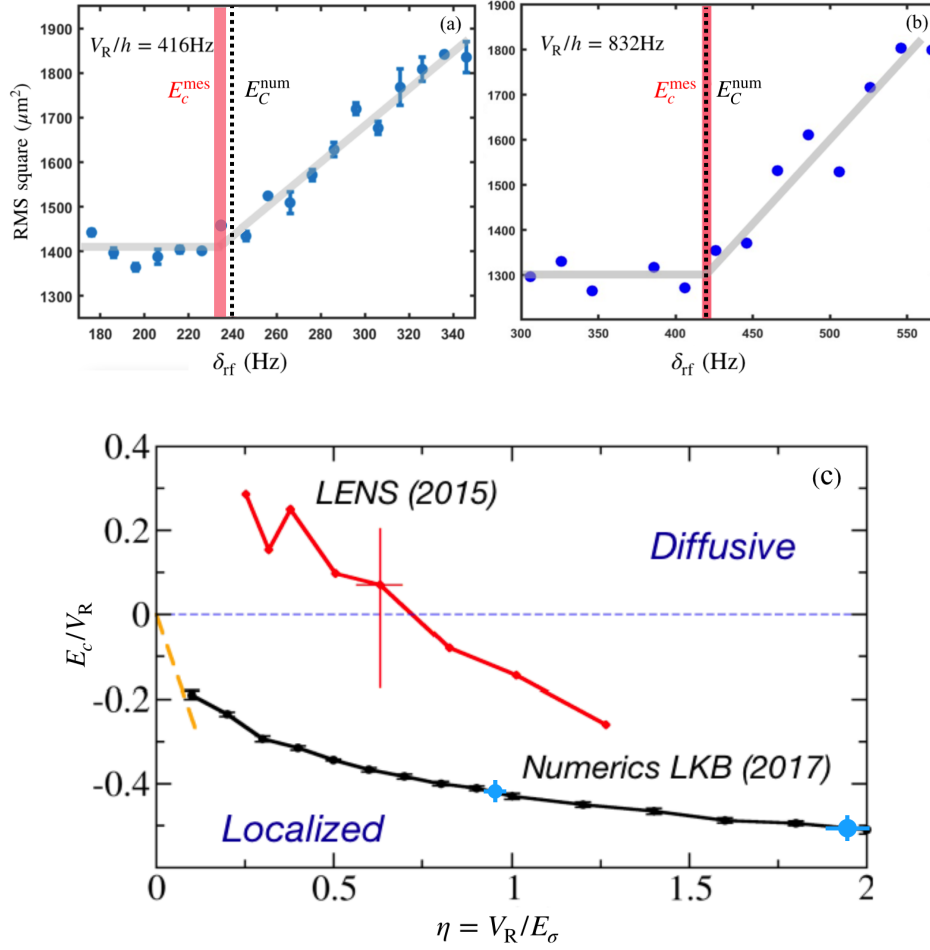


FIGURE 7.6: **The size of atomic cloud for different δ_{rf} at fixed t_{exp} .** **a.** $V_{\text{R}}/h = 416 \text{ Hz}$. **b.** $V_{\text{R}}/h = 832 \text{ Hz}$. **c.** Comparison of our critical energy with the numerical curve by Pasek et al.[36]. The two blue dots are the critical energies estimated from the data in figures **a** and **b**, for $V_{\text{R}}/h = 416 \text{ Hz}$ ($\eta = V_{\text{R}}/E_{\sigma} \simeq 0.94$) and $V_{\text{R}}/h = 832 \text{ Hz}$ ($\eta = V_{\text{R}}/E_{\sigma} \simeq 1.89$). The error bars show the horizontal and vertical uncertainty of our measurements. The horizontal uncertainty is given by 1. the uncertainty of the estimation of E_{σ} , which is from the uncertainty of the correlation lengths of the speckle, 2. the uncertainty of measurement of V_{R} . The vertical uncertainty is given by 1. the uncertainty of measurement of V_{R} , 2. the finite energy resolution of the rf-transfer when determining the critical energy E_c .

previous experimental results with ultracold atoms [34, 35], our results are significantly closer to the numerical curve.

7.3.3 Analysis of the central density

By looking at the r.m.s. of the atomic profile, we have found the hint of Anderson transition and estimated the critical energy E_c . There is another way to observe the signal of Anderson transition, by looking at the decay of the central density of the atomic cloud. For diffusive states, the decay of the central density is expected to be faster than that of localized states. In addition, for localized states, we expect to see the central density tending towards a steady value over a long time of expansion.

Figure 7.7 a shows the decay of the central density of the atomic cloud for $V_R/h = 416\text{Hz}$ at different energies $E_f = h\delta_{\text{rf}}$: $\delta_{\text{rf}} = 156\text{Hz}$, $\delta_{\text{rf}} = 216\text{Hz}$, $\delta_{\text{rf}} = 276\text{Hz}$, $\delta_{\text{rf}} = 336\text{Hz}$. In the figure, in order to eliminate the effect of atom loss due to photon scattering by the speckle potential, we normalized the central density data by the corresponding initial atom number. Each group of data is normalized to the value at $t = 0$ in order to compare them together at the same scale.

According to the figure, we find that for $\delta_{\text{rf}} = 336\text{Hz}$ and $\delta_{\text{rf}} = 276\text{Hz}$, the decay of the central density is evidently faster than the decay for $\delta_{\text{rf}} = 216\text{Hz}$ and $\delta_{\text{rf}} = 156\text{Hz}$.

To further emphasize the difference in behavior between the two regimes, we choose to compare the central density at a fixed expansion time of $t_{\text{exp}} = 2.11\text{s}$ for different energies δ_{rf} , as shown in Figure 7.8 a. We can see that there is a sharp transition with a critical energy $E_c \simeq 236\text{ Hz}$ that separates the two regimes: for energies lower than E_c , the decay of the central density is very slow, while for energies above E_c , the decay is much stronger.

We can also look at the atomic profile of these different energies at the fixed expansion time of $t_{\text{exp}} = 2.11\text{s}$, as shown in figure 7.8 b. We see two regimes in the figure: for the low energies, $E_f < 236\text{ Hz}$ (dark blue and orange profiles), the decay of the central peak is very weak; by comparison, for the high energies, $E_f > 236\text{ Hz}$ (purple, green and light blue profiles), the decay of the central peak is much stronger and the diffusion is more

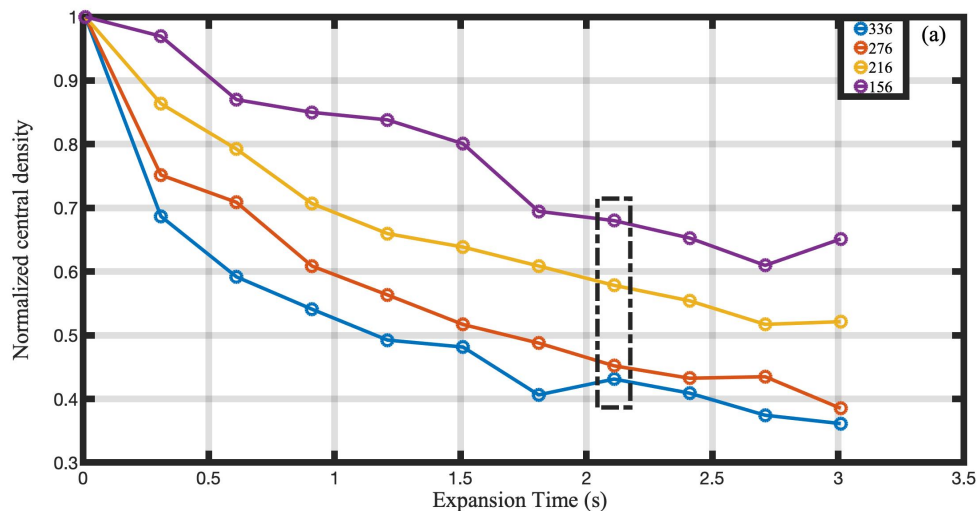


FIGURE 7.7: **Time evolution of the central density for different energies.** The blue data is for $\delta_{\text{rf}} = 336\text{Hz}$, the orange data is for $\delta_{\text{rf}} = 276\text{Hz}$, the yellow data is for $\delta_{\text{rf}} = 216\text{Hz}$, and the purple data is for $\delta_{\text{rf}} = 156\text{Hz}$. The atom number is normalized to eliminate the loss due to the photon scattering by the speckle.

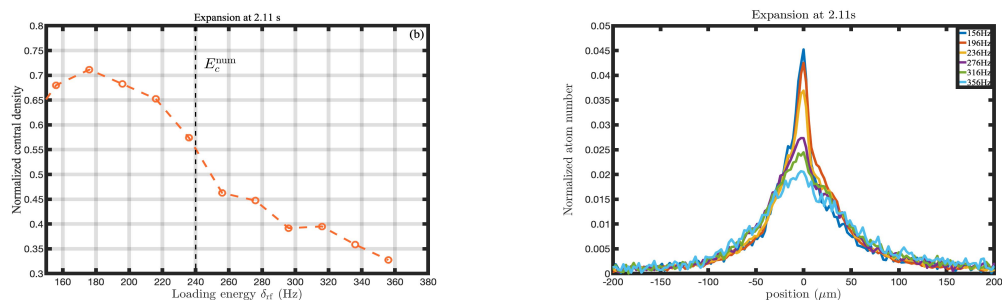


FIGURE 7.8: **The analysis of the central density.** a. Compare the central density with different energies for $t_{\text{exp}} = 2.11\text{s}$. The black dashed vertical line is the numerical prediction of the mobility edge. b. The atomic profile of different energies for expansion time = 2.11 s. The treatment of the atomic profile is the same as above.

evident. So the different behaviors of the atomic profiles also indicates a transition at critical energy $E_c \simeq 236\text{ Hz}$ between the two regimes.

This sharp transition in the behavior of central density and the atomic profile for a long time expansion of 2.11 seconds is consistent with the properties expected to see for the Anderson transition. If we believe that we have indeed observed the Anderson transition for $V_R/h = 416\text{Hz}$, then the critical energy $E_c/h \simeq 236\text{ Hz}$ that separates the two regimes should be the mobility edge. Our experimental measurements are thus in good agreement with the numerical prediction of $E_c^{\text{num}} \simeq 240\text{Hz}$.

7.3.4 Temporal dynamics

Despite everything, we need to admit our results are not perfect yet. In figures 7.8 b, we see that after a long expansion of 2.11 s, even for the low energy states, e.g. $\delta_{\text{rf}} = 156\text{Hz}$ and $\delta_{\text{rf}} = 216\text{Hz}$, which are expected to be in the localized phase, we observe some unexpected diffusion in the wings of the atomic profile. The diffusion in the wings seems to be similar for low-energy states and high-energy states. The same issue can be seen in figure 7.7, for $\delta_{\text{rf}} = 156\text{Hz}$ and $\delta_{\text{rf}} = 216\text{Hz}$, the decay of the central density is somewhat stronger than expected. So there seems to be some excitation present during the expansion of atoms, and the atoms at low energy states can be excited to some diffusive states at higher energies, thus causing the unexpected diffusion. This excitation can make the distinction between the localized and diffusive regimes less clear. However, the source of the excitation is not yet clear to us. We will analyze the temporal dynamics of the atomic cloud in disorder to get some insights.

To observe the temporal dynamics of the atomic cloud, we calculated the root mean square (r.m.s.) of the atomic cloud and examined how the r.m.s. at different energies evolves with expansion time. In the ideal case, for energies in the localized regime, we expect to see that the r.m.s. of the cloud expands extremely slowly and tends to a steady value. On the other hand, for energies in the diffusive regime, we expect to observe the square of the r.m.s. evolving linearly in time, which is a characteristic property of diffusive states.

In figure 7.9, we plot our measurements for $V_{\text{R}}/h = 416\text{Hz}$ for different energies. From the figure, we can see that the temporal dynamics of the atomic cloud is not as clear as we expected. Even for the energies $\delta_{\text{rf}} = 156\text{ Hz}$ and $\delta_{\text{rf}} = 216\text{ Hz}$, which are expected to be in the localized regime, the r.m.s. still increases in time and does not seem to saturate. If we fit these data with a linear function in time, then we estimate the diffusion constant $D \sim \frac{\text{r.m.s.}^2}{t}$, we find that the diffusion is very similar for all of these four energies. As discussed above, the excitation induces unexpected diffusion for the low-energy states. Therefore, there is some fundamental diffusion present for all the energies, making it difficult to clearly distinguish between the localized and diffusive regimes by looking at the temporal dynamics of the r.m.s..

One possible explanation for this observation is fluctuations in the disordered potential. In section 6.4.1, we have verified that the power fluctuation of the speckle beam is on the order of 1%, which we do not believe is the source of the excitation.

We suspect that despite the reduction by two orders of magnitude in photon scattering of the atoms in the bichromatic disorder compared to the monochromatic speckle, scattering can still excite some atoms to higher energies during the long expansion. This may explain the diffusion of low-energy states. To further study the localization properties, we can try to improve the photon scattering lifetime of the disordered states, which may help to weaken the excitation and observe a more clear signal of localization in the localized regime

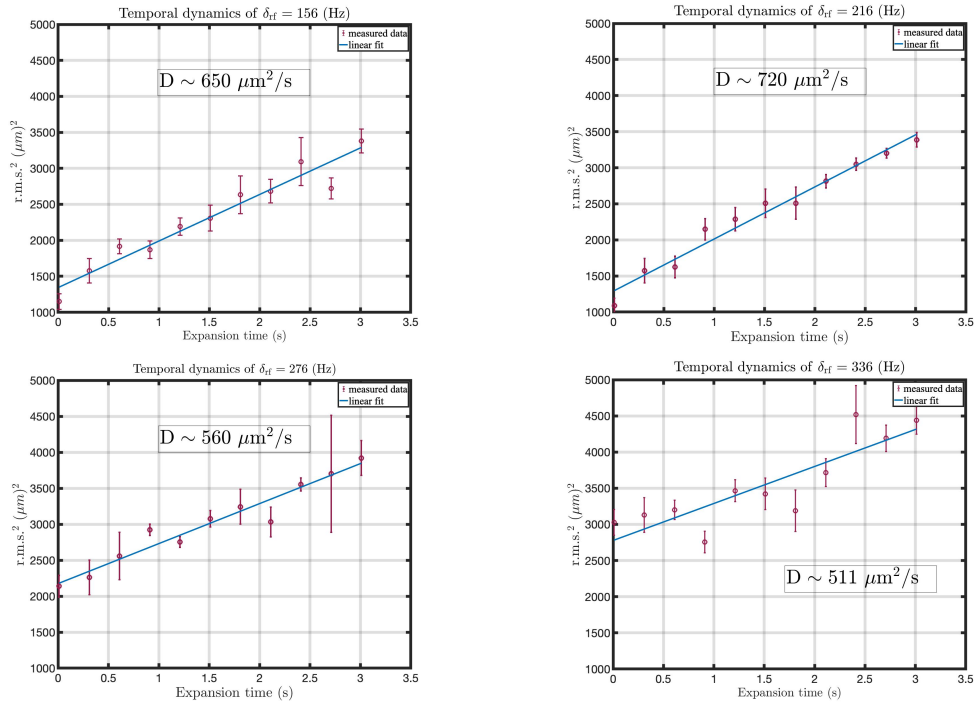


FIGURE 7.9: **Temporal dynamics for different energies.** The purple dots are the r.m.s. calculated from our data. The error bar is from five repeated measurements. The diffusion constant D is estimated by fitting the r.m.s.² versus time with the linear function (blue line): $\text{r.m.s.}^2 \sim Dt$.

7.4 Future improvements

We have shown our experimental results and we see there are still some imperfections in our measurements. In this section, we will list some improvements that we will try to do

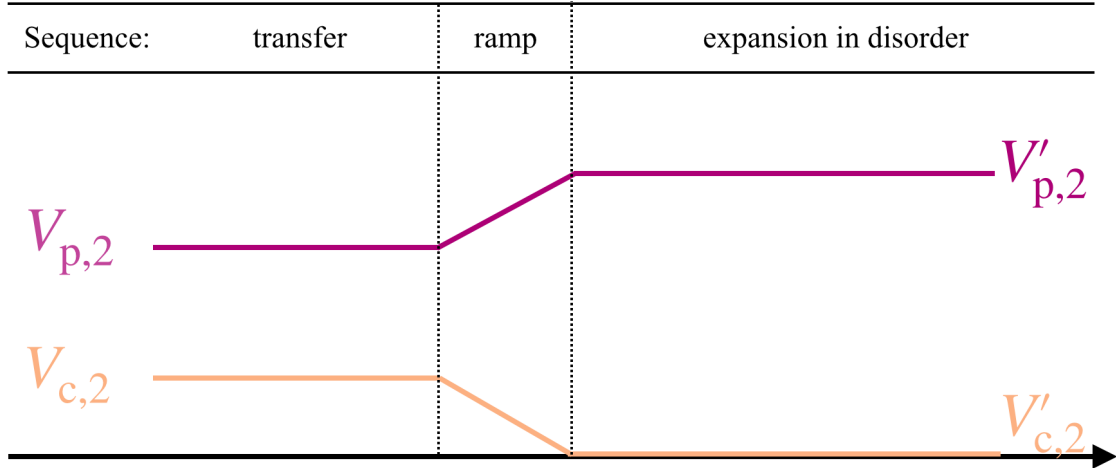


FIGURE 7.10: **Experimental sequence for longer lifetime of atoms in disorder.** Up to the step of rf-transfer, the sequence is the same as the normal sequence. But once the rf-transfer is finished, we ramp down the power of compensating laser to zero and ramp up the power of the principal laser, keeping V_2 unchanged during the ramp. Then we do the expansion in this configuration of disorder. The optimal ramp duration is yet to be found.

in the near future in addition to the search for the excitation source.

7.4.1 Improve the lifetime of disordered states

In the last section, we noted that photon scattering of the atoms in the disorder may be one of the sources of excitation, which can excite some atoms from localized states to diffusive states. So we to suppress this photons scattering and improve the lifetime of the atoms.

As described in section 6.3, the lifetime of the disordered states (state $|2\rangle$) is primarily limited by the compensating laser as it is closer to the resonances of atoms. One way to suppress the photon scattering is shown in figure 7.10. In this scheme, we still do the same rf-transfer in the state-dependent disorder, and once the atoms are transferred from state $|1\rangle$ to state $|2\rangle$, we do not care about the disorder-insensitivity of state $|1\rangle$ anymore, so we can ramp down the power of the compensating laser to zero. But it is necessary to keep the amplitude of disorder V_R in state $|2\rangle$ constant during the ramp, so we need to ramp up the power of the principal laser simultaneously, and the ramp of the two lasers is designed to keep the amplitude of the disorder V_R in state $|2\rangle$ constant.

By implementing this ramping technique, we can in principle greatly reduce the photon scattering of the atoms during expansion. Take again the configuration of bichromatic speckle in table 6.1 for $V_R/h = 416\text{Hz}$, by this ramping technique, the lifetime Γ_2^{-1} of the atoms in the disorder can be improved from 1.66s to about 10s, by one order of magnitude. This longer lifetime of atoms in disorder may help to reduce the fundamental excitation and allow us to probe the transport properties with longer expansion time, providing more precise estimates of the mobility edge E_c . We have already started to try this technique. We have proved that we could improve the lifetime of the atoms in the disorder of $V_R/h = 416\text{ Hz}$ from 1.66 s to more than 7 s. But there was some technical problem with the ramp of the principal laser, which induced more excitation to the atoms. We have solved this problem recently and we will try again to see whether we can have a cleaner improvement of the lifetime or not.

7.4.2 Horizontal trap due to magnetic levitation

We mentioned in section 7.2 that we only measure the expansion of the atomic cloud in the disorder along the y-axis (vertical direction). The reason is due to the residual horizontal trap along the x- and z-axis induced by our magnetic levitation, and the corresponding trap frequency $\omega_\perp = \omega_{x,z}$ depends on the bias B_0 : $\omega_\perp \propto 1/\sqrt{B_0}$. With the magic magnetic field $B_0^* \simeq 3.23\text{G}$, the trap frequency $\omega_\perp \simeq 2\pi \times 7\text{ Hz}$. In the end, the expansion in the disorder is locally 3D in this condition. In order to perform the expansion which is completely 'free'(no trap) in the disorder in 3d, we have two possible solutions.

7.4.2.1 Open the trap by increasing the bias field

Since the trap frequency of the residual trap depends on the bias field as $\omega_\perp \propto 1/\sqrt{B_0}$, we can increase the bias field B_0 to reduce the trap frequency ω_\perp . We have discussed in chapter 3.11 the dependence of the trap frequency ω_\perp in function of B_0 in figure 3.17. We can estimate that by increasing the bias field B_0 from 3.23 G to about 2000 G, we can reduce the trap frequency ω_\perp from 7 Hz to about 0.3 Hz.

But in section 3.11, we have shown that to levitate the atoms by the magnetic gradient b' , we need to satisfy the levitation condition: $b' = \frac{mg}{m_F g_F, m_F \mu_B}$. Since the Landé factor

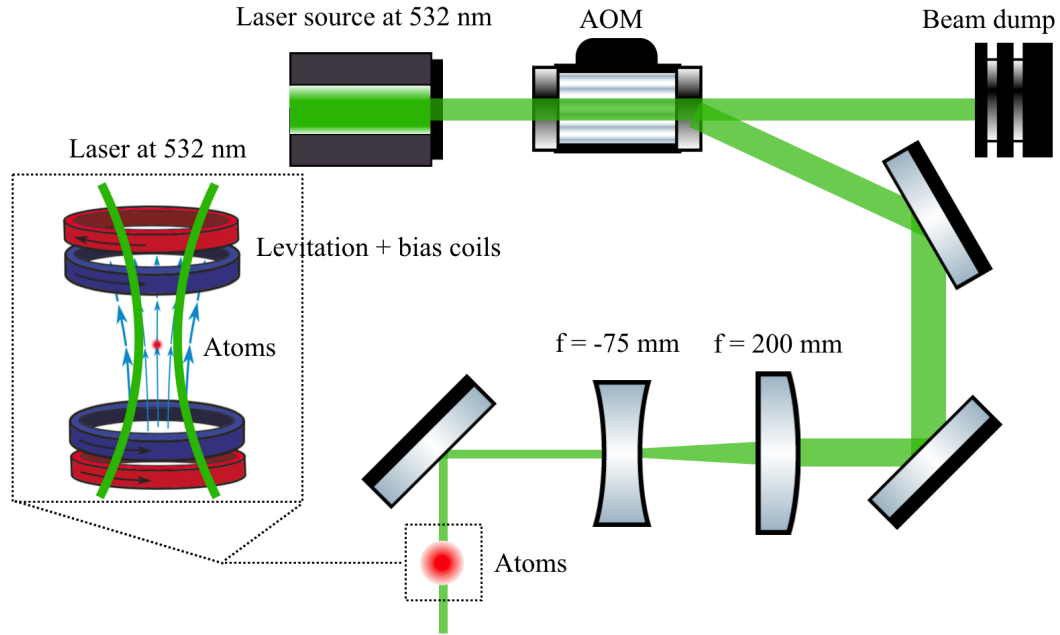


FIGURE 7.11: **Set-up of the anti-trap.** The laser comes from a source of high-power laser of 532 nm. The beam waist is about 1.125 mm. It is diffracted by an AOM, and the order 0 is shone into a beam dump for security. Then beam is shaped to have a small waist of about $420 \mu\text{m}$ by a telescope, and goes to the atoms. Near the atoms, the beam is along the y-axis (vertical direction), therefore the anti-trap is for the x- and z-axis.

g_{F,m_F} change with the bias B_0 , we need to adjust b' to keep the atoms levitated when increasing B_0 . Figure 3.16 shows the dependence of the gradient b' on the bias B_0 under the levitation condition.

7.4.2.2 Optical anti-trap

Another method to suppress the residual magnetic trap along the x- and z-axis is to shine a blue-detuned Gaussian beam along the y-axis to the atoms, as shown in figure 7.11. Since the beam is blue-detuned with respect to the atomic resonances, it produces a potential that gives an effect of anti-trapping on the atoms along the x- and z-axis. As shown in figure 7.12, by combining the quadratic magnetic trap and the Gaussian anti-trap, along the x- and z-axis, we can get a potential with a flat bottom where the atoms do not experience residual trapping effect.

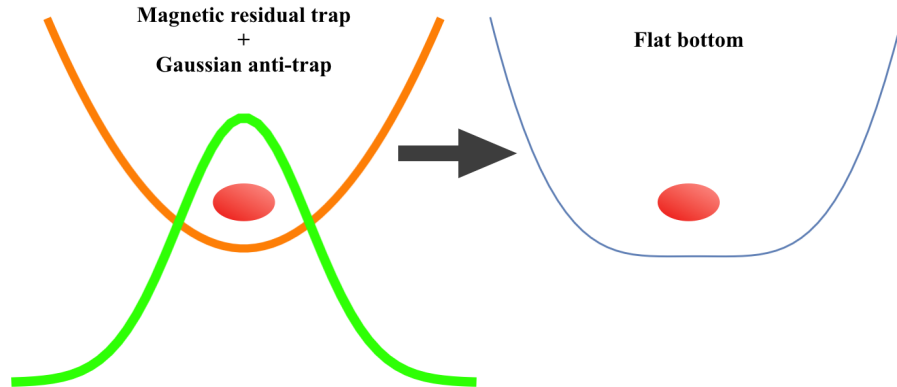


FIGURE 7.12: **Compensate the residual magnetic trap with a Gaussian anti-trap.** The orange line represents the residual magnetic trap along x and z direction, the green line represents the Gaussian anti-trap along x and z direction. The blue line is the total potential by combining the quadratic magnetic trap and Gaussian anti-trap.

In our experiment, as shown in figure 7.11, we use a laser at 532nm to do the anti-trap. The beam waist of the laser is about $1.125 \pm 10\%$ mm and can provide power of up to 18 W. We use an AOM to control the power of the beam. Then we use a telescope composed of a lens with $f = 200$ mm and a lens with $f = -75$ mm to reduce the beam waist w_0 to about $420 \mu\text{m}$ and shine it on the atoms. The potential V_{anti} generated by the Gaussian beam can be expanded up to the quartic term:

$$V_{\text{anti}}(x) = -\frac{1}{2}m\omega^2x^2 + m\omega^2\frac{x^4}{w_0^4} \quad (7.5)$$

where w_0 is the waist and ω is the frequency of the residual magnetic trap. The parameters of the Gaussian potential is set so that the quadratic term can cancel the harmonic potential of the residual magnetic trap. We can define that in the Gaussian potential, within a region of $w_0/2$, the quadratic term dominates over the quartic term so that the Gaussian potential can be well approximately seen as a harmonic potential. So the size of the flat region of the total potential can be about $\sim 210 \mu\text{m}$. That means the atoms can expand 'freely' (no trapping effect) in a flat region of about $\sim 210 \mu\text{m}$ in the disorder. Considering that in most cases of our measurement, the size of the diffusion of the cloud is within $80 \mu\text{m}$, so the flat region of $\sim 210 \mu\text{m}$ is large enough for our measurement of mobility edge.

7.5 Conclusion

Due to our bichromatic speckle scheme, we have improved the lifetime of the atoms in the disorder by two orders of magnitude. This improvement allows the atoms to expand in the disorder for a time scale of seconds, opening the possibility of exploring the transport properties of the atoms in the disorder. In this chapter, we have presented the preliminary results of our measurements toward the Anderson transition and mobility edge. We first show our direct measurement of the time evolution of the atomic profile at different energies in the speckle $V_R/h = 416\text{Hz}$. Using our bichromatic speckle scheme allows us to observe the long-time evolution for approximately 3s. Then we show our measurements of the size of the cloud after 2.11s of expansion at different energies for $V_R/h = 416\text{Hz}$ and $V_R/h = 832\text{Hz}$. The data provide the first hint for the Anderson transition. Our estimates of the mobility edge based on these data agree excellently with the numerical predictions of Pasek et al.[36]. We also analyze the decay of the central density of the atomic cloud and the sharp transition in figure 7.8 further shows the behavior of the Anderson transition, with an estimated mobility edge that agrees excellently with numerical predictions.

Overall, the excellent agreement of our preliminary results with the numerical predictions is very encouraging. However, it is important to note that there is still some imperfection in our results. Particularly, there is excitation present during the expansion that causes some fundamental diffusion for all the states, with high or low energies, which makes the distinction between the localized and diffusive regimes less clear. We suspect that the excitation is due to photon scattering and we provide a possible solution to improve the photon scattering lifetime of atoms.

Then we discussed the residual trap induced by our magnetic levitation, which may perturb our expansion of atoms in a larger 3D region. We have suggested two ideas to suppress the residual trap: open the trap by ramping the magnetic fields or use a blue-detuned laser beam to compensate for the residual magnetic trap.

We should admit that, although the data for $V_R/h = 416\text{Hz}$ and $V_R/h = 832\text{Hz}$ agree well with the numerical prediction, for lower amplitudes of disorder, such as $V_R/h \sim 121\text{Hz}$, we have not yet obtained similar agreement. The reason for the discrepancy is currently unclear and requires further investigation.

So to conclude, we have some encouraging results for $V_R/h = 416\text{Hz}$ and $V_R/h = 832\text{Hz}$, but there are some imperfections in our measurement and we have some clues to overcome the problems. Once our measurement of the mobility edge is more compelling, we will try to measure the mobility edge for more amplitudes of disorder V_R , especially for lower amplitudes of disorder.

Chapter 8

Conclusion and perspectives

In summary, this thesis presents a detailed study of the Anderson transition in 3D using ultracold atoms. Our team has proposed a spectroscopy to overcome the challenges of energy-resolved loading of atoms in disorder and has successfully measured the spectral function in 2018 [28]. However, the near-resonant speckle potential used in 2018 resulted in strong photon scattering of atoms in disorder, preventing further study of the Anderson transition. To address this issue, we proposed a bichromatic speckle potential composed of two lasers [88] and experimentally confirmed the state-dependence of the potential. We then used this potential to reproduce the spectral function as in 2018 and verified the improvement of the lifetime of atoms in disorder by two orders of magnitude.

Then we introduced our method to measure the mobility edge with the bichromatic speckle potential and presented preliminary experimental results, which provide the hint for the 3D Anderson transition. The mobility edge estimated based on our measurements showed excellent agreement with numerical predictions in Pasek et al.[36]. We also presented some imperfections in our data and we have provided possible solutions to improve the measurement. Overall, this work represents a significant advancement in the field of Anderson localization and ultracold atoms, and opens up new possibilities for future research.

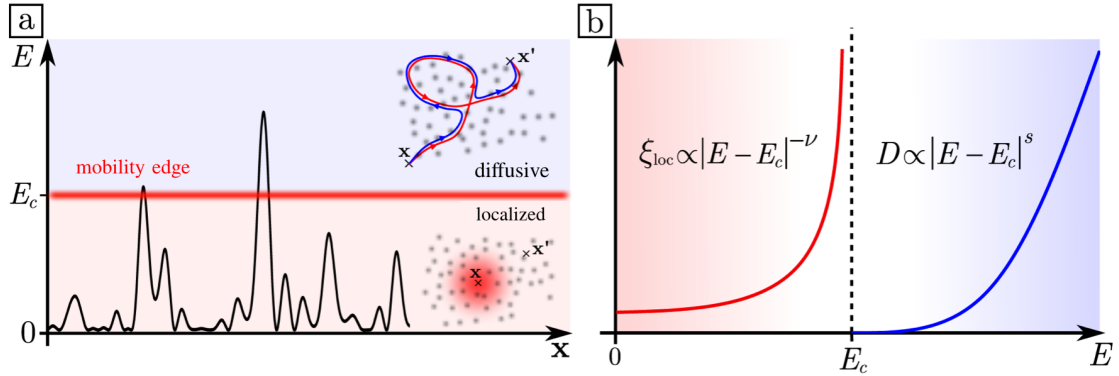


FIGURE 8.1: The same figure as in 2.5 in section 2.1.0.4.

8.1 Study near the critical regime

Once we locate the mobility edge, we can focus on the critical regime. Our energy-resolved loading of atoms in the disorder opens up the possibility to study the intriguing physics in this regime. Two key areas of interest for our research community include measuring the critical exponent and studying the multifractality of the wavefunction.

8.1.1 Critical exponent

In section 2.1.0.4, we introduced the scaling theory which can predict the Anderson transition in 3D. According to [43], the scaling theory predicts that near the critical regime, the localization length ξ_{loc} and the diffusion constant D follow a power law with respect to the energy E , with critical exponents ν and s , as shown in figure 8.1.

In our experiment, we can measure the time evolution of the r.m.s. of the cloud to estimate the diffusion constant D , according to $\langle \mathbf{x}^2 \rangle \propto Dt$. By obtaining the diffusion constants at different energies, fitted by $D \propto |E - E_c|^s$, we aim to estimate the critical exponent s . However, in figure 7.9, we observed that the unexpected excitations in our measurement caused similar diffusion constants D for all energies, from low to high energy states. Therefore, once we address this issue of the excitation, we expect to measure the diffusion constant in different energies and determine the critical exponent.

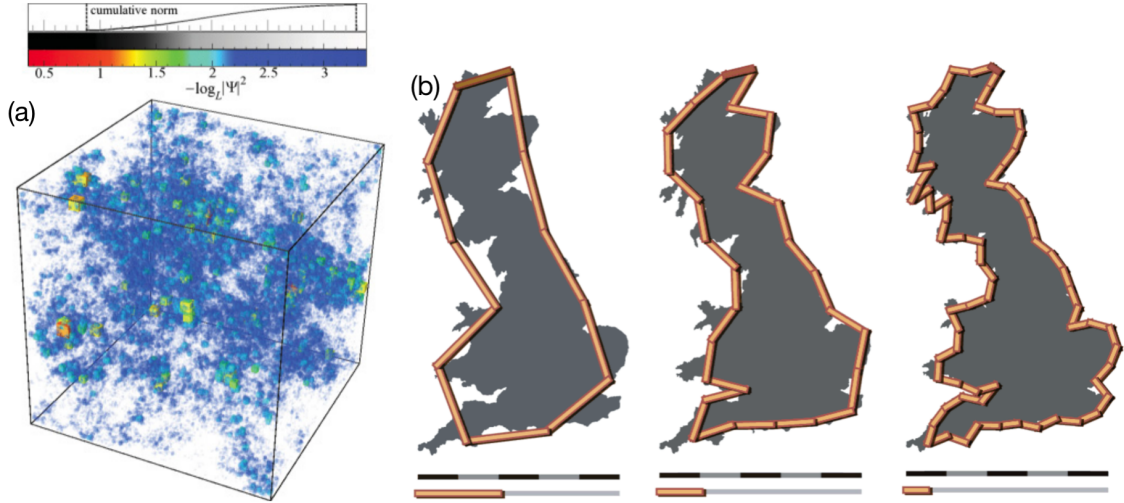


FIGURE 8.2: (a). Example of the wavefunction near the critical regime. The lines represents isovalue of $|\psi(\mathbf{x})|^2$. The figure is from [93]. (b). The example of fractal dimension. From left to right, the length of stick \mathcal{L} : 200 km, 100 km, 50 km, the length measured of the coastline \mathcal{C} : 2300 km, 2800 km, 3500 km.

8.1.2 Multi-fractality near the critical regime

It is predicted that near the mobility edge E_c , the wavefunction of the atoms in disorder $\psi(\mathbf{x})$ exhibits multi-fractal structure [90, 91, 92] and the probability of the atoms $|\psi(\mathbf{x})|^2$ presents large fluctuations in space, i.e., it can be unexpectedly large in some region and unexpectedly small in some other region as shown in figure 8.2 a.

First, we need to briefly introduce the concept of fractal dimension. It is an index used to quantify the complexity of fractal patterns by measuring the ratio of change in detail to change in scale. An example of this is shown in figure 8.2 b. When measuring the length of a coastline using a stick, we find that as the length of the measuring stick, \mathcal{L} , is scaled smaller and smaller, the total length of the coastline, \mathcal{C} , increases. This can be represented by the relationship $\mathcal{C} \sim \mathcal{L}^{-d}$, where d is the fractal dimension.

Figure 8.2 a shows an example of the wavefunction of atoms near the mobility edge of the Anderson transition. We can define such 'coastline' by connecting the isovalue of $|\psi(\mathbf{x})|^2$ and we can thus deduce the corresponding fractal dimension of these lines. It is shown theoretically that the wavefunction near the mobility edge of the Anderson transition presents a multi-fractal structure, and the fractal dimension d depends continuously on the isovalue of $|\psi(\mathbf{x})|^2$ [91, 94, 95, 96]. The ensemble of the fractal dimensions is called multifractality

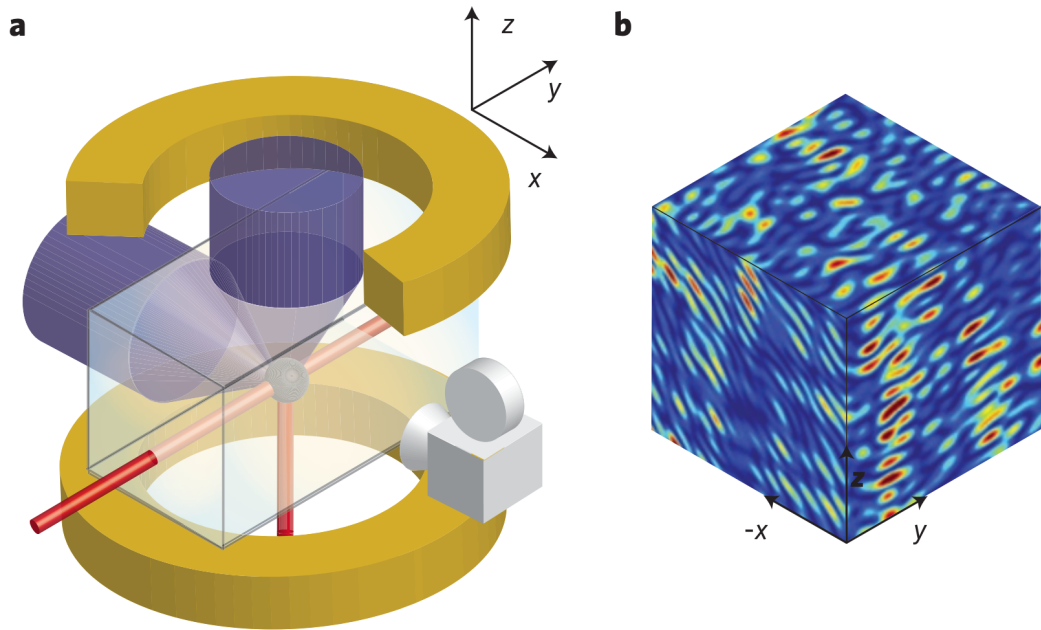


FIGURE 8.3: a. The schema of the experimental set-up of the two crossed speckle beams (blue beams in the figure). Yellow coils are the coils of magnetic gradient. b. False color representation of a realization of the disorder by the two crossed speckle.

spectrum.

Although tried in many experiments, a convincing measurement of the multifractal spectrum remains missing for lacking of energy resolution. In fact it is a very delicate task because the multifractal behavior is the property of a single eigenstate, so the mixture of eigenstates makes it hard to observe. Motivated by this bottleneck, Werner et al. [97] propose to use the spectroscopy method in a state-dependent disorder to address the critical state in a narrow energy window. That is exactly our experiment scheme.

8.2 Investigate various configurations of speckle

We can also perform the measurement of mobility edge with different speckle geometries. For example, as shown in figure 7.3, we can try the single speckle with different numerical apertures, leading to different anisotropy and different correlation energy E_σ . We can also try to use two-crossed speckle beams to generate a more isotropic disorder as what was

used in 2012 [33], as illustrated in figure 8.3. Measuring the mobility edge with different speckle geometries can test the universality of the scaling law of mobility edge versus the amplitude of disorder: $E_c/V_R = \mathcal{F}(V_R/E_\sigma)$ in figure 2.11.

Another interest of using an isotropic speckle is that we can have much higher correlation energy E_σ by one order of magnitude. That means the normalized amplitude of disorder V_R/E_σ can be much lower, thus, it is more convenient to investigate the quantum regime (low disorder), as the regime of the yellow data in figure 2.11 measured in Palaiseau[33] in 2012. In the experiment in 2012, with the two crossed speckle, with the correlation lengths of the speckle potential are: $\sigma_x = 0.11 \mu\text{m}$, $\sigma_y = 0.27 \mu\text{m}$, $\sigma_x = 0.08 \mu\text{m}$, resulting in a high correlation energy $E_\sigma \simeq 6.5 \text{ kHz}$. We can also investigate the red speckles, and the behaviors of the mobility edge in red speckle potential is predicted to be significantly different from that in blue ones [48]. We can also use a spatial light modulator to generate various disorder [98].

Appendix A

Optical evaporation

Remember that in section 3.9, we mention that to do the optical evaporation, we ramp down the laser power as:

$$P(t) = \frac{P_0}{(1 + t\tau)^\beta}. \quad (\text{A.1})$$

In this appendix, we explain why we use this ramp.

Note U the trap depth U , and T the temperature of the atoms. Define $\eta = \frac{U}{k_B T}$, when $\eta \gg 1$, the evaporation rate is proportional to $\Gamma_{el}(\eta - 4)e^{-\eta}$ [99], as shown in figure A.1, where Γ_{el} is the rate of elastic collision. If the trap depth U is a constant, then $\eta = \frac{U}{k_B T}$ will increase when the temperature of the atoms is getting lower. Thus the evaporation rate $\Gamma_{el}(\eta - 4)e^{-\eta}$ will decrease exponentially, thus, the evaporation becomes less and less

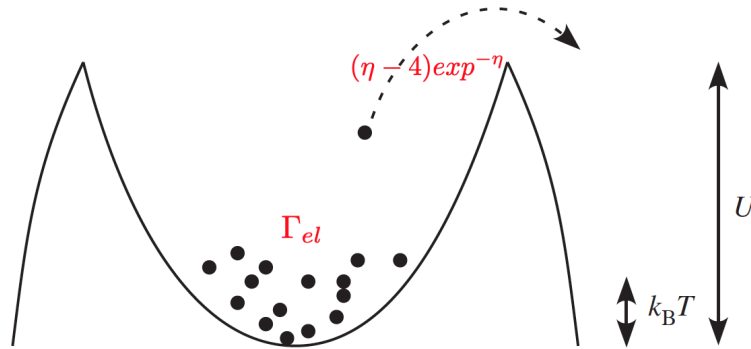


FIGURE A.1: **Evaporation induced by elastic collision.** The trap depth is U . The temperature of the gas in the trap is T . The elastic collision rate is Γ_{el} . The rate for a particle leaving the trap by elastic collision (evaporation rate) is $(\eta - 4)\exp(-\eta)$.

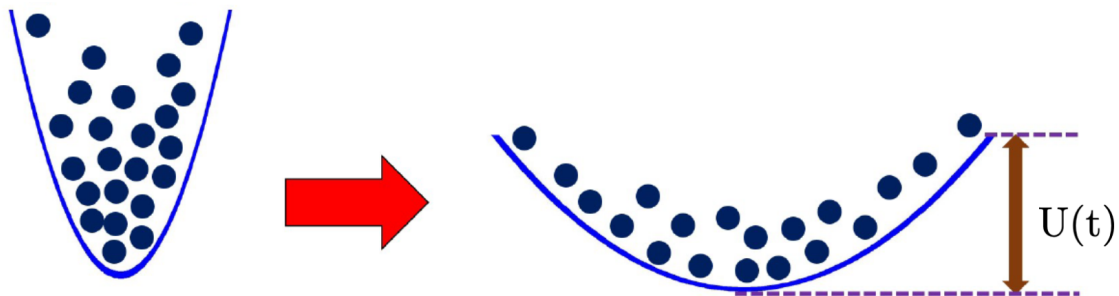


FIGURE A.2: **Decompression of optical trap.** For optical trap, the trap depth is proportional to the square of the trap frequency: $U \propto \omega^2$, so lowering the trap depth also decompresses the trap.

efficient and the time scale becomes larger than the experimental one. This mechanism is natural evaporation. Therefore, to keep the cooling efficiency always high enough along with the evaporation, we need to ramp down progressively the trap depth U , thus decreasing η . In optical evaporation, generally, η is about 10 and can be seen as a constant if the gas is kept at equilibrium.

Consider the loss of atoms $dN \ll N$, the loss of energy dE_1 of the gas due to the loss of atoms dN is:

$$dE_1 = dN(U + \kappa k_B T) = dN(\eta + \kappa)k_B T, \quad (\text{A.2})$$

where $\kappa k_B T$ represents the part of the energy in excess of the trap depth of the atom leaving the trap, and $\kappa = \frac{\eta-5}{\eta-4}$ for a 3-d deep harmonic trap [99].

For optical evaporation, both the trap depth and trap frequency are decided by laser power, so they are not independent. Therefore lowering the trap depth U will also lower the trap frequency ω simultaneously, thus decompressing the trap, as shown in figure A.2. We can quantify this correlation between the trap depth U and trap frequency ω by defining a quantity $\nu = \frac{\dot{\omega}/\omega}{\dot{U}/U}$. e.g. for optical dipole trap, $\omega \propto \sqrt{U}$, so $\nu = 1/2$. For the RF-evaporation in a magnetic trap, as we do in the cooling chamber before loading the optical tweezer, the trap frequency is given by the magnetic potential, the trap depth is truncated by the RF-knife. Hence, the trap frequency and depth can be independently controlled, so $\nu = 0$.

The decompression of the optical trap contributes another term for the loss of energy dE_2 :

$$dE_2 = \nu \frac{E}{T} dT \quad (\text{A.3})$$

where E is the total energy of the gas, T is the temperature of the gas.

By summing up the two contributions of the loss of energy dE_1 in equation A.2, and dE_2 in equation A.3, the total loss of energy dE is:

$$dE = N(\eta + \kappa)k_B T + \nu \frac{E}{T} dT. \quad (\text{A.4})$$

Now let us establish the equation describing the thermalization of the gas. The total energy of the trapped gas is:

$$E = 3Nk_B T, \quad (\text{A.5})$$

so the loss of energy can be expressed in function with the loss of atoms and the lowering of temperature:

$$dE = 3k_B T dN + 3Nk_B dT. \quad (\text{A.6})$$

The loss of energy in equation A.4 and in equation A.6 are equal:

$$N(\eta + \kappa)k_B T + \nu \frac{E}{T} dT = 3k_B T dN + 3Nk_B dT, \quad (\text{A.7})$$

and by reforming the equation, we get a scaling relation between the temperature T and atom number N :

$$\frac{dT}{T} = \alpha \frac{dN}{N}, \quad (\text{A.8})$$

where $\alpha = \frac{\eta + \kappa - 3}{3(1 - \nu)}$.

In harmonic trap with trap frequency ω , the phase-space density (PSD) is:

$$D = n_0 \lambda_{\text{dB}}^3 = \frac{N \hbar^3 \omega^3}{k_B^3 T^3}. \quad (\text{A.9})$$

We see that the phase-space density is in power law with the temperature. Recall the scaling relation between the temperature T and the atom number N , we can build the scaling law for the phase-space density and the atom number:

$$\frac{dD}{D} = -\gamma \frac{dN}{N}, \quad (\text{A.10})$$

where $\gamma = -(\eta + \kappa - 4)$. This γ is the efficiency of the evaporation, and shows how many atoms are lost when increasing the phase-space density.

The elastic collision rate between the atoms in the harmonic trap is:

$$\Gamma_{el} = \sqrt{\frac{2}{\pi}} n_0 \sigma \bar{v} = \frac{m\omega^3 \sigma N}{2\pi^2 k_B T}, \quad (\text{A.11})$$

where n_0 is the atomic density, σ is the cross section of the s-wave collision, \bar{v} is the average velocity of the atoms. Thus we have the scaling law of elastic collision rate and atom number:

$$\frac{d\Gamma_{el}}{\Gamma_{el}} = [1 - \alpha(1 - 3\nu)] \frac{dN}{N}. \quad (\text{A.12})$$

For $1 - \alpha(1 - 3\nu) > 0$, the elastic collision rate decreases with the loss of atoms. Therefore, during the evaporative cooling, the evaporation decelerates and becomes less efficient. Standard optical evaporation where $\nu = 1/2$ is an example.

On the contrary, for $1 - \alpha(1 - 3\nu) < 0$, the elastic collision rate increases along with the loss of atoms, so the evaporation accelerates and becomes more and more efficient. RF evaporation in a magnetic trap where $\nu = 0$ is an example.

The regime where evaporation accelerates is called *runaway* evaporative cooling. In optical evaporation, it is possible to control ν to accelerate the evaporation by controlling the optical trap with some special tilting [100] [101]. In our experiment, we do not tilt the optical trap, so our optical evaporation is standard optical evaporation where $\nu = 1/2$. Even though the elastic collision rate Γ_{el} decreases during the evaporation for the standard optical trap, the large value of Γ_{el} assures the evaporation is efficient enough. Generally, for RF-evaporation in a magnetic trap, the collision rate Γ_{el} is in the order of 10^2 s^{-1} . For optical evaporation, at the beginning of the evaporation, the starting collision rate Γ_{el} is in the order of 10^3 s^{-1} .

The time evolution of the atom number in the trap is:

$$\frac{dN}{dt} = -(\Gamma_{\text{evap}} + \Gamma_{1b} + \Gamma_{3b})N, \quad (\text{A.13})$$

where Γ_{evap} is the rate of the loss of atoms due to evaporation, Γ_{1b} is the rate of loss of atoms due to the collision of the atoms with the background gas in the vacuum and Γ_{3b} is the rate of three-body loss.

In our experiment, the pressure in the vacuum is about 1×10^{-11} mbar, and the lifetime of the atoms due to the collision with the background gas is measured to be more than 20 seconds. Our evaporation lasts about 2 seconds, so the loss due to collision with background gas (Γ_{1b}) can be neglected. The three-body loss (Γ_{3b}) is a nonlinear term, so it is hard to get an analytical form for this term. Three-body loss dominates only at the very beginning of evaporation when the atomic density is very high. In our 2s' evaporation, the effect of three-body loss can be neglected after ~ 300 ms. So in order to simplify the problem, we neglect this term. So the time evolution of the atom number can be written as :

$$\frac{dN}{dt} = -\Gamma_{\text{evap}}N = -\Gamma_{\text{el}}(\eta - 4)e^{-\eta}N. \quad (\text{A.14})$$

By solving this equation, we get the time evolution of atom number N :

$$N(t) = N_0 \left(1 + \frac{t}{\tau}\right)^{-b}, \quad (\text{A.15})$$

where a and b are constants associated with η . As we mentioned above, $\eta = \frac{U}{k_{\text{B}}T}$ can be supposed to be constant during the ramp, so $\frac{dU}{U} = \frac{dT}{T} = \alpha \frac{dN}{N}$, therefore, to keep the gas at equilibrium, we need to ramp the trap depth U as:

$$U(t) = U_0 \left(1 + \frac{t}{\tau}\right)^{-\beta}. \quad (\text{A.16})$$

Since trap depth is proportional to the power of the laser, $U \propto P$, the power of the laser should follow the same ramp given by equation A.16, and that explains why we ramp the power as the equation 3.20 in section 3.9.

Appendix B

Calculation of the normalized bichromatic correlation function

B.1 Bichromatic correlation function of the diffuser

Remind in section 4.1, we have introduced the monochromatic correlation function of the diffuser in equation 4.6:

$$C_{\text{diff}}(\mathbf{r}_0, \mathbf{r}'_0) = \overline{t_{\text{diff}}(\mathbf{r}_0)t_{\text{diff}}^*(\mathbf{r}'_0)} = \overline{e^{i(\phi(\mathbf{r}_0) - \phi(\mathbf{r}'_0))}}. \quad (\text{B.1})$$

Monochromatic correlation shows how the fluctuation of transmission through the diffuser of a laser with a single wavelength is correlated over the surface of the diffuser. There we define the bichromatic correlation function of the diffuser:

$$C_{\text{diff}}(\mathbf{r}_0, \mathbf{r}'_0, \lambda_p, \lambda_c) = \overline{t_{\text{diff}}(\mathbf{r}_0, \lambda_p)t_{\text{diff}}^*(\mathbf{r}'_0, \lambda_c)} = \overline{e^{i(\phi_p(\mathbf{r}_0) - \phi_c(\mathbf{r}'_0))}}. \quad (\text{B.2})$$

We can easily recover the monochromatic correlation function by setting $\lambda_p = \lambda_c$ in the bichromatic correlation function. Remind that in section 4.1, we have discussed that the fluctuation of the thickness of diffuser is Gaussian distributed with standard deviation σ_e , therefore the phase fluctuation introduced to the laser by passing through the diffuser is also Gaussian distributed with standard deviation $\sigma_\phi = 2\pi(n - 1)\sigma_e/\lambda$. Therefore the phase difference $\phi_p(\mathbf{r}_0) - \phi_c(\mathbf{r}'_0)$ in equation B.2 is Gaussian distribution as well and we

can calculate the bichromatic correlation $C_{\text{diff}}(\mathbf{r}_0, \mathbf{r}'_0, \lambda_p, \lambda_c)$:

$$\begin{aligned} C_{\text{diff}}(\mathbf{r}_0, \mathbf{r}'_0, \lambda_p, \lambda_c) &= \overline{t_{\text{diff}}(\mathbf{r}_0, \lambda_p) t_{\text{diff}}^*(\mathbf{r}'_0, \lambda_c)} = \overline{e^{i(\phi_p(\mathbf{r}_0) - \phi_c(\mathbf{r}'_0))}} \\ &= \exp \left[-2\pi^2 (n-1)^2 \sigma_e^2 \left(\frac{1}{\lambda_p^2} + \frac{1}{\lambda_c^2} \right) \right] \\ &\times \exp \left[4\pi^2 (n-1)^2 \frac{2}{\lambda_p \lambda_c} \overline{\delta e(\mathbf{r}_0) \delta e(\mathbf{r}'_0)} \right]. \end{aligned} \quad (\text{B.3})$$

As mentioned in section 4.1, the surface of the diffuser is considered to be extreme rough, and that leads to the condition $\sigma_e \gg \lambda$ (equivalently $\sigma_\phi \gg 2\pi$). The correlation of the thickness of diffuser $\overline{\delta e(\mathbf{r}_0) \delta e(\mathbf{r}'_0)}$ can be expressed as:

$$\frac{\overline{\delta e(\mathbf{r}_0) \delta e(\mathbf{r}'_0)}}{\sigma_1^2} \simeq 1 - \frac{(\mathbf{r}_0 - \mathbf{r}'_0)^2}{2r_e^2}, \quad (\text{B.4})$$

for $|\mathbf{r}_0 - \mathbf{r}'_0| \ll r_e$. r_1 is the correlation length of the thickness correlation of the diffuser and it characterizes the typical size of a grain in the surface of diffuser. Finally by substituting the expression of $\overline{\delta e(\mathbf{r}_0) \delta e(\mathbf{r}'_0)}$ into the bichromatic diffuser correlation function $C_{\text{diff}}(\mathbf{r}_0, \mathbf{r}'_0, \lambda_p, \lambda_c)$:

$$C_{\text{diff}}(\mathbf{r}_0, \mathbf{r}'_0, \lambda_p, \lambda_c) = \exp \left(-\frac{\sigma_{\Delta\phi}^2}{2} \right) \times \exp \left(-\frac{(\mathbf{r}_0 - \mathbf{r}'_0)^2}{2r_{\text{diff},p} r_{\text{diff},c}} \right), \quad (\text{B.5})$$

where $\sigma_{\Delta\phi}^2 = (\sigma_{\phi_p} - \sigma_{\phi_c})^2$ is the variance of the local phase difference $\Delta\phi(\mathbf{r}_0) = \phi_p(\mathbf{r}_0) - \phi_c(\mathbf{r}'_0)$, and r_{diff} has been defined in section 4.1, $r_{\text{diff}} = r_e / \sigma_\phi$ (σ_ϕ is different for principle and compensating lasers).

B.2 Correlation function of the amplitude

To approach the correlation of the intensity, we first need to calculate the correlation function of the amplitude. First, we consider the amplitude of a monochromatic laser passing through the diffuser and converged by a lens right before the diffuser, its amplitude at position $\mathbf{r}_d = \{x, y, z\}$ is:

$$E(\mathbf{r}_d) = \frac{e^{ikz}}{i\lambda z} \int d\mathbf{r}_0 E_{\text{inc}}(\mathbf{r}_0) t_{\text{diff}}(\mathbf{r}_0) \exp \left(-ik \frac{x_0^2 + y_0^2}{2f} \right) \exp \left(-ik \frac{(x - x_0)^2 + (y - y_0)^2}{2z} \right). \quad (\text{B.6})$$

In the expression, $E_{\text{inc}}(\mathbf{r}_0)$ is the amplitude of the incident laser, $t_{\text{diff}}(\mathbf{r}_0)$ is the transmission of the diffuser, the term $\exp \left(-ik \frac{x_0^2 + y_0^2}{2f} \right)$ is the phase mask of the converging lens, the

term $\exp\left(-ik\frac{(x-x_0)^2+(y-y_0)^2}{2z}\right)$ is the accumulation of the phase while propagation according to the principle of Fresnel diffraction.

Now we consider the general two-point correlation function of bichromatic speckle field, at position \mathbf{r} and \mathbf{r}' , for lasers with different wavelength λ_p and λ_c . The correlation function is expressed as:

$$\begin{aligned}\Gamma(\mathbf{r}, \mathbf{r}', \lambda_p, \lambda_c) &= \overline{E(\mathbf{r}', \lambda_c)E^*(\mathbf{r}, \lambda_p)} \\ &= \frac{e^{ik_p\left(\bar{z}+\frac{x^2+y^2}{2\bar{z}}\right)} e^{-ik_c\left(\bar{z}'+\frac{x'^2+y'^2}{2\bar{z}'}\right)}}{\lambda_p\lambda_c\bar{z}\bar{z}'} \\ &\times \int d\mathbf{r}_0 d\mathbf{r}'_0 t_{\text{diff}}(\mathbf{r}_0, \lambda_p) t_{\text{diff}}^*(\mathbf{r}'_0, \lambda_c) \\ &\times E_{\text{inc}}(\mathbf{r}_0, \lambda_c) E_{\text{inc}}^*(\mathbf{r}'_0, \lambda_p) \\ &\times e^{ik_p\frac{\mathbf{r}_0^2}{2d_{\text{eff}}}} e^{-ik_c\frac{\mathbf{r}'_0^2}{2d'_{\text{eff}}}} e^{-ik_p\frac{\mathbf{r}\cdot\mathbf{r}_0}{\bar{z}}} e^{ik_c\frac{\mathbf{r}'\cdot\mathbf{r}'_0}{\bar{z}'}},\end{aligned}\tag{B.7}$$

where the effective distance d_{eff} are defined with respect to the focal plane by $1/d_{\text{eff}} = 1/\bar{z} - 1/f$. $\bar{z} = z + f$ is the longitudinal distance compared to the diffuser (z being the distance only to the Fourier plane, so for the distance to the diffuser, we need to add f , see Fig 4.4). Actually, remind that the bichromatic correlation function of the diffuser is just $C_{\text{diff}}(\mathbf{r}_0, \mathbf{r}'_0, \lambda_p, \lambda_c) = \overline{t_{\text{diff}}(\mathbf{r}_0, \lambda_p) t_{\text{diff}}^*(\mathbf{r}'_0, \lambda_c)}$.

Then we change the variables $\{\mathbf{r}_0, \mathbf{r}'_0\} \rightarrow \{\mathbf{r}_{c,0} = (\mathbf{r}_0 + \mathbf{r}'_0)/2, \Delta\mathbf{r}_0 = \mathbf{r}'_0 - \mathbf{r}_0\}$, we obtain:

$$\begin{aligned}\Gamma(\mathbf{r}, \mathbf{r}', \lambda_p, \lambda_c) &= \frac{e^{ik_p\left(\bar{z}+\frac{x^2+y^2}{2\bar{z}}\right)} e^{-ik_c\left(\bar{z}'+\frac{x'^2+y'^2}{2\bar{z}'}\right)}}{\lambda_p\lambda_c\bar{z}\bar{z}'} \\ &\times \int d\mathbf{r}_{c,0} d\Delta\mathbf{r}_0 C_{\text{diff}}(\Delta\mathbf{r}_0, \lambda_p, \lambda_c) \\ &\times E_{\text{inc}}(\mathbf{r}_{c,0} - \Delta\mathbf{r}_0/2, \lambda_p) E_{\text{inc}}^*(\mathbf{r}_{c,0} + \Delta\mathbf{r}_0/2, \lambda_c) \\ &\times e^{i\mathbf{r}_{c,0}\left(\frac{k_c\mathbf{r}'}{\bar{z}'} - \frac{k_p\mathbf{r}}{\bar{z}}\right)} e^{i\frac{\Delta\mathbf{r}_0}{2}\left(\frac{k_p\mathbf{r}}{\bar{z}} + \frac{k_c\mathbf{r}'}{\bar{z}'}\right)} e^{i\frac{\mathbf{r}_{c,0}^2}{2}\left(\frac{k_p}{d_{\text{diff}}} - \frac{k_c}{d'_{\text{diff}}}\right)} \\ &\times e^{-i\frac{\Delta\mathbf{r}_0\cdot\mathbf{r}_{c,0}}{2}\left(\frac{k_p}{d_{\text{eff}}} + \frac{k_c}{d'_{\text{eff}}}\right)} e^{i\frac{\Delta\mathbf{r}_0^2}{8}\left(\frac{k_p}{d_{\text{eff}}} - \frac{k_c}{d'_{\text{eff}}}\right)}.\end{aligned}\tag{B.8}$$

Remind that $C_{\text{diff}}(\Delta\mathbf{r}_0, \lambda_p, \lambda_c) \propto \exp\left(-\frac{\Delta\mathbf{r}_0^2}{2r_{\text{diff},p}r_{\text{diff},c}}\right)$, so the typical width of C_{diff} is in the order of $r_{\text{diff},p}r_{\text{diff},c}$. As shown in section 4.1, r_{diff} represents a typical size of the grain, and it is very small. So the region of interest that we consider is $\Delta\mathbf{r} < r_{\text{diff},p}r_{\text{diff},c}$, so in this

regime, we can approximately suppose that: $E_{\text{inc}}(\mathbf{r}_{c,0} - \Delta\mathbf{r}_0/2, \lambda_p)E_{\text{inc}}^*(\mathbf{r}_{c,0} + \Delta\mathbf{r}_0/2, \lambda_c) \simeq E_{\text{inc}}(\mathbf{r}_{c,0}, \lambda_p)E_{\text{inc}}^*(\mathbf{r}_{c,0}, \lambda_c) = I(\mathbf{r}_0)$, $I(\mathbf{r}_0)$ being the incident illumination. Then we find:

$$\begin{aligned} \Gamma(\mathbf{r}, \mathbf{r}', \lambda_p, \lambda_c) &= \frac{e^{ik_p\left(\bar{z} + \frac{x^2+y^2}{2\bar{z}}\right)} e^{-ik_c\left(\bar{z}' + \frac{x'^2+y'^2}{2\bar{z}'}\right)}}{\lambda_p \lambda_c \bar{z} \bar{z}'} \\ &\times \int d\mathbf{r}_0 I(\mathbf{r}_0) e^{i\frac{\mathbf{r}_0^2}{2}\left(\frac{k_p}{d_{\text{eff}}} - \frac{k_c}{d'_{\text{eff}}}\right)} e^{i\mathbf{r}_0 \cdot \left(\frac{k_c \mathbf{r}'}{\bar{z}'} - \frac{k_p \mathbf{r}}{\bar{z}}\right)} \\ &\times \int d\Delta\mathbf{r}_0 C_{\text{diff}}(\Delta\mathbf{r}_0, \lambda_p, \lambda_c) e^{-i\frac{\Delta\mathbf{r}_0 \cdot \mathbf{r}_0}{2}\left(\frac{k_p}{d_{\text{eff}}} + \frac{k_c}{d'_{\text{eff}}}\right)} \\ &\times e^{i\frac{\Delta\mathbf{r}_0}{2}\left(\frac{k_p \mathbf{r}}{\bar{z}} + \frac{k_c \mathbf{r}'}{\bar{z}'}\right)}. \end{aligned} \quad (\text{B.9})$$

B.3 3D monochromatic correlation close to the Fourier plane

In this part, we will derive the expression of spatial autocorrelation function of monochromatic laser speckle field, in three dimension close to the Fourier plane. It will be used for the derivation of the bichromatic correlation function. The two point autocorrelation function is defined as:

$$c_{3D}(\Delta\mathbf{r}_\perp, \Delta z) = \frac{\overline{\delta I(\mathbf{r}_\perp + \Delta\mathbf{r}_\perp, z + \Delta z) \delta I(\mathbf{r}_\perp, z)}}{\overline{\delta I^2}}, \quad (\text{B.10})$$

with $\mathbf{r}_\perp = \{x, y\}$. Close to the Fourier plane, where $z = 0$, and close to the optical axis, where $\mathbf{r}_\perp = \mathbf{0}$, the numerator reads as $\overline{\delta I(\Delta\mathbf{r}_\perp, \Delta z) \delta I(\mathbf{0}, 0)}$, and is computed using Wick's theorem:

$$\begin{aligned} \overline{\delta I(\Delta\mathbf{r}_\perp, \Delta z) \delta I(\mathbf{0}, 0)} &= |\Gamma(\Delta\mathbf{r}_\perp, \Delta z)|^2 \\ &= \left| \overline{E_{\text{inc}}(\Delta\mathbf{r}_\perp, \Delta z) E_{\text{inc}}^*(\mathbf{0}, 0)} \right|^2 \\ &= \left| \frac{1}{\lambda^2 f^2} \int d\mathbf{r}_0 I(\mathbf{r}_0) e^{-i\frac{\mathbf{r}_0^2 k \Delta z}{2f^2}} e^{-i\frac{k\mathbf{r}_0 \cdot \Delta\mathbf{r}_\perp}{f}} \right. \\ &\quad \times \left. \int d\Delta\mathbf{r}_0 C_{\text{diff}}(\Delta\mathbf{r}_0) e^{i\frac{\Delta\mathbf{r}_0 \cdot \mathbf{r}_0 k \Delta z}{2f^2}} e^{i\frac{k\Delta\mathbf{r}_0 \cdot \Delta\mathbf{r}_\perp}{2f}} \right|^2 \end{aligned} \quad (\text{B.11})$$

As mentioned in the previous part, C_{diff} is a Gaussian distribution with width $\sim r_{\text{diff}}$, r_{diff} is very small, and as the result, the second integral is negligible compared to the first

integral. After normalization by $\left| \overline{I(\mathbf{0}, 0)} \right|^2$, and identifying a Fourier transform, we obtain:

$$c_{3D}(\Delta \mathbf{r}_\perp, \Delta z) = \frac{\left| \text{FT} \left[I(\mathbf{r}_0) e^{-i \frac{\mathbf{r}_0^2 k \Delta z}{2f^2}} \right] \right|_{\frac{k \Delta \mathbf{r}_\perp}{f}}^2}{\left| \int d\mathbf{r}_0 I(\mathbf{r}_0) \right|^2}. \quad (\text{B.12})$$

B.4 Bichromatic correlation function of the speckle

With all the element above, now we can consider the bichromatic correlation function $c_{2\lambda}(\mathbf{r}_\perp, z, \lambda_p, \lambda_c)$ between the two potentials created at different wavelength speckle pattern at a single point located by $\mathbf{r} = \{\mathbf{r}_\perp, z\}$ compared to the center of the Fourier plane. As discussed in equation 6.5, the correlation between the two speckles disorder potentials is:

$$c_{2\lambda}(\mathbf{r}, \lambda_p, \lambda_c) = \frac{\overline{\delta V_{p,1}(\mathbf{r}) \delta V_{c,1}(\mathbf{r})}}{\overline{V}_{p,1} \overline{V}_{c,1}}. \quad (\text{B.13})$$

We express it in intensity of the lasers:

$$c_{2\lambda}(\mathbf{r}_\perp, z, \lambda_p, \lambda_c) = \frac{\overline{\delta I(\mathbf{r}_\perp, z, \lambda_p) \delta I(\mathbf{r}_\perp, z, \lambda_c)}}{\overline{I(\mathbf{z}_\perp, z, \lambda_p) I(\mathbf{z}_\perp, z, \lambda_c)}}. \quad (\text{B.14})$$

In the equation above, we can compute the numerator $\overline{\delta I(\mathbf{r}_\perp, z, \lambda_p) \delta I(\mathbf{r}_\perp, z, \lambda_c)}$ using the Wick's theorem, then we have:

$$\overline{\delta I(\mathbf{r}_\perp, z, \lambda_p) \delta I(\mathbf{r}_\perp, z, \lambda_c)} = |\Gamma_{\mathcal{A}}(\mathbf{r}_\perp, z, \lambda_p, \lambda_c)|^2, \quad (\text{B.15})$$

with:

$$\begin{aligned} |\Gamma_{\mathcal{A}}(\mathbf{r}_\perp, z, \lambda_p, \lambda_c)|^2 &= \left| \overline{\mathcal{A}(\mathbf{r}_\perp, z, \lambda_p) \mathcal{A}^*(\mathbf{r}_\perp, z, \lambda_c)} \right|^2 \\ &= \left| \frac{1}{\lambda_p \lambda_c z^2} \int d\mathbf{r}_0 I(\mathbf{r}_0) e^{-i \frac{\mathbf{r}_0^2 z}{2f^2} (k_p - k_c)} \right. \\ &\quad \times e^{i \frac{\mathbf{r}_\perp \cdot \mathbf{r}_0}{f} (k_c - k_p)} \int d\Delta \mathbf{r}_0 C_{\text{diff}}(\Delta \mathbf{r}_0, \lambda_p, \lambda_c) \\ &\quad \left. \times e^{i \frac{\Delta \mathbf{r}_0 \cdot \mathbf{r}_0 z}{f^2} \frac{k_c + k_p}{2}} e^{i \frac{\Delta \mathbf{r}_0 \cdot \mathbf{r}_\perp}{f^2} \frac{k_c + k_p}{2}} \right|. \end{aligned} \quad (\text{B.16})$$

Using (i) the same approximation as in equation B.11 for the phase exponentials in the second integral, (ii) the normalization by the average intensity profile around the center

$|\overline{I(\mathbf{0}, 0)}|^2$, and (iii) $\delta\lambda = |\lambda_c - \lambda_p| \ll \lambda_{p,c} \sim \lambda$, we obtain:

$$\begin{aligned}
& c_{2\lambda}(\mathbf{r}_\perp, z, \lambda_p, \lambda_c) \\
&= \frac{|\int d\Delta\mathbf{r}_0 C_{\text{diff}}(\Delta\mathbf{r}_0, \lambda_p, \lambda_c)|^2}{\int d\Delta\mathbf{r}_0 C_{\text{diff}}(\Delta\mathbf{r}_0, \lambda_p) \int d\Delta\mathbf{r}_0 C_{\text{diff}}(\Delta\mathbf{r}_0, \lambda_c)} \\
&\times \frac{\left| \int d\mathbf{r}_0 I(\mathbf{r}_0) e^{-ik\frac{\mathbf{r}_0^2 z}{2f^2} \frac{\delta\lambda}{\lambda}} e^{ik\frac{\mathbf{r}_\perp \cdot \mathbf{r}_0}{f} \frac{\delta\lambda}{\lambda}} \right|^2}{\int |d\mathbf{r}_0 I(\mathbf{r}_0)|^2}
\end{aligned} \tag{B.17}$$

consisting of two terms. The first one features the decorrelation effect induced by the diffuser, and the second one features the effect of the free space propagation after the diffuser. The first term can be computed as:

$$\int d\Delta\mathbf{r}_0 C_{\text{diff}}(\Delta\mathbf{r}_0, \lambda) = 2\pi r_{\text{diff}}^2. \tag{B.18}$$

Thus at the end, the normalized bichromatic correlation function reads as:

$$\begin{aligned}
& c_{2\lambda}(\mathbf{r}_\perp, z, \lambda_p, \lambda_c) \\
&= C_{\text{diff}}^2(\mathbf{0}, \lambda_p, \lambda_c) \frac{\left| \text{FT} \left[I(\mathbf{r}_0) e^{-ik\frac{\mathbf{r}_0^2 z}{2f^2}} \right]_{\frac{k\mathbf{r}_\perp}{f} \frac{\delta\lambda}{\lambda}} \right|^2}{\left| \int d\mathbf{r}_0 I(\mathbf{r}_0) \right|^2} \\
&= e^{-\sigma_{\Delta\phi}^2} c_{3D} \left(\mathbf{r}_\perp \frac{\delta\lambda}{\lambda}, z \frac{\delta\lambda}{\lambda} \right).
\end{aligned} \tag{B.19}$$

Appendix C

Green function

The Hamiltonian of a quantum particle in a disordered potential can be written as:

$$\hat{\mathcal{H}} = \hat{\mathcal{H}}_0 + \hat{V}, \quad (\text{C.1})$$

where \hat{V} is the disordered potential and $\hat{\mathcal{H}}_0$ is the kinetic energy whose eigenstates are momentum states $\{|\mathbf{k}\rangle\}$

If the Hamiltonian is time-independent, the evolution of wave function $\Psi(\mathbf{x}, t)$ can be written as:

$$\begin{aligned} \Psi(\mathbf{x}, t) &= \langle \mathbf{x} | \Psi(t) \rangle \\ &= \langle \mathbf{x} | e^{-it\hat{\mathcal{H}}/\hbar} | \Psi(t=0) \rangle \\ &= \int d\mathbf{x}' \langle \mathbf{x} | e^{-it\hat{\mathcal{H}}/\hbar} | \mathbf{x}' \rangle \langle \mathbf{x}' | \Psi(t=0) \rangle \\ &= \int d\mathbf{x}' \mathcal{G}(\mathbf{x}', \mathbf{x}, t) \Psi(\mathbf{x}', t=0). \end{aligned} \quad (\text{C.2})$$

We see that the solution for the wave function $\Psi(\mathbf{x}, t)$ at time t is just a convolution between the initial wave function $\Psi(\mathbf{x}', t=0)$ and the function connecting the initial and the final state $\mathcal{G}(\mathbf{x}', \mathbf{x}, t)$. This function $\mathcal{G}(\mathbf{x}', \mathbf{x}, t)$ is *Green function*. Green function is very useful to describe the evolution of quantum systems. It represents the amplitude of the quantum path of the particle initially at position $|\mathbf{x}'\rangle$ being detected at position $|\mathbf{x}\rangle$ after a time of evolution t , under the Hamiltonian $\hat{\mathcal{H}}$. By Fourier transform, we get the Green function in the domain of energy:

$$\hat{\mathcal{G}}(E) = \frac{1}{E - \hat{\mathcal{H}} + i0^+}. \quad (\text{C.3})$$

For a free particle, the Hamiltonian $\hat{\mathcal{H}}_0$ is only kinetic energy, and the eigenstates are momentum $\{|\mathbf{k}\rangle\}$. The Green function operator $\hat{\mathcal{G}}_0$ for the free particle is:

$$\hat{\mathcal{G}}_0 = \frac{1}{E - \hat{\mathcal{H}}_0 + i0^+}. \quad (\text{C.4})$$

We can express the Green function for the free particle in the base of momentum $\{|\mathbf{k}\rangle\}$:

$$\mathcal{G}_0(\mathbf{k}, E) = \langle \mathbf{k} | \hat{\mathcal{G}}_0(E) | \mathbf{k} \rangle = \frac{1}{E - \varepsilon_{\mathbf{k}} + i0^+}, \quad (\text{C.5})$$

where $\varepsilon_{\mathbf{k}} = \frac{\hbar^2 \mathbf{k}^2}{2m}$ is the dispersion for a free particle.

Now let us add the disordered potential. By replacing the Hamiltonian $\hat{\mathcal{H}} = \hat{\mathcal{H}}_0 + \hat{V}$ in the Green function operator in equation C.3, the Green function can be demonstrated to be the solution of Dyson equation written in the base of momentum $\{|\mathbf{k}\rangle\}$:

$$\mathcal{G}(\mathbf{k}, E) = \mathcal{G}_0(\mathbf{k}, E) + \mathcal{G}_0(\mathbf{k}, E) \hat{V} \mathcal{G}(\mathbf{k}, E). \quad (\text{C.6})$$

This iteration equation allows us to define a quantity called *self-energy* $\Sigma(\mathbf{k}, E)$:

$$\mathcal{G}(\mathbf{k}, E) = \mathcal{G}_0(\mathbf{k}, E) + \mathcal{G}_0(\mathbf{k}, E) \Sigma(\mathbf{k}, E) \mathcal{G}_0(\mathbf{k}, E), \quad (\text{C.7})$$

where the self-energy $\Sigma(\mathbf{k}, E)$ is:

$$\Sigma(\mathbf{k}, E) = \sum \langle \mathbf{k} | \hat{V} (\hat{\mathcal{G}}_0(E) \hat{V})^n | \mathbf{k} \rangle. \quad (\text{C.8})$$

Then with the help of the self-energy $\Sigma(\mathbf{k}, E)$, the Green function can be expressed as:

$$\mathcal{G}(\mathbf{k}, E) = \frac{1}{E - \varepsilon_{\mathbf{k}} - \Sigma(\mathbf{k}, E)}. \quad (\text{C.9})$$

The information of how the interaction between the particle and the disordered potential is encoded in the self-energy $\Sigma(\mathbf{k}, E)$. The interaction of the particle and the disordered potential induces an energy shift of the particle and a broadening of the spectrum of energy. We see in the next section how these effects are encoded in the self-energy.

Bibliography

- [1] Baptiste Lecoutre, Yukun Guo, Xudong Yu, M Niranjan, Musawwadah Mukhtar, Valentin V Volchkov, Alain Aspect, and Vincent Josse. Bichromatic state-dependent disordered potential for anderson localization of ultracold atoms. *The European Physical Journal D*, 76(11):1–15, 2022.
- [2] Philip W Anderson. Absence of diffusion in certain random lattices. *Physical review*, 109(5):1492, 1958.
- [3] YUEQIANG GUXIAO CHENXINBO WANGSHIFENG JINLINLIN ZHAOWEI ZHANGAND XIAOLONG CHEN TIANPING YING. Anderson localization of electrons in single crystals: Lixfe7se8. *Science advance*, 2:2, 2016.
- [4] I. Shlimak, M. Kaveh, R. Ussyshkin, V. Ginodman, and L. Resnick. Determination of the critical conductivity exponent for the metal-insulator transition at nonzero temperatures: Universality of the transition. *Phys. Rev. Lett.*, 77:1103–1106, Aug 1996.
- [5] G. A. Thomas M. A. Paalanen, T. F. Rosenbaum and R. N. Bhatt. Critical scaling of the conductance in a disordered insulator. *Physical review letter*, 51:1896, 1983.
- [6] H Volker M Woda P Merkelbach C Schlockermann M Wuttig T Siegrist 1, P Jost. Disorder-induced localization in crystalline phase-change materials. *Nat Mater*, 10(3):202–8, 2011.
- [7] Diederik S Wiersma, Paolo Bartolini, Ad Lagendijk, and Roberto Righini. Localization of light in a disordered medium. *Nature*, 390(6661):671–673, 1997.
- [8] Martin Störzer, Peter Gross, Christof M Aegerter, and Georg Maret. Observation of the critical regime near anderson localization of light. *Physical review letters*, 96(6):063904, 2006.

-
- [9] Yoav Lahini, Assaf Avidan, Francesca Pozzi, Marc Sorel, Roberto Morandotti, Demetrios N Christodoulides, and Yaron Silberberg. Anderson localization and non-linearity in one-dimensional disordered photonic lattices. *Physical Review Letters*, 100(1):013906, 2008.
- [10] Tal Schwartz, Guy Bartal, Shmuel Fishman, and Mordechai Segev. Transport and anderson localization in disordered two-dimensional photonic lattices. *Nature*, 446(7131):52–55, 2007.
- [11] Mordechai Segev, Yaron Silberberg, and Demetrios N Christodoulides. Anderson localization of light. *Nature Photonics*, 7(3):197–204, 2013.
- [12] A. Z. Genack and N. Garcia. Observation of photon localization in a three-dimensional disordered system. *Phys. Rev. Lett.*, 66:2064–2067, Apr 1991.
- [13] Alexander Figotin and Abel Klein. Localization of classical waves i: Acoustic waves. *Communications in mathematical physics*, 180(2):439–482, 1996.
- [14] Hefei Hu, A Strybulevych, JH Page, Sergey E Skipetrov, and Bart A van Tiggelen. Localization of ultrasound in a three-dimensional elastic network. *Nature Physics*, 4(12):945–948, 2008.
- [15] Richard L Weaver. Anderson localization of ultrasound. *Wave motion*, 12(2):129–142, 1990.
- [16] Ad Lagendijk Roberto Righini Diederik S. Wiersma, Paolo Bartolini. Anderson localization of ultrasound. *Wave motion*, 12:97–195, 1990.
- [17] Ling Ye, George Cody, Minyao Zhou, Ping Sheng, and Andrew N. Norris. Observation of bending wave localization and quasi mobility edge in two dimensions. *Phys. Rev. Lett.*, 69:3080–3083, Nov 1992.
- [18] M. H. ANDERSON J. R. ENSHERM. R. MATTHEWSC. E. WIEMAN AND E. A. CORNELL. Observation of bose-einstein condensation in a dilute atomic vapor. *Science*, 269:198–201, 1995.
- [19] K. B. Davis, M. O. Mewes, M. R. Andrews, N. J. van Druten, D. S. Durfee, D. M. Kurn, and W. Ketterle. Bose-einstein condensation in a gas of sodium atoms. *Phys. Rev. Lett.*, 75:3969–3973, Nov 1995.
- [20] Tilman Esslinger Theodor W. Hänsch Immanuel Bloch Markus Greiner, Olaf Mandel. Quantum phase transition from a superfluid to a mott insulator in a gas of ultracold atoms. *Nature*, 415:39–44, 2002.

-
- [21] Immanuel Bloch, Jean Dalibard, and Sylvain Nascimbene. Quantum simulations with ultracold quantum gases. *Nature Physics*, 8(4):267–276, 2012.
- [22] Cheng Chin, Rudolf Grimm, Paul Julienne, and Eite Tiesinga. Feshbach resonances in ultracold gases. *Reviews of Modern Physics*, 82(2):1225, 2010.
- [23] Jacob F Sherson, Christof Weitenberg, Manuel Endres, Marc Cheneau, Immanuel Bloch, and Stefan Kuhr. Single-atom-resolved fluorescence imaging of an atomic mott insulator. *Nature*, 467(7311):68–72, 2010.
- [24] Waseem S Bakr, Jonathon I Gillen, Amy Peng, Simon Fölling, and Markus Greiner. A quantum gas microscope for detecting single atoms in a hubbard-regime optical lattice. *Nature*, 462(7269):74–77, 2009.
- [25] R Chang, Q Bouton, H Cayla, C Qu, Alain Aspect, CI Westbrook, and D Clément. Momentum-resolved observation of thermal and quantum depletion in a bose gas. *Physical review letters*, 117(23):235303, 2016.
- [26] CA Regal, M Greiner, S Giorgini, M Holland, and DS Jin. Momentum distribution of a fermi gas of atoms in the bcs-bec crossover. *Physical review letters*, 95(25):250404, 2005.
- [27] Tom Jelte, John M McNamara, Wim Hogervorst, Wim Vassen, Valentina Krachmalnicoff, Martijn Schellekens, Aurélien Perrin, Hong Chang, Denis Boiron, Alain Aspect, et al. Comparison of the hanbury brown–twiss effect for bosons and fermions. *Nature*, 445(7126):402–405, 2007.
- [28] Valentin V Volchkov, Michael Pasek, Vincent Denechaud, Musawwadah Mukhtar, Alain Aspect, Dominique Delande, and Vincent Josse. Measurement of spectral functions of ultracold atoms in disordered potentials. *Physical Review Letters*, 120(6):060404, 2018.
- [29] Alain Aspect and Massimo Inguscio. Anderson localization of ultracold atoms. *Phys. Today*, 62(8):30, 2009.
- [30] Yurii B Ovchinnikov Rudolf Grimm, Matthias Weidemüller. Optical dipole traps for neutral atoms. 42:95–170, 2000.
- [31] Zhanchun Zuo Alain Bernard Ben Hambrecht Pierre Lugan David Clément Laurent Sanchez-Palencia Philippe Bouyer Alain Aspect Juliette Billy, Vincent Josse. Direct observation of anderson localization of matter waves in a controlled disorder. *Nature*, 453:891–894, 2008.

-
- [32] Leonardo Fallani Marco Fattori Chiara Fort Matteo Zaccanti Giovanni Modugno Michele Modugno Massimo Inguscio Giacomo Roati, Chiara D’Errico. Anderson localization of a non-interacting bose–einstein condensate. *Nature*, 453:895–898, 2008.
- [33] Fred Jendrzejewski, Alain Bernard, Killian Mueller, Patrick Cheinet, Vincent Josse, Marie Piraud, Luca Pezzé, Laurent Sanchez-Palencia, Alain Aspect, and Philippe Bouyer. Three-dimensional localization of ultracold atoms in an optical disordered potential. *Nature Physics*, 8(5):398–403, 2012.
- [34] P. Castilho S. Roy G. Spagnolli A. Trenkwalder M. Fattori M. Inguscio G. Modugno G. Semeghini, M. Landini. Measurement of the mobility edge for 3d anderson localization. *Nature Physics*, 11:554–559, 2015.
- [35] SS Kondov, WR McGehee, JJ Zirbel, and B DeMarco. Three-dimensional anderson localization of ultracold matter. *Science*, 334(6052):66–68, 2011.
- [36] Michael Pasek, Giuliano Orso, and Dominique Delande. Anderson localization of ultracold atoms: Where is the mobility edge? *Phys. Rev. Lett.*, 118:170403, Apr 2017.
- [37] Hans Fischer. *A history of the central limit theorem: from classical to modern probability theory*. Springer, 2011.
- [38] Eric Akkermans and Gilles Montambaux. *Mesoscopic physics of electrons and photons*. Cambridge university press, 2007.
- [39] Cord A Müller and Dominique Delande. Disorder and interference: localization phenomena. *arXiv preprint arXiv:1005.0915*, 2010.
- [40] Donald H White, Thomas A Haase, Dylan J Brown, Maarten D Hoogerland, Mojdeh S Najafabadi, John L Helm, Christopher Gies, Daniel Schumayer, and David AW Hutchinson. Observation of two-dimensional anderson localisation of ultracold atoms. *Nature communications*, 11(1):1–8, 2020.
- [41] AF Ioffe and AR Regel. Non-crystalline, amorphous and liquid electronic semiconductors. *Prog. Semicond*, 4(89):237–291, 1960.
- [42] JT Edwards and DJ Thouless. Numerical studies of localization in disordered systems. *Journal of Physics C: Solid State Physics*, 5(8):807, 1972.

-
- [43] E. Abrahams, P. W. Anderson, D. C. Licciardello, and T. V. Ramakrishnan. Scaling theory of localization: Absence of quantum diffusion in two dimensions. *Phys. Rev. Lett.*, 42:673–676, Mar 1979.
- [44] Yoichi Asada, Keith Slevin, and Tomi Ohtsuki. Anderson transition in two-dimensional systems with spin-orbit coupling. *Physical review letters*, 89(25):256601, 2002.
- [45] BL Altshuller, AG Aronov, and DE Khmelnitsky. Suppression of localization effects by the high frequency field and the nyquist noise. *Solid State Communications*, 39(5):619–623, 1981.
- [46] Jian Wei, S Pereverzev, and ME Gershenson. Microwave-induced dephasing in one-dimensional metal wires. *Physical review letters*, 96(8):086801, 2006.
- [47] Keith Slevin and Tomi Ohtsuki. Critical exponent for the anderson transition in the three-dimensional orthogonal universality class. *New Journal of Physics*, 16(1):015012, 2014.
- [48] Benoit Vermersch, Dominique Delande, and Jean Claude Garreau. Anderson transition of bogoliubov quasiparticles in the quasiperiodic kicked rotor. *arXiv preprint arXiv:1410.2587*, 2014.
- [49] Fritz Haake. Quantum signatures of chaos. 3. rev. and enl. 2010.
- [50] Giulio Casati, Italo Guarneri, and DL Shepelyansky. Anderson transition in a one-dimensional system with three incommensurate frequencies. *Physical review letters*, 62(4):345, 1989.
- [51] Rachida Dalichaouch, JP Armstrong, Sheldon Schultz, PM Platzman, and SL McCall. Microwave localization by two-dimensional random scattering. *Nature*, 354(6348):53–55, 1991.
- [52] AA Chabanov, M Stoytchev, and AZ Genack. Statistical signatures of photon localization. *Nature*, 404(6780):850–853, 2000.
- [53] Sergey E Skipetrov and Igor M Sokolov. Absence of anderson localization of light in a random ensemble of point scatterers. *Physical review letters*, 112(2):023905, 2014.
- [54] F. Jendrzejewski, K. Müller, J. Richard, A. Date, T. Plisson, P. Bouyer, A. Aspect, and V. Josse. Coherent backscattering of ultracold atoms. *Phys. Rev. Lett.*, 109:195302, Nov 2012.

-
- [55] K. Müller, J. Richard, V. V. Volchkov, V. Denechaud, P. Bouyer, A. Aspect, and V. Josse. Suppression and revival of weak localization through control of time-reversal symmetry. *Phys. Rev. Lett.*, 114:205301, May 2015.
- [56] Shmuel Fishman, DR Grempel, and RE Prange. Chaos, quantum recurrences, and anderson localization. *Physical Review Letters*, 49(8):509, 1982.
- [57] R Graham, M Schlautmann, and P Zoller. Dynamical localization of atomic-beam deflection by a modulated standing light wave. *Physical Review A*, 45(1):R19, 1992.
- [58] FL Moore, JC Robinson, CF Bharucha, Bala Sundaram, and MG Raizen. Atom optics realization of the quantum δ -kicked rotor. *Physical Review Letters*, 75(25):4598, 1995.
- [59] Julien Chabé, Gabriel Lemarié, Benoît Grémaud, Dominique Delande, Pascal Szriftgiser, and Jean Claude Garreau. Experimental observation of the anderson metal-insulator transition with atomic matter waves. *Physical review letters*, 101(25):255702, 2008.
- [60] Gabriel Lemarié, Julien Chabé, Pascal Szriftgiser, Jean Claude Garreau, Benoît Grémaud, and Dominique Delande. Observation of the anderson metal-insulator transition with atomic matter waves: Theory and experiment. *Physical Review A*, 80(4):043626, 2009.
- [61] J A Retter¹ L Sanchez-Palencia¹ A Aspect¹ D Clément¹, A F Varón¹ and P Bouyer. Experimental study of the transport of coherent interacting matter-waves in a 1d random potential induced by laser speckle. *New journal of physics*, 8:165, 2006.
- [62] Cord A. Müller and Boris Shapiro. Comment on “three-dimensional anderson localization in variable scale disorder”. *Phys. Rev. Lett.*, 113:099601, Aug 2014.
- [63] Joseph W Goodman. *Speckle phenomena in optics: theory and applications*. Roberts and Company Publishers, 2007.
- [64] Christopher J Pethick and Henrik Smith. *Bose–Einstein condensation in dilute gases*. Cambridge university press, 2008.
- [65] Franco Dalfovo, Stefano Giorgini, Lev P Pitaevskii, and Sandro Stringari. Theory of bose-einstein condensation in trapped gases. *Reviews of modern physics*, 71(3):463, 1999.
- [66] Eugene P Gross. Structure of a quantized vortex in boson systems. *Il Nuovo Cimento (1955-1965)*, 20(3):454–477, 1961.

-
- [67] Lev P Pitaevskii. Vortex lines in an imperfect bose gas. *Sov. Phys. JETP*, 13(2):451–454, 1961.
- [68] Daniel A Steck. Rubidium 87 d line data. 2001.
- [69] Alain Bernard. *Transport quantique d’ondes atomiques ultrafroides: localisation d’Anderson et laser à atomes guidé*. PhD thesis, Université Pierre et Marie Curie-Paris VI, 2010.
- [70] Gregory Breit and II Rabi. Measurement of nuclear spin. *Physical Review*, 38(11):2082, 1931.
- [71] Jean Dalibard. Une brève histoire des atomes froids. *Cours du Collège de France*, 143, 2015.
- [72] Eric L Raab, Mara Prentiss, Alex Cable, Steven Chu, and David E Pritchard. Trapping of neutral sodium atoms with radiation pressure. *Physical review letters*, 59(23):2631, 1987.
- [73] Marie Fauquembergue. *Réalisation d’un dispositif de condensation de Bose-Einstein et de transport d’un échantillon cohérent d’atomes*. PhD thesis, Université Paris Sud-Paris XI, 2004.
- [74] David E Pritchard. Cooling neutral atoms in a magnetic trap for precision spectroscopy. *Physical Review Letters*, 51(15):1336, 1983.
- [75] Vincent Denechaud. *Vers une étude spectroscopique de la transition d’Anderson*. PhD thesis, Université Paris-Saclay (ComUE), 2018.
- [76] Jeremie Richard. *Propagation d’atomes ultra-froids en milieu désordonné-Étude dans l’espace des impulsions de phénomènes de diffusion et de localisation*. PhD thesis, Université Paris Saclay (COMUE), 2015.
- [77] M I Trappe, D Delande, and C A Müller. Semiclassical spectral function for matter waves in random potentials. *Journal of Physics A: Mathematical and Theoretical*, 48(24):245102, may 2015.
- [78] Tony Prat, Nicolas Cherroret, and Dominique Delande. Semiclassical spectral function and density of states in speckle potentials. *Phys. Rev. A*, 94:022114, Aug 2016.
- [79] Pierre Pelletier, Dominique Delande, Vincent Josse, Alain Aspect, Svitlana Mayboroda, Douglas N. Arnold, and Marcel Filoche. Spectral functions and localization-landscape theory in speckle potentials. *Phys. Rev. A*, 105:023314, Feb 2022.

-
- [80] Gilbert Grynberg, Alain Aspect, and Claude Fabre. *Introduction to quantum optics: from the semi-classical approach to quantized light*. Cambridge university press, 2010.
- [81] Ivan H. Deutsch and Poul S. Jessen. Quantum-state control in optical lattices. *Phys. Rev. A*, 57:1972–1986, Mar 1998.
- [82] Olaf Mandel, Markus Greiner, Artur Widera, Tim Rom, Theodor W. Hänsch, and Immanuel Bloch. Coherent transport of neutral atoms in spin-dependent optical lattice potentials. *Phys. Rev. Lett.*, 91:010407, Jul 2003.
- [83] Bryce Gadway, Daniel Pertot, René Reimann, and Dominik Schneble. Superfluidity of interacting bosonic mixtures in optical lattices. *Phys. Rev. Lett.*, 105:045303, Jul 2010.
- [84] Henrik Bruus and Karsten Flensberg. *Many-body quantum theory in condensed matter physics: an introduction*. OUP Oxford, 2004.
- [85] GM Moy, JJ Hope, and CM Savage. Born and markov approximations for atom lasers. *Physical Review A*, 59(1):667, 1999.
- [86] MW Jack, M Naraschewski, MJ Collett, and DF Walls. Markov approximation for the atomic output coupler. *Physical Review A*, 59(4):2962, 1999.
- [87] Fabrice Gerbier, Philippe Bouyer, and Alain Aspect. Quasicontinuous atom laser in the presence of gravity. *Physical Review Letters*, 86(21):4729, 2001.
- [88] Baptiste Lecoutre. *Transport quantique d’atomes ultra-froids en milieu désordonné: Temps de diffusion élastique et fonctions spectrales*. PhD thesis, Université Paris-Saclay, 2020.
- [89] Jérémie Richard, Lih-King Lim, Vincent Denechaud, Valentin V Volchkov, Baptiste Lecoutre, Musawwadah Mukhtar, Fred Jendrzejewski, Alain Aspect, Adrien Signoles, Laurent Sanchez-Palencia, et al. Elastic scattering time of matter waves in disordered potentials. *Physical Review Letters*, 122(10):100403, 2019.
- [90] Michael Schreiber and Heiko Grussbach. Multifractal wave functions at the anderson transition. *Physical review letters*, 67(5):607, 1991.
- [91] AD Mirlin and Ferdinand Evers. Multifractality and critical fluctuations at the anderson transition. *Physical Review B*, 62(12):7920, 2000.
- [92] VE Kravtsov, IV Lerner, BL Altshuler, and AG Aronov. Universal spectral correlations at the mobility edge. *Physical review letters*, 72(6):888, 1994.

-
- [93] Alberto Rodriguez, Louella J Vasquez, Keith Slevin, and Rudolf A Römer. Multifractal finite-size scaling and universality at the anderson transition. *Physical Review B*, 84(13):134209, 2011.
- [94] Ferdinand Evers and Alexander D Mirlin. Anderson transitions. *Reviews of Modern Physics*, 80(4):1355, 2008.
- [95] Nikita Medvedev and Igor Milov. Electron-phonon coupling in metals at high electronic temperatures. *Physical Review B*, 102(6):064302, 2020.
- [96] Hideo Aoki. Critical behaviour of extended states in disordered systems. *Journal of Physics C: Solid State Physics*, 16(6):L205, 1983.
- [97] Miklós Antal Werner, Eugene Demler, Alain Aspect, and Gergely Zaránd. Selective final state spectroscopy and multifractality in two-component ultracold bose-einstein condensates: a numerical study. *arXiv preprint arXiv:1709.08993*, 2017.
- [98] Hideki Funamizu and Jun Uozumi. Generation of fractal speckles by means of a spatial light modulator. *Optics express*, 15(12):7415–7422, 2007.
- [99] S. R. Granade K. M. O’Hara, M. E. Gehm and J. E. Thomas. Scaling laws for evaporative cooling in time-dependent optical traps. *Physical Review A*, 64:051403, 2001.
- [100] M. Robert de Saint Vincent R.A. Nyman A. Aspect T. Bourdel J.-F. Clément, J.-P. Brantut and P. Bouyer. All-optical runaway evaporation to bose-einstein condensation. *Physical Review A*, 79:061406, 2009.
- [101] Nathan Gemelke Cheng Chin Chen-Lung Hung, Xibo Zhang. Accelerating evaporative cooling of atoms into bose-einstein condensation in optical traps. *Physical Review A*, 78:011604, 2008.
- [102] Felix Bloch. Über die quantenmechanik der elektronen in kristallgittern. *Zeitschrift für physik*, 52(7):555–600, 1929.
- [103] Alexander D Mirlin. Statistics of energy levels and eigenfunctions in disordered systems. *Physics Reports*, 326(5-6):259–382, 2000.
- [104] RC Kuhn, O Sigwarth, C Miniatura, D Delande, and CA Müller. Coherent matter wave transport in speckle potentials. *New Journal of Physics*, 9(6):161, 2007.

-
- [105] S. E. Skipetrov, A. Minguzzi, B. A. van Tiggelen, and B. Shapiro. Anderson localization of a bose-einstein condensate in a 3d random potential. *Phys. Rev. Lett.*, 100:165301, Apr 2008.
- [106] M Piraud, L Pezzé, and L Sanchez-Palencia. Quantum transport of atomic matter waves in anisotropic two-dimensional and three-dimensional disorder. *New Journal of Physics*, 15(7):075007, jul 2013.
- [107] Marie Piraud, Laurent Sanchez-Palencia, and Bart van Tiggelen. Anderson localization of matter waves in three-dimensional anisotropic disordered potentials. *Phys. Rev. A*, 90:063639, Dec 2014.
- [108] A. Marte, T. Volz, J. Schuster, S. Dürr, G. Rempe, E. G. M. van Kempen, and B. J. Verhaar. Feshbach resonances in rubidium 87: Precision measurement and analysis. *Phys. Rev. Lett.*, 89:283202, Dec 2002.
- [109] Michael Schreiber, Sean S. Hodgman, Pranjal Bordia, Henrik P. Lüschen, Mark H. Fischer, Ronen Vosk, Ehud Altman, Ulrich Schneider, and Immanuel Bloch. Observation of many-body localization of interacting fermions in a quasirandom optical lattice. *Science*, 349(6250):842–845, 2015.
- [110] Marcel Filoche and Svitlana Mayboroda. Universal mechanism for anderson and weak localization. *Proceedings of the National Academy of Sciences*, 109(37):14761–14766, 2012.
- [111] T. Karpiuk, N. Cherroret, K. L. Lee, B. Grémaud, C. A. Müller, and C. Miniatura. Coherent forward scattering peak induced by anderson localization. *Phys. Rev. Lett.*, 109:190601, Nov 2012.
- [112] T. Micklitz, C. A. Müller, and A. Altland. Echo spectroscopy of anderson localization. *Phys. Rev. B*, 91:064203, Feb 2015.
- [113] Clément Hainaut, Isam Manai, Jean-François Clément, Jean Claude Garreau, Pascal Szriftgiser, Gabriel Lemarié, Nicolas Cherroret, Dominique Delande, and Radu Chicireanu. Controlling symmetry and localization with an artificial gauge field in a disordered quantum system. *Nature Communications*, 9(1):1382, 2018.
- [114] Sanjib Ghosh, Christian Miniatura, Nicolas Cherroret, and Dominique Delande. Coherent forward scattering as a signature of anderson metal-insulator transitions. *Phys. Rev. A*, 95:041602, Apr 2017.

-
- [115] Maxime Martinez, Gabriel Lemarié, Bertrand Georgeot, Christian Miniatura, and Olivier Giraud. Coherent forward scattering peak and multifractality. *Phys. Rev. Research*, 3:L032044, Aug 2021.
- [116] T. Schulte, S. Drenkelforth, J. Kruse, W. Ertmer, J. Arlt, K. Sacha, J. Zakrzewski, and M. Lewenstein. Routes towards anderson-like localization of bose-einstein condensates in disordered optical lattices. *Phys. Rev. Lett.*, 95:170411, Oct 2005.
- [117] L. Fallani, J. E. Lye, V. Guarrera, C. Fort, and M. Inguscio. Ultracold atoms in a disordered crystal of light: Towards a bose glass. *Phys. Rev. Lett.*, 98:130404, Mar 2007.
- [118] B. DEMARCO and D. S. JIN. Onset of fermi degeneracy in a trapped atomic gas. *Science*, 285:1703–1706, 1999.
- [119] Franco Dalfovo, Stefano Giorgini, Lev P Pitaevskii, and Sandro Stringari. Theory of bose-einstein condensation in trapped gases. *Reviews of modern physics*, 71(3):463, 1999.
- [120] C. J. Pethick and H. Smith. *Bose–Einstein condensation in dilute gases*. Cambridge university press, 2008.
- [121] Daniel Steck. Rubidium 87 d line data. 2003.
- [122] DJ Wineland and HG Dehmelt. Principles of the stored ion calorimeter. *Journal of Applied Physics*, 46(2):919–930, 1975.
- [123] Theodor W Hänsch and Arthur L Schawlow. Cooling of gases by laser radiation. *Optics Communications*, 13(1):68–69, 1975.
- [124] Paul D Lett, William D Phillips, SL Rolston, Carol E Tanner, RN Watts, and CI Westbrook. Optical molasses. *JOSA B*, 6(11):2084–2107, 1989.
- [125] L. Sanchez-Palencia, D. Clément, P. Lugan, P. Bouyer, G. V. Shlyapnikov, and A. Aspect. Anderson localization of expanding bose-einstein condensates in random potentials. *Phys. Rev. Lett.*, 98:210401, May 2007.
- [126] Nicolas Cherroret, Tomasz Karpiuk, Cord A. Müller, Benoît Grémaud, and Christian Miniatura. Coherent backscattering of ultracold matter waves: Momentum space signatures. *Phys. Rev. A*, 85:011604, Jan 2012.

-
- [127] Berthold Jäck, Fabian Zinser, Elio J König, Sune NP Wissing, Anke B Schmidt, Markus Donath, Klaus Kern, and Christian R Ast. Visualizing the multifractal wave functions of a disordered two-dimensional electron gas. *Physical Review Research*, 3(1):013022, 2021.
- [128] Dominique Delande and Giuliano Orso. Mobility edge for cold atoms in laser speckle potentials. *Physical review letters*, 113(6):060601, 2014.
- [129] Adrien Signoles, Baptiste Lecoutre, Jérémie Richard, Lih-King Lim, Vincent Denechaud, Valentin V Volchkov, Vasiliki Angelopoulou, Fred Jendrzejewski, Alain Aspect, Laurent Sanchez-Palencia, et al. Ultracold atoms in disordered potentials: elastic scattering time in the strong scattering regime. *New Journal of Physics*, 21(10):105002, 2019.